COMPATIBLE-STRAIN MIXED FINITE ELEMENT METHODS FOR NONLINEAR ELASTICITY

A Dissertation
Presented to
The Academic Faculty

By

Mostafa Faghih Shojaei

In Partial Fulfillment
of the Requirements for the Degree
Doctor of Philosophy in the
School of Civil and Environmental Engineering

Georgia Institute of Technology

May 2019

COMPATIBLE-STRAIN MIXED FINITE ELEMENT METHODS FOR NONLINEAR ELASTICITY

Approved by:

Dr. Arash Yavari, Advisor
School of Civil and Environmental Engineering
Georgia Institute of Technology

Dr. Phanish Suryanarayana
School of Civil and Environmental Engineering
Georgia Institute of Technology

Dr. Julian J. Rimoli
School of Aerospace Engineering
Georgia Institute of Technology

Dr. Ting Zhu
School of Mechanical Engineering
Georgia Institute of Technology

Dr. Hamid Garmestani
School of Materials Science and Engineering
Georgia Institute of Technology

Date Approved: April 16, 2019

ACKNOWLEDGEMENTS

I am very grateful to my advisor, Dr. Arash Yavari, for his support, insight, and guidance in the course of my Ph.D. research. I extend my gratitude to my committee members for their support, and particularly to Dr. Julian Rimoli and Dr. Phanish Suryanarayana for the discussions that were helpful in the development of this work. I also thank Dr. Arzhang Angoshtari for his valuable contributions in the early stages of this work.

TABLE OF CONTENTS

LIST OF TABLES

LIST OF FIGURES

SUMMARY

A new family of mixed finite element methods–compatible-strain mixed finite element methods (CSFEMs)–are introduced for compressible and incompressible nonlinear elasticity problems in dimensions two and three. A Hu-Washizu-type mixed formulation is considered and the displacement, the displacement gradient, and the first Piola-Kirchhoff stress are chosen as the independent unknowns. To impose incompressibility, a pressure-like field is introduced as the fourth independent unknown. Using the Hilbert complexes of nonlinear elasticity that describe the kinematics and the kinetics of motion, we identify the solution spaces that the independent unknown fields belong to. In particular, we define the displacement in H^1, the displacement gradient in $H(\mathrm{curl})$, the stress in $H(\mathrm{div})$, and the pressure field in L^2. The test spaces of the mixed formulations are chosen to be the same as their corresponding solution spaces. In a conforming setting, we approximate the solution and the test spaces with some piecewise polynomial subspaces of them. Among these approximation spaces are the tensorial analogues of the standard Nédélec and Raviart-Thomas finite element spaces of vector fields. This approach results in mixed finite element methods that, by construction, satisfy both the Hadamard jump conditions and the continuity of traction at the discrete level regardless of the refinement level of the mesh. This, in particular, makes CSFEMs quite efficient for modeling heterogeneous solids. We assess the performance of CSFEMs by solving several numerical examples in dimensions two and three and demonstrate their good performance for bending problems, for bodies with complex geometries, for different material models, and in the nearly incompressible regime. Using CSFEMs, one can model deformations with very large strains and accurately approximate stresses and the pressure field. Moreover, in our numerical examples, we do not observe any numerical artifacts such as checkerboarding of pressure, hourglass instability, or locking.

CHAPTER 1
INTRODUCTION

Developing well-performing finite element methods for large deformations of solids is a challenging problem. It is well-known that in many important applications such as bending problems, domains with complex geometries, and in the near-incompressible regime, the standard single-field finite element methods for nonlinear elasticity written in terms of the displacement field have poor convergence behavior. It is also well-established that simple extensions of the well-performing methods for small deformations of solids to large deformations can lead to numerical schemes with poor performances due to the appearance of numerical artifacts and unphysical instabilities (see [1, 2, 3] and references therein).

Numerous approaches have been proposed in the literature for obtaining better numerical methods for large deformations, some of which include: mesh-free methods [4, 5]; the numerical manifold method [6, 7]; methods based on the enrichment of trial spaces including the partition of unity method [8, 9], the generalized finite element method [10, 11, 12], and the extended finite element method [13, 14, 15]; methods using reduced integration and stabilization [16, 17, 18, 19]; and mixed finite element methods [20, 21, 22].

Mixed finite element methods are based on saddle-point variational principles. For nonlinear elasticity, there are various choices of saddle-point principles such as the two-field Hellinger-Reissner principle and the three-field Hu-Washizu principle, e.g. see [21, §1.5]. Mixed methods such as enhanced strain methods have good convergence behavior for bending problems and also in the incompressible and near-incompressible regimes. Other features of mixed methods include good accuracy for coarse meshes, no sensitivity against mesh distortions, and simple implementation of nonlinear constitutive relations. Moreover, since the stress is usually considered as an independent variable

in mixed methods, it can be computed with higher accuracy. On the other hand, mixed methods are more complicated than standard methods based on single-field formulations and one has to consider several degrees of freedom for each element. It is also well-known that the trial and test spaces of mixed methods need to satisfy certain compatibility conditions, e.g. the Ladyzhenskaya-Babuška-Brezzi condition [23, 24, 25]. Arbitrary selections of trial spaces can lead to numerical artifacts such as the checkerboard instability or the locking effect, e.g. see [26, §4.2]. Another unphysical instability observed in mixed methods is the hourglass instability of enhanced strain methods [1].

A novel approach for deriving mixed finite element methods for compressible linear elasticity was introduced by Arnold *et al.* [27]. They obtained the first stable mixed finite element methods for the displacement-stress formulation of 2D linear elasticity by using the notion of differential complexes. Differential complexes are sequences of linear operators such that the image of each operator is a subset of the kernel of the next operator. The differential complex of linear elasticity introduced by Kröner [28] contains information about topological properties of bodies. Arnold *et al.* [27] obtained compatible finite element spaces for the mixed formulation of linear elasticity by appropriately discretizing the linear elasticity complex such that the discrete complexes preserve all the topological information of the linear elasticity complex. By generalizing this approach, Arnold and his coworkers [29, 30] showed that it is also possible to obtain stable mixed methods for some linear operators associated to specific classes of differential complexes.

It has been known for quite some time in the finite element literature that internal constraints, and in particular, incompressibility constraint should be treated very carefully to avoid numerical artifacts and instabilities. For incompressible solids, addition of the volume-preserving constraint and the pressure as an extra independent unknown results in a saddle-point problem. The well-posedness of a saddle-point problem requires that the two independent unknowns, which are the displacement and pressure in this context, are defined in some compatible spaces. This requirement is commonly represented by

an inf-sup condition referred to as the LBB condition after the celebrated works of Ladyzhenskaya [23], Babuška [24], and Brezzi [25]. Satisfaction of this condition at the discrete level is a necessary condition for the stability of the finite element method and causes some complications for constructing the finite element spaces of displacement and pressure. There are different approaches for constructing finite elements that satisfy the LBB conditions, among which are enriching the space of displacement with some bubble functions in each element, e.g., mini element (triangular with $\mathbb{P}1 \bigoplus b3 - \mathbb{P}1$) [31], using quadratic or higher-order shape functions, e.g., quadrilateral Taylor-Hood element ($\mathbb{Q}2 - \mathbb{Q}1$) [32] or its triangular variant ($\mathbb{P}2 - \mathbb{P}1$) [33], with the proof of stability given for both by Bercovier *et al.* [34], pairing a composite displacement element with a piecewise constant pressure element, e.g., [34], and using non-conforming displacement elements, e.g., Crouzeix *et al.* [35]. All these well-known methods are mainly developed for the Stokes saddle-point problem and the proofs of stability are given for linear two-field mixed formulations. Although, these elements can be used for modeling incompressible linear solids, they may not perform well in nonlinear problems, especially in capturing large strains. It is shown in [2] that some of the above elements may exhibit some numerical artifacts when used in incompressible nonlinear elasticity. It is further highlighted that increasing the amplitude of the external loads and the way the incompressibility constraint is imposed may affect the performance of the above elements in nonlinear problems. As another example, see the result given in [36, §5.2] obtained by the modified quadratic displacement-linear pressure with hourglass control (CPE6MH) in ABAQUS, which shows the shortcomings of the above approaches in capturing large strains in incompressible nonlinear elasticity problems.

Over the years different approaches have been presented to avoid the difficulties associated with a saddle-point problem, among which are choosing different trial and test spaces (Petrov-Galerkin method), statically condensing out the pressure from the corresponding matrix formulations, and stabilizing the system by adding some extra

terms to the mixed formulations to alter the saddle-point problem. These approaches may be implemented individually or a combination of more than one approach may be used. Another common saddle-point problem in elasticity is the stress-displacement mixed formulation associated with the Hellinger-Reissner principle, which has mostly been implemented for linear elasticity. In this method, spaces of stress and displacement must be defined carefully. Inspired by the work of Hughes *et al.* [37] for the Stokes problem, Franca *et al.* [38] developed a mixed Petrov-Galerkin finite element method for nearly incompressible linear elastic solids. The method is based on the modification of the weak formulation associated with the critical point of the Hellinger-Reissner principle by adding some additional terms to improve stability without compromising consistency. The goal in such methods is an equal-order conforming approximation of the displacement and the Cauchy stress.

For the (nearly) incompressible nonlinear elasticity problems, Simo *et al.* [39] proposed a kinematic splitting of the volumetric and volume-preserving parts of the deformation gradient and used it in a three-field form of the Hu-Washizu variational principle. For compressible and near incompressible nonlinear solids, Simo *et al.* [20] used an additive decomposition of displacement gradient into a compatible part and an enhanced part. For a continuum problem the enhanced part vanishes pointwise. However, they observed that at the discrete level using mixed finite elements the enhanced part does not vanish and leads to a better representation of strain. For transversely isotropic incompressible solids, Weiss *et al.* [40] exploited Simo *et al.* [39]'s idea of splitting the deformation gradient and used the deformation mapping, dilation, and pressure as independent variables in their mixed finite element formulation of incompressible transversely isotropic solids. For imposing the incompressibility constraint, they used an augmented Lagrangian method. Lamichhane [41] developed a displacement-pressure mixed finite element method for 2D nearly incompressible nonlinear elasticity. Both the trial and test spaces of displacement are discretized using linear Lagrange finite elements enriched with standard cubic bubble

functions so that the inf-sup condition is satisfied. In addition, using a Petrov-Galerkin approach, the trial space of pressure is discretized by linear Lagrange finite elements, but the shape functions of the test space of pressure are obtained by assuming a biorthogonality condition between the trial and test spaces of pressure. Using this setting, one can statically condense out the pressure from the corresponding algebraic system and solve a displacement-based problem. Chi *et al.* [36] used polygonal finite elements to discretize a two-field mixed formulation of 2D (nearly) incompressible nonlinear elasticity. The displacements are interpolated by choosing the barycentric coordinates over each polygon as the shape functions and the values of displacements at the polygon vertices as the degrees of freedom, which results in a C^0 approximation over the entire domain. The pressure is approximated by a piecewise constant scalar over each polygon. Their numerical studies showed that the method is stable and is able to capture very large stretches.

In this work, we introduce a new family of mixed finite element methods–*compatible-strain mixed finite element methods* (CSFEMs)–for compressible and incompressible nonlinear elasticity problems in dimensions two and three, see also Angoshtari *et al.* [42] and Faghih Shojaei and Yavari [43, 44].

We write a four-field mixed formulation of incompressible nonlinear elastostatics in terms of the displacement, displacement gradient, the first Piola-Kirchhoff stress, and a pressure-like field by extremizing a Hu-Washizu-type functional. Eliminating the pressure and the incompressibility constraint from the four-field mixed formulation reduces it to a three-field mixed formulation of compressible solids. Comparing with [42], in this work, we use a symmetric mixed formulation, which is computationally more efficient. we impose the displacement boundary conditions strongly and the traction boundary conditions weakly. More specifically, only the displacement boundary condition is imposed by the standard elimination approach in the system of algebraic equations; the traction boundary condition is built into the governing equations, and hence, there is no need to directly compute the degrees of freedom of stress on the boundary. Based on our

observation of the numerical examples, we have concluded that this treatment of the boundary conditions improves the accuracy and robustness of the mixed FEMs and is also easier to implement.

We use the Hilbert complexes of nonlinear elasticity [45, 46], which are suitable for describing the kinematics and the kinetics of large deformations, to identify the spaces of the four independent unknown field variables. In particular, we define the displacement in H^1, the displacement gradient in $H(\mathrm{curl})$, the stress in $H(\mathrm{div})$, and the pressure field in L^2. This setting is different from the ones that are commonly used for the mixed formulation of linear elasticity written based on the Hellinger-Reissner principle, where the Cauchy stress and the displacement are defined in a symmetric $H(\mathrm{div})$ space and L^2, respectively, e.g., see [27, 47]. Other variants of the mixed stress-displacement method for linear elasticity were introduced in [48] and[49]. In[48], the displacement is assumed in H^1 and stress in a symmetric L^2 space, while in[49] the displacement is assumed in $H(\mathrm{curl})$ and stress is approximated by a symmetric non-conforming $H(\mathrm{div})$ space. Although in some aspects the above-mentioned formulations are similar to our work, they cannot be used in drawing any conclusion on the convergence or stability; linear and nonlinear elasticity are quite different and the mixed formulation of the present work is based on a Hu-Washizu-type functional, which is not directly related to the Hellinger-Reissner principle. The main difference between our methods and the enhanced strain methods [20] is that the displacement gradient is implicitly assumed to be of L^2-class in enhanced strain methods.

Next, in a conforming setting, we approximate the solution and the test spaces of the mixed formulations with some piecewise polynomial subspaces of them. Among these approximation spaces are the tensorial analogues of the Nédélec and Raviart-Thomas finite element spaces of vector fields. This approach results in mixed finite element methods that are structure preserving in the sense that the differential complex structure of nonlinear elasticity [45] is preserved at the discrete level. In particular, in our mixed finite element methods for compressible and incompressible nonlinear elasticity, both the

Hadamard jump conditions and the continuity of traction are satisfied at the discrete level independently of the refinement level of the mesh. The Hadamard jump condition is a necessary compatibility condition for displacement gradient, which inspired us to call the introduced methods *compatible-strain* mixed finite element methods. The continuity of traction is also required by localization of the balance of linear momentum.

We extend CSFEMs to 3D compressible and incompressible nonlinear elasticity by using $H(\mathrm{curl})$ and $H(\mathrm{div})$-conforming tetrahedral elements, see also Faghih Shojaei *et al.* [44]. This work is quite challenging simply because one cannot use the same approach of 2D to develop CSFEMs in 3D. More precisely, we show that keeping the same mixed formulations and finite element spaces of 2D and just switching triangular elements with the counterpart tetrahedron elements always result in singular mixed methods in 3D. Therefore, more modifications are needed. To overcome this issue, we added some stabilization terms to the mixed formulations without compromising the consistency of the discretization scheme. We also enriched the first-order finite element space of strain by adding some higher order $H(\mathrm{curl})$-conforming bubble functions to its basis. These modifications can also help to introduce a convergent mixed method with a fewer degrees of freedom, which is greatly beneficial for computationally intensive 3D problems. An example of such modifications is the work of Hughes *et al.* [37] on the Stokes problem, where they introduced a stabilized mixed finite element method using an equal-order C^0 interpolation of both velocity and pressure. Furthermore, inspired by the work of Hughes *et al.* [37], Franca *et al.* [38] developed a mixed finite element method for nearly incompressible linear elastic solids by adding stabilization terms to the weak formulation associated with the critical point of the Hellinger-Reissner principle, and Klaas *et al.* [50] developed a stabilized displacement-pressure mixed finite element method for 3D finite elasticity by using linear shape functions for both displacement and pressure. In these works, the combinations of the finite element spaces are unstable according to the Ladyzhenskaya-Babuška-Brezzi (LBB) condition and result in unphysical solutions.

However, adding the stabilization terms resulted in convergent mixed methods.

We study the performance of CSFEMs by solving several numerical examples. We observe that these methods preform well for bending problems, in the near incompressible and incompressible regimes, for bodies with complex geometries, and in capturing very large strains. We observe that CSFEMs are capable of accurately approximating stress and pressure. They also perform well in problems that standard enhanced strain methods suffer from the hourglass instability or the standard two-field mixed methods suffer from checkerboard instability, numerical artifacts, or the locking phenomenons. We also show that CSFEMs provide an efficient framework for modeling inhomogeneities.

This work is organized as follows. In Chapter 2, we introduce the mixed formulations that we will later use for CSFEMs. In §2.1, we first discuss some preliminaries and then review the Hilbert complexes that describe the kinematics and the kinetics of nonlinear elasticity. In §2.2, by defining suitable Hu-Washizu-type energy functionals, we derive a three-field mixed formulation for compressible elastostatics and a four-field mixed formulation for incompressible elastostatics. The solution and the test spaces of theses mixed formulations are the underlying spaces of the Hilbert complexes of nonlinear elasticity. In Chapter 3 (Chapter 4), we discuss the finite element approximations of the mixed formulations for 2D (3D) nonlinear elasticity. In §3.1 (§4.1), we discuss the discrete versions of the Hilbert complexes in dimension two (three) using some polynomial tensor fields. In §3.2 (§4.2), we define the reference finite elements for the displacement, displacement gradient, stress, and pressure in 2D (3D). Moreover, we discuss some linear mappings, winch preserve the structure of their domains, and use them to generate the finite elements of an arbitrary element from their reference counterparts. In §3.3 (§4.3), we define the 2D (3D) finite element spaces. In §3.4 (§4.4), we introduce CSFEMs for 2D (3D) compressible and incompressible nonlinear elasticity. The implementation of CSFEMs for 2D (3D) nonlinear elasticity is the subject of §3.5 and §3.6 (§4.5 and §4.6). We discuss the solvability and stability of 2D (3D) elements in §3.7 (§4.7). To study the performance of

CSFEMs, we consider several numerical examples in Chapter 5 for both compressible and incompressible solids in dimensions two and three. Finally, in Chapter 6, we give some concluding remarks. We also we briefly discuss the application of CSFEMs for nonlinear elastic solids with distributed finite eigenstrains.

CHAPTER 2

MIXED FORMULATIONS FOR NONLINEAR ELASTICITY

In this chapter, we write weak formulations for compressible and incompressible nonlinear elasticity problems in dimensions two and three, which will be used for obtaining mixed finite element methods.

2.1 Preliminaries

We first briefly review some definitions and notation, and then discuss the relations between some Hilbert complexes and the kinematics and kinetics of motion of nonlinear solids. Next based on these relationships, we will define the domains of definition of displacement, displacement gradient, stress, and pressure, the four independent field variables that we use in our mixed formulations.

Assume that the reference configuration $\mathcal{B} \subset \mathbb{R}^n$, $n = 2, 3$ is a bounded domain with the boundary $\partial\mathcal{B}$. Let $\{\mathrm{X}^I\}$, $I = 1, \ldots, n$ be the Cartesian coordinates of $\mathbb{R}^n$, $n = 2, 3$. For any vector field $\boldsymbol{U}$ and any $\binom{2}{0}$-tensor field $\boldsymbol{T}$ in $\mathbb{R}^n$, one can define a $\binom{2}{0}$-tensor $\mathbf{grad}\,\boldsymbol{U}$ and a vector field $\mathbf{div}\,\boldsymbol{T}$ with components

$$(\mathbf{grad}\,\boldsymbol{U})^{IJ} := \partial U^I/\partial \mathrm{X}^J \quad \text{and} \quad (\mathbf{div}\,\boldsymbol{T})^I := \partial T^{IJ}/\partial \mathrm{X}^J, \tag{2.1}$$

where summation convention for repeated indices is assumed. In $\mathbb{R}^3$, one can also define a $\binom{2}{0}$-tensor as

$$(\mathbf{curl}\,\boldsymbol{T})^{IJ} := \varepsilon_{JKL}\partial T^{IL}/\partial \mathrm{X}^K, \tag{2.2}$$

where ε_{JKL} is the standard permutation symbol. In addition, one can define the operators $\mathbf{c}$ and $\mathbf{s}$ in $\mathbb{R}^2$, with $\mathbf{c}(\boldsymbol{T})$ being a vector field (the 2D curl operator) and $\mathbf{s}(\boldsymbol{U})$ being a

$\binom{2}{0}$-tensor field given by

$$\mathbf{c}(\boldsymbol{T}))^I := \partial T^{I2}/\partial \mathrm{X}^1 - T^{I1}/\partial \mathrm{X}^2 \quad \text{and} \quad (\mathbf{s}(\boldsymbol{U}))^{IJ} := (\partial U^I/\partial \mathrm{X}^2)\delta^{1J} - (\partial U^I/\partial \mathrm{X}^1)\delta^{2J}, \tag{2.3}$$

where δ^{IJ} is the Kronecker delta.

Let $L^2(\mathcal{B})$, $L^2(T\mathcal{B})$, and $L^2(\otimes^2 T\mathcal{B})$ be the spaces of square integrable scalar fields, vector fields, and $\binom{2}{0}$-tensor fields on $\mathcal{B}$, respectively. Consider the following spaces:

$$\begin{aligned} H^1(T\mathcal{B}) &:= \left\{\boldsymbol{U} \in L^2(T\mathcal{B}) : \mathbf{grad}\, \boldsymbol{U} \in L^2(\otimes^2 T\mathcal{B})\right\}, \\ H^{\mathbf{d}}(\mathcal{B}) &:= \left\{\boldsymbol{T} \in L^2(\otimes^2 T\mathcal{B}) : \mathbf{div}\, \boldsymbol{T} \in L^2(T\mathcal{B})\right\}, \\ H^{\mathbf{c}}(\mathcal{B}) &:= \left\{\boldsymbol{T} \in L^2(\otimes^2 T\mathcal{B}) : \mathbf{curl}\, \boldsymbol{T} \in L^2(\otimes^2 T\mathcal{B})\right\}, \quad \text{for } \mathcal{B} \subset \mathbb{R}^3, \\ H^{\mathbf{c}}(\mathcal{B}) &:= \left\{\boldsymbol{T} \in L^2(\otimes^2 T\mathcal{B}) : \mathbf{c}(\boldsymbol{T}) \in L^2(T\mathcal{B})\right\}, \qquad \text{for } \mathcal{B} \subset \mathbb{R}^2. \end{aligned} \tag{2.4}$$

Note that the partial derivatives and operators in the above spaces are defined in the distributional sense (weak sense). For any distribution f, which may not be differentiable pointwise, we extend the notion of derivative to a linear mapping $\frac{\partial f}{\partial \mathrm{X}^I} : \mathcal{D}(\mathcal{B}) \ni \phi \longmapsto \int_{\mathcal{B}} \frac{\partial f}{\partial \mathrm{X}^I}\phi \, dA = -\int_{\mathcal{B}} f \frac{\partial \phi}{\partial \mathrm{X}^I} \, dA \in \mathbb{R}$, where $\mathcal{D}(\mathcal{B})$ is the vector space of smooth functions with compact support in $\mathcal{B}$. In the same context, we can similarly extend the operators defined in (2.1), (2.2), and (2.3), e.g., the distributional (or weak) divergence is calculated as $\int_{\mathcal{B}} \mathbf{div}\, \boldsymbol{v}\, \phi = -\int_{\mathcal{B}} \langle \boldsymbol{v}, \mathbf{grad}\, \phi \rangle$, where $\langle , \rangle$ is the standard inner product in $\mathbb{R}^n$.

Let us assume that $\mathcal{B} \subset \mathbb{R}^2$. Then, for any vector field $\boldsymbol{V}$ in $H^1(T\mathcal{B})$, one can show that

$$\mathbf{c}(\mathbf{grad}(\boldsymbol{V})) = \mathbf{0} \quad \text{and} \quad \mathbf{div}(\mathbf{s}(\boldsymbol{V})) = \mathbf{0}. \tag{2.5}$$

Owing to the above relations and the definition of the above spaces, one can extend the

linear operators of (2.1) and (2.3) to the following mappings:

$$\begin{aligned} \mathbf{grad} : H^1(T\mathcal{B}) \to H^{\mathbf{c}}(\mathcal{B}), \qquad \mathbf{c} : H^{\mathbf{c}}(\mathcal{B}) \to L^2(T\mathcal{B}), \\ \mathbf{s} : H^1(T\mathcal{B}) \to H^{\mathbf{d}}(\mathcal{B}), \quad \mathbf{div} : H^{\mathbf{d}}(\mathcal{B}) \to L^2(T\mathcal{B}). \end{aligned} \tag{2.6}$$

One can concisely write (2.5) and (2.6) using the following Hilbert complexes for $\mathcal{B} \subset \mathbb{R}^2$ [45, 46]:

$$0 \longrightarrow H^1(T\mathcal{B}) \xrightarrow{\mathbf{grad}} H^{\mathbf{c}}(\mathcal{B}) \xrightarrow{\mathbf{c}} L^2(T\mathcal{B}) \longrightarrow 0, \tag{2.7a}$$

$$0 \longrightarrow H^1(T\mathcal{B}) \xrightarrow{\mathbf{s}} H^{\mathbf{d}}(\mathcal{B}) \xrightarrow{-\mathbf{div}} L^2(T\mathcal{B}) \longrightarrow 0, \tag{2.7b}$$

where the first arrows on the left are trivial operators, which send zero to zero, and the last arrows on the right indicate the zero operator, which maps the L^2-space to zero. We use $-\mathbf{div}$ instead of $\mathbf{div}$ in the second complex, so that (2.7b) is the dual complex of (2.7a). Assuming that $\mathcal{B} \subset \mathbb{R}^3$, one can show that $\mathbf{curl}\,(\mathbf{grad}\,\boldsymbol{Y}) = \mathbf{0}$ and $\mathbf{div}(\mathbf{curl}\,\boldsymbol{T}) = \mathbf{0}$. Hence, one can write the following differential complex for $\mathcal{B} \subset \mathbb{R}^3$ [45, 46] :

$$0 \longrightarrow H^1(T\mathcal{B}) \xrightarrow{\mathbf{grad}} H^{\mathbf{c}}(\mathcal{B}) \xrightarrow{\mathbf{curl}} H^{\mathbf{d}}(\mathcal{B}) \xrightarrow{\mathbf{div}} L^2(T\mathcal{B}) \longrightarrow 0\,, \tag{2.8}$$

where the first arrow is a trivial operator sending zero to zero, and the last arrow indicates the zero operator mapping the L^2-space to zero.

Let $\boldsymbol{U}$, $\boldsymbol{K}$, and $\boldsymbol{P}$ be the displacement vector, the displacement gradient tensor, and the first Piola-Kirchhoff stress tensor, respectively. We choose these fields to be the primary variables in our description of nonlinear elasticity. This mixed formulation allows one to impose compatibility of displacement gradient and to accurately compute stresses by approximating them in some proper spaces that are given in (2.4). Note that both $\boldsymbol{K}$ and $\boldsymbol{P}$ are two-point tensors (and hence it does not even make sense to ask if they are symmetric). Therefore, the difficulties associated with imposing the symmetry of a tensor

in finite element approximation will not be encountered. See [27, 47] for the symmetry imposing issues encountered in finite element approximation of linear elasticity.

Next, we discuss the physical interpretation of the differential complexes defined above. Let $\boldsymbol{U}(\mathbf{X}) := \varphi(\mathbf{X}) - \mathbf{X}$, $\mathbf{X} \in \mathcal{B} \subset \mathbb{R}^2$, be the displacement field associated with a motion $\varphi : \mathcal{B} \to \mathbb{R}^2$. Then, $\boldsymbol{K} := \mathbf{grad}\, \boldsymbol{U}$ is the displacement gradient and $\mathbf{c}(\boldsymbol{K}) = \mathbf{0}$ is a necessary condition for the compatibility of $\boldsymbol{K}$. Therefore, $\boldsymbol{U}$ belongs to the domain of the operator $\mathbf{grad}$ and $\boldsymbol{K}$ belongs to the kernel of the operator $\mathbf{c}$. According to the Hilbert complex (2.7a), this is the case whenever $\boldsymbol{U} \in H^1(T\mathcal{B})$ and $\boldsymbol{K} \in \ker(\mathbf{c}) \subset H^{\mathbf{c}}(\mathcal{B})$. Moreover, in the absence of body force, the static equilibrium equation $\mathbf{div}\boldsymbol{P} = \mathbf{0}$ is the necessary condition for the existence of a stress function $\boldsymbol{\Psi}$ such that $\boldsymbol{P} = \mathbf{s}(\boldsymbol{\Psi})$. Therefore, $\boldsymbol{P}$ belongs to the kernel of the operator $\mathbf{div}$, which gives $\boldsymbol{P} \in \ker(\mathbf{d}) \subset H^{\mathbf{d}}(\mathcal{B})$, based on (2.7b). Note that the Hilbert complex (2.7a) is related to the kinematics of motion, while the Hilbert complex (2.7b) is related to the kinetics of motion. Give a motion $\varphi : \mathcal{B} \to \mathbb{R}^3$, $\mathbf{curl}\, \boldsymbol{K} = \mathbf{0}$ is the necessary condition for the compatibility of $\boldsymbol{K}$ and $\mathbf{div}\, \boldsymbol{P} = \mathbf{0}$ is the necessary condition for the existence of a stress function $\boldsymbol{\Psi}$ such that $\boldsymbol{P} = \mathbf{curl}\, \boldsymbol{\Psi}$. According to (2.8), this holds whenever $\boldsymbol{U} \in H^1(T\mathcal{B})$, $\boldsymbol{K} \in \ker(\mathbf{curl}) \subset H^{\mathbf{c}}(\mathcal{B})$, and $\boldsymbol{P} \in \ker(\mathbf{div}) \subset H^{\mathbf{d}}(\mathcal{B})$.

The deformation gradient is defined as $\boldsymbol{F} := \boldsymbol{I} + \boldsymbol{K}$, where $\boldsymbol{I}$ is the identity tensor, and $J := \det \boldsymbol{F}$ (in Cartesian coordinates for both the reference and current configurations). One can show that $dv = JdV$, where dV and dv are the volume elements (area elements in 2D) of the undeformed and deformed configurations, respectively. For incompressible solids, $J = 1$. To weakly impose $J - 1 = 0$, one considers a Lagrange multiplier p as an independent field variable, which physically is realized as a pressure-like variable. At the discrete level, the restriction of J to an element is a scaler describing the change of volume (change of area in 2D) of that element [51]. Hence, one can assume that discrete pressure p is also defined on each element, and in general, it is not continuous across the element interfaces in a mesh. Therefore, as a discontinuous scalar-valued field, $p \in L^2(\mathcal{B})$.

2.2 Mixed Formulations

Let ρ_0 be the mass density of the body $\mathcal{B} \subset \mathbb{R}^n$, $n = 2, 3$, and $\boldsymbol{B}$ be the body force per unit mass. For the sake of simplicity, we assume that the boundary of the body is a disjoint union of two subsets $\partial\mathcal{B} = \Gamma_d \sqcup \Gamma_t$ such that the boundary displacement $\overline{\boldsymbol{U}}$ is imposed on Γ_d and the boundary traction $\overline{\boldsymbol{T}}$ is imposed on Γ_t. Let $\boldsymbol{N}$ be the unit outward normal vector field of $\partial\mathcal{B}$ in the reference configuration. We consider a formulation of nonlinear elasticity in which displacement $\boldsymbol{U} \in H^1(T\mathcal{B})$, displacement gradient $\boldsymbol{K} \in H^{\mathbf{c}}(\mathcal{B})$, and the first Piola-Kirchhoff stress $\boldsymbol{P} \in H^{\mathbf{d}}(\mathcal{B})$ are the primary variables. We build the displacement boundary condition $\boldsymbol{U}\big|_{\Gamma_d} = \overline{\boldsymbol{U}}$ directly into the space of definition of $\boldsymbol{U}$, and define

$$H^1(T\mathcal{B}, \Gamma_d, \overline{\boldsymbol{U}}) := \left\{\boldsymbol{U} \in H^1(T\mathcal{B}) : \boldsymbol{U}|_{\Gamma_d} = \overline{\boldsymbol{U}}\right\} \quad \text{and} \quad H^1(T\mathcal{B}, \Gamma_d) := H^1(T\mathcal{B}, \Gamma_d, \mathbf{0}),$$

where $\overline{\boldsymbol{U}}$ is of $H^{1/2}$-class. Now, we set $\boldsymbol{U} \in H^1(T\mathcal{B}, \Gamma_d, \overline{\boldsymbol{U}})$, $\boldsymbol{K} \in H^{\mathbf{c}}(\mathcal{B})$, and $\boldsymbol{P} \in H^{\mathbf{d}}(\mathcal{B})$ and define a Hu-Washizu functional. The traction boundary condition $(\boldsymbol{P}\boldsymbol{N})\big|_{\Gamma_t} = \overline{\boldsymbol{T}}$ will be built into the functional. Let $\langle , \rangle$ be the standard inner product of $\mathbb{R}^n$. Also, suppose $\langle\!\langle , \rangle\!\rangle$ denotes the L^2-inner products of scalar, vector, and tensor fields, which are defined as $\langle\!\langle f, g \rangle\!\rangle := \int_{\mathcal{B}} f g \, dV$, $\langle\!\langle \boldsymbol{Y}, \boldsymbol{Z} \rangle\!\rangle := \int_{\mathcal{B}} Y^I Z^I dV$, and $\langle\!\langle \boldsymbol{S}, \boldsymbol{T} \rangle\!\rangle := \int_{\mathcal{B}} S^{IJ} T^{IJ} dV$, respectively. Let $\mathcal{D} := H^1(T\mathcal{B}, \Gamma_d, \overline{\boldsymbol{U}}) \times H^{\mathbf{c}}(\mathcal{B}) \times H^{\mathbf{d}}(\mathcal{B})$ and define a Hu-Washizu-type functional $\mathcal{I} : \mathcal{D} \to \mathbb{R}$ as

$$\mathcal{I}(\boldsymbol{U}, \boldsymbol{K}, \boldsymbol{P}) = \int_{\mathcal{B}} W(\mathbf{X}, \boldsymbol{K}) dV - \langle\!\langle \boldsymbol{P}, \boldsymbol{K} - \mathbf{grad}\, \boldsymbol{U} \rangle\!\rangle - \langle\!\langle \rho_0 \boldsymbol{B}, \boldsymbol{U} \rangle\!\rangle - \int_{\Gamma_t} \langle \overline{\boldsymbol{T}}, \boldsymbol{U} \rangle dA, \quad (2.9)$$

where $W(\mathbf{X}, \boldsymbol{K})$ is the stored energy function of a hyperelastic material. The energy function of an isotropic solid has the form $W = \widehat{W}(\mathbf{X}, I_1, I_2, I_3)$, where $I_1 = \operatorname{tr} \boldsymbol{C}$, $I_2 = \frac{1}{2}[(\operatorname{tr} \boldsymbol{C})^2 - \operatorname{tr} \boldsymbol{C}^2]$, and $I_3 = \det \boldsymbol{C}$ are the invariants of the right Cauchy-Green deformation tensor $\boldsymbol{C} = \boldsymbol{F}^{\mathsf{T}} \boldsymbol{F}$. In 2D, one has $W = \widehat{W}(\mathbf{X}, I_1, I_2)$, where $I_1 = \operatorname{tr} \boldsymbol{C}$ and $I_2 = \det \boldsymbol{C}$. Our formulation is not restricted to isotropic solids, however, in all our

numerical examples we assume isotropic solids. Note that $J = \sqrt{I_3}$ ($J = \sqrt{I_2}$ in 2D). If the material is incompressible, there is no volume change (area change in 2D), i.e., $J = 1$. Accordingly, we modify (2.9) by defining

$$\overline{\mathcal{I}}(\boldsymbol{U}, \boldsymbol{K}, \boldsymbol{P}, p) = \mathcal{I}(\boldsymbol{U}, \boldsymbol{K}, \boldsymbol{P})\Big|_{J(\boldsymbol{K})=1} + \int_{\mathcal{B}} p\, C\big(J(\boldsymbol{K})\big)\, dV, \tag{2.10}$$

where $p \in L^2(\mathcal{B})$ is a pressure-like scalar field that acts as a Lagrange multiplier in (2.10), to which we may refer simply as pressure, and $C : \mathbb{R}^+ \to \mathbb{R}$ is a smooth function such that $C(J) = 0$ if and only if $J = 1$. Two examples that have been used in the literature are $C(J) = J - 1$, and $C(J) = \ln J$.

Remark 1. One may define a pseudo energy function $\overline{W}(\mathbf{X}, \boldsymbol{K}, p) := \widehat{W}(\mathbf{X}, I_1, I_2, I_3)\big|_{I_3=1} + p\, C(J)$, and replace W in (2.9) with $\overline{W}$ to obtain the same $\overline{\mathcal{I}}$ in (2.10).

Remark 2. One may be tempted to think that an incompressible nonlinear elasticity problem can be numerically solved using a scheme for compressible nonlinear elasticity. This is not the case; a general constitutive equation for incompressible elasticity cannot be recovered from any compressible constitutive equation when some parameter(s) becomes larger and larger (or smaller and smaller). Instead, one must enforce the constraint $J = 1$ and this requires introducing a pressure field p.

For 3D computations, in order to improve the stability of the mixed finite element methods, we add a stabilizing term to (2.10) as

$$\mathcal{J}(\boldsymbol{U}, \boldsymbol{K}, \boldsymbol{P}, p) = \overline{\mathcal{I}}(\boldsymbol{U}, \boldsymbol{K}, \boldsymbol{P}, p) + \frac{\alpha}{2} \langle\!\langle \boldsymbol{K} - \mathbf{grad}\, \boldsymbol{U}, \boldsymbol{K} - \mathbf{grad}\, \boldsymbol{U} \rangle\!\rangle, \tag{2.11}$$

where $\alpha \geqslant 0$ is a penalty constant for enforcing $\boldsymbol{K} = \mathbf{grad}\, \boldsymbol{U}$. Extremizing $\mathcal{J}$ results in a mixed formulation of incompressible nonlinear elasticity.

To find the critical points of $\mathcal{J}$ given in (2.11), we proceed as follows. Let

$(\boldsymbol{U}+\epsilon_1\boldsymbol{\Upsilon},\boldsymbol{K}+\epsilon_2\boldsymbol{\kappa},\boldsymbol{P}+\epsilon_3\boldsymbol{\pi},p+\epsilon_4 q)\in\mathcal{D}\times L^2(\mathcal{B})$ such that $(\boldsymbol{U},\boldsymbol{K},\boldsymbol{P},p)\in\mathcal{D}\times L^2(\mathcal{B})$, $\epsilon_i\in\mathbb{R}$ for $i=1,...,4$, and $(\boldsymbol{\Upsilon},\boldsymbol{\kappa},\boldsymbol{\pi},q)\in H^1(T\mathcal{B},\Gamma_d)\times H^{\mathbf{c}}(\mathcal{B})\times H^{\mathbf{d}}(\mathcal{B})\times L^2(\mathcal{B})$ are arbitrary. Next, define

$$\widehat{\mathcal{J}}(\epsilon_1,\epsilon_2,\epsilon_3,\epsilon_4):=\mathcal{J}(\boldsymbol{U}+\epsilon_1\boldsymbol{\Upsilon},\boldsymbol{K}+\epsilon_2\boldsymbol{\kappa},\boldsymbol{P}+\epsilon_3\boldsymbol{\pi},p+\epsilon_4 q). \tag{2.12}$$

Note that

$$\frac{\partial}{\partial\epsilon_2}\int_{\mathcal{B}}\widetilde{W}\big(\mathbf{X},I_1(\boldsymbol{K}+\epsilon_2\boldsymbol{\kappa}),I_2(\boldsymbol{K}+\epsilon_2\boldsymbol{\kappa})\big)dV\Big|_{\epsilon_2=0}=\langle\!\langle\widetilde{\boldsymbol{P}}(\boldsymbol{K}),\boldsymbol{\kappa}\rangle\!\rangle,$$
$$\frac{\partial}{\partial\epsilon_2}\int_{\mathcal{B}}p\,C\big(J(\boldsymbol{K}+\epsilon_2\boldsymbol{\kappa})\big)dV\Big|_{\epsilon_2=0}=\langle\!\langle p\boldsymbol{Q}(\boldsymbol{K}),\boldsymbol{\kappa}\rangle\!\rangle,$$

where $\widetilde{W}=\widehat{W}(\mathbf{X},I_1,I_2,I_3)\big|_{I_3=1}$, $\widetilde{\boldsymbol{P}}(\boldsymbol{K})=\partial\widetilde{W}/\partial\boldsymbol{K}$ is the constitutive part of the stress, and $\boldsymbol{Q}(\boldsymbol{K})=\partial C/\partial\boldsymbol{K}=C'(J)(\boldsymbol{F}^{-1})^{\mathsf{T}}$ comes from enforcing the incompressibility condition $J=1$. Extremizing the Hu-Washizu functional requires that

$$\left(\frac{\partial\widehat{\mathcal{J}}}{\partial\epsilon_1},\frac{\partial\widehat{\mathcal{J}}}{\partial\epsilon_2},\frac{\partial\widehat{\mathcal{J}}}{\partial\epsilon_3},\frac{\partial\widehat{\mathcal{J}}}{\partial\epsilon_4}\right)\Bigg|_{\epsilon_i=0}=(0,0,0,0).$$

The result is the following weak formulation of the boundary-value problem for 3D incompressible nonlinear elastostatics:

Given a body force $\boldsymbol{B}$ of L^2-class, a boundary displacement $\overline{\boldsymbol{U}}$ on Γ_d of $H^{1/2}$-class, a boundary traction $\overline{\boldsymbol{T}}$ on Γ_t of L^2-class, and a stability constant $\alpha \geqslant 0$, find $(\boldsymbol{U}, \boldsymbol{K}, \boldsymbol{P}, p) \in H^1(T\mathcal{B}, \Gamma_d, \overline{\boldsymbol{U}}) \times H^{\mathbf{c}}(\mathcal{B}) \times H^{\mathbf{d}}(\mathcal{B}) \times L^2(\mathcal{B})$ such that

$$
\begin{aligned}
\langle\!\langle \boldsymbol{P}, \mathbf{grad}\, \boldsymbol{\Upsilon} \rangle\!\rangle + \alpha s_1(\boldsymbol{U}, \boldsymbol{K}, \boldsymbol{\Upsilon}) &= f(\boldsymbol{\Upsilon}), \ \forall \boldsymbol{\Upsilon} \in H^1(T\mathcal{B}, \Gamma_d), \\
\langle\!\langle \widetilde{\boldsymbol{P}}(\boldsymbol{K}), \boldsymbol{\kappa} \rangle\!\rangle - \langle\!\langle \boldsymbol{P}, \boldsymbol{\kappa} \rangle\!\rangle + \langle\!\langle p\boldsymbol{Q}(\boldsymbol{K}), \boldsymbol{\kappa} \rangle\!\rangle + \alpha s_2(\boldsymbol{U}, \boldsymbol{K}, \boldsymbol{\kappa}) &= 0, \qquad \forall \boldsymbol{\kappa} \in H^{\mathbf{c}}(\mathcal{B}), \\
\langle\!\langle \mathbf{grad}\, \boldsymbol{U}, \boldsymbol{\pi} \rangle\!\rangle - \langle\!\langle \boldsymbol{K}, \boldsymbol{\pi} \rangle\!\rangle &= 0, \qquad \forall \boldsymbol{\pi} \in H^{\mathbf{d}}(\mathcal{B}), \\
\langle\!\langle C(J), q \rangle\!\rangle &= 0, \qquad \forall q \in L^2(\mathcal{B}),
\end{aligned}
\tag{2.13}
$$

where

$$
f(\boldsymbol{\Upsilon}) = \langle\!\langle \rho_0 \boldsymbol{B}, \boldsymbol{\Upsilon} \rangle\!\rangle + \int_{\Gamma_t} \langle \overline{\boldsymbol{T}}, \boldsymbol{\Upsilon} \rangle dA, \tag{2.14}
$$

and

$$
\begin{aligned}
s_1(\boldsymbol{U}, \boldsymbol{K}, \boldsymbol{\Upsilon}) &= \langle\!\langle \mathbf{grad}\, \boldsymbol{U}, \mathbf{grad}\, \boldsymbol{\Upsilon} \rangle\!\rangle - \langle\!\langle \boldsymbol{K}, \mathbf{grad}\, \boldsymbol{\Upsilon} \rangle\!\rangle, \\
s_2(\boldsymbol{U}, \boldsymbol{K}, \boldsymbol{\kappa}) &= \langle\!\langle \boldsymbol{K}, \boldsymbol{\kappa} \rangle\!\rangle - \langle\!\langle \mathbf{grad}\, \boldsymbol{U}, \boldsymbol{\kappa} \rangle\!\rangle.
\end{aligned}
\tag{2.15}
$$

Note that the solution of the above problem is the critical point of the Hu-Washizu-type functional (2.11). In (2.13), the displacement (essential) boundary condition $\boldsymbol{U}\big|_{\Gamma_d} = \overline{\boldsymbol{U}}$ is imposed strongly in the solution space $H^1(T\mathcal{B}, \Gamma_d, \overline{\boldsymbol{U}})$while the traction (natural) boundary condition $(\boldsymbol{PN})\big|_{\Gamma_t} = \overline{\boldsymbol{T}}$ is imposed weakly in (2.14).

Green's formula allows one to write

$$
\langle\!\langle \mathbf{div}(\boldsymbol{P}), \boldsymbol{\Upsilon} \rangle\!\rangle = -\langle\!\langle \boldsymbol{P}, \mathbf{grad}(\boldsymbol{\Upsilon}) \rangle\!\rangle + \int_{\partial\mathcal{B}} \langle \boldsymbol{PN}, \boldsymbol{\Upsilon} \rangle dA, \ \forall \boldsymbol{\Upsilon} \in H^1(T\mathcal{B}, \Gamma_d). \tag{2.16}
$$

We assume the following weak statement of the traction boundary condition:

$$
\int_{\partial\mathcal{B}} \langle \boldsymbol{PN}, \boldsymbol{\Upsilon} \rangle dA = \int_{\Gamma_t} \langle \overline{\boldsymbol{T}}, \boldsymbol{\Upsilon} \rangle dA, \ \forall \boldsymbol{\Upsilon} \in H^1(T\mathcal{B}, \Gamma_d). \tag{2.17}
$$

Then, it is straightforward to show that (2.13) results in the following set of governing

equations for incompressible nonlinear elastostatics:

$$\left.\begin{aligned} &\mathbf{div}\boldsymbol{P} + \rho_0 \boldsymbol{B} = \boldsymbol{0}, && (2.18a)\\ &\boldsymbol{P} = \widetilde{\boldsymbol{P}}(\boldsymbol{K}) + p\boldsymbol{Q}(\boldsymbol{K}), && (2.18b)\\ &\boldsymbol{K} = \mathbf{grad}(\boldsymbol{U}), && (2.18c)\\ &J = 1, && (2.18d) \end{aligned}\right\} \quad \text{on } \mathcal{B},$$

$$\boldsymbol{U} = \overline{\boldsymbol{U}}, \qquad \text{on } \Gamma_d, \qquad (2.18e)$$

$$\boldsymbol{P}\boldsymbol{N} = \overline{\boldsymbol{T}}, \qquad \text{on } \Gamma_t. \qquad (2.18f)$$

Conversely, one can show that (2.18) results in (2.13), see [42, §2.2]. Note that (2.18b) is the constitutive relation of an incompressible solid, which in terms of the Cauchy stress $\boldsymbol{\sigma}$ reads $\boldsymbol{\sigma} = \widetilde{\boldsymbol{P}}(\boldsymbol{K})\boldsymbol{F}^{\mathsf{T}} + \bar{p}\boldsymbol{I}$, where $\bar{p} = p\,C'(J)$. Note that adding the stabilizing terms (2.15) to the weak formulation (2.13) does not change the set of governing equations (2.18). In other words, these terms will vanish for the exact solutions of (2.18). Hence, with proper discretization, the extra terms (2.15) may improve the stability of the resulting mixed finite element methods without compromising their consistency. We discuss this further in the next chapters.

Remark 3. For a neo-Hookean solid with $\widetilde{W} = \frac{\mu}{2}(I_1 - 3)$, where μ is the shear modulus at the ground state, one has the constitutive equation $\boldsymbol{P} = \mu\boldsymbol{F} + pC'(J)(\boldsymbol{F}^{-1})^{\mathsf{T}}$. In the absence of residual stresses, the body is stress free when there are no external forces. Hence, if $\boldsymbol{F} = \boldsymbol{I}$, then $\boldsymbol{P} = \boldsymbol{0}$. This gives us $(\mu + pC'(1))\boldsymbol{I} = \boldsymbol{0}$, which implies that $p = -\mu/C'(1)$ in the absence of external forces. Therefore, one should be careful to choose C such that $C'(1) \neq 0$. Also, the choice of the function $C(J)$ may affect the solution of the discrete system and may cause numerical instabilities at large deformations [2]. Our numerical examples indicate that our mixed FEMs work well with both $C(J) = J - 1$ and $C(J) = \ln J$.

By setting $p = q = 0$ in (2.13) and replacing $\widetilde{\boldsymbol{P}}(\boldsymbol{K})$ with $\widehat{\boldsymbol{P}}(\boldsymbol{K}) = \partial\widehat{W}/\partial\boldsymbol{K}$, one

can readily arrive at the following weak formulation of the boundary-value problem for 3D compressible nonlinear elastostatics:

Given $\boldsymbol{B}$, $\overline{\boldsymbol{U}}$, $\boldsymbol{T}$, *and* $\alpha \geqslant 0$, *find* $(\boldsymbol{U}, \boldsymbol{K}, \boldsymbol{P}) \in H^1(T\mathcal{B}, \Gamma_d, \overline{\boldsymbol{U}}) \times H^{\mathbf{c}}(\mathcal{B}) \times H^{\mathbf{d}}(\mathcal{B})$ *such that*

$$\begin{aligned} \langle\!\langle \boldsymbol{P}, \mathbf{grad}\, \boldsymbol{\Upsilon} \rangle\!\rangle + \alpha s_1(\boldsymbol{U}, \boldsymbol{K}, \boldsymbol{\Upsilon}) &= f(\boldsymbol{\Upsilon}), \quad && \forall \boldsymbol{\Upsilon} \in H^1(T\mathcal{B}, \Gamma_d), \\ \langle\!\langle \widehat{\boldsymbol{P}}(\boldsymbol{K}), \boldsymbol{\kappa} \rangle\!\rangle - \langle\!\langle \boldsymbol{P}, \boldsymbol{\kappa} \rangle\!\rangle + \alpha s_2(\boldsymbol{U}, \boldsymbol{K}, \boldsymbol{\kappa}) &= 0, && \forall \boldsymbol{\kappa} \in H^{\mathbf{c}}(\mathcal{B}), \\ \langle\!\langle \mathbf{grad}\, \boldsymbol{U}, \boldsymbol{\pi} \rangle\!\rangle - \langle\!\langle \boldsymbol{K}, \boldsymbol{\pi} \rangle\!\rangle &= 0, && \forall \boldsymbol{\pi} \in H^{\mathbf{d}}(\mathcal{B}). \end{aligned} \tag{2.19}$$

One can show that (2.19) results in the following set of governing equations for compressible nonlinear elastostatics:

$$\left.\begin{aligned} &\mathbf{div}\, \boldsymbol{P} + \rho_0 \boldsymbol{B} = \boldsymbol{0}, \\ &\boldsymbol{P} = \widehat{\boldsymbol{P}}(\boldsymbol{K}), \\ &\boldsymbol{K} = \mathbf{grad}\, \boldsymbol{U}, \end{aligned}\right\} \quad \text{on } \mathcal{B},$$

$$\begin{aligned} &\boldsymbol{U} = \overline{\boldsymbol{U}}, && \text{on } \Gamma_d, \\ &\boldsymbol{P}(\boldsymbol{N}) = \overline{\boldsymbol{T}}, && \text{on } \Gamma_t. \end{aligned}$$

For obtaining well-performing mixed finite element methods for 2D nonlinear elasticity, one does not need to consider the stabilizing terms (2.15) in the mixed formulations (2.13) and (2.19). Therefore, $\alpha = 0$ for 2D problems. This results in the following weak formulation of the boundary-value problem for 2D incompressible nonlinear elastostatics:

Given $\boldsymbol{B}$, $\overline{\boldsymbol{U}}$, *and* $\boldsymbol{T}$, *find* $(\boldsymbol{U},\boldsymbol{K},\boldsymbol{P},p)\in H^1(T\mathcal{B},\Gamma_d,\overline{\boldsymbol{U}})\times H^{\mathbf{c}}(\mathcal{B})\times H^{\mathbf{d}}(\mathcal{B})\times L^2(\mathcal{B})$ *such that*

$$\begin{aligned}
\langle\!\langle \rho_0\boldsymbol{B},\boldsymbol{\Upsilon}\rangle\!\rangle+\int_{\Gamma_t}\langle\overline{\boldsymbol{T}},\boldsymbol{\Upsilon}\rangle dS, &= \langle\!\langle \boldsymbol{P},\mathbf{grad}\,\boldsymbol{\Upsilon}\rangle\!\rangle \quad && \forall\boldsymbol{\Upsilon}\in H^1(T\mathcal{B},\Gamma_d),\\
\langle\!\langle \widetilde{\boldsymbol{P}}(\boldsymbol{K}),\boldsymbol{\kappa}\rangle\!\rangle-\langle\!\langle \boldsymbol{P},\boldsymbol{\kappa}\rangle\!\rangle+\langle\!\langle p\boldsymbol{Q}(\boldsymbol{K}),\boldsymbol{\kappa}\rangle\!\rangle &= 0, && \forall\boldsymbol{\kappa}\in H^{\mathbf{c}}(\mathcal{B}),\\
\langle\!\langle \mathbf{grad}\,\boldsymbol{U},\boldsymbol{\pi}\rangle\!\rangle-\langle\!\langle \boldsymbol{K},\boldsymbol{\pi}\rangle\!\rangle &= 0, && \forall\boldsymbol{\pi}\in H^{\mathbf{d}}(\mathcal{B}),\\
\langle\!\langle C(J),q\rangle\!\rangle &= 0, && \forall q\in L^2(\mathcal{B}).
\end{aligned}\tag{2.21}$$

Note that the solution of the above problem is the critical point of the Hu-Washizu-type functional $\overline{\mathcal{I}}$ given in (2.10).

Remark 4. The weak formulation (2.13) corresponds to a saddle point of the Hu-Washizu-type functional (2.10). To see this, one needs to calculate the 4×4 matrix $\boldsymbol{H}=\left[\frac{\partial^2\hat{\mathcal{I}}}{\partial\epsilon_i\partial\epsilon_j}\right]$ at $\epsilon_i,\epsilon_j=0$, where $\hat{\mathcal{I}}(\epsilon_1,\epsilon_2,\epsilon_3,\epsilon_4):=\overline{\mathcal{I}}(\boldsymbol{U}+\epsilon_1\boldsymbol{\Upsilon},\boldsymbol{K}+\epsilon_2\boldsymbol{\kappa},\boldsymbol{P}+\epsilon_3\boldsymbol{\pi},p+\epsilon_4 q)$. It is straightforward to show that $\boldsymbol{H}$ is symmetric and has a non-negative determinant. Also, if $\boldsymbol{H}$ is invertible, it has two positive and two negative eigenvalues.

Setting $p=q=0$ and replacing $\widetilde{\boldsymbol{P}}(\boldsymbol{K})$ with $\hat{\boldsymbol{P}}(\boldsymbol{K})=\partial\widehat{W}/\partial\boldsymbol{K}$ in in (2.21) gives the following weak formulation of the boundary-value problem for 2D compressible nonlinear elastostatics:

Given $\boldsymbol{B}$, $\overline{\boldsymbol{U}}$, *and* $\boldsymbol{T}$, *find* $(\boldsymbol{U},\boldsymbol{K},\boldsymbol{P})\in H^1(T\mathcal{B},\Gamma_d,\overline{\boldsymbol{U}})\times H^{\mathbf{c}}(\mathcal{B})\times H^{\mathbf{d}}(\mathcal{B})$ *such that*

$$\begin{aligned}
\langle\!\langle \boldsymbol{P},\mathbf{grad}\,\boldsymbol{\Upsilon}\rangle\!\rangle &= \langle\!\langle \rho_0\boldsymbol{B},\boldsymbol{\Upsilon}\rangle\!\rangle+\int_{\Gamma_t}\langle\overline{\boldsymbol{T}},\boldsymbol{\Upsilon}\rangle dS, \quad && \forall\boldsymbol{\Upsilon}\in H^1(T\mathcal{B},\Gamma_d),\\
\langle\!\langle \hat{\boldsymbol{P}}(\boldsymbol{K}),\boldsymbol{\kappa}\rangle\!\rangle-\langle\!\langle \boldsymbol{P},\boldsymbol{\kappa}\rangle\!\rangle &= 0, && \forall\boldsymbol{\kappa}\in H^{\mathbf{c}}(\mathcal{B}),\\
\langle\!\langle \mathbf{grad}\,\boldsymbol{U},\boldsymbol{\pi}\rangle\!\rangle-\langle\!\langle \boldsymbol{K},\boldsymbol{\pi}\rangle\!\rangle &= 0, && \forall\boldsymbol{\pi}\in H^{\mathbf{d}}(\mathcal{B}).
\end{aligned}\tag{2.22}$$

The solution of (2.22) is the critical point of the Hu-Washizu-type functional (2.9).

Remark 5. Assume that the reference configuration of the body $\mathcal{B}\subset\mathbb{R}^2$ is a non-simply-connected domain. More specifically, it is a connected 2D domain that contains

n_h holes. In this setting, $\mathbf{c}(\boldsymbol{K}) = \mathbf{0}$ is necessary for the compatibility of $\boldsymbol{K}$ but is not sufficient; in addition to $\mathbf{c}(\boldsymbol{K}) = \mathbf{0}$ the following auxiliary compatibility equations must hold [52]:

$$\int_{\partial\mathcal{H}_i} \boldsymbol{K}\boldsymbol{T}_{\partial\mathcal{H}_i} ds = \mathbf{0}, \quad \text{for } i = 1, 2, ..., n_h, \tag{2.23}$$

where $\partial\mathcal{H}_i$ is the boundary of the i-th hole and $\boldsymbol{T}_{\partial\mathcal{H}_i}$ denotes the unit tangent vector field of $\partial\mathcal{H}_i$ in the reference configuration. Note that $\partial\mathcal{H}_i$ is chosen for convenience; the above integral for each hole can be taken over an arbitrary closed-path within the domain that encloses only that hole, i.e., any closed path that is homologous to $\partial\mathcal{H}_i$ [52]. Note that in our mixed formulation we weakly impose $\boldsymbol{K} = \mathbf{grad}\, \boldsymbol{U}$, and hence, one does not need to impose compatibility.

CHAPTER 3

COMPATIBLE-STRAIN MIXED FINITE ELEMENT METHODS FOR 2D NONLINEAR ELASTICITY

3.1 Polynomial Tensor Fields

We begin our discussion by introducing some polynomial fields in $\mathbb{R}^2$, which will be used for defining the finite elements. Let $\mathcal{P}_r(\mathbb{R}^2)$ be the space of $\mathbb{R}$-valued polynomials in two variables $\{\mathrm{X}^1, \mathrm{X}^2\}$ of degree at most $r \geqslant 0$ and let $\mathcal{H}_r(\mathbb{R}^2) \subset \mathcal{P}_r(\mathbb{R}^2)$ be the space of homogeneous polynomials of degree r, i.e. all terms of members of $\mathcal{H}_r(\mathbb{R}^2)$ are of degree r. These spaces are assumed to be empty if $r < 0$. The spaces of polynomial vector and $\binom{2}{0}$-tensor fields in $\mathbb{R}^2$ with Cartesian components in $\mathcal{P}_r(\mathbb{R}^2)$ are denoted by $\mathcal{P}_r(T\mathbb{R}^2)$ and $\mathcal{P}_r(\bigotimes^2 T\mathbb{R}^2)$, respectively. The spaces of homogeneous polynomial fields $\mathcal{H}_r(T\mathbb{R}^2)$ and $\mathcal{H}_r(\bigotimes^2 T\mathbb{R}^2)$ are defined analogously. It is straightforward to show that

$$\dim \mathcal{P}_r(\bigotimes^2 T\mathbb{R}^2) = 2 \dim \mathcal{P}_r(T\mathbb{R}^2) = 2(r+1)(r+2),$$

$$\dim \mathcal{H}_r(\bigotimes^2 T\mathbb{R}^2) = 2 \dim \mathcal{H}_r(T\mathbb{R}^2) = 4(r+1).$$

One can use $\mathcal{P}_r$ fields to write the following polynomial complexes

$$\begin{aligned} 0 \longrightarrow \mathcal{P}_{r+2}(T\mathbb{R}^2) \xrightarrow{\mathbf{grad}} \mathcal{P}_{r+1}(\bigotimes^2 T\mathbb{R}^2) \xrightarrow{\mathbf{c}} \mathcal{P}_r(T\mathbb{R}^2) \longrightarrow 0, \\ 0 \longrightarrow \mathcal{P}_{r+2}(T\mathbb{R}^2) \xrightarrow{\mathbf{s}} \mathcal{P}_{r+1}(\bigotimes^2 T\mathbb{R}^2) \xrightarrow{\mathbf{-div}} \mathcal{P}_r(T\mathbb{R}^2) \longrightarrow 0. \end{aligned} \tag{3.1}$$

Next, we introduce two subspaces of $\mathcal{P}_r(\bigotimes^2 T\mathbb{R}^2)$. Suppose $Y^I(\mathrm{X}^1, \mathrm{X}^2)$ and $T^{IJ}(\mathrm{X}^1, \mathrm{X}^2)$, $I, J = 1, 2$, are the Cartesian components of a vector field $\boldsymbol{Y}$and a $\binom{2}{0}$-tensor field $\boldsymbol{T}$. We define the operators $\mathbf{K}_1, \widetilde{\mathbf{K}}_1 : \mathcal{P}_r(\bigotimes^2 T\mathbb{R}^2) \to \mathcal{P}_{r+1}(T\mathbb{R}^2)$ and $\mathbf{K}_2, \widetilde{\mathbf{K}}_2 : \mathcal{P}_r(T\mathbb{R}^2) \to$

$\mathcal{P}_{r+1}(\otimes^2 T\mathbb{R}^2)$ as

$$\mathbf{K}_1(\boldsymbol{T}) := \begin{bmatrix} \mathrm{X}^1\, T^{11} + \mathrm{X}^2\, T^{12} \\ \mathrm{X}^1\, T^{21} + \mathrm{X}^2\, T^{22} \end{bmatrix}, \quad \widetilde{\mathbf{K}}_1(\boldsymbol{T}) := \begin{bmatrix} -\mathrm{X}^1\, T^{12} + \mathrm{X}^2\, T^{11} \\ -\mathrm{X}^1\, T^{22} + \mathrm{X}^2\, T^{21} \end{bmatrix},$$

$$\mathbf{K}_2(\boldsymbol{Y}) := \begin{bmatrix} -\mathrm{X}^2\, Y^1 & \mathrm{X}^1\, Y^1 \\ -\mathrm{X}^2\, Y^2 & \mathrm{X}^1\, Y^2 \end{bmatrix}, \quad \widetilde{\mathbf{K}}_2(\boldsymbol{Y}) := \begin{bmatrix} \mathrm{X}^1\, Y^1 & \mathrm{X}^2\, Y^1 \\ \mathrm{X}^1\, Y^2 & \mathrm{X}^2\, Y^2 \end{bmatrix}.$$

It is straightforward to show that $\mathbf{K}_1 \circ \mathbf{K}_2 = \mathbf{0}$, and $\widetilde{\mathbf{K}}_1 \circ \widetilde{\mathbf{K}}_2 = \mathbf{0}$, and therefore, these operators give rise to the following polynomial complexes

$$0 \longrightarrow \mathcal{P}_r(T\mathbb{R}^2) \xrightarrow{\mathbf{K}_2} \mathcal{P}_{r+1}(\otimes^2 T\mathbb{R}^2) \xrightarrow{\mathbf{K}_1} \mathcal{P}_{r+2}(T\mathbb{R}^2) \longrightarrow 0, \tag{3.2}$$

$$0 \longrightarrow \mathcal{P}_r(T\mathbb{R}^2) \xrightarrow{\widetilde{\mathbf{K}}_2} \mathcal{P}_{r+1}(\otimes^2 T\mathbb{R}^2) \xrightarrow{\widetilde{\mathbf{K}}_1} \mathcal{P}_{r+2}(T\mathbb{R}^2) \longrightarrow 0. \tag{3.3}$$

It turns out that any $\boldsymbol{T} \in \mathcal{H}_r(\otimes^2 T\mathbb{R}^2)$ can be decomposed as

$$\boldsymbol{T} = \mathbf{K}_2(\boldsymbol{W_T}) + \mathbf{grad}(\boldsymbol{Y_T}) = \widetilde{\mathbf{K}}_2(\widetilde{\boldsymbol{W}}_{\boldsymbol{T}}) + \mathbf{s}(\widetilde{\boldsymbol{Y}}_{\boldsymbol{T}}),$$

where $\boldsymbol{W_T}, \widetilde{\boldsymbol{W}}_{\boldsymbol{T}} \in \mathcal{H}_{r-1}(T\mathbb{R}^2)$ and $\boldsymbol{Y_T}, \widetilde{\boldsymbol{Y}}_{\boldsymbol{T}} \in \mathcal{H}_{r+1}(T\mathbb{R}^2)$. This result can be stated as follows.

Theorem 6. *The following decompositions hold:*

$$\mathcal{H}_r(\otimes^2 T\mathbb{R}^2) = \mathbf{K}_2\big(\mathcal{H}_{r-1}(T\mathbb{R}^2)\big) \oplus \mathbf{grad}\big(\mathcal{H}_{r+1}(T\mathbb{R}^2)\big),$$

$$\mathcal{H}_r(\otimes^2 T\mathbb{R}^2) = \widetilde{\mathbf{K}}_2\big(\mathcal{H}_{r-1}(T\mathbb{R}^2)\big) \oplus \mathbf{s}\big(\mathcal{H}_{r+1}(T\mathbb{R}^2)\big),$$

where

$$\dim \mathbf{K}_2\big(\mathcal{H}_{r-1}(T\mathbb{R}^2)\big) = \dim \widetilde{\mathbf{K}}_2\big(\mathcal{H}_{r-1}(T\mathbb{R}^2)\big) = 2r,$$

$$\dim \mathbf{grad}\big(\mathcal{H}_{r+1}(T\mathbb{R}^2)\big) = \dim \mathbf{s}\big(\mathcal{H}_{r+1}(T\mathbb{R}^2)\big) = 2(r+2).$$

Proof. As discussed in [46, §3.1], there is an isomorphism between the Hilbert complexes (2.7a) and (2.7b) and the de Rham complex. One can show that this isomorphism induces an isomorphism between the complexes (3.2) and (3.3) and a standard complex in differential geometry called the Koszul complex (for more details on this complex see [30, §5.1.2] or [53, §3.4.6]). Consequently, the above decompositions directly follow from the decomposition of polynomial 1-forms induced by the exterior derivative and the Koszul differential, which is introduced by [29, page 32]. □

Since $\mathcal{P}_r(\bigotimes^2 T\mathbb{R}^2) = \mathcal{P}_{r-1}(\bigotimes^2 T\mathbb{R}^2) \oplus \mathcal{H}_r(\bigotimes^2 T\mathbb{R}^2)$, the decompositions introduced in the above theorem allow one to define the following subspaces of $\mathcal{P}_r(\bigotimes^2 T\mathbb{R}^n)$:

$$\begin{aligned} \mathcal{P}_r^-(\bigotimes^2 T\mathbb{R}^2) &:= \mathcal{P}_{r-1}(\bigotimes^2 T\mathbb{R}^2) \oplus \mathbf{K}_2\big(\mathcal{H}_{r-1}(T\mathbb{R}^2)\big)\,, \\ \mathcal{P}_r^{\ominus}(\bigotimes^2 T\mathbb{R}^2) &:= \mathcal{P}_{r-1}(\bigotimes^2 T\mathbb{R}^2) \oplus \widetilde{\mathbf{K}}_2\big(\mathcal{H}_{r-1}(T\mathbb{R}^2)\big)\,, \end{aligned} \tag{3.4}$$

where $\dim \mathcal{P}_r^-(\bigotimes^2 T\mathbb{R}^2) = \dim \mathcal{P}_r^{\ominus}(\bigotimes^2 T\mathbb{R}^2) = 2r(r+2)$.

Example 7. Let $(X, Y) = (\mathrm{X}^1, \mathrm{X}^2)$. For $r = 1$, the 12-dimensional space $\mathcal{P}_1(\bigotimes^2 T\mathbb{R}^2)$ can be written as

$$\mathcal{P}_1(\bigotimes^2 T\mathbb{R}^2) = \left\{ \mathbf{A}_0 + X \cdot \mathbf{A}_1 + Y \cdot \mathbf{A}_2,\ \forall \mathbf{A}_i \in \mathbb{R}^{2\times 2} \right\},$$

where $\mathbb{R}^{2\times 2}$ is the space of 2×2 matrices. The subspaces $\mathcal{P}_1^-(\bigotimes^2 T\mathbb{R}^2)$ and $\mathcal{P}_1^{\ominus}(\bigotimes^2 T\mathbb{R}^2)$ are 6-dimensional and are given by

$$\begin{aligned} \mathcal{P}_1^-(\bigotimes^2 T\mathbb{R}^2) &= \left\{ \mathbf{A} + \begin{bmatrix} -aY & aX \\ -bY & bX \end{bmatrix},\ \forall a, b \in \mathbb{R},\ \forall \mathbf{A} \in \mathbb{R}^{2\times 2} \right\}, \\ \mathcal{P}_1^{\ominus}(\bigotimes^2 T\mathbb{R}^2) &= \left\{ \mathbf{A} + \begin{bmatrix} aX & aY \\ bX & bY \end{bmatrix},\ \forall a, b \in \mathbb{R},\ \forall \mathbf{A} \in \mathbb{R}^{2\times 2} \right\}. \end{aligned}$$

For $r=2$, we have $\dim \mathcal{P}_2(\bigotimes^2 T\mathbb{R}^2)=24$, and $\dim \mathcal{P}_2^-(\bigotimes^2 T\mathbb{R}^2)=\dim \mathcal{P}_2^{\ominus}(\bigotimes^2 T\mathbb{R}^2)=16$, where

$$\mathcal{P}_2(\bigotimes^2 T\mathbb{R}^2)=\left\{\mathbf{A}_0+X\cdot\mathbf{A}_1+Y\cdot\mathbf{A}_2+X^2\cdot\mathbf{A}_3+XY\cdot\mathbf{A}_4+Y^2\cdot\mathbf{A}_5,\forall\mathbf{A}_i\in\mathbb{R}^{2\times 2}\right\},$$

$$\mathcal{P}_2^-(\bigotimes^2 T\mathbb{R}^2)=\left\{\mathbf{A}_0+X\cdot\mathbf{A}_1+Y\cdot\mathbf{A}_2 + \begin{bmatrix} -a_1XY-a_2Y^2 & a_1X^2+a_2XY \\ -b_1XY-b_2Y^2 & b_1X^2+b_2XY \end{bmatrix},\ \forall a_i,b_j\in\mathbb{R},\ \forall\mathbf{A}_k\in\mathbb{R}^{2\times 2}\right\},$$

$$\mathcal{P}_2^{\ominus}(\bigotimes^2 T\mathbb{R}^2)=\left\{\mathbf{A}_0+X\cdot\mathbf{A}_1+Y\cdot\mathbf{A}_2 + \begin{bmatrix} a_1X^2+a_2XY & a_1XY+a_2Y^2 \\ b_1X^2+b_2XY & b_1XY+b_2Y^2 \end{bmatrix},\ \forall a_i,b_j\in\mathbb{R},\ \forall\mathbf{A}_k\in\mathbb{R}^{2\times 2}\right\}.$$

The subspaces defined in (3.4) give rise to the following polynomial complexes:

$$\begin{aligned} 0\longrightarrow\mathcal{P}_{r+1}(T\mathbb{R}^2)\xrightarrow{\mathbf{grad}}\mathcal{P}_{r+1}^-(\bigotimes^2 T\mathbb{R}^2)\xrightarrow{\mathbf{c}}\mathcal{P}_r(T\mathbb{R}^2)\longrightarrow 0,\\ 0\longrightarrow\mathcal{P}_{r+1}(T\mathbb{R}^2)\xrightarrow{\mathbf{s}}\mathcal{P}_{r+1}^{\ominus}(\bigotimes^2 T\mathbb{R}^2)\xrightarrow{\mathbf{-div}}\mathcal{P}_r(T\mathbb{R}^2)\longrightarrow 0. \end{aligned} \tag{3.5}$$

Remark 8. By using a subspace of the space of polynomial 1-forms introduced in [29, §3.3], one can write the following subspaces of $\mathcal{P}_r(T\mathbb{R}^2)$:

$$\begin{aligned} \mathcal{P}_r^-(T\mathbb{R}^2)&:=\mathcal{P}_{r-1}(T\mathbb{R}^2)\oplus \mathrm{K}_2\big(\mathcal{H}_{r-1}(\mathbb{R}^2)\big),\\ \mathcal{P}_r^{\ominus}(T\mathbb{R}^2)&:=\mathcal{P}_{r-1}(T\mathbb{R}^2)\oplus \widetilde{\mathrm{K}}_2\big(\mathcal{H}_{r-1}(\mathbb{R}^2)\big), \end{aligned} \tag{3.6}$$

where

$$\mathrm{K}_2(f):=\begin{bmatrix} -\mathrm{X}^2 f \\ \mathrm{X}^1 f \end{bmatrix},\quad \widetilde{\mathrm{K}}_2(f):=\begin{bmatrix} \mathrm{X}^1 f \\ \mathrm{X}^2 f \end{bmatrix}.$$

Clearly, the spaces defined in (3.4) are the tensorial analogues of (3.6) that are obtained by identifying $\binom{2}{0}$-tensors with the two vector fields associated to their rows.

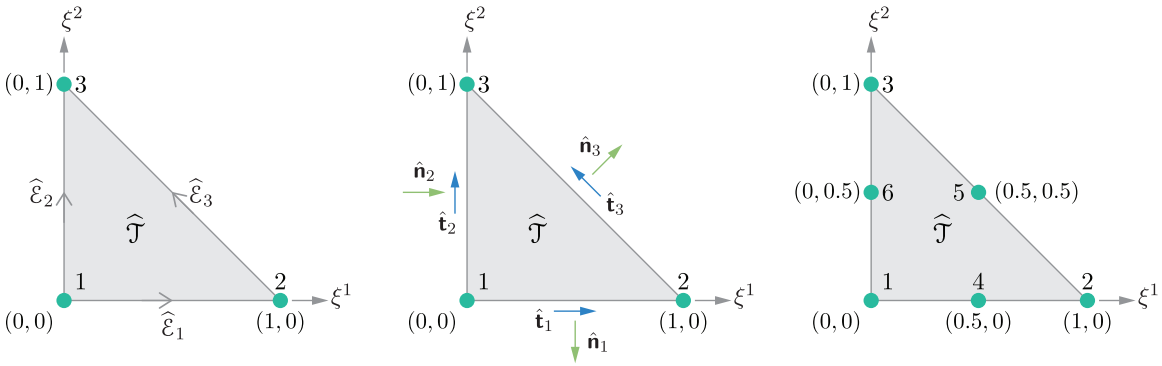

Figure 3.1: The three-node reference element and edge numbers and orientations (left), the reference directions for the unit tangent and normal vectors (middle), and the six-node reference element (right).

3.2 Finite Elements

Following [54], we define a finite element as a triplet $(\mathcal{T}, \mathcal{P}(\mathcal{T}), \Sigma)$, where $\mathcal{T}$ is a triangle in $\mathbb{R}^2$, $\mathcal{P}(\mathcal{T})$ is a space of polynomials on $\mathcal{T}$, and Σ is a set of linear functionals $\{\sigma_1, \sigma_2, ..., \sigma_{n_s}\}$ acting on the members of $\mathcal{P}(\mathcal{T})$ such that $\forall p \in \mathcal{P}(\mathcal{T})$, $\sigma_i(p) \in \mathbb{R}$, and the liner mapping $p \longmapsto (\sigma_1(p), \sigma_2(p), ..., \sigma_{n_s}(p)) \in \mathbb{R}^{n_s}$ is a bijection. Equivalently, there exists a unique basis $\{\theta_1, \theta_2, ..., \theta_{n_s}\}$ in $\mathcal{P}(\mathcal{T})$ such that $\sigma_i(\theta_j) = \delta_{ij}$, $i, j = 1, 2, ..., n_s$. σ_i's and θ_i's are called the local degrees of freedom (DOF) and the local shape functions, respectively. Following [26], in the definition of a finite element, we always implicitly assume that there exits a linear space $V(\mathcal{T})$ of functions $v : \mathcal{T} \to \mathbb{R}^m$ such that $\mathcal{P}(\mathcal{T}) \subset V(\mathcal{T})$, and Σ can be extended to its dual space $V(\mathcal{T})^\star$. Then, the local interpolation operator is defined as

$$\mathrm{I}_\mathcal{T} : V(\mathcal{T}) \longrightarrow \mathcal{P}(\mathcal{T}), \quad \mathrm{I}_\mathcal{T}(v) = \sum_{i=0}^{n_s} \sigma_i(v)\theta_i.$$

Note that $\mathrm{I}_\mathcal{T}$ is a projection of $V(\mathcal{T})$ into $\mathcal{P}(\mathcal{T})$ that is not bijective, in general. In practice, by having the shape functions, we accept $\mathrm{I}_\mathcal{T}(v)$ as an approximation of v and find the degrees of freedom as the unknowns.

Suppose $\widehat{\mathcal{T}}$ as shown in Figure 3.1 is a reference triangular element with coordinates $\boldsymbol{\xi} = (\xi^1, \xi^2)$. We denote the edges of $\widehat{\mathcal{T}}$ by $\widehat{\mathcal{E}}_i, i = 1, 2, 3$ and their corresponding lengths

by $\hat{\ell}_i, i = 1, 2, 3$. For an edge joining two vertices i and j, we define a unique orientation as $i \to j$, where $i < j$. According to Figure 3.1, orientations $1 \to 2$, $1 \to 3$, and $2 \to 3$ are assigned to $\widehat{\mathcal{E}}_1$, $\widehat{\mathcal{E}}_2$, and $\widehat{\mathcal{E}}_3$, respectively. Moreover, we define a unit tangent vector $\hat{\mathbf{t}}_i$ and a unit normal vector $\hat{\mathbf{n}}_i$ on each edge; $\hat{\mathbf{t}}_i$ must agree with the edge orientation, and $\hat{\mathbf{n}}_i$ is obtained by a 90 degrees clockwise rotation of $\hat{\mathbf{t}}_i$, that is $\hat{\mathbf{n}}_i = \mathsf{R}\hat{\mathbf{t}}_i$, where

$$\mathsf{R} = \begin{bmatrix} 0 & 1 \\ -1 & 0 \end{bmatrix}. \tag{3.7}$$

We consider the following *reference* finite elements for our four field variables:

$$\begin{aligned}
&\left(\widehat{\mathfrak{T}}, \mathcal{P}_r(T\widehat{\mathfrak{T}}), \Sigma^{\hat{\mathfrak{T}},1}\right) && \text{for displacement } \boldsymbol{U}, \\
&\left(\widehat{\mathfrak{T}}, \mathcal{P}_r(\otimes^2 T\widehat{\mathfrak{T}}), \Sigma^{\hat{\mathfrak{T}},\mathbf{c}}\right), \left(\widehat{\mathfrak{T}}, \mathcal{P}_r^-(\otimes^2 T\widehat{\mathfrak{T}}), \Sigma^{\hat{\mathfrak{T}},\mathbf{c}-}\right) && \text{for displacement gradient } \boldsymbol{K}, \\
&\left(\widehat{\mathfrak{T}}, \mathcal{P}_r(\otimes^2 T\widehat{\mathfrak{T}}), \Sigma^{\hat{\mathfrak{T}},\mathbf{d}}\right), \left(\widehat{\mathfrak{T}}, \mathcal{P}_r^{\ominus}(\otimes^2 T\widehat{\mathfrak{T}}), \Sigma^{\hat{\mathfrak{T}},\mathbf{d}-}\right) && \text{for stress } \boldsymbol{P}, \\
&\left(\widehat{\mathfrak{T}}, \mathcal{P}_r(\widehat{\mathfrak{T}}), \Sigma^{\hat{\mathfrak{T}},\ell}\right) && \text{for the pressure-like field } p.
\end{aligned} \tag{3.8}$$

In the following, our main focus is to provide explicit expressions for some bases of the above polynomial spaces, also known as local shape functions. We will consider $r = 1, 2$ for the corresponding polynomial spaces of $\boldsymbol{U}$, $\boldsymbol{K}$ and $\boldsymbol{P}$, and $r = 0, 1, 2$ for the corresponding polynomial space of p.

The Lagrange polynomials on the three-node $\widehat{\mathfrak{T}}$ are

$$l_1^1 = 1 - \xi^1 - \xi^2, \quad l_2^1 = \xi^1, \quad l_3^1 = \xi^2. \tag{3.9}$$

Using (3.9), the Lagrange polynomials on the six-node $\widehat{\mathfrak{T}}$ can be written as $l_i^2 = l_i^1(2l_i^1 - 1)$

and $l^2_{3+i} = 4l^1_i l^1_{i+1}$, where $i = 1, 2, 3$ and $l^1_4 = l^1_1$. For $r = 1, 2$, a basis of $\mathcal{P}_r(T\widehat{\mathfrak{T}})$ includes

$$\boldsymbol{h}^{\hat{\mathfrak{T}}}_{2i-1} = \begin{bmatrix} l^r_i \\ 0 \end{bmatrix}, \quad \boldsymbol{h}^{\hat{\mathfrak{T}}}_{2i} = \begin{bmatrix} 0 \\ l^r_i \end{bmatrix}, \quad i = 1, 2, ..., 3r,$$

and the set of local degrees of freedom is $\Sigma^{\hat{\mathfrak{T}},1} = \{V^1(\boldsymbol{\xi}_1), V^2(\boldsymbol{\xi}_1), ..., V^1(\boldsymbol{\xi}_{3r}), V^2(\boldsymbol{\xi}_{3r})\}$, where $\boldsymbol{\xi}_i$ is the coordinates of the i-th node of the $3r$-node $\widehat{\mathfrak{T}}$ as shown in Figure 3.1. We will use $\mathcal{P}_r(T\widehat{\mathfrak{T}}), r = 1, 2$ spanned by $\boldsymbol{h}^{\hat{\mathfrak{T}}}_i$ to construct the approximation space of $\boldsymbol{U}$.

Table 3.1: Tensorial analogues of some classical finite elements for vector fields.

Vector Fields	*Second-Order Tensors*
Nédélec 1^{st}-kind (N1) $H(\text{curl})$ element [55]	$(\mathfrak{T}, \mathcal{P}^-_r(\bigotimes^2 T\mathfrak{T}), \Sigma^{\mathfrak{T},\mathbf{c}-})$
Nédélec 2^{nd}-kind (N2) $H(\text{curl})$ element [56]	$(\mathfrak{T}, \mathcal{P}_r(\bigotimes^2 T\mathfrak{T}), \Sigma^{\mathfrak{T},\mathbf{c}})$
Raviart-Thomas (RT) $H(\text{div})$ element [57]	$(\mathfrak{T}, \mathcal{P}^{\ominus}_r(\bigotimes^2 T\mathfrak{T}), \Sigma^{\mathfrak{T},\mathbf{d}-})$
Brezzi-Douglas-Marini (BDM) $H(\text{div})$ element [58]	$(\mathfrak{T}, \mathcal{P}_r(\bigotimes^2 T\mathfrak{T}), \Sigma^{\mathfrak{T},\mathbf{d}})$

Remark 9. We have listed some of the common vector-valued finite elements in the literature in the left column of Table 3.1. Nédélec's original finite elements are in $\mathbb{R}^3$ for both H(curl) and H(div) and for arbitrary polynomial degree [55, 56]. He introduced N1 and N2 H(curl) elements for $\mathbb{R}^3$. He also generalized RT and BDM elements to $\mathbb{R}^3$ by developing H(div) version of N1 and N2, respectively. Following his works, the 2D version of H(curl) elements are also called Nédélec elements, but as he himself pointed out in the conclusion of [55], in 2D, H(curl) elements can be easily obtained by a 90 degree rotation of bases of H(div) elements.

For $\boldsymbol{K} \in H^{\mathbf{c}}$ and $\boldsymbol{P} \in H^{\mathbf{d}}$, we write the tensorial analogues of some classical finite elements for vector fields as summarized in Table 3.1 (also see Remark 9). All the finite element spaces given in the left column of Table 3.1 are generalized by Arnold *et al.* [59] to two spaces of finite element differential forms with arbitrary order for any degree of polynomials and any number of dimensions. Moreover, they derived geometric decomposition of these spaces, which provides explicit local bases for them. See [60, 61]

for a more intuitive generalization of these vector-valued finite elements. Here, based on the results of [59], we write some analogues tensorial bases for the reference element $\widehat{\mathfrak{T}}$ and $r = 1, 2$. By using Theorem 7 in [42], one can calculate these tensorial bases implicitly, e.g., see [42, Examples 9 and 10]. Let us ignore the superscript of l_i^1 in (3.9) and let $\nabla l_i = \begin{bmatrix} \partial l_i/\partial \xi^1 & \partial l_i/\partial \xi^2 \end{bmatrix}$ be a row vector. Also, for each edge of a triangular element with orientation $i \to j$, consider the Whitney function

$$\boldsymbol{w}_{ij} = l_i \nabla l_j - l_j \nabla l_i. \tag{3.10}$$

The bases for polynomial spaces of N1 and N2, which we respectively denote by $\mathcal{P}_r^-(T\widehat{\mathfrak{T}})$ and $\mathcal{P}_r(T\widehat{\mathfrak{T}})$ are given in Table 3.2 for the orders $r = 1, 2$ [59]. Local shape functions $\boldsymbol{v}_J^{\hat{\mathfrak{T}},\hat{\mathcal{E}}_k}$ associated with the edge $\widehat{\mathcal{E}}_k$ with orientation $i \to j$, which is indicated in Figure 3.1, and local shape functions $\boldsymbol{v}_J^{\hat{\mathfrak{T}},\hat{\mathfrak{T}}}$ are associated with the reference element $\widehat{\mathfrak{T}}$ itself and defined for $r \geqslant 2$. The tangent component of a shape function $\boldsymbol{v}$ on an edge $\mathcal{E}_i$ is denoted by $\langle \boldsymbol{v}, \mathbf{t}_i \rangle$. For a given r, both $\mathcal{P}_r^-(T\widehat{\mathfrak{T}})$ and $\mathcal{P}_r(T\widehat{\mathfrak{T}})$ contain polynomials of the same order, but

$$\begin{aligned}
&\left\{ \left\langle \boldsymbol{v}_J^{\hat{\mathfrak{T}},\hat{\mathcal{E}}_k}, \mathbf{t}_k \right\rangle : \boldsymbol{v}_J^{\hat{\mathfrak{T}},\hat{\mathcal{E}}_k} \in \mathcal{P}_r^-(T\widehat{\mathfrak{T}}), J = 1, 2, ..., r \right\} && \text{is a basis of} \quad \mathcal{P}_{r-1}(\widehat{\mathcal{E}}_k), \\
&\left\{ \left\langle \boldsymbol{v}_J^{\hat{\mathfrak{T}},\hat{\mathcal{E}}_k}, \mathbf{t}_k \right\rangle : \boldsymbol{v}_J^{\hat{\mathfrak{T}},\hat{\mathcal{E}}_k} \in \mathcal{P}_r(T\widehat{\mathfrak{T}}), J = 1, 2, ..., r+1 \right\} && \text{is a basis of} \quad \mathcal{P}_r(\widehat{\mathcal{E}}_k),
\end{aligned}$$

where $\mathcal{P}_r(\widehat{\mathcal{E}}_k)$ denotes the one-dimensional polynomial space of order r on the edge $\widehat{\mathcal{E}}_k$. Also, for any J, $\boldsymbol{v}_J^{\hat{\mathfrak{T}},\hat{\mathfrak{T}}}$ is a zero-tangent bubble polynomial of order r on $\widehat{\mathfrak{T}}$, meaning that its tangent components are zero on all the three edges. Some examples of these shape functions are depicted in Figure 3.2. To interpolate $\boldsymbol{K} \in H^{\mathrm{c}}$, we define the following tensorial shape functions:

$$\boldsymbol{r}_{1,J}^{\hat{\mathfrak{T}},\hat{\mathcal{E}}_k} = \begin{bmatrix} \boldsymbol{v}_J^{\hat{\mathfrak{T}},\hat{\mathcal{E}}_k} \\ \mathbf{0} \end{bmatrix}, \quad \boldsymbol{r}_{2,J}^{\hat{\mathfrak{T}},\hat{\mathcal{E}}_k} = \begin{bmatrix} \mathbf{0} \\ \boldsymbol{v}_J^{\hat{\mathfrak{T}},\hat{\mathcal{E}}_k} \end{bmatrix}, \quad \boldsymbol{r}_{1,J}^{\hat{\mathfrak{T}},\hat{\mathfrak{T}}} = \begin{bmatrix} \boldsymbol{v}_J^{\hat{\mathfrak{T}},\hat{\mathfrak{T}}} \\ \mathbf{0} \end{bmatrix}, \quad \boldsymbol{r}_{2,J}^{\hat{\mathfrak{T}},\hat{\mathfrak{T}}} = \begin{bmatrix} \mathbf{0} \\ \boldsymbol{v}_J^{\hat{\mathfrak{T}},\hat{\mathfrak{T}}} \end{bmatrix}. \tag{3.11}$$

Table 3.2: Vector valued bases for polynomial spaces of N1 denoted by $\mathcal{P}_r^-(T\widehat{\mathfrak{T}})$ and N2 denoted by $\mathcal{P}_r(T\widehat{\mathfrak{T}})$ for $r = 1, 2$.

	$\mathcal{P}_r^-(T\widehat{\mathfrak{T}})$		$\mathcal{P}_r(T\widehat{\mathfrak{T}})$	
r	$\boldsymbol{v}_J^{\widehat{\mathfrak{T}},\widehat{\mathcal{E}}_k}$	$\boldsymbol{v}_J^{\widehat{\mathfrak{T}},\widehat{\mathfrak{T}}}$	$\boldsymbol{v}_J^{\widehat{\mathfrak{T}},\widehat{\mathcal{E}}_k}$	$\boldsymbol{v}_J^{\widehat{\mathfrak{T}},\widehat{\mathfrak{T}}}$
1	$\boldsymbol{w}_{ij}$		$l_i\nabla l_j,\ l_j\nabla l_i$	
2	$l_i\boldsymbol{w}_{ij},\ l_j\boldsymbol{w}_{ij}$	$l_3\boldsymbol{w}_{12},\ l_2\boldsymbol{w}_{13}$	$l_i^2\nabla l_j,\ l_j^2\nabla l_i,\ l_il_j\nabla(l_j-l_i)$	$l_1l_2\nabla l_3,\ l_1l_3\nabla l_2,\ l_2l_3\nabla l_1$

	$\mathcal{P}_r^-(T\widehat{\mathfrak{T}})$		$\mathcal{P}_r(T\widehat{\mathfrak{T}})$	
r	$\boldsymbol{v}_1^{\widehat{\mathfrak{T}},\widehat{\mathcal{E}}_3}$	$\boldsymbol{v}_2^{\widehat{\mathfrak{T}},\widehat{\mathfrak{T}}}$	$\boldsymbol{v}_1^{\widehat{\mathfrak{T}},\widehat{\mathcal{E}}_3}$	$\boldsymbol{v}_3^{\widehat{\mathfrak{T}},\widehat{\mathfrak{T}}}$
1	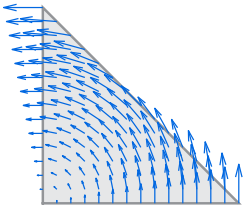		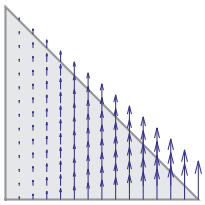	
2	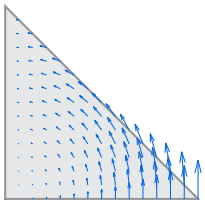	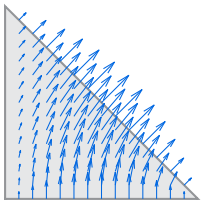	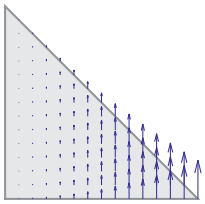	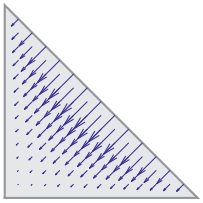

Figure 3.2: The illustration of some of the bases given in Table 3.2.

Accordingly, $\mathcal{P}_r^-(\otimes^2 T\widehat{\mathfrak{T}})$ in $(3.8)_2$ is defined by spanning the set of local shape functions $\left\{\boldsymbol{r}_{I,J}^{\widehat{\mathfrak{T}},\widehat{\mathcal{E}}_k}, \boldsymbol{r}_{I,J}^{\widehat{\mathfrak{T}},\widehat{\mathfrak{T}}}\right\}$ that is obtained from $\mathcal{P}_r^-(T\widehat{\mathfrak{T}})$. $\mathcal{P}_r(\otimes^2 T\widehat{\mathfrak{T}})$ in $(3.8)_2$ is defined similarly by using $\mathcal{P}_r(T\widehat{\mathfrak{T}})$. The explicit form of the spaces $\mathcal{P}_r^-(\otimes^2 T\widehat{\mathfrak{T}})$ and $\mathcal{P}_r(\otimes^2 T\widehat{\mathfrak{T}})$ are given in Example 7. Suppose $\overrightarrow{\boldsymbol{T}}_I := \begin{bmatrix} T^{I1} & T^{I2} \end{bmatrix}^{\mathsf{T}}$ is a column vector containing the elements of the I-th row of a $\binom{2}{0}$-tensor $\boldsymbol{T}$. The sets $\Sigma^{\widehat{\mathfrak{T}},\mathbf{c}}$ and $\Sigma^{\widehat{\mathfrak{T}},\mathbf{c}-}$ in $(3.8)_2$ consist of the following local degrees of freedom:

$$\phi_{I,J}^{\widehat{\mathfrak{T}},\widehat{\mathcal{E}}_k}(\boldsymbol{T}) = \int_{\widehat{\mathcal{E}}_k} \left(\frac{\hat{s}}{\hat{\ell}_k}\right)^{J-1} \langle \overrightarrow{\boldsymbol{T}}_I, \hat{\mathbf{t}}_k \rangle \, d\hat{s}, \qquad \phi_{I,J}^{\widehat{\mathfrak{T}},\widehat{\mathfrak{T}}}(\boldsymbol{T}) = \int_{\widehat{\mathfrak{T}}} \langle \overrightarrow{\boldsymbol{T}}_I, \hat{\boldsymbol{v}}_J \rangle \, d\hat{A}, \tag{3.12}$$

where $\hat{\boldsymbol{v}}_J$ is a vector-valued polynomial in $\mathbb{R}^2$, see [42, Theorem 7]. Note that $\phi_{I,J}^{\widehat{\mathfrak{T}},\widehat{\mathcal{E}}_k}$ and $\phi_{I,J}^{\widehat{\mathfrak{T}},\widehat{\mathfrak{T}}}$ are associated to the edges $\widehat{\mathcal{E}}_k$ and the area of the reference triangle $\widehat{\mathfrak{T}}$, respectively. In

practice, degrees of freedom are obtained by numerically solving the final discrete system so their direct calculation is needed only when we impose some of the boundary conditions strongly. Hence, in 2D, we do not directly compute the degrees of freedom such as $\phi_{I,J}^{\hat{\mathfrak{T}},\hat{\mathfrak{T}}}$ that are defined over the area of elements, and hence specifying $\hat{\boldsymbol{v}}_J$ is not required. Also, we choose the polynomials $(\hat{s}/\hat{\ell}_k)^{J-1}$, $J = 1, 2, 3$ to simplify the calculation of $\phi_{I,J}^{\hat{\mathfrak{T}},\hat{\mathcal{E}}_k}$ at the domain boundaries. The choice for these polynomials is not unique, in general. In finite element approximation, degrees of freedom must be a dual basis for the space spanned by the shape functions. Hence, we define some modified shape functions $\bar{\boldsymbol{r}}_{I,J}^{\hat{\mathfrak{T}},\hat{\mathcal{E}}_k}$ by writing a linear combination of $\boldsymbol{r}_{I,J}^{\hat{\mathfrak{T}},\hat{\mathcal{E}}_k}$ over J such that

$$\phi_{M,N}^{\hat{\mathfrak{T}},\hat{\mathcal{E}}_l}\left(\bar{\boldsymbol{r}}_{I,J}^{\hat{\mathfrak{T}},\hat{\mathcal{E}}_k}\right) = \begin{cases} 1, & \text{if } k = l \text{ and } I = M \text{ and } J = N, \\ 0, & \text{otherwise.} \end{cases} \tag{3.13}$$

In the case of $\mathcal{P}_r^-(\otimes^2 T\widehat{\mathfrak{T}})$, we have $\bar{\boldsymbol{r}}_{I,1}^{\hat{\mathfrak{T}},\hat{\mathcal{E}}_k} = \boldsymbol{r}_{I,1}^{\hat{\mathfrak{T}},\hat{\mathcal{E}}_k}$ for $r = 1$, and the following shape functions for $r = 2$:

$$\bar{\boldsymbol{r}}_{I,1}^{\hat{\mathfrak{T}},\hat{\mathcal{E}}_k} = 4\,\boldsymbol{r}_{I,1}^{\hat{\mathfrak{T}},\hat{\mathcal{E}}_k} - 2\,\boldsymbol{r}_{I,2}^{\hat{\mathfrak{T}},\hat{\mathcal{E}}_k}, \qquad \bar{\boldsymbol{r}}_{I,2}^{\hat{\mathfrak{T}},\hat{\mathcal{E}}_k} = -6\,\boldsymbol{r}_{I,1}^{\hat{\mathfrak{T}},\hat{\mathcal{E}}_k} + 6\,\boldsymbol{r}_{I,2}^{\hat{\mathfrak{T}},\hat{\mathcal{E}}_k},$$

Considering $\mathcal{P}_r(\otimes^2 T\widehat{\mathfrak{T}})$, one obtains

$$\bar{\boldsymbol{r}}_{I,1}^{\hat{\mathfrak{T}},\hat{\mathcal{E}}_k} = 4\,\boldsymbol{r}_{I,1}^{\hat{\mathfrak{T}},\hat{\mathcal{E}}_k} + 2\,\boldsymbol{r}_{I,2}^{\hat{\mathfrak{T}},\hat{\mathcal{E}}_k}, \qquad \bar{\boldsymbol{r}}_{I,2}^{\hat{\mathfrak{T}},\hat{\mathcal{E}}_k} = -6\,\boldsymbol{r}_{I,1}^{\hat{\mathfrak{T}},\hat{\mathcal{E}}_k} - 6\,\boldsymbol{r}_{I,2}^{\hat{\mathfrak{T}},\hat{\mathcal{E}}_k}.$$

for $r = 1$, and the following for $r = 2$:

$$\begin{aligned} \bar{\boldsymbol{r}}_{I,1}^{\hat{\mathfrak{T}},\hat{\mathcal{E}}_k} &= 9\,\boldsymbol{r}_{I,1}^{\hat{\mathfrak{T}},\hat{\mathcal{E}}_k} - 3\,\boldsymbol{r}_{I,2}^{\hat{\mathfrak{T}},\hat{\mathcal{E}}_k} - 9\,\boldsymbol{r}_{I,3}^{\hat{\mathfrak{T}},\hat{\mathcal{E}}_k}, \\ \bar{\boldsymbol{r}}_{I,2}^{\hat{\mathfrak{T}},\hat{\mathcal{E}}_k} &= -36\,\boldsymbol{r}_{I,1}^{\hat{\mathfrak{T}},\hat{\mathcal{E}}_k} + 24\,\boldsymbol{r}_{I,2}^{\hat{\mathfrak{T}},\hat{\mathcal{E}}_k} + 60\,\boldsymbol{r}_{I,3}^{\hat{\mathfrak{T}},\hat{\mathcal{E}}_k}, \\ \bar{\boldsymbol{r}}_{I,3}^{\hat{\mathfrak{T}},\hat{\mathcal{E}}_k} &= 30\,\boldsymbol{r}_{I,1}^{\hat{\mathfrak{T}},\hat{\mathcal{E}}_k} - 30\,\boldsymbol{r}_{I,2}^{\hat{\mathfrak{T}},\hat{\mathcal{E}}_k} + 60\,\boldsymbol{r}_{I,3}^{\hat{\mathfrak{T}},\hat{\mathcal{E}}_k}. \end{aligned}$$

Moreover, by choosing $\hat{\boldsymbol{v}}_J$ properly in $(3.12)_2$, one can show that

$$\phi^{\hat{\mathfrak{T}},\hat{\mathcal{E}}_k}_{M,N}\Big(\boldsymbol{r}^{\hat{\mathfrak{T}},\hat{\mathfrak{T}}}_{I,J}\Big) = \phi^{\hat{\mathfrak{T}},\hat{\mathfrak{T}}}_{M,N}\Big(\bar{\boldsymbol{r}}^{\hat{\mathfrak{T}},\hat{\mathcal{E}}_k}_{I,J}\Big) = 0,$$
$$\phi^{\hat{\mathfrak{T}},\hat{\mathfrak{T}}}_{M,N}\Big(\boldsymbol{r}^{\hat{\mathfrak{T}},\hat{\mathfrak{T}}}_{I,J}\Big) = \begin{cases} 1, & \text{if } I = M \text{ and } J = N, \\ 0, & \text{otherwise.} \end{cases} \tag{3.14}$$

We will use the set of reference shape functions $\Big\{\bar{\boldsymbol{r}}^{\hat{\mathfrak{T}},\hat{\mathcal{E}}_k}_{I,J}, \boldsymbol{r}^{\hat{\mathfrak{T}},\hat{\mathfrak{T}}}_{I,J}\Big\}$ to approximate $\boldsymbol{K} \in H^{\mathrm{c}}$.

In 2D, the spaces of type H^{c} and H^{d} are transformed to each other by a 90 degree rotation. To see this, recall the definitions of H^{c} and H^{d} in the distributional sense and observe that $\mathbf{grad}(q) = \mathbf{R}^{\mathsf{T}}\,\mathbf{s}(q)$, where q is a smooth function. Therefore, to construct $(3.8)_3$ for approximating $\boldsymbol{P} \in H^{\mathrm{d}}$, we simply need the following shape functions:

$$\bar{\boldsymbol{s}}^{\hat{\mathfrak{T}},\hat{\mathcal{E}}_k}_{I,J} = \bar{\boldsymbol{r}}^{\hat{\mathfrak{T}},\hat{\mathcal{E}}_k}_{I,J}\mathbf{R}^{\mathsf{T}}, \quad \boldsymbol{s}^{\hat{\mathfrak{T}},\hat{\mathfrak{T}}}_{I,J} = \boldsymbol{r}^{\hat{\mathfrak{T}},\hat{\mathfrak{T}}}_{I,J}\mathbf{R}^{\mathsf{T}}. \tag{3.15}$$

The corresponding local degrees of freedom are

$$\psi^{\hat{\mathfrak{T}},\hat{\mathcal{E}}_k}_{I,J}(\boldsymbol{T}) = \int_{\hat{\mathcal{E}}_k} \Big(\frac{\hat{s}}{\hat{\ell}_k}\Big)^{J-1} \langle \overrightarrow{\boldsymbol{T}}_I, \hat{\mathbf{n}}_k\rangle\, d\hat{s}, \quad \psi^{\hat{\mathfrak{T}},\hat{\mathfrak{T}}}_{I,J}(\boldsymbol{T}) = \int_{\hat{\mathfrak{T}}} \langle \overrightarrow{\boldsymbol{T}}_I, \mathbf{R}\hat{\boldsymbol{v}}_J\rangle\, d\hat{A}. \tag{3.16}$$

Note that $\psi^{\hat{\mathfrak{T}},\hat{\mathcal{E}}_l}_{M,N}\Big(\bar{\boldsymbol{s}}^{\hat{\mathfrak{T}},\hat{\mathcal{E}}_k}_{I,J}\Big) = \psi^{\hat{\mathfrak{T}},\hat{\mathcal{E}}_l}_{M,N}\Big(\bar{\boldsymbol{r}}^{\hat{\mathfrak{T}},\hat{\mathcal{E}}_k}_{I,J}\mathbf{R}^{\mathsf{T}}\Big) = \phi^{\hat{\mathfrak{T}},\hat{\mathcal{E}}_l}_{M,N}\Big(\bar{\boldsymbol{r}}^{\hat{\mathfrak{T}},\hat{\mathcal{E}}_k}_{I,J}\Big)$, and thus, the condition (3.13) holds for $\psi^{\hat{\mathfrak{T}},\hat{\mathcal{E}}_k}_{I,J}$ and $\bar{\boldsymbol{s}}^{\hat{\mathfrak{T}},\hat{\mathcal{E}}_k}_{I,J}$ as well. Similarly, one can write the condition (3.14) for (3.15) and (3.16). The space $\mathcal{P}^{\ominus}_r(\bigotimes^2 T\widehat{\mathfrak{T}})$ in $(3.8)_3$ is spanned by the set $\Big\{\bar{\boldsymbol{s}}^{\hat{\mathfrak{T}},\hat{\mathcal{E}}_k}_{I,J}, \boldsymbol{s}^{\hat{\mathfrak{T}},\hat{\mathfrak{T}}}_{I,J}\Big\}$, which is obtained from a 90 degree rotation of the bases of $\mathcal{P}^{-}_r(T\widehat{\mathfrak{T}})$. The same set spans $\mathcal{P}_r(\bigotimes^2 T\widehat{\mathfrak{T}})$ in $(3.8)_3$ if it is written by a 90 degree rotation of the bases of $\mathcal{P}_r(T\widehat{\mathfrak{T}})$. Also, note that $\mathcal{P}^{-}_r(\bigotimes^2 T\widehat{\mathfrak{T}})$ and $\mathcal{P}^{\ominus}_r(\bigotimes^2 T\widehat{\mathfrak{T}})$ in (3.8) are transformed to each other by a 90 degree rotation. The explicit expression of these spaces are given in Example 7.

For the reference finite element of pressure $(3.8)_4$, the set of local shape functions $\big\{t^{\hat{\mathfrak{T}}}_i\big\}$, which spans $\mathcal{P}_r(\widehat{\mathfrak{T}})$, is $\{1\}$ for $r = 0$, $\{1, \xi^1, \xi^2\}$ for $r = 1$, and $\{1, \xi^1, \xi^2, (\xi^1)^2, (\xi^2)^2, \xi^1\xi^2\}$

Table 3.3: Numbers of local degrees of freedom (DOF) in terms of the order of the corresponding polynomial spaces r.

DOF	number of DOF			
	for each node	for each edge	for $\mathcal{T}$	total
$\Sigma^{\mathcal{T},1}$	2	0	0	$6r$
$\Sigma^{\mathcal{T},\mathbf{c}-}$, $\Sigma^{\mathcal{T},\mathbf{d}-}$	0	$2r$	$2(r^2-r)$	$2r(r+2)$
$\Sigma^{\mathcal{T},\mathbf{c}}$, $\Sigma^{\mathcal{T},\mathbf{d}}$	0	$2(r+1)$	$2(r^2-1)$	$2(r+1)(r+2)$
$\Sigma^{\mathcal{T},\ell}$	0	0	$(r+1)(r+2)/2$	$(r+1)(r+2)/2$

for $r = 2$. The corresponding local degrees of freedom are of the form

$$\omega_i^{\hat{\mathcal{T}}}(f) = \frac{1}{\hat{A}} \int_{\hat{\mathcal{T}}} \hat{p}_i^r f \, d\hat{A}, \tag{3.17}$$

where $\hat{p}_i^r$, $i = 1, 2, ..., n_s$ are polynomials of order r on $\widehat{\mathcal{T}}$, which can be calculated by solving $\omega_i^{\hat{\mathcal{T}}}(t_j^{\hat{\mathcal{T}}}) = \delta_{ij}$. However, as was discussed earlier, we do not calculate $\omega_i^{\hat{\mathcal{T}}}$ directly, and hence, calculating $\hat{p}_i^r$ is not necessary.

The numbers of local degrees of freedom (the number of local shape functions) for the four types of finite elements that we discussed above are summarized in Table 3.3. This holds for the reference finite elements (3.8) and any finite elements that we will generate from them for an arbitrary triangle $\mathcal{T}$.

Next we explain how to construct a family of finite elements for a given mesh based on the reference finite elements (3.8). Let $\mathcal{B}_h$ denote a triangulation (or simply a mesh) of the reference configuration $\mathcal{B}$, where $\mathcal{B}_h$ consists of arbitrary triangles $\mathcal{T}$, and $h := \max \operatorname{diam} \mathcal{T}$, $\forall \mathcal{T} \in \mathcal{B}_h$. Note that the intersection of any two distinct triangles of $\mathcal{B}_h$ can be empty, a common edge joining two common vertices, or only a vertex of those two triangles. We locally assign the numbers $1, 2, 3$ to vertices of each $\mathcal{T} \in \mathcal{B}_h$, to which we will refer as the ordering of vertices. Let $\mathbf{X}_i = (\mathrm{X}_i^1, \mathrm{X}_i^2)$ denote the Cartesian coordinates of the i-th vertex of $\mathcal{T}$. The reference triangle $\widehat{\mathcal{T}}$ shown in Figure 3.1 can be mapped onto

any $\mathcal{T} \in \mathcal{B}_h$ by an affine transformation $\mathbf{T}_\mathcal{T}$ given by

$$\mathbf{T}_\mathcal{T} : \widehat{\mathcal{T}} \longrightarrow \mathcal{T}, \quad \mathbf{T}_\mathcal{T}(\boldsymbol{\xi}) := \mathbf{J}_\mathcal{T}\boldsymbol{\xi} + \mathbf{a}_\mathcal{T}, \tag{3.18}$$

where

$$\mathbf{J}_\mathcal{T} = \begin{bmatrix} \mathrm{X}_2^1 - \mathrm{X}_1^1 & \mathrm{X}_3^1 - \mathrm{X}_1^1 \\ \mathrm{X}_2^2 - \mathrm{X}_1^2 & \mathrm{X}_3^2 - \mathrm{X}_1^2 \end{bmatrix} \quad \text{and} \quad \mathbf{a}_\mathcal{T} = \begin{bmatrix} \mathrm{X}_1^1 \\ \mathrm{X}_1^2 \end{bmatrix}.$$

The above mapping is bijective and $\mathbf{J}_\mathcal{T}$ is invertible. Let $\mathcal{E}_i^\mathcal{T} = \mathbf{T}_\mathcal{T}(\widehat{\mathcal{E}}_i)$, $i = 1, 2, 3$ denote the edges of $\mathcal{T}$. Also, assume that $\mathcal{E}_i^\mathcal{T}$ inherits the orientation of $\widehat{\mathcal{E}}_i$, i.e., if the orientation of $\widehat{\mathcal{E}}_i$ in terms of the coordinates is $\boldsymbol{\xi}_k \rightarrow \boldsymbol{\xi}_l$, then the orientation of $\mathcal{E}_i^\mathcal{T}$ is $\mathbf{T}_\mathcal{T}(\boldsymbol{\xi}_k) = \mathbf{X}_k \rightarrow \mathbf{X}_l = \mathbf{T}_\mathcal{T}(\boldsymbol{\xi}_l)$. Similar to what we discussed for the reference element, the tangent vector $\mathbf{t}_i$ defined on $\mathcal{E}_i^\mathcal{T}$ accepts the orientation of $\mathcal{E}_i^\mathcal{T}$, and the normal vector on $\mathcal{E}_i^\mathcal{T}$ is obtained by $\mathbf{n}_i = \mathbf{R}\mathbf{t}_i$.

We use the numbering scheme discussed in [62] for convenience in defining global shape functions and degrees of freedom of conforming H^{c} and H^{d} finite elements and also for their efficient assembly. In this scheme, a global number is assigned to each vertex of the mesh. Then, the ordering of the three vertices of each element $\mathcal{T}$ is defined based on the ascending order of the global numbers associated to them, i.e., the first vertex of each $\mathcal{T}$ has the smallest global number among the three vertices and the third vertex has the largest. Using this ordering and the edge orientations of the reference element (see Figure 3.1), the orientation of every edge in the mesh joining two vertices will be from the vertex with the smaller to the vertex with the larger global number. The advantage of this scheme is that the orientation of an edge shared by two adjacent elements in the mesh is identical to that of the edge in either of the two elements. More precisely, assume that $\mathcal{T}$ and $\mathcal{T}'$ are adjacent in $\mathcal{B}_h$ and share a common edge $\mathcal{E}$ such that $\mathcal{E} \cap \mathcal{T} = \mathcal{E}_i^\mathcal{T}$ and $\mathcal{E} \cap \mathcal{T}' = \mathcal{E}_{i'}^{\mathcal{T}'}$. The scheme gaurantees that $\mathcal{E}_i^\mathcal{T}$ and $\mathcal{E}_{i'}^{\mathcal{T}'}$ inherit an identical orientation from $\widehat{\mathcal{E}}_i$ and $\widehat{\mathcal{E}}_{i'}$, regardless of their local edge numberings i and i'. For an illustration of this, see [62, Figue 5.1]. It

follows that both the tangent and the normal vectors that are defined on $\mathcal{E}_i^{\mathcal{T}}$ and $\mathcal{E}_{i'}^{\mathcal{T}'}$ are identical.

Note that the above scheme violates the standard convention that the three vertices of every element in the mesh have a counterclockwise ordering. Therefore, one should keep in mind that not all the normal vectors of the exterior edges lying on the boundaries of the mesh are pointed outward, and not all their tangent vectors are oriented in the counterclockwise direction. Also, $\det \mathbf{J}_{\mathcal{T}}$ can be either positive or negative, so it would be useful to define the following constant for each element:

$$o_{\mathcal{T}} = \operatorname{sign}\left(\det \mathbf{J}_{\mathcal{T}}\right).$$

Note that $o_{\mathcal{T}} = 1$ if the three vertices of $\mathcal{T}$ have the counterclockwise ordering, and $o_{\mathcal{T}} = -1$ otherwise.

In a general setting, let $\left(\widehat{\mathcal{T}}, \mathcal{P}(\widehat{\mathcal{T}}), \Sigma^{\hat{\mathcal{T}}}\right)$ be a reference finite element and let $V(\widehat{\mathcal{T}})$ be a linear space of $\mathbb{R}^m$-valued functions in $\widehat{\mathcal{T}}$ such that $\mathcal{P}(\widehat{\mathcal{T}}) \subset V(\widehat{\mathcal{T}})$ and $\Sigma^{\hat{\mathcal{T}}}$ can be extended to $V(\widehat{\mathcal{T}})^\star$. Also, for any $\mathcal{T} \in \mathcal{B}_h$, suppose $\Psi_{\mathcal{T}} : V(\widehat{\mathcal{T}}) \longrightarrow V(\mathcal{T})$ is a linear bijective mapping, which preserves the structure between $V(\widehat{\mathcal{T}})$ and its counterpart $V(\mathcal{T})$, i.e., $\Psi_{\mathcal{T}}$ is an isomorphism. Then, by using the reference finite element and the following proposition, one can define a set of finite elements for all $\mathcal{T}$ in $\mathcal{B}_h$ [26].

Proposition 10. *Let $\Psi_{\mathcal{T}} : V(\widehat{\mathcal{T}}) \longrightarrow V(\mathcal{T})$ be a linear bijection. For any $\mathcal{T} \in \mathcal{B}_h$, $\left(\mathcal{T}, \mathcal{P}(\mathcal{T}), \Sigma^{\mathcal{T}}\right)$ defined as*

$$\begin{cases} \mathcal{T} = \mathbf{T}_{\mathcal{T}}(\widehat{\mathcal{T}}) \\ \mathcal{P}(\mathcal{T}) = \left\{\Psi_{\mathcal{T}}(\hat{p}) : \hat{p} \in \mathcal{P}(\widehat{\mathcal{T}})\right\} \\ \Sigma^{\mathcal{T}} = \left\{\sigma_1^{\mathcal{T}}, \sigma_2^{\mathcal{T}}, ...\sigma_{n_s}^{\mathcal{T}} : \sigma_i^{\mathcal{T}}(p) = \sigma_i^{\hat{\mathcal{T}}}\left(\Psi_{\mathcal{T}}^{-1}(p)\right), \forall p \in \mathcal{P}(\mathcal{T}), i = 1, 2, ..., n_s\right\} \end{cases}$$

is a finite element with the local shape functions $\theta_i^{\mathcal{T}} = \Psi_{\mathcal{T}}\left(\theta_i^{\hat{\mathcal{T}}}\right)$, $i = 1, 2, ..., n_s$, and the

local interpolation operator

$$\mathrm{I}_{\mathcal{T}} : V(\mathcal{T}) \longrightarrow \mathcal{P}(\mathcal{T}), \quad \mathrm{I}_{\mathcal{T}}(v) = \sum_{i=0}^{n_s} \sigma_i^{\mathcal{T}}(v)\theta_i^{\mathcal{T}}. \tag{3.19}$$

Proof. By assumption, $\hat{p} = \Psi_{\mathcal{T}}^{-1}(p)$ is bijective, $\forall p \in \mathcal{P}(\mathcal{T})$, and the mapping $\hat{p} \longmapsto \left(\sigma_1^{\hat{\mathcal{T}}}(\hat{p}), ..., \sigma_{n_s}^{\hat{\mathcal{T}}}(\hat{p})\right)$ is a bijection, $\forall \hat{p} \in \mathcal{P}(\widehat{\mathcal{T}})$. Therefore, the composition mapping $p \longmapsto \left(\sigma_1^{\mathcal{T}}(p), ..., \sigma_{n_s}^{\mathcal{T}}(p)\right)$ is bijective, $\forall p \in \mathcal{P}(\mathcal{T})$, and $\left(\mathcal{T}, \mathcal{P}(\mathcal{T}), \Sigma^{\mathcal{T}}\right)$ is a finite element. $\theta_i^{\mathcal{T}} \in \mathcal{P}^{\mathcal{T}}$ and $\sigma_j^{\mathcal{T}}\left(\theta_i^{\mathcal{T}}\right) = \sigma_j^{\hat{\mathcal{T}}}\left(\Psi_{\mathcal{T}}^{-1}\left(\theta_i^{\mathcal{T}}\right)\right) = \sigma_j^{\hat{\mathcal{T}}}\left(\theta_i^{\hat{\mathcal{T}}}\right) = \delta_{ij}$, for $i, j = 1, 2, ..., n_s$, and hence, $\theta_i^{\mathcal{T}}$, $i = 1, 2, ..n_s$ are the local shape functions. Next we show that the local interpolation operator $\mathrm{I}_{\mathcal{T}}$ is well-defined. If $q \in P(\mathcal{T})$, there exists $\hat{q} \in P(\widehat{\mathcal{T}}) \subset V(\widehat{\mathcal{T}})$ such that $q = \Psi_{\mathcal{T}}(\hat{q})$, so $q \in V(\mathcal{T})$, and we conclude that $P(\mathcal{T}) \subset V(\mathcal{T})$. Also, knowing that $\sigma_i^{\hat{\mathcal{T}}}$ can be calculated for elements of $V(\widehat{\mathcal{T}})$, one can write $\sigma_i^{\mathcal{T}}(v) = \sigma_i^{\hat{\mathcal{T}}}\left(\Psi_{\mathcal{T}}^{-1}(v)\right)$ for any $v \in V(\mathcal{T})$, and hence, $\Sigma^{\mathcal{T}}$ can be extended to $V(\mathcal{T})^\star$. □

Consider the reference finite element of displacement $\left(\widehat{\mathcal{T}}, \mathcal{P}_r(T\widehat{\mathcal{T}}), \Sigma^{\hat{\mathcal{T}},1}\right)$. Let $V(\widehat{\mathcal{T}}) = C^0(T\widehat{\mathcal{T}})$ and define $V(\mathcal{T})$ similarly. Use the mapping

$$\mathbf{T}_{\mathcal{T}}^1 : C^0(T\widehat{\mathcal{T}}) \longrightarrow C^0(T\mathcal{T}), \quad \mathbf{T}_{\mathcal{T}}^1(\widehat{\boldsymbol{V}}) := \widehat{\boldsymbol{V}} \circ \mathbf{T}_{\mathcal{T}}^{-1}, \tag{3.20}$$

and generate the family of finite elements $\left\{\left(\mathcal{T}, \mathcal{P}_r(T\mathcal{T}), \Sigma^{\mathcal{T},1}\right)\right\}_{\mathcal{T}\in\mathcal{B}_h}$ as described in Proposition 10. Accordingly, the local shape functions are $\boldsymbol{h}_k^{\mathcal{T}} = \mathbf{T}_{\mathcal{T}}^1\left(\boldsymbol{h}_k^{\hat{\mathcal{T}}}\right)$. It is straightforward to check that $\boldsymbol{h}_k^{\mathcal{T}}$ is a Lagrange polynomial on $\mathcal{T}$, and members of the set of degrees of freedom $\Sigma^{\mathcal{T},1}$ are the values of the interpolated function at the nodes of $\mathcal{T}$.

The mapping (3.20) does not transform $H^{\mathbf{c}}(T\widehat{\mathcal{T}})$ into $H^{\mathbf{c}}(T\mathcal{T})$ or $H^{\mathbf{d}}(T\widehat{\mathcal{T}})$ into $H^{\mathbf{d}}(T\mathcal{T})$. Instead, one needs to use the Piola transforms. Considering the affine mapping (3.18), the Piola transforms $\mathbf{T}_{\mathcal{T}}^{\mathbf{c}}$ and $\mathbf{T}_{\mathcal{T}}^{\mathbf{d}}$ are defined as

$$\mathbf{T}_{\mathcal{T}}^{\mathbf{c}} : H^{\mathbf{c}}(T\widehat{\mathcal{T}}) \longrightarrow H^{\mathbf{c}}(T\mathcal{T}), \quad \mathbf{T}_{\mathcal{T}}^{\mathbf{c}}(\widehat{\boldsymbol{V}}) := \mathbf{J}_{\mathcal{T}}^{-\mathsf{T}}\widehat{\boldsymbol{V}} \circ \mathbf{T}_{\mathcal{T}}^{-1}, \tag{3.21}$$

$$\mathbf{T}_{\mathcal{T}}^{\mathbf{d}} : H^{\mathbf{d}}(T\widehat{\mathcal{T}}) \longrightarrow H^{\mathbf{d}}(T\mathcal{T}), \quad \mathbf{T}_{\mathcal{T}}^{\mathbf{d}}(\widehat{\boldsymbol{V}}) := \frac{1}{\det \mathbf{J}_{\mathcal{T}}} \mathbf{J}_{\mathcal{T}} \widehat{\boldsymbol{V}} \circ \mathbf{T}_{\mathcal{T}}^{-1}. \tag{3.22}$$

For a $\binom{2}{0}$-tensor $\boldsymbol{T}$, one calculates the Piola transformations separately for each row:

$$\mathbf{T}_{\mathcal{T}}^{\mathbf{c}}(\boldsymbol{T}) = \begin{bmatrix} \mathbf{T}_{\mathcal{T}}^{\mathbf{c}}(\overrightarrow{\boldsymbol{T}}_1)^{\mathsf{T}} \\ \mathbf{T}_{\mathcal{T}}^{\mathbf{c}}(\overrightarrow{\boldsymbol{T}}_2)^{\mathsf{T}} \end{bmatrix}, \quad \mathbf{T}_{\mathcal{T}}^{\mathbf{d}}(\boldsymbol{T}) = \begin{bmatrix} \mathbf{T}_{\mathcal{T}}^{\mathbf{d}}(\overrightarrow{\boldsymbol{T}}_1)^{\mathsf{T}} \\ \mathbf{T}_{\mathcal{T}}^{\mathbf{d}}(\overrightarrow{\boldsymbol{T}}_2)^{\mathsf{T}} \end{bmatrix}. \tag{3.23}$$

The Piola mapping $\mathbf{T}_{\mathcal{T}}^{\mathbf{c}}$ is an isomorphism of $H^{\mathbf{c}}(T\widehat{\mathcal{T}})$ onto $H^{\mathbf{c}}(T\mathcal{T})$, and the Piola mapping $\mathbf{T}_{\mathcal{T}}^{\mathbf{d}}$ is an isomorphism of $H^{\mathbf{d}}(T\widehat{\mathcal{T}})$ onto $H^{\mathbf{d}}(T\mathcal{T})$. This and other useful properties of these mappings can be summarized in the following Lemma.

Lemma 11. *Using the numbering scheme discussed above, assume that $\mathcal{T} = \mathbf{T}_{\mathcal{T}}(\widehat{\mathcal{T}})$ is an arbitrary element with edge lengths ℓ_k, unit tangent vectors $\mathbf{t}_k$, and unit normal vectors $\mathbf{n}_k$. Let $\widehat{\boldsymbol{V}} \in H^{\mathbf{c}}(T\widehat{\mathcal{T}})$ and $\widehat{\boldsymbol{U}} \in H^{\mathbf{d}}(T\widehat{\mathcal{T}})$, and set $\boldsymbol{V} = \mathbf{T}_{\mathcal{T}}^{\mathbf{c}}(\widehat{\boldsymbol{V}})$ and $\boldsymbol{U} = \mathbf{T}_{\mathcal{T}}^{\mathbf{d}}(\widehat{\boldsymbol{U}})$. Also, assume that $q = \hat{q} \circ \mathbf{T}_{\mathcal{T}}^{-1}$, where $\hat{q} \in C^0(\widehat{\mathcal{T}})$. Define $\boldsymbol{v}_J := o_{\mathcal{T}} \mathbf{T}_{\mathcal{T}}^{\mathbf{d}}(\hat{\boldsymbol{v}}_J)$ and $\hat{p}_k(\hat{s}) := \sum_{i=0}^{n} a_i \big(\hat{s}/\hat{\ell}_k\big)^i$, and construct $p_k = \hat{p}_k \circ g_k^{-1}$ with $g_k(\hat{s}) = \frac{\ell_k}{\hat{\ell}_k}\hat{s}$. Recall the linear operators (2.1) and (2.3) and set $I = 1$, and note that operators with the hat symbol are written with respect to the reference element coordinates $\boldsymbol{\xi} = (\xi^1, \xi^2)$. The following relations hold:*

(i) $\int_{\mathcal{T}} \big\langle \mathbf{c}(\boldsymbol{V}), q \big\rangle \, dA = o_{\mathcal{T}} \int_{\widehat{\mathcal{T}}} \big\langle \widehat{\mathbf{c}}(\widehat{\boldsymbol{V}}), \hat{q} \big\rangle \, d\hat{A}$, *and* $\int_{\mathcal{T}} \big\langle \boldsymbol{V}, \mathbf{s}(q) \big\rangle \, dA = o_{\mathcal{T}} \int_{\widehat{\mathcal{T}}} \big\langle \widehat{\boldsymbol{V}}, \widehat{\mathbf{s}}(\hat{q}) \big\rangle \, d\hat{A}$,

(ii) $\int_{\mathcal{T}} \big\langle \mathbf{div}(\boldsymbol{U}), q \big\rangle \, dA = o_{\mathcal{T}} \int_{\widehat{\mathcal{T}}} \big\langle \widehat{\mathbf{div}}(\widehat{\boldsymbol{U}}), \hat{q} \big\rangle \, d\hat{A}$, *and* $\int_{\mathcal{T}} \big\langle \boldsymbol{U}, \mathbf{grad}(q) \big\rangle \, dA = o_{\mathcal{T}} \int_{\widehat{\mathcal{T}}} \big\langle \widehat{\boldsymbol{U}}, \widehat{\mathbf{grad}}(\hat{q}) \big\rangle \, d\hat{A}$,

(iii) $\int_{\mathcal{E}_k} p_k \big\langle \boldsymbol{V}, \mathbf{t}_k \big\rangle \, ds = \int_{\widehat{\mathcal{E}}_k} \hat{p}_k \big\langle \widehat{\boldsymbol{V}}, \hat{\mathbf{t}}_k \big\rangle \, d\hat{s}$, *and* $\int_{\mathcal{T}} \big\langle \boldsymbol{V}, \boldsymbol{v}_J \big\rangle \, dA = \int_{\widehat{\mathcal{T}}} \big\langle \widehat{\boldsymbol{V}}, \hat{\boldsymbol{v}}_J \big\rangle \, d\hat{A}$,

(iv) $\int_{\mathcal{E}_k} p_k \big\langle \boldsymbol{U}, \mathbf{n}_k \big\rangle \, ds = \int_{\widehat{\mathcal{E}}_k} \hat{p}_k \big\langle \widehat{\boldsymbol{U}}, \hat{\mathbf{n}}_k \big\rangle \, d\hat{s}$, *and* $\int_{\mathcal{T}} \big\langle \boldsymbol{U}, \mathbf{R}\boldsymbol{v}_J \big\rangle \, dA = \int_{\widehat{\mathcal{T}}} \big\langle \widehat{\boldsymbol{U}}, \mathbf{R}\hat{\boldsymbol{v}}_J \big\rangle \, d\hat{A}$,

(v) $\int_{\mathcal{T}} \big\langle \boldsymbol{U}, \boldsymbol{V} \big\rangle \, dA = o_{\mathcal{T}} \int_{\widehat{\mathcal{T}}} \big\langle \widehat{\boldsymbol{U}}, \widehat{\boldsymbol{V}} \big\rangle \, d\hat{A}$.

Proof. The second identities in (iii) and (v) can be derived directly form the assumptions. Other identities are the consequences of the following relations:

(i) $\mathbf{c}(\boldsymbol{V}) = \frac{1}{\det \mathbf{J}_{\mathcal{T}}} \widehat{\mathbf{c}}(\widehat{\boldsymbol{V}}) \circ \mathbf{T}_{\mathcal{T}}^{-1}$, and $\mathbf{s}(q) = \frac{1}{\det \mathbf{J}_{\mathcal{T}}} \mathbf{J}_{\mathcal{T}} \widehat{\mathbf{s}}(\hat{q}) \circ \mathbf{T}_{\mathcal{T}}^{-1}$,

(ii) $\mathbf{div}\, \boldsymbol{U} = \frac{1}{\det \mathbf{J}_{\mathcal{T}}} \widehat{\mathbf{div}}\, \widehat{\boldsymbol{U}} \circ \mathbf{T}_{\mathcal{T}}^{-1}$, and $\mathbf{grad}\, q = \mathbf{J}_{\mathcal{T}}^{-\mathsf{T}} \widehat{\mathbf{grad}}\, \hat{q} \circ \mathbf{T}_{\mathcal{T}}^{-1}$,

(iii) $\mathbf{t}_k = \frac{\hat{\ell}_k}{\ell_k} \mathbf{J}_{\mathcal{T}} \hat{\mathbf{t}}_k$,

(iv) $\mathbf{n}_k = \frac{\hat{\ell}_k}{\ell_k} (\det \mathbf{J}_{\mathcal{T}}) \mathbf{J}_{\mathcal{T}}^{-\mathsf{T}} \hat{\mathbf{n}}_k$, and $\frac{1}{\det \mathbf{J}_{\mathcal{T}}} \mathbf{R} \mathbf{J}_{\mathcal{T}} = \mathbf{J}_{\mathcal{T}}^{-\mathsf{T}} \mathbf{R}$.

□

Consider the two reference finite elements for displacement gradient $\left(\widehat{\mathcal{T}}, \mathcal{P}_r(\otimes^2 T\widehat{\mathcal{T}}), \Sigma^{\widehat{\mathcal{T}},\mathbf{c}}\right)$ and $\left(\widehat{\mathcal{T}}, \mathcal{P}_r^-(\otimes^2 T\widehat{\mathcal{T}}), \Sigma^{\widehat{\mathcal{T}},\mathbf{c}-}\right)$. Let $V(\widehat{\mathcal{T}}) = H^{\mathbf{c}}(\widehat{\mathcal{T}})$ and $V(\mathcal{T}) = H^{\mathbf{c}}(\mathcal{T})$, and use the Piola mapping (3.21), and relation $(3.23)_1$. Then, based on Proposition 10, construct two families of finite elements $\left\{\left(\mathcal{T}, \mathcal{P}_r(\otimes^2 T\mathcal{T}), \Sigma^{\mathcal{T},\mathbf{c}}\right)\right\}_{\mathcal{T}\in\mathcal{B}_h}$ and $\left\{\left(\mathcal{T}, \mathcal{P}_r^-(\otimes^2 T\mathcal{T}), \Sigma^{\mathcal{T},\mathbf{c}-}\right)\right\}_{\mathcal{T}\in\mathcal{B}_h}$. The local shape functions are $\bar{\boldsymbol{r}}_{I,J}^{\mathcal{T},\mathcal{E}_k} = \mathbf{T}_{\mathcal{T}}^{\mathbf{c}}\left(\bar{\boldsymbol{r}}_{I,J}^{\widehat{\mathcal{T}},\widehat{\mathcal{E}}_k}\right)$, $\boldsymbol{r}_{I,J}^{\mathcal{T},\mathcal{T}} = \mathbf{T}_{\mathcal{T}}^{\mathbf{c}}\left(\boldsymbol{r}_{I,J}^{\widehat{\mathcal{T}},\widehat{\mathcal{T}}}\right)$, and the local degrees of freedom read $\phi_{I,J}^{\mathcal{T},\mathcal{E}_k}(\boldsymbol{T}) = \left(\phi_{I,J}^{\widehat{\mathcal{T}},\widehat{\mathcal{E}}_k} \circ \mathbf{T}_{\mathcal{T}}^{\mathbf{c}\,-1}\right)(\boldsymbol{T})$ and $\phi_{I,J}^{\mathcal{T},\mathcal{T}}(\boldsymbol{T}) = \left(\phi_{I,J}^{\widehat{\mathcal{T}},\widehat{\mathcal{T}}} \circ \mathbf{T}_{\mathcal{T}}^{\mathbf{c}\,-1}\right)(\boldsymbol{T})$. Lemma 11, (iii) implies that $\phi_{I,J}^{\mathcal{T},\mathcal{E}_k}$ and $\phi_{I,J}^{\mathcal{T},\mathcal{T}}$ are in fact (3.12) with all the hat symbols removed.

Similarly, by using the Piola mapping (3.22), $(3.23)_2$, and Proposition 10 generate two families $\left\{\left(\mathcal{T}, \mathcal{P}_r(\otimes^2 T\mathcal{T}), \Sigma^{\mathcal{T},\mathbf{d}}\right)\right\}_{\mathcal{T}\in\mathcal{B}_h}$ and $\left\{\left(\mathcal{T}, \mathcal{P}_r^{\ominus}(\otimes^2 T\mathcal{T}), \Sigma^{\mathcal{T},\mathbf{d}-}\right)\right\}_{\mathcal{T}\in\mathcal{B}_h}$ from the two reference finite elements for stress $\left(\widehat{\mathcal{T}}, \mathcal{P}_r(\otimes^2 T\widehat{\mathcal{T}}), \Sigma^{\widehat{\mathcal{T}},\mathbf{d}}\right)$ and $\left(\widehat{\mathcal{T}}, \mathcal{P}_r^{\ominus}(\otimes^2 T\widehat{\mathcal{T}}), \Sigma^{\widehat{\mathcal{T}},\mathbf{d}-}\right)$. The local shape functions read $\bar{\boldsymbol{s}}_{I,J}^{\mathcal{T},\mathcal{E}_k} = \mathbf{T}_{\mathcal{T}}^{\mathbf{d}}\left(\bar{\boldsymbol{s}}_{I,J}^{\widehat{\mathcal{T}},\widehat{\mathcal{E}}_k}\right)$, $\boldsymbol{s}_{I,J}^{\mathcal{T},\mathcal{T}} = \mathbf{T}_{\mathcal{T}}^{\mathbf{d}}\left(\boldsymbol{s}_{I,J}^{\widehat{\mathcal{T}},\widehat{\mathcal{T}}}\right)$. Also, according to Lemma 11, (iv), the local degrees of freedom $\psi_{I,J}^{\mathcal{T},\mathcal{E}_k}$, $\psi_{I,J}^{\mathcal{T},\mathcal{T}}$ are (3.16) without the hat symbols.

Recall the reference finite element of the pressure-like field $(\widehat{\mathcal{T}}, \mathcal{P}_r(\widehat{\mathcal{T}}), \Sigma^{\widehat{\mathcal{T}},\ell})$. Set $V(\widehat{\mathcal{T}}) = L^2(\widehat{\mathcal{T}})$ and $V(\mathcal{T}) = L^2(\mathcal{T})$. Then, use the mapping

$$\mathbf{T}_{\mathcal{T}}^{\ell} : L^2(\widehat{\mathcal{T}}) \longrightarrow L^2(\mathcal{T}), \quad \mathbf{T}_{\mathcal{T}}^{\ell}(\hat{f}) := \hat{f} \circ \mathbf{T}_{\mathcal{T}}^{-1}. \tag{3.24}$$

and Proposition 10 to generate $\left\{\left(\mathcal{T}, \mathcal{P}_r(\mathcal{T}), \Sigma^{\mathcal{T},\ell}\right)\right\}_{\mathcal{T}\in\mathcal{B}_h}$. The local shape functions become $t_i^{\mathcal{T}} = \mathbf{T}_{\mathcal{T}}^{\ell}(t_i^{\widehat{\mathcal{T}}})$, and by recalling (3.17), it is straightforward to show that the local degrees of

freedom are $\omega_i^{\mathcal{T}}(f) = \frac{1}{A}\int_{\mathcal{T}} p_i^r f \, dA$, where $p_i^r = \hat{p}_i^r \circ \mathbf{T}_{\mathcal{T}}^{-1}$.

3.3 Finite Element Spaces

In order to define suitable conforming finite element spaces, we first define the following notions of jump across the edges of a 2D mesh for vector and tensor fields. We denote the set of all interior edges of the mesh by $\mathcal{E}_h^i$. For an edge $\mathcal{E} \in \mathcal{E}_h^i$, there exist two elements $\mathcal{T}, \mathcal{T}' \in \mathcal{B}_h$ such that $\mathcal{E} = \mathcal{T} \cap \mathcal{T}'$. Also, let $\mathbf{n}$ be the unit normal vector of $\mathcal{E}$ such that it points from $\mathcal{T}$ to $\mathcal{T}'$. Let $\boldsymbol{V}$ be a vector-valued function and $\boldsymbol{T}$ a tensor-valued function that are both defined on $\mathcal{B}_h$ and have limits on both sides of the edge $\mathcal{E}$. We define the jump of $\boldsymbol{V}$ across $\mathcal{E}$ as

$$[\![\boldsymbol{V}]\!]_{\mathcal{E}} := \boldsymbol{V}_{\mathcal{T}'} - \boldsymbol{V}_{\mathcal{T}},$$

where $\boldsymbol{V}_{\mathcal{T}} = \boldsymbol{V}|_{\mathcal{T}}$ and $\boldsymbol{V}_{\mathcal{T}'} = \boldsymbol{V}|_{\mathcal{T}'}$. Recall that $\mathbf{t} = \mathbf{R}^{\mathsf{T}}\mathbf{n}$ is the unit tangent of $\mathcal{E}$ and set $\boldsymbol{T}_{\mathcal{T}} = \boldsymbol{T}|_{\mathcal{T}}$ and $\boldsymbol{T}_{\mathcal{T}'} = \boldsymbol{T}|_{\mathcal{T}'}$. Then, the jump of the tangent traction and the normal traction of $\boldsymbol{T}$ across $\mathcal{E}$ are defined as

$$[\![\mathsf{t}\boldsymbol{T}]\!]_{\mathcal{E}} := (\boldsymbol{T}_{\mathcal{T}'} - \boldsymbol{T}_{\mathcal{T}})\,\mathbf{t},$$
$$[\![\mathsf{n}\boldsymbol{T}]\!]_{\mathcal{E}} := (\boldsymbol{T}_{\mathcal{T}'} - \boldsymbol{T}_{\mathcal{T}})\,\mathbf{n}.$$

Note that all the above jumps are vector-valued functions in 2D and their domain is the set of interior edges of the mesh.

We are now in a position to define the following finite element spaces:

$$
\begin{aligned}
V_{h,r}^{1} &:= \left\{ \boldsymbol{V}_h \in L^2(T\mathcal{B}_h) : \forall \mathcal{T} \in \mathcal{B}_h,\ \boldsymbol{V}_h|_{\mathcal{T}} \in \mathcal{P}_r(T\mathcal{T}),\ \forall \mathcal{E} \in \mathcal{E}_h^i,\ [\![\boldsymbol{V}_h]\!]_{\mathcal{E}} = \boldsymbol{0} \right\}, \\
V_{h,r}^{\mathbf{c}-} &:= \left\{ \boldsymbol{T}_h \in L^2(\otimes^2 T\mathcal{B}_h) : \forall \mathcal{T} \in \mathcal{B}_h,\ \boldsymbol{T}_h|_{\mathcal{T}} \in \mathcal{P}_r^{-}(\otimes^2 T\mathcal{T}),\ \forall \mathcal{E} \in \mathcal{E}_h^i,\ [\![\mathsf{t}\boldsymbol{T}_h]\!]_{\mathcal{E}} = \boldsymbol{0} \right\}, \\
V_{h,r}^{\mathbf{c}} &:= \left\{ \boldsymbol{T}_h \in L^2(\otimes^2 T\mathcal{B}_h) : \forall \mathcal{T} \in \mathcal{B}_h,\ \boldsymbol{T}_h|_{\mathcal{T}} \in \mathcal{P}_r(\otimes^2 T\mathcal{T}),\ \forall \mathcal{E} \in \mathcal{E}_h^i,\ [\![\mathsf{t}\boldsymbol{T}_h]\!]_{\mathcal{E}} = \boldsymbol{0} \right\}, \\
V_{h,r}^{\mathbf{d}-} &:= \left\{ \boldsymbol{T}_h \in L^2(\otimes^2 T\mathcal{B}_h) : \forall \mathcal{T} \in \mathcal{B}_h,\ \boldsymbol{T}_h|_{\mathcal{T}} \in \mathcal{P}_r^{\ominus}(\otimes^2 T\mathcal{T}),\ \forall \mathcal{E} \in \mathcal{E}_h^i,\ [\![\mathsf{n}\boldsymbol{T}_h]\!]_{\mathcal{E}} = \boldsymbol{0} \right\}, \\
V_{h,r}^{\mathbf{d}} &:= \left\{ \boldsymbol{T}_h \in L^2(\otimes^2 T\mathcal{B}_h) : \forall \mathcal{T} \in \mathcal{B}_h,\ \boldsymbol{T}_h|_{\mathcal{T}} \in \mathcal{P}_r(\otimes^2 T\mathcal{T}),\ \forall \mathcal{E} \in \mathcal{E}_h^i,\ [\![\mathsf{n}\boldsymbol{T}_h]\!]_{\mathcal{E}} = \boldsymbol{0} \right\}, \\
V_{h,r}^{\ell} &:= \left\{ f_h \in L^2(\mathcal{B}_h) : \forall \mathcal{T} \in \mathcal{B}_h,\ f_h|_{\mathcal{T}} \in \mathcal{P}_r(\mathcal{T}) \right\}.
\end{aligned}
$$

In addition, let $\breve{V}_{h,r}^{\mathbf{c}}$ be either $V_{h,r}^{\mathbf{c}-}$ or $V_{h,r}^{\mathbf{c}}$, and let $\breve{V}_{h,r}^{\mathbf{d}}$ be either $V_{h,r}^{\mathbf{d}-}$ or $V_{h,r}^{\mathbf{d}}$. The above spaces are conforming according to the following theorem.

Theorem 12. *$V_{h,r}^{1} \subset H^1(T\mathcal{B}_h)$, $\breve{V}_{h,r}^{\mathbf{c}} \subset H^{\mathbf{c}}(\mathcal{B}_h)$, $\breve{V}_{h,r}^{\mathbf{d}} \subset H^{\mathbf{d}}(\mathcal{B}_h)$, and $V_{h,r}^{\ell} \subset L^2(\mathcal{B}_h)$.*

Proof. $V_{h,r}^{\ell} \subset L^2(\mathcal{B}_h)$ is trivial. For proof of $V_{h,r}^{1} \subset H^1(T\mathcal{B}_h)$ see [26, Proposition 1.74]. $\breve{V}_{h,r}^{\mathbf{c}} \subset H^{\mathbf{c}}(\mathcal{B}_h)$ and $\breve{V}_{h,r}^{\mathbf{d}} \subset H^{\mathbf{d}}(\mathcal{B}_h)$ can be proved similarly by following the steps of the proof for $V_{h,r}^{1} \subset H^1(T\mathcal{B}_h)$ and recalling the distributional definitions of the operators $\mathbf{c}$ and $\mathbf{div}$ and the Green's formulas (2.16) and

$$
\langle\!\langle \mathbf{c}(\boldsymbol{M}), \boldsymbol{V} \rangle\!\rangle = \langle\!\langle \boldsymbol{M}, \mathbf{s}(\boldsymbol{V}) \rangle\!\rangle + \int_{\partial\mathcal{B}} \langle \boldsymbol{M}\boldsymbol{T}_{\partial\mathcal{B}}, \boldsymbol{V} \rangle ds,
$$

where $\boldsymbol{M}$ is a $\binom{2}{0}$-tensor, $\boldsymbol{V}$ is a vector, and $\boldsymbol{T}_{\partial\mathcal{B}}$ is the oriented unit tangent vector field of $\partial\mathcal{B}$. □

To interpolate the four field variables $(\boldsymbol{U}, \boldsymbol{K}, \boldsymbol{P}, p)$ over the entire mesh $\mathcal{B}_h$, we next define the global shape functions analogous to the local shape functions $\left(\left\{ \boldsymbol{h}_k^{\mathcal{T}} \right\}, \left\{ \bar{\boldsymbol{r}}_{I,J}^{\mathcal{T},\mathcal{E}_k}, \boldsymbol{r}_{I,J}^{\mathcal{T},\mathcal{T}} \right\}, \left\{ \bar{\boldsymbol{s}}_{I,J}^{\mathcal{T},\mathcal{E}_k}, \boldsymbol{s}_{I,J}^{\mathcal{T},\mathcal{T}} \right\}, \left\{ t_i^{\mathcal{T}} \right\} \right)$ of an element $\mathcal{T}$. Let $\boldsymbol{H}_I^{\mathcal{N}}$, $I = 1, 2$ denote

the two global shape functions of each node $\mathcal{N} \in \mathcal{B}_h$. $\boldsymbol{H}^{\mathcal{N}}$ is defined on $\mathcal{B}_h$ such that

$$\boldsymbol{H}_I^{\mathcal{N}}\Big|_{\mathcal{T}} = \begin{cases} \boldsymbol{h}_{2(i-1)+I}^{\mathcal{T}} & \text{if } \mathcal{N} \cap \mathcal{T} = \mathcal{N}_i, \\ \mathbf{0}_{2\times 1}, & \text{if } \mathcal{N} \cap \mathcal{T} = \varnothing, \end{cases} \quad \forall \mathcal{T} \in \mathcal{B}_h,$$

where $\mathcal{N}_i$ is i-th node of $\mathcal{T}$. Hence, the support of the function $\boldsymbol{H}_I^{\mathcal{N}}$ in its domain $\mathcal{B}_h$ is all those adjacent elements of $\mathcal{B}_h$ that share the node $\mathcal{N}$. Considering properties of the Lagrange polynomials, one can show that $\boldsymbol{H}_I^{\mathcal{N}}$ is continuous everywhere in $\mathcal{B}_h$, and hence $\boldsymbol{H}_I^{\mathcal{N}} \in V_{h,r}^1$. If we interpolate a vector-valued function on $\mathcal{B}_h$ by using $V_{h,r}^1$, the global degree of freedom associated with $\boldsymbol{H}_I^{\mathcal{N}}$ is the value of the I-th component of that vector-valued function at the node $\mathcal{N}$.

Let $\boldsymbol{R}_{I,J}^{\mathcal{E}}$, $\boldsymbol{R}_{I,J}^{\mathcal{T}}$ be the global shape functions corresponding to $\bar{\boldsymbol{r}}_{I,J}^{\mathcal{T},\mathcal{E}_k}$, $\boldsymbol{r}_{I,J}^{\mathcal{T},\mathcal{T}}$. We define them on $\mathcal{B}_h$ such that

$$\boldsymbol{R}_{I,J}^{\mathcal{E}}\Big|_{\mathcal{T}} = \begin{cases} \bar{\boldsymbol{r}}_{I,J}^{\mathcal{T},\mathcal{E}_k}, & \text{if } \mathcal{E} \cap \mathcal{T} = \mathcal{E}_k, \\ \mathbf{0}_{2\times 2}, & \text{if } \mathcal{E} \cap \mathcal{T} = \varnothing, \end{cases} \quad \forall \mathcal{T} \in \mathcal{B}_h, \quad \text{and} \quad \boldsymbol{R}_{I,J}^{\mathcal{T}} = \begin{cases} \boldsymbol{r}_{I,J}^{\mathcal{T},\mathcal{T}}, & \text{on } \mathcal{T}, \\ \mathbf{0}_{2\times 2}, & \text{otherwise.} \end{cases}$$

Note that $\mathcal{E}_k$ is an edge of $\mathcal{T}$ and $k \in \{1,2,3\}$ is its local numbering in $\mathcal{T}$. If $\mathcal{E}$ is an exterior edge, i.e., $\mathcal{E} \in \partial\mathcal{B}_h$, the support of $\boldsymbol{R}_{I,J}^{\mathcal{E}}$ in $\mathcal{B}_h$ is only one element that contains $\mathcal{E}$, and if $\mathcal{E}$ is an interior edge, the support of $\boldsymbol{R}_{I,J}^{\mathcal{E}}$ are two adjacent elements that have $\mathcal{E}$ in common. Let $L^{\mathcal{E}}$ be the union of the support boundaries of $\boldsymbol{R}_{I,J}^{\mathcal{E}}$ and the corresponding edge $\mathcal{E}$, and let $\mathbf{t}_L$ be the unit tangent vector field on $L^{\mathcal{E}}$. On $L^{\mathcal{E}}$ the function $\boldsymbol{R}_{I,J}^{\mathcal{E}}$ is multi-valued. However, $\boldsymbol{R}_{I,J}^{\mathcal{E}}\mathbf{t}_L$ is continuous (single-valued) across $L^{\mathcal{E}}$. Here, we emphasize that the above description of $\boldsymbol{R}_{I,J}^{\mathcal{E}}$ is valid if we use the numbering scheme discussed in Section 3.2. The support of the global shape function $\boldsymbol{R}_{I,J}^{\mathcal{T}}$ in $\mathcal{B}_h$ is the corresponding element $\mathcal{T}$. $\boldsymbol{R}_{I,J}^{\mathcal{T}}$ is multi-valued on $\partial\mathcal{T}$ while $\boldsymbol{R}_{I,J}^{\mathcal{T}}\mathbf{t}_{\partial\mathcal{T}}$ is continuous across $\partial\mathcal{T}$. Based on the above discussion, one can conclude that $[\![\mathtt{t}\boldsymbol{R}_{I,J}^{\mathcal{E}}]\!]_{\mathcal{E}'} = \mathbf{0}$ and $[\![\mathtt{t}\boldsymbol{R}_{I,J}^{\mathcal{T}}]\!]_{\mathcal{E}'} = \mathbf{0}$, $\forall \mathcal{E}' \in \mathcal{B}_h$, and hence $\boldsymbol{R}_{I,J}^{\mathcal{E}}, \boldsymbol{R}_{I,J}^{\mathcal{T}} \in \breve{V}_{h,r}^{\mathtt{c}}$. Let us now define the global degrees of freedom. Suppose $\mathcal{T}$ and $\mathcal{T}'$ are adjacent in $\mathcal{B}_h$

such that their common edge $\mathcal{E}$ is numbered $\mathcal{E}_k$ in $\mathcal{T}$ and $\mathcal{E}_{k'}$ in $\mathcal{T}'$, where k is not necessary equal to k'. The numbering scheme of Section 3.2 gaurantees that $\phi_{I,J}^{\mathcal{T},\mathcal{E}_k} = \phi_{I,J}^{\mathcal{T}',\mathcal{E}_{k'}}$, $\forall I, J$. This equivalence enables one to use either of them for calculating the global degrees of freedom for $\mathcal{E}$ (this is also necessary for the assembly of finite elements). Therefore, it is well-defined to write $\Phi_{I,J}^{\mathcal{E}} : \breve{V}_{h,r}^{\mathbf{c}} \longrightarrow \mathbb{R},\ \Phi_{I,J}^{\mathcal{E}}(\boldsymbol{T}_h) := \phi_{I,J}^{\mathcal{T},\mathcal{E}_k}(\boldsymbol{T}_h|_{\mathcal{T}})$ as the global degree of freedom associated with $\boldsymbol{R}_{I,J}^{\mathcal{E}}$. Also, the global degree of freedom associated with $\boldsymbol{R}_{I,J}^{\mathcal{T}}$ is $\Phi_{I,J}^{\mathcal{T}} : \breve{V}_{h,r}^{\mathbf{c}} \longrightarrow \mathbb{R},\ \Phi_{I,J}^{\mathcal{T}}(\boldsymbol{T}_h) := \phi_{I,J}^{\mathcal{T},\mathcal{T}}(\boldsymbol{T}_h|_{\mathcal{T}})$. Note that $\Phi_{I,J}^{\mathcal{E}}, \Phi_{I,J}^{\mathcal{T}} \in (\breve{V}_{h,r}^{\mathbf{c}})^\star$, but they can be extended to $H^{\mathbf{c}}(\mathcal{B}_h)^\star$.

Similarly, one can define the global shape functions $\boldsymbol{S}_{I,J}^{\mathcal{E}}$, $\boldsymbol{S}_{I,J}^{\mathcal{T}}$ and the global degrees of freedom $\Psi_{I,J}^{\mathcal{E}}$,$\Psi_{I,J}^{\mathcal{T}}$ based on the corresponding local shape functions $\bar{\boldsymbol{s}}_{I,J}^{\mathcal{T},\mathcal{E}_k}$, $\boldsymbol{s}_{I,J}^{\mathcal{T},\mathcal{T}}$ and degrees of freedom $\psi_{I,J}^{\mathcal{T},\mathcal{E}_k}$, $\psi_{I,J}^{\mathcal{T},\mathcal{T}}$. One can also obtain the global shape functions directly as $\boldsymbol{S}_{I,J}^{\mathcal{E}} = \boldsymbol{R}_{I,J}^{\mathcal{E}}\mathbf{R}^{\mathsf{T}}$ and $\boldsymbol{S}_{I,J}^{\mathcal{T}} = \boldsymbol{R}_{I,J}^{\mathcal{T}}\mathbf{R}^{\mathsf{T}}$. Therefore, $[\![\mathsf{n}\boldsymbol{S}_{I,J}^{\mathcal{E}}]\!]_{\mathcal{E}'} = \mathbf{0}$ and $[\![\mathsf{n}\boldsymbol{S}_{I,J}^{\mathcal{T}}.]\!]_{\mathcal{E}'} = \mathbf{0}$, $\forall \mathcal{E}' \in \mathcal{B}_h$, and $\boldsymbol{S}_{I,J}^{\mathcal{E}}, \boldsymbol{S}_{I,J}^{\mathcal{T}} \in \breve{V}_{h,r}^{\mathbf{d}}$. In Figure 3.3, we illustrate the first (nonzero) rows of $\boldsymbol{R}_{1,1}^{\mathcal{E}} \in V_{h,1}^{\mathbf{c}-}$ and $\boldsymbol{S}_{1,1}^{\mathcal{E}} \in V_{h,1}^{\mathbf{d}-}$ on their supports. See $\boldsymbol{v}_2^{\hat{\mathcal{T}},\hat{\mathcal{T}}}$ and $\boldsymbol{v}_3^{\hat{\mathcal{T}},\hat{\mathcal{T}}}$ in Figure 3.2 for some examples of nonzero rows of $\boldsymbol{R}_{I,J}^{\mathcal{T}}$ on its support.

To define the global shape function analogous to $t_i^{\mathcal{T}}$, consider the function $T_i^{\mathcal{T}}$ on $\mathcal{B}_h$ with support $\mathcal{T}$ such that $T_i^{\mathcal{T}} = t_i^{\mathcal{T}}$ on $\mathcal{T}$. It is straightforward to show that $T_i^{\mathcal{T}} \in V_{h,r}^{\ell}$. For interpolating a scaler field f on $\mathcal{B}_h$ using $V_{h,r}^{\ell}$, one simply uses $\omega_i^{\mathcal{T}}(f|_{\mathcal{T}})$ as the global degree of freedom associate with $T_i^{\mathcal{T}}$.

Theorem 13. *$\left\{\boldsymbol{H}_I^{\mathcal{N}}\right\}_{\mathcal{N}\in\mathcal{B}_h}$ is a basis for $V_{h,r}^1$, $\left\{\boldsymbol{R}_{I,J}^{\mathcal{E}}, \boldsymbol{R}_{I,J}^{\mathcal{T}}\right\}_{\mathcal{E},\mathcal{T}\in\mathcal{B}_h}$ is a basis for $\breve{V}_{h,r}^{\mathbf{c}}$, $\left\{\boldsymbol{S}_{I,J}^{\mathcal{E}}, \boldsymbol{S}_{I,J}^{\mathcal{T}}\right\}_{\mathcal{E},\mathcal{T}\in\mathcal{B}_h}$ is a basis for $\breve{V}_{h,r}^{\mathbf{d}}$, and $\left\{T_i^{\mathcal{T}}\right\}_{\mathcal{T}\in\mathcal{B}_h}$ is a basis for $V_{h,r}^{\ell}$.*

Proof. See [26, Lemma 1.77 and Proposition 1.78] for the proof of the first statement. The other three statements can be proved similarly considering [26, Lemma 1.86, Proposition 1.87, Lemma 1.92, and Proposition 1.93]. □

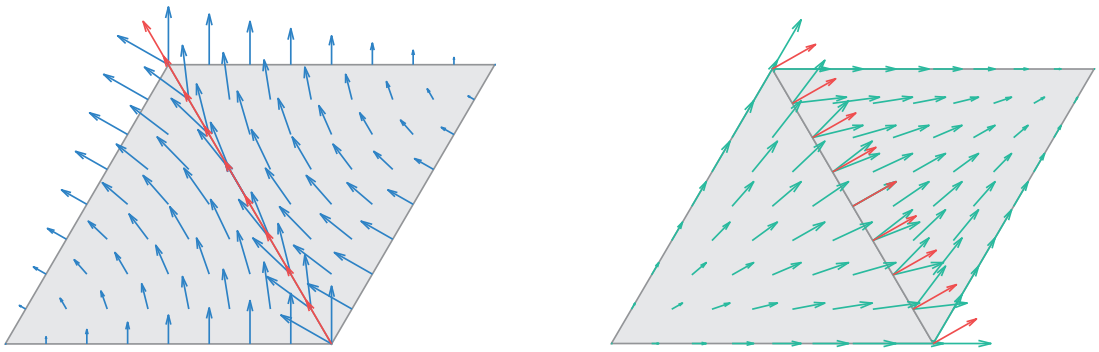

Figure 3.3: The nonzero row of the global shape functions $\boldsymbol{R}^{\mathcal{E}}_{1,1} \in V^{\mathbf{c}-}_{h,1}$ (left) and $\boldsymbol{S}^{\mathcal{E}}_{1,1} \in V^{\mathbf{d}-}_{h,1}$ (right), where $\mathcal{E}$ is the common edge of the two adjacent elements. Observe that $\boldsymbol{S}^{\mathcal{E}}_{1,1} = \boldsymbol{R}^{\mathcal{E}}_{1,1}\mathsf{R}^{\mathsf{T}}$. The tangent (normal) components of the fields, which are shown with red arrows, are continuous across $\mathcal{E}$ in the left (right) plot.

3.4 Compatible-Strain Mixed Finite Element Methods

Using the approximation spaces defined in the previous section, one writes the following mixed finite element methods for the the mixed formulation of *incompressible* nonlinear elasticity given in (2.21):

Given a body force $\boldsymbol{B}$ of L^2-class, a boundary displacement $\overline{\boldsymbol{U}}$ on Γ_d of $H^{1/2}$-class, and a boundary traction $\overline{\boldsymbol{T}}$ on Γ_t of L^2-class, find $(\boldsymbol{U}_h, \boldsymbol{K}_h, \boldsymbol{P}_h, p_h) \in V^1_{h,m}(\Gamma_d, \overline{\boldsymbol{U}}) \times \breve{V}^{\mathbf{c}}_{h,n} \times \breve{V}^{\mathbf{d}}_{h,r} \times V^{\ell}_{h,s}$ such that

$$
\begin{aligned}
\langle\!\langle \rho_0 \boldsymbol{B}, \boldsymbol{\Upsilon}_h \rangle\!\rangle + \int_{\Gamma_t} \langle \overline{\boldsymbol{T}}, \boldsymbol{\Upsilon}_h \rangle \, dS &= \langle\!\langle \boldsymbol{P}_h, \mathbf{grad}\, \boldsymbol{\Upsilon}_h \rangle\!\rangle, && \forall \boldsymbol{\Upsilon}_h \in V^1_{h,m}(\Gamma_d), \\
\langle\!\langle \widetilde{\boldsymbol{P}}(\boldsymbol{K}_h), \boldsymbol{\kappa}_h \rangle\!\rangle - \langle\!\langle \boldsymbol{P}_h, \boldsymbol{\kappa}_h \rangle\!\rangle + \langle\!\langle p_h \boldsymbol{Q}(\boldsymbol{K}_h), \boldsymbol{\kappa}_h \rangle\!\rangle &= 0, && \forall \boldsymbol{\kappa}_h \in \breve{V}^{\mathbf{c}}_{h,n}, \\
\langle\!\langle \mathbf{grad}\, \boldsymbol{U}_h, \boldsymbol{\pi}_h \rangle\!\rangle - \langle\!\langle \boldsymbol{K}_h, \boldsymbol{\pi}_h \rangle\!\rangle &= 0, && \forall \boldsymbol{\pi}_h \in \breve{V}^{\mathbf{d}}_{h,r}, \\
\langle\!\langle C(J_h), q_h \rangle\!\rangle &= 0, && \forall q_h \in V^{\ell}_{h,s}.
\end{aligned}
\tag{3.25}
$$

Similarly, one can write the following mixed finite element methods based on the mixed formulation of *compressible* nonlinear elasticity given in (2.22)

Given $(\boldsymbol{B}, \overline{\boldsymbol{U}}, \overline{\boldsymbol{T}})$*, find* $(\boldsymbol{U}_h, \boldsymbol{K}_h, \boldsymbol{P}_h) \in V^1_{h,m}(\Gamma_d, \overline{\boldsymbol{U}}) \times \breve{V}^{\mathbf{c}}_{h,n} \times \breve{V}^{\mathbf{d}}_{h,r}$ *such that*

$$\begin{aligned}
\langle\!\langle \boldsymbol{P}_h, \mathbf{grad}\, \boldsymbol{\Upsilon}_h \rangle\!\rangle &= \langle\!\langle \rho_0 \boldsymbol{B}, \boldsymbol{\Upsilon}_h \rangle\!\rangle + \int_{\Gamma_t} \langle \overline{\boldsymbol{T}}, \boldsymbol{\Upsilon}_h \rangle ds, \quad && \forall \boldsymbol{\Upsilon}_h \in V^1_{h,m}(\Gamma_d), \\
\langle\!\langle \widetilde{\boldsymbol{P}}(\boldsymbol{K}_h), \boldsymbol{\kappa}_h \rangle\!\rangle - \langle\!\langle \boldsymbol{P}_h, \boldsymbol{\kappa}_h \rangle\!\rangle &= 0, && \forall \boldsymbol{\kappa}_h \in \breve{V}^{\mathbf{c}}_{h,n}, \\
\langle\!\langle \mathbf{grad}\, \boldsymbol{U}_h, \boldsymbol{\pi}_h \rangle\!\rangle - \langle\!\langle \boldsymbol{K}_h, \boldsymbol{\pi}_h \rangle\!\rangle &= 0, && \forall \boldsymbol{\pi}_h \in \breve{V}^{\mathbf{d}}_{h,r}.
\end{aligned} \tag{3.26}$$

Remark 14 (Compatibility of Strain and Continuity of Traction)**.**

(i) Let $\boldsymbol{K}_h$ be a displacement gradient field on $\mathcal{B}_h$. The zero jump $[\![\mathsf{t} \boldsymbol{K}_h]\!]_{\mathcal{E}} = \mathbf{0}$ is known as the Hadamard jump condition along the edge $\mathcal{E}$. If $\boldsymbol{K}_h \in \breve{V}^{\mathbf{c}}_{h,r} \subset H^{\mathbf{c}}(\mathcal{B}_h)$, the Hadamard jump condition is satisfied for all the internal edges of $\mathcal{B}_h$ independently of the refinement level of the mesh. This is a necessary compatibility condition for the existence of a displacement field $\boldsymbol{U}_h \in H^1(T\mathcal{B}_h)$ (continuous along edges) such that $\boldsymbol{K}_h = \mathbf{grad}\, \boldsymbol{U}_h$ [63].

(ii) Suppose $\boldsymbol{P}_h$ is a stress field on $\mathcal{B}_h$. The zero jump condition $[\![\mathsf{n} \boldsymbol{P}_h]\!]_{\mathcal{E}} = \mathbf{0}$ indicates that traction vector associated with $\boldsymbol{P}_h$ is continuous across the edge $\mathcal{E}$. If $\boldsymbol{P}_h \in \breve{V}^{\mathbf{d}}_{h,r} \subset H^{\mathbf{d}}(\mathcal{B}_h)$, the continuity of traction holds for all the internal edges of $\mathcal{B}_h$ independently of the refinement level of the mesh. This is required by localization of the balance of linear momentum.

Inspired by Remark 14 (i), we call finite element methods introduced in (3.25) and (3.26) the *compatible-strain mixed finite element methods* (CSFEMs). We also use the notations

$$\mathsf{H}m\mathsf{c}n(\bar{n})\mathsf{d}r(\bar{r}) \quad \text{in case of} \quad V^1_{h,m} \times V^{\mathbf{c}}_{h,n}(V^{\mathbf{c}-}_{h,n}) \times V^{\mathbf{d}}_{h,r}(V^{\mathbf{d}-}_{h,r}),$$

for referring to (3.26) and

$$\mathsf{H}m\mathsf{c}n(\bar{n})\mathsf{d}r(\bar{r})\mathsf{L}s \quad \text{in case of} \quad V^1_{h,m} \times V^{\mathbf{c}}_{h,n}(V^{\mathbf{c}-}_{h,n}) \times V^{\mathbf{d}}_{h,r}(V^{\mathbf{d}-}_{h,r}) \times V^{\ell}_{h,s},$$

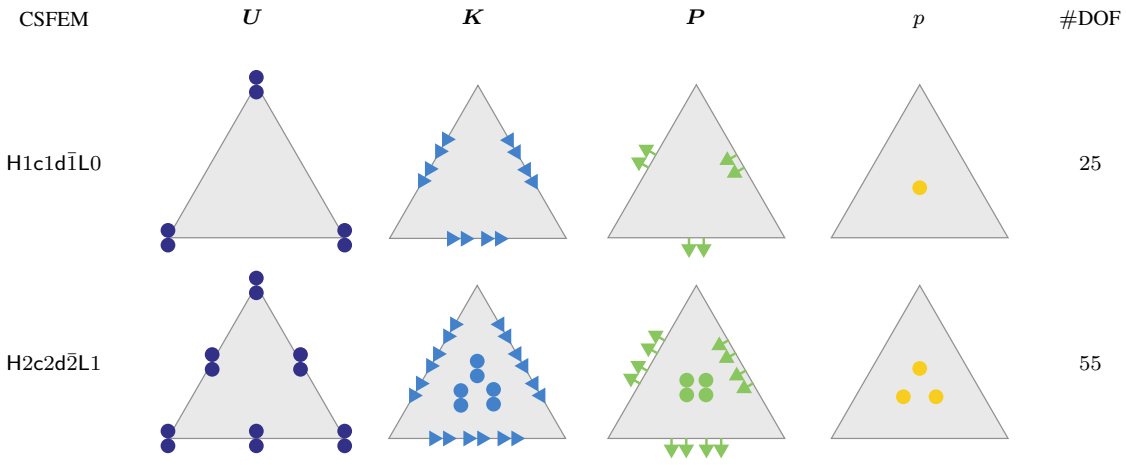

Figure 3.4: The schematic diagrams for some first-order and second-order mixed finite elements

for referring to (3.25), where $m, n, r = 1, 2$ and $s = 0, 1, 2$. This results in 96 (32) possible choices of CSFEMs for incompressible (compressible) solids. However, since (3.25) or (3.26) corresponds to a saddle point of a variational problem (see Remark 4) not all these choices lead to convergent (consistent and stable) methods as the solution and test spaces need to satisfy certain conditions. We will discuss this further in Section 3.7 and in the numerical examples. We will conclude that the well-performing choices of CSFEMs among the first and second-order elements are H1c1dl̄L0 and H2c2dl̄L1 for incompressible solids (schematic diagrams are given in Figure 3.4) and H1c1dl̄ and H2c2dl̄ for compressible solids.

3.5 Matrix Formulation

In this section, we focus on the implementation of CSFEMs. In particular, we discuss how to represent (3.25) as a nonlinear system of algebraic (polynomial) equations, which can be solved using Newton's method. We define the vector representation of a second-order

tensor $\boldsymbol{T}$ and the matrix representation of a vector $\boldsymbol{V}$ with 4 entries by

$$[\boldsymbol{T}] := \begin{bmatrix} T^{11} & T^{12} & T^{21} & T^{22} \end{bmatrix}^{\mathsf{T}} \quad \text{and} \quad [\boldsymbol{V}] := \begin{bmatrix} V^1 & V^2 \\ V^3 & V^4 \end{bmatrix}.$$

One can show that $\langle\!\langle \boldsymbol{Y}, \boldsymbol{Z} \rangle\!\rangle = \langle\!\langle [\boldsymbol{Y}], [\boldsymbol{Z}] \rangle\!\rangle = \int_{\mathcal{B}} [\boldsymbol{Y}]^{\mathsf{T}} [\boldsymbol{Z}] dA = \int_{\mathcal{B}} [\boldsymbol{Z}]^{\mathsf{T}} [\boldsymbol{Y}] dA$. Let $[\breve{V}^{\mathbf{c}}_{h,r}] := \left\{ [\boldsymbol{T}_h] : \boldsymbol{T}_h \in \breve{V}^{\mathbf{c}}_{h,r} \right\}$ and define $[\breve{V}^{\mathbf{d}}_{h,r}]$ similarly. Then, (3.25) can be rewritten as

Find $(\boldsymbol{U}_h, [\boldsymbol{K}_h], [\boldsymbol{P}_h], p_h) \in V^1_{h,m}(\Gamma_d, \overline{\boldsymbol{U}}) \times [\breve{V}^{\mathbf{c}}_{h,n}] \times [\breve{V}^{\mathbf{d}}_{h,r}] \times V^{\ell}_{h,s}$ *such that*

$$\begin{aligned}
&\int_{\mathcal{B}_h} [\mathbf{grad}\, \boldsymbol{\Upsilon}_h]^{\mathsf{T}} [\boldsymbol{P}_h]\, dA - \int_{\mathcal{B}_h} \rho_0 \boldsymbol{\Upsilon}_h^{\mathsf{T}} \boldsymbol{B}\, dA - \int_{\Gamma_t} \boldsymbol{\Upsilon}_h^{\mathsf{T}} \overline{\boldsymbol{T}}\, dS = 0, && \forall \boldsymbol{\Upsilon}_h \in V^1_{h,m}(\Gamma_d), \\
&\int_{\mathcal{B}_h} [\boldsymbol{\kappa}_h]^{\mathsf{T}} \left(\left[\widetilde{\boldsymbol{P}}(\boldsymbol{K}_h) \right] + p_h \left[\boldsymbol{Q}(\boldsymbol{K}_h) \right] \right) dA - \int_{\mathcal{B}_h} [\boldsymbol{\kappa}_h]^{\mathsf{T}} [\boldsymbol{P}_h]\, dA = 0, && \forall [\boldsymbol{\kappa}_h] \in [\breve{V}^{\mathbf{c}}_{h,n}], \\
&\int_{\mathcal{B}_h} [\boldsymbol{\pi}_h]^{\mathsf{T}} \left[\mathbf{grad}\, \boldsymbol{U}_h \right] dA - \int_{\mathcal{B}_h} [\boldsymbol{\pi}_h]^{\mathsf{T}} [\boldsymbol{K}_h]\, dA = 0, && \forall [\boldsymbol{\pi}_h] \in [\breve{V}^{\mathbf{d}}_{h,r}], \\
&\int_{\mathcal{B}_h} q_h\, C(J_h)\, dA = 0, && \forall q_h \in V^{\ell}_{h,s}.
\end{aligned} \tag{3.27}$$

The local shape functions are discussed in Section 3.2. Here, to be consistent with (3.27), we define the following vector representations of the local shape functions:

$$\begin{aligned}
&\mathbf{g}^1_{\mathcal{T},j}(\mathbf{X}) := \left[\mathbf{grad}\, \boldsymbol{h}^{\mathcal{T}}_j(\mathbf{X}) \right], \\
&\mathbf{b}^{\mathbf{c}}_{\mathcal{T},k}(\mathbf{X}) := \left[\bar{\boldsymbol{r}}^{\mathcal{T},\mathcal{E}_i}_{I,J}(\mathbf{X}) \right], \quad \mathbf{b}^{\mathbf{c}}_{\mathcal{T},l}(\mathbf{X}) := \left[\boldsymbol{r}^{\mathcal{T},\mathcal{T}}_{I,J}(\mathbf{X}) \right], \\
&\mathbf{b}^{\mathbf{d}}_{\mathcal{T},k}(\mathbf{X}) := \left[\bar{\boldsymbol{s}}^{\mathcal{T},\mathcal{E}_i}_{I,J}(\mathbf{X}) \right], \quad \mathbf{b}^{\mathbf{d}}_{\mathcal{T},l}(\mathbf{X}) := \left[\boldsymbol{s}^{\mathcal{T},\mathcal{T}}_{I,J}(\mathbf{X}) \right],
\end{aligned} \tag{3.28}$$

where $j = 1, 2, ..., 2r$ for $\boldsymbol{U}_h \in V^1_{h,r}$, and the numberings k and l are specified as

$$k := I + 2(J-1) + 2(i-1) \max J, \quad l := I + 2(J-1) + \max k, \tag{3.29}$$

where $i = 1, 2, 3$ and $I = 1, 2$. For $\boldsymbol{K}_h \in V^{\mathbf{c}-}_{h,1}$ and $\boldsymbol{P}_h \in V^{\mathbf{d}-}_{h,1}$, we have $J = 1$, using $V^{\mathbf{c}}_{h,1}$, $V^{\mathbf{c}-}_{h,2}$, $V^{\mathbf{d}}_{h,1}$, and $V^{\mathbf{d}-}_{h,2}$ we have $J = 1, 2$, and $J = 1, 2, 3$ for $V^{\mathbf{c}}_{h,2}$ and $V^{\mathbf{d}}_{h,2}$. Note that in

(3.28), $\mathbf{b}^{\mathbf{d}}_{\mathcal{T},l}$ and $\mathbf{b}^{\mathbf{c}}_{\mathcal{T},l}$ are defined only for second or higher-order finite element spaces, i.e., $\breve{V}^{\mathbf{c}}_{h,r}$ and $\breve{V}^{\mathbf{d}}_{h,r}$ with $r \geqslant 2$. These relations can also be realized from Table 3.3. Let us write the following sparse matrices using the local shape functions of displacement and pressure and (3.28):

$$
\begin{aligned}
\mathbf{B}^{1}_{\mathcal{T}} &= \begin{bmatrix} \boldsymbol{h}^{\mathcal{T}}_{1} & \boldsymbol{h}^{\mathcal{T}}_{2} & \cdots & \boldsymbol{h}^{\mathcal{T}}_{n^1} \end{bmatrix}_{2\times n^1}, \\
\mathbf{G}^{1}_{\mathcal{T}} &= \begin{bmatrix} \mathbf{g}^{1}_{\mathcal{T},1} & \mathbf{g}^{1}_{\mathcal{T},2} & \cdots & \mathbf{g}^{1}_{\mathcal{T},n^1} \end{bmatrix}_{4\times n^1}, \\
\mathbf{B}^{\mathbf{c}}_{\mathcal{T}} &= \begin{bmatrix} \mathbf{b}^{\mathbf{c}}_{\mathcal{T},1} & \mathbf{b}^{\mathbf{c}}_{\mathcal{T},2} & \cdots & \mathbf{b}^{\mathbf{c}}_{\mathcal{T},n^c} \end{bmatrix}_{4\times n^c}, \\
\mathbf{B}^{\mathbf{d}}_{\mathcal{T}} &= \begin{bmatrix} \mathbf{b}^{\mathbf{d}}_{\mathcal{T},1} & \mathbf{b}^{\mathbf{d}}_{\mathcal{T},2} & \cdots & \mathbf{b}^{\mathbf{d}}_{\mathcal{T},n^d} \end{bmatrix}_{4\times n^d}, \\
\mathbf{B}^{\ell}_{\mathcal{T}} &= \begin{bmatrix} t^{\mathcal{T}}_{1} & t^{\mathcal{T}}_{2} & \cdots & t^{\mathcal{T}}_{n^\ell} \end{bmatrix}_{1\times n^\ell},
\end{aligned}
\tag{3.30}
$$

where n^1, n^c, n^d, and n^ℓ depend on the order of the corresponding approximation spaces and are given in the last column of Table 3.3. For a solution or test variable $\boldsymbol{V}_h$, one defines $\boldsymbol{V}_{\mathcal{T}} := \boldsymbol{V}_h|_{\mathcal{T}}$. Next, recalling (3.19), one writes the following local interpolation operators for each $\mathcal{T}$:

$$
\begin{aligned}
&\boldsymbol{U}_{\mathcal{T}} = \mathbf{B}^{1}_{\mathcal{T}}\mathbf{q}^{1}_{\mathcal{T}}, \quad \big[\mathbf{grad}\,\boldsymbol{U}_{\mathcal{T}}\big] = \mathbf{G}^{1}_{\mathcal{T}}\mathbf{q}^{1}_{\mathcal{T}}, \quad \big[\boldsymbol{K}_{\mathcal{T}}\big] = \mathbf{B}^{\mathbf{c}}_{\mathcal{T}}\mathbf{q}^{\mathbf{c}}_{\mathcal{T}}, \quad \big[\boldsymbol{P}_{\mathcal{T}}\big] = \mathbf{B}^{\mathbf{d}}_{\mathcal{T}}\mathbf{q}^{\mathbf{d}}_{\mathcal{T}}, \quad p_{\mathcal{T}} = \mathbf{B}^{\ell}_{\mathcal{T}}\mathbf{q}^{\ell}_{\mathcal{T}}, \\
&\boldsymbol{\Upsilon}_{\mathcal{T}} = \mathbf{B}^{1}_{\mathcal{T}}\mathbf{t}^{1}_{\mathcal{T}}, \quad \big[\mathbf{grad}\,\boldsymbol{\Upsilon}_{\mathcal{T}}\big] = \mathbf{G}^{1}_{\mathcal{T}}\mathbf{t}^{1}_{\mathcal{T}}, \quad \big[\boldsymbol{\kappa}_{\mathcal{T}}\big] = \mathbf{B}^{\mathbf{c}}_{\mathcal{T}}\mathbf{t}^{\mathbf{c}}_{\mathcal{T}}, \quad \big[\boldsymbol{\pi}_{\mathcal{T}}\big] = \mathbf{B}^{\mathbf{d}}_{\mathcal{T}}\mathbf{t}^{\mathbf{d}}_{\mathcal{T}}, \quad q_{\mathcal{T}} = \mathbf{B}^{\ell}_{\mathcal{T}}\mathbf{t}^{\ell}_{\mathcal{T}},
\end{aligned}
\tag{3.31}
$$

where $\mathbf{t}^{1}_{\mathcal{T}}$, $\mathbf{t}^{\mathbf{c}}_{\mathcal{T}}$, $\mathbf{t}^{\mathbf{d}}_{\mathcal{T}}$, and $\mathbf{t}^{\ell}_{\mathcal{T}}$ are some column vectors containing arbitrary real numbers. These vectors are associated with the corresponding test spaces. $\mathbf{q}^{1}_{\mathcal{T}}$, $\mathbf{q}^{\mathbf{c}}_{\mathcal{T}}$, $\mathbf{q}^{\mathbf{d}}_{\mathcal{T}}$, and $\mathbf{q}^{\ell}_{\mathcal{T}}$ are vectors of

unknown local degrees of freedom, that is

$$
\begin{aligned}
\mathbf{q}^{1}_{\mathcal{T}} &= \begin{bmatrix} \mathsf{q}^{1}_{\mathcal{T},1} & \mathsf{q}^{1}_{\mathcal{T},2} & \cdots & \mathsf{q}^{1}_{\mathcal{T},n^1} \end{bmatrix}^{\mathsf{T}}, \quad \mathsf{q}^{1}_{\mathcal{T},m} = U_h^J(\mathbf{X}_i), \\
\mathbf{q}^{\mathbf{c}}_{\mathcal{T}} &= \begin{bmatrix} \mathsf{q}^{\mathbf{c}}_{\mathcal{T},1} & \mathsf{q}^{\mathbf{c}}_{\mathcal{T},2} & \cdots & \mathsf{q}^{\mathbf{c}}_{\mathcal{T},n^c} \end{bmatrix}^{\mathsf{T}}, \quad \mathsf{q}^{\mathbf{c}}_{\mathcal{T},k} = \phi_{I,J}^{\mathcal{T},\mathcal{E}_i}(\boldsymbol{K}_{\mathcal{T}}), \quad \mathsf{q}^{\mathbf{c}}_{\mathcal{T},l} = \phi_{I,J}^{\mathcal{T},\mathcal{T}}(\boldsymbol{K}_{\mathcal{T}}), \\
\mathbf{q}^{\mathbf{d}}_{\mathcal{T}} &= \begin{bmatrix} \mathsf{q}^{\mathbf{d}}_{\mathcal{T},1} & \mathsf{q}^{\mathbf{d}}_{\mathcal{T},2} & \cdots & \mathsf{q}^{\mathbf{d}}_{\mathcal{T},n^d} \end{bmatrix}^{\mathsf{T}}, \quad \mathsf{q}^{\mathbf{d}}_{\mathcal{T},k} = \psi_{I,J}^{\mathcal{T},\mathcal{E}_i}(\boldsymbol{P}_{\mathcal{T}}), \quad \mathsf{q}^{\mathbf{d}}_{\mathcal{T},l} = \psi_{I,J}^{\mathcal{T},\mathcal{T}}(\boldsymbol{P}_{\mathcal{T}}), \\
\mathbf{q}^{\ell}_{\mathcal{T}} &= \begin{bmatrix} \mathsf{q}^{\ell}_{\mathcal{T},1} & \mathsf{q}^{\ell}_{\mathcal{T},2} & \cdots & \mathsf{q}^{\ell}_{\mathcal{T},n^\ell} \end{bmatrix}^{\mathsf{T}}, \quad \mathsf{q}^{\ell}_{\mathcal{T},i} = \omega_i^{\mathcal{T}}(p_{\mathcal{T}}).
\end{aligned}
\tag{3.32}
$$

Note that $U_h^J(\mathbf{X}_i)$, $J = 1, 2$ is the value of the displacement at the i-th node of $\mathcal{T}$, and $m := J + 2(i-1)$. Also, $\phi_{I,J}^{\mathcal{T},\mathcal{E}_i}$, $\phi_{I,J}^{\mathcal{T},\mathcal{T}}$ and $\psi_{I,J}^{\mathcal{T},\mathcal{E}_i}$, $\psi_{I,J}^{\mathcal{T},\mathcal{T}}$ are given in (3.12) and (3.16) with the hat symbols removed. The numberings k and l are defined in (3.29), and the size of the vectors ($\mathbf{q}^{1}_{\mathcal{T}}$, $\mathbf{q}^{\mathbf{c}}_{\mathcal{T}}$, $\mathbf{q}^{\mathbf{d}}_{\mathcal{T}}$, $\mathbf{q}^{\ell}_{\mathcal{T}}$) and ($\mathbf{t}^{1}_{\mathcal{T}}$, $\mathbf{t}^{\mathbf{c}}_{\mathcal{T}}$, $\mathbf{t}^{\mathbf{d}}_{\mathcal{T}}$, $\mathbf{t}^{\ell}_{\mathcal{T}}$) is (n^1, n^c, n^d, n^ℓ). Inserting (3.31) into the restriction of (3.27) to an element $\mathcal{T}$, and then summing over $\mathcal{T} \in \mathcal{B}_h$ results in the following representation of (3.27):

$$
\begin{aligned}
&\sum_{\mathcal{T}\in\mathcal{B}_h} (\mathbf{t}^{1}_{\mathcal{T}})^{\mathsf{T}} \left(\mathbf{K}^{\mathbf{1d}}_{\mathcal{T}} \mathbf{q}^{\mathbf{d}}_{\mathcal{T}} - \mathbf{F}^{1}_{\mathcal{T}} - \mathbf{F}^{1}_{\mathcal{E}_t^{\mathcal{T}}} \right) = 0, \\
&\sum_{\mathcal{T}\in\mathcal{B}_h} (\mathbf{t}^{\mathbf{c}}_{\mathcal{T}})^{\mathsf{T}} \left(\mathbf{N}^{\mathbf{c}}_{\mathcal{T}}(\mathbf{q}^{\mathbf{c}}_{\mathcal{T}}, \mathbf{q}^{\ell}_{\mathcal{T}}) + \mathbf{K}^{\mathbf{cd}}_{\mathcal{T}} \mathbf{q}^{\mathbf{d}}_{\mathcal{T}} \right) = 0, \\
&\sum_{\mathcal{T}\in\mathcal{B}_h} (\mathbf{t}^{\mathbf{d}}_{\mathcal{T}})^{\mathsf{T}} \left(\mathbf{K}^{\mathbf{d}1}_{\mathcal{T}} \mathbf{q}^{1}_{\mathcal{T}} + \mathbf{K}^{\mathbf{dc}}_{\mathcal{T}} \mathbf{q}^{\mathbf{c}}_{\mathcal{T}} \right) = 0, \\
&\sum_{\mathcal{T}\in\mathcal{B}_h} (\mathbf{t}^{\ell}_{\mathcal{T}})^{\mathsf{T}} \left(\mathbf{N}^{\ell}_{\mathcal{T}}(\mathbf{q}^{\mathbf{c}}_{\mathcal{T}}) \right) = 0.
\end{aligned}
\tag{3.33}
$$

The new local matrices and vectors used in the above relations are defined as

$$
\mathbf{K}^{\mathbf{1d}}_{\mathcal{T}} = \int_{\mathcal{T}} (\mathbf{G}^{1}_{\mathcal{T}})^{\mathsf{T}} \mathbf{B}^{\mathbf{d}}_{\mathcal{T}} \, dA, \quad \mathbf{K}^{\mathbf{d}1}_{\mathcal{T}} = (\mathbf{K}^{\mathbf{1d}}_{\mathcal{T}})^{\mathsf{T}}, \tag{3.34}
$$

$$
\mathbf{K}^{\mathbf{cd}}_{\mathcal{T}} = -\int_{\mathcal{T}} (\mathbf{B}^{\mathbf{c}}_{\mathcal{T}})^{\mathsf{T}} \mathbf{B}^{\mathbf{d}}_{\mathcal{T}} \, dA, \quad \mathbf{K}^{\mathbf{dc}}_{\mathcal{T}} = (\mathbf{K}^{\mathbf{cd}}_{\mathcal{T}})^{\mathsf{T}}, \tag{3.35}
$$

$$
\mathbf{N}^{\mathbf{c}}_{\mathcal{T}}(\mathbf{q}^{\mathbf{c}}_{\mathcal{T}}, \mathbf{q}^{\ell}_{\mathcal{T}}) = \int_{\mathcal{T}} (\mathbf{B}^{\mathbf{c}}_{\mathcal{T}})^{\mathsf{T}} \left(\left| \widetilde{\boldsymbol{P}}\big([\mathbf{B}^{\mathbf{c}}_{\mathcal{T}} \mathbf{q}^{\mathbf{c}}_{\mathcal{T}}]\big) \right| + \big(\mathbf{B}^{\ell}_{\mathcal{T}} \mathbf{q}^{\ell}_{\mathcal{T}}\big) \left| \boldsymbol{Q}\big([\mathbf{B}^{\mathbf{c}}_{\mathcal{T}} \mathbf{q}^{\mathbf{c}}_{\mathcal{T}}]\big) \right| \right) \, dA, \tag{3.36}
$$

$$\mathbf{N}^{\ell}_{\mathcal{T}}(\mathbf{q}^{\mathbf{c}}_{\mathcal{T}}) = \int_{\mathcal{T}} (\mathbf{B}^{\ell}_{\mathcal{T}})^{\mathsf{T}} C\big(J_{\mathcal{T}}(\mathbf{q}^{\mathbf{c}}_{\mathcal{T}})\big)\, dA, \quad J_{\mathcal{T}}(\mathbf{q}^{\mathbf{c}}_{\mathcal{T}}) = \det(\boldsymbol{I} + [\mathbf{B}^{\mathbf{c}}_{\mathcal{T}}\mathbf{q}^{\mathbf{c}}_{\mathcal{T}}]), \tag{3.37}$$

$$\mathbf{F}^{1}_{\mathcal{T}} = \int_{\mathcal{T}} (\mathbf{B}^{1}_{\mathcal{T}})^{\mathsf{T}} \rho_0 \boldsymbol{B}\, dA, \tag{3.38}$$

$$\mathbf{F}^{1}_{\mathcal{E}^{\mathcal{T}}_t} = \begin{cases} \int_{\mathcal{E}^{\mathcal{T}}_t} (\mathbf{B}^{1}_{\mathcal{E}^{\mathcal{T}}_t})^{\mathsf{T}} \overline{\boldsymbol{T}}\, ds, & \text{if } \mathcal{T} \cap \Gamma_t = \mathcal{E}^{\mathcal{T}}_t, \\ \mathbf{0}_{n^1 \times 1}, & \text{otherwise.} \end{cases} \tag{3.39}$$

The term $\mathcal{E}^{\mathcal{T}}_t$ in (3.39) denotes the edge of $\mathcal{T}$ that lies on the traction boundary Γ_t. Also, to define $\mathbf{B}^{1}_{\mathcal{E}_t}$ in (3.39), consider a zero matrix of size $2 \times n^1$, and then substitute 1D Lagrange polynomials over $\mathcal{E}^{\mathcal{T}}_t$ into those columns that are associated with $\mathcal{E}^{\mathcal{T}}_t$. Let $\mathbf{K}^{\mathbf{1d}}_{\widehat{\mathcal{T}}} = \int_{\widehat{\mathcal{T}}} (\mathbf{G}^{1}_{\widehat{\mathcal{T}}})^{\mathsf{T}} \mathbf{B}^{\mathbf{d}}_{\widehat{\mathcal{T}}}\, d\hat{A}$ and $\mathbf{K}^{\mathbf{cd}}_{\widehat{\mathcal{T}}} = -\int_{\widehat{\mathcal{T}}} (\mathbf{B}^{\mathbf{c}}_{\widehat{\mathcal{T}}})^{\mathsf{T}} \mathbf{B}^{\mathbf{d}}_{\widehat{\mathcal{T}}}\, d\hat{A}$ be the counterparts of (3.34) and (3.35) for the reference finite element $\widehat{\mathcal{T}}$, where $\mathbf{G}^{1}_{\widehat{\mathcal{T}}}$, $\mathbf{B}^{\mathbf{c}}_{\widehat{\mathcal{T}}}$, and $\mathbf{B}^{\mathbf{d}}_{\widehat{\mathcal{T}}}$ are obtained according to (3.30) but using the reference local shape functions. For all $\mathcal{T} \in \mathcal{B}_h$, Lemma 11, (ii) and (v) imply the following relations:

$$\mathbf{K}^{\mathbf{1d}}_{\mathcal{T}} = o_{\mathcal{T}} \mathbf{K}^{\mathbf{1d}}_{\widehat{\mathcal{T}}}, \quad \mathbf{K}^{\mathbf{cd}}_{\mathcal{T}} = o_{\mathcal{T}} \mathbf{K}^{\mathbf{cd}}_{\widehat{\mathcal{T}}}. \tag{3.40}$$

Therefore, the local matrices $\mathbf{K}^{\mathbf{1d}}_{\mathcal{T}}$, $\mathbf{K}^{\mathbf{d1}}_{\mathcal{T}}$, $\mathbf{K}^{\mathbf{cd}}_{\mathcal{T}}$, and $\mathbf{K}^{\mathbf{dc}}_{\mathcal{T}}$ are independent of the geometry of $\mathcal{T}$ and depend only on the ordering of the three vertices of $\mathcal{T}$. In practice, the relations (3.40) enable one to obtain (3.34) and (3.35) $\forall \mathcal{T} \in \mathcal{B}_h$ with much less computational cost. It is also practical to change the domain variables of the integrals (3.36)-(3.39) from $\mathbf{X} \in \mathcal{T}$ to $\boldsymbol{\xi} \in \widehat{\mathcal{T}}$. For example, (3.36) and (3.38) can be obtained as

$$\mathbf{N}^{\mathbf{c}}_{\mathcal{T}}(\mathbf{q}^{\mathbf{c}}_{\mathcal{T}}, \mathbf{q}^{\ell}_{\mathcal{T}}) = \big|\det \mathbf{J}_{\mathcal{T}}\big| \int_{\widehat{\mathcal{T}}} (\bar{\mathbf{B}}^{\mathbf{c}}_{\mathcal{T}})^{\mathsf{T}} \left(\left| \widetilde{\boldsymbol{P}}\big([\bar{\mathbf{B}}^{\mathbf{c}}_{\mathcal{T}}\mathbf{q}^{\mathbf{c}}_{\mathcal{T}}]\big) \right| + \big(\mathbf{B}^{\ell}_{\widehat{\mathcal{T}}}\mathbf{q}^{\ell}_{\mathcal{T}}\big) \left| \boldsymbol{Q}\big([\bar{\mathbf{B}}^{\mathbf{c}}_{\mathcal{T}}\mathbf{q}^{\mathbf{c}}_{\mathcal{T}}]\big) \right| \right) d\hat{A},$$

$$\mathbf{F}^{1}_{\mathcal{T}} = \big|\det \mathbf{J}_{\mathcal{T}}\big| \int_{\widehat{\mathcal{T}}} (\mathbf{B}^{1}_{\widehat{\mathcal{T}}})^{\mathsf{T}} \rho_0 (\boldsymbol{B} \circ \mathbf{T}_{\mathcal{T}})\, d\hat{A},$$

where $\bar{\mathbf{B}}^{\mathbf{c}}_{\mathcal{T}} = \mathbf{B}^{\mathbf{c}}_{\mathcal{T}} \circ \mathbf{T}_{\mathcal{T}}$, and $\mathbf{B}^{\ell}_{\widehat{\mathcal{T}}}$ and $\mathbf{B}^{1}_{\widehat{\mathcal{T}}}$ are actually $\mathbf{B}^{\ell}_{\mathcal{T}}$ and $\mathbf{B}^{1}_{\mathcal{T}}$ but are written using the reference local shape functions.

Next we assemble (3.34)-(3.39) for all $\mathcal{T} \in \mathcal{B}_h$ and then accordingly write the global

counterparts of the vectors of local degrees of freedom (3.32) and $\mathbf{t}^1_{\mathcal{T}}$, $\mathbf{t}^{\mathbf{c}}_{\mathcal{T}}$, $\mathbf{t}^{\mathbf{d}}_{\mathcal{T}}$, and $\mathbf{t}^{\ell}_{\mathcal{T}}$. We use the subscript h for both the assembled and the global matrices and vectors, e.g., we denote the assembled form of $\mathsf{K}^{\mathbf{cd}}_{\mathcal{T}}$ and $\mathsf{F}^1_{\mathcal{T}}$ by $\mathsf{K}^{\mathbf{cd}}_h$ and F^1_h, respectively, and the global counterparts of $\mathbf{q}^1_{\mathcal{T}}$ and $\mathbf{t}^1_{\mathcal{T}}$ by $\mathbf{q}^1_h$ and $\mathbf{t}^1_h$, respectively. Next, according to (3.33), one defines

$$\begin{gathered}
\mathbb{Q}_h = \begin{bmatrix} \mathbf{q}^1_h \\ \mathbf{q}^{\mathbf{c}}_h \\ \mathbf{q}^{\mathbf{d}}_h \\ \mathbf{q}^{\ell}_h \end{bmatrix}, \quad \mathbb{T}_h = \begin{bmatrix} \mathbf{t}^1_h \\ \mathbf{t}^{\mathbf{c}}_h \\ \mathbf{t}^{\mathbf{d}}_h \\ \mathbf{t}^{\ell}_h \end{bmatrix}, \quad \mathbb{K}_h = \begin{bmatrix} \mathbf{0} & \mathbf{0} & \mathsf{K}^{\mathbf{1d}}_h & \mathbf{0} \\ \mathbf{0} & \mathbf{0} & \mathsf{K}^{\mathbf{cd}}_h & \mathbf{0} \\ \mathsf{K}^{\mathbf{d1}}_h & \mathsf{K}^{\mathbf{dc}}_h & \mathbf{0} & \mathbf{0} \\ \mathbf{0} & \mathbf{0} & \mathbf{0} & \mathbf{0} \end{bmatrix}, \\
\mathbb{N}_h(\mathbb{Q}_h) = \begin{bmatrix} \mathbf{0} \\ \mathsf{N}^{\mathbf{c}}_h(\mathbf{q}^{\mathbf{c}}_h, \mathbf{q}^{\ell}_h) \\ \mathbf{0} \\ \mathsf{N}^{\ell}_h(\mathbf{q}^{\mathbf{c}}_h) \end{bmatrix}, \quad \mathbb{F}_h = \begin{bmatrix} \mathsf{F}^1_h + \mathsf{F}^1_{\Gamma_t} \\ \mathbf{0} \\ \mathbf{0} \\ \mathbf{0} \end{bmatrix},
\end{gathered} \tag{3.41}$$

where $\mathbb{Q}_h$ includes all the unknown degrees of freedom of the problem and a few known degrees of freedom in its $\mathbf{q}^1_h$, which comes from the displacement boundary $\boldsymbol{U}|_{\Gamma_d} = \overline{\boldsymbol{U}}$. $\mathbb{T}_h$ is a vector of arbitrary real numbers with a few fixed zero elements in its $\mathbf{t}^1_h$ as a result of $\boldsymbol{\Upsilon}|_{\Gamma_d} = \mathbf{0}$. Suppose n is the total number of nodes in the mesh except those lying on Γ_d, and $n_{\mathcal{E}}$ and $n_{\mathcal{T}}$ are the total numbers of edges and elements in the mesh, respectively. After imposing the displacement boundary conditions, the total number of degrees of freedom is

$$N = 2n + (e^c + e^d)n_{\mathcal{E}} + (a^c + a^d + a^\ell)n_{\mathcal{T}},$$

where e^c (e^d) and a^c (a^d) are the numbers of local degrees of freedom for displacement gradient $\boldsymbol{K}$ (stress $\boldsymbol{P}$), which are defined on each edge and on each element, respectively. Also, a^ℓ is the number of local degrees of freedom for the pressure-like variable p, which is defined only on each element. These numbers depend on the choice of CSFEMs and the orders of their approximation spaces; e^c and e^d can be read from the third column of

Table 3.3 and a^c, a^d, and a^ℓ from its fourth column. Recalling n^c and n^d in (3.30), we have $n^c = 3e^c + a^c$ and $n^d = 3e^d + a^d$. The size of the sparse matrix $\mathbb{K}_h$ is $N \times N$, and the size of the vectors $\mathbb{T}_h$, $\mathbb{Q}_h$, $\mathbb{N}_h$, and, $\mathbb{F}_h$ is $N \times 1$. Let $N^1 = 2n$, $N^c = n_{\mathcal{E}} e^c + n_{\mathcal{T}} a^c$, $N^d = n_{\mathcal{E}} e^d + n_{\mathcal{T}} a^d$, and $N^\ell = n_{\mathcal{T}} a^\ell$. Then, the size of the global vectors $\left(\mathbf{q}_h^1, \mathbf{q}_h^{\mathbf{c}}, \mathbf{q}_h^{\mathbf{d}}, \mathbf{q}_h^\ell\right)$ and $\left(\mathbf{t}_h^1, \mathbf{t}_h^{\mathbf{c}}, \mathbf{t}_h^{\mathbf{d}}, \mathbf{t}_h^\ell\right)$ is (N^1, N^c, N^d, N^ℓ).

Remark 15. From (3.40), the symmetric sparse matrix $\mathbb{K}_h$ does not depend on the geometry and dimensions, but only on the connectivity and numbering of the elements of the mesh. That is, the matrix $\mathbb{K}_h$ is identical for homeomorphic (topologically equivalent) meshes.

By using (3.41), one can write (3.33) as $\mathbb{T}_h^{\mathsf{T}}\Big(\mathbb{K}_h\mathbb{Q}_h + \mathbb{N}_h(\mathbb{Q}_h) - \mathbb{F}_h\Big) = 0$. Since $\mathbb{T}_h$ is arbitrary, one obtains the following nonlinear system of algebraic equations:

$$\mathbb{K}_h\mathbb{Q}_h + \mathbb{N}_h(\mathbb{Q}_h) = \mathbb{F}_h. \tag{3.42}$$

Define $\mathbb{R}_h(\mathbb{Q}_h) := \mathbb{K}_h\mathbb{Q}_h + \mathbb{N}_h(\mathbb{Q}_h) - \mathbb{F}_h$ as the residual of the nonlinear equation (3.42). Using Newton's method, the solution of (3.42) can be obtained iteratively by $\mathbb{Q}_h^{(i+1)} = \mathbb{Q}_h^{(i)} - \mathbb{K}_{t_h}^{-1}\left(\mathbb{Q}_h^{(i)}\right)\mathbb{R}_h\left(\mathbb{Q}_h^{(i)}\right)$ starting form an initial guess, where i is the iteration number and $\mathbb{K}_{t_h}$ is the tangent stiffness matrix (Jacobian matrix) given by

$$\mathbb{K}_{t_h} = \begin{bmatrix} \mathbf{0} & \mathbf{0} & \mathbf{K}_h^{\mathbf{1d}} & \mathbf{0} \\ \mathbf{0} & \mathbf{H}_h^{\mathbf{cc}} & \mathbf{K}_h^{\mathbf{cd}} & \mathbf{H}_h^{\mathbf{c}\ell} \\ \mathbf{K}_h^{\mathbf{d}1} & \mathbf{K}_h^{\mathbf{dc}} & \mathbf{0} & \mathbf{0} \\ \mathbf{0} & \mathbf{H}_h^{\ell\mathbf{c}} & \mathbf{0} & \mathbf{0} \end{bmatrix}. \tag{3.43}$$

Here, $\mathbf{H}_h^{\ell\mathbf{c}} = (\mathbf{H}_h^{\mathbf{c}\ell})^{\mathsf{T}}$, and $\mathbf{H}_h^{\mathbf{cc}}$ and $\mathbf{H}_h^{\mathbf{c}\ell}$ are obtained by assembling the following matrices

for all $\mathcal{T} \in \mathcal{B}_h$:

$$\begin{aligned} \mathsf{H}^{\mathbf{cc}}_{\mathcal{T}}(\mathbf{q}^{\mathbf{c}}_{\mathcal{T}}, \mathbf{q}^{\ell}_{\mathcal{T}}) &= \int_{\mathcal{T}} (\mathsf{B}^{\mathbf{c}}_{\mathcal{T}})^{\mathsf{T}} \widetilde{\mathsf{A}} \left(\mathsf{B}^{\mathbf{c}}_{\mathcal{T}} \mathbf{q}^{\mathbf{c}}_{\mathcal{T}}, \mathsf{B}^{\ell}_{\mathcal{T}} \mathbf{q}^{\ell}_{\mathcal{T}} \right) \mathsf{B}^{\mathbf{c}}_{\mathcal{T}} \, dA, \\ \mathsf{H}^{\mathbf{c}\ell}_{\mathcal{T}}(\mathbf{q}^{\mathbf{c}}_{\mathcal{T}}) &= \int_{\mathcal{T}} (\mathsf{B}^{\mathbf{c}}_{\mathcal{T}})^{\mathsf{T}} \Big| \boldsymbol{Q}\big([\mathsf{B}^{\mathbf{c}}_{\mathcal{T}} \mathbf{q}^{\mathbf{c}}_{\mathcal{T}}]\big) \Big| \mathsf{B}^{\ell}_{\mathcal{T}} \, dA, \end{aligned} \tag{3.44}$$

where $\widetilde{\mathsf{A}}(\boldsymbol{K}, p)$ in 2D is a 4×4 matrix representation of the 4th-order elasticity tensor obtained form the derivative of components of the constitutive relation $\boldsymbol{P} = \widetilde{\boldsymbol{P}}(\boldsymbol{K}) + p\boldsymbol{Q}(\boldsymbol{K})$ with respect to components of $\boldsymbol{K}$. Note that the tangent stiffness matrix $\mathbb{K}_{t_h}$ is symmetric and indefinite; this is closely related to Remark 4.

For compressible solids, we eliminate p_h, $\mathbf{q}^{\ell}_{\mathcal{T}}$, and $\mathbf{t}^{\ell}_{\mathcal{T}}$, and hence the matrices (3.41) are simplified to

$$\mathbb{Q}_h = \begin{bmatrix} \mathbf{q}^{1}_h \\ \mathbf{q}^{\mathbf{c}}_h \\ \mathbf{q}^{\mathbf{d}}_h \end{bmatrix}, \quad \mathbb{T}_h = \begin{bmatrix} \mathbf{t}^{1}_h \\ \mathbf{t}^{\mathbf{c}}_h \\ \mathbf{t}^{\mathbf{d}}_h \end{bmatrix}, \quad \mathbb{K}_h = \begin{bmatrix} \mathbf{0} & \mathbf{0} & \mathsf{K}^{\mathbf{1d}}_h \\ \mathbf{0} & \mathbf{0} & \mathsf{K}^{\mathbf{cd}}_h \\ \mathsf{K}^{\mathbf{d1}}_h & \mathsf{K}^{\mathbf{dc}}_h & \mathbf{0} \end{bmatrix},$$

$$\mathbb{N}_h(\mathbb{Q}_h) = \begin{bmatrix} \mathbf{0} \\ \mathsf{N}^{\mathbf{c}}_h(\mathbf{q}^{\mathbf{c}}_h) \\ \mathbf{0} \end{bmatrix}, \quad \mathbb{F}_h = \begin{bmatrix} \mathsf{F}^{1}_h + \mathsf{F}^{1}_{\Gamma_t} \\ \mathbf{0} \\ \mathbf{0} \end{bmatrix}.$$

Accordingly, the tangent stiffness matrix (3.43) is reduced to

$$\mathbb{K}_{t_h} = \begin{bmatrix} \mathbf{0} & \mathbf{0} & \mathsf{K}^{\mathbf{1d}}_h \\ \mathbf{0} & \mathsf{H}^{\mathbf{cc}}_h & \mathsf{K}^{\mathbf{cd}}_h \\ \mathsf{K}^{\mathbf{d1}}_h & \mathsf{K}^{\mathbf{dc}}_h & \mathbf{0} \end{bmatrix}. \tag{3.45}$$

3.6 Constitutive Equations

In this section, we discuss the constitutive equations that we will use in our numerical examples.

For compressible solids in 2D, we consider the neo-Hookean materials with the energy

functions $W_1(\boldsymbol{K})$ and $W_2(\boldsymbol{K})$, and Ogden materials with the energy function $W_3(\boldsymbol{K})$ as follows:

$$W_1(\boldsymbol{K}) = \frac{\mu}{2}(I_1 - 2) - \frac{\mu}{2}\ln I_2 + \frac{\kappa}{2}(I_2^{1/2} - 1)^2, \tag{3.46a}$$

$$W_2(\boldsymbol{K}) = \frac{\mu}{2}(I_1 - 2) - \frac{\mu}{2}\ln I_2 + \frac{\kappa}{8}(\ln I_2)^2, \tag{3.46b}$$

$$W_3(\boldsymbol{K}) = \sum_{i=1}^{m} \frac{\mu_i}{\alpha_i}(\lambda_1^{\alpha_i} + \lambda_2^{\alpha_i} - 2) + \frac{\kappa}{2}(I_2^{1/2} - 1)^2, \tag{3.46c}$$

where μ and κ are the shear and bulk moduli for infinitesimal strains, respectively. Recall that $\boldsymbol{F} = \boldsymbol{I} + \boldsymbol{K}$ is the deformation gradient, and I_i, $i = 1, 2$, are the principal invariants of the right Cauchy-Green deformation tensor $\boldsymbol{C} = \boldsymbol{F}^{\mathsf{T}}\boldsymbol{F}$, where $I_1 = \mathrm{tr}(\boldsymbol{C})$ and $I_2 = \mathrm{det}\boldsymbol{C}$. In (3.46c), $\lambda_i,\ i = 1, 2$, are the principal stretches in 2D and μ_i's and α_i's are some material constants. Using (3.46), the constitutive relations read

$$\widetilde{\boldsymbol{P}}_1(\boldsymbol{K}) = \mu\left(\boldsymbol{F} - \boldsymbol{F}^{-\mathsf{T}}\right) + \kappa\left(J^2 - J\right)\boldsymbol{F}^{-\mathsf{T}}, \tag{3.47a}$$

$$\widetilde{\boldsymbol{P}}_2(\boldsymbol{K}) = \mu\left(\boldsymbol{F} - \boldsymbol{F}^{-\mathsf{T}}\right) + \kappa(\ln J)\boldsymbol{F}^{-\mathsf{T}}, \tag{3.47b}$$

$$\widetilde{\boldsymbol{P}}_3(\boldsymbol{K}) = \sum_{i=1}^{m} \mu_i J^{-\frac{\alpha_i}{3}}\boldsymbol{F}^{-\mathsf{T}}\left(-\frac{1}{3}\mathrm{tr}(\boldsymbol{C}^{\frac{\alpha_i}{2}})\boldsymbol{I} + \boldsymbol{C}^{\frac{\alpha_i}{2}}\right) + \kappa\left(J^2 - J\right)\boldsymbol{F}^{-\mathsf{T}}. \tag{3.47c}$$

For the neo-Hookean materials (3.46a) and (3.46b), the elasticity tensors have the following matrix representations:

$$\widetilde{\mathbf{C}}_1(\boldsymbol{K}) = \mu\mathbf{I} + \left(\frac{\mu}{J} - \kappa(J-1)\right)\bar{\mathbf{I}} + (\mu + \kappa J^2)\left[\boldsymbol{F}^{-\mathsf{T}}\right]\left[\boldsymbol{F}^{-\mathsf{T}}\right]^{\mathsf{T}}, \tag{3.48a}$$

$$\widetilde{\mathbf{C}}_2(\boldsymbol{K}) = \mu\mathbf{I} + \frac{\mu - \kappa\ln J}{J}\bar{\mathbf{I}} + (\mu + \kappa(1 - \ln J))\left[\boldsymbol{F}^{-\mathsf{T}}\right]\left[\boldsymbol{F}^{-\mathsf{T}}\right]^{\mathsf{T}}, \tag{3.48b}$$

where $\mathbf{I}$ is the 4×4 identity matrix, and $\bar{\mathbf{I}}$ denotes an anti-diagonal matrix with non-zero components $\bar{\mathsf{I}}^{14} = \bar{\mathsf{I}}^{41} = -1$ and $\bar{\mathsf{I}}^{23} = \bar{\mathsf{I}}^{32} = 1$. One can show that $\boldsymbol{F}^{-\mathsf{T}} = \frac{1}{J}\left(\boldsymbol{I} + \mathbf{R}\boldsymbol{K}\mathbf{R}^{-\mathsf{T}}\right)$. We use (3.48) for calculating the tangent stiffness matrix (3.45).

For incompressible solids, we consider a neo-Hookean model by defining $\widetilde{W} =$

$W_1|_{J=1} = W_2|_{J=1}$, which gives

$$\widetilde{W}(\boldsymbol{K}) = \frac{\mu}{2}(I_1 - 2). \tag{3.49}$$

The constitutive part of stress reads $\widetilde{P}(\boldsymbol{K}) = \mu(\boldsymbol{I} + \boldsymbol{K})$. We also use the following constraint functions to impose the incompressibility condition $J = 1$:

$$C_1(J) = J - 1 \quad \text{and} \quad C_2(J) = \ln J.$$

We have observed in our numerical examples that $C_1(J)$ has a better performance over $C_1(J)$ in problems with tension loadings, while in bending problems with very refined meshes, $C_2(J)$ has a better performance over $C_1(J)$. Recall that, for incompressible solids, the constitutive relation reads $\boldsymbol{P} = \widetilde{P}(\boldsymbol{K}) + p\boldsymbol{Q}(\boldsymbol{K})$. Using the above constraint functions, the corresponding $\boldsymbol{Q}$ and the corresponding matrix representations of the elasticity tensors are

$$\begin{aligned} &\boldsymbol{Q}_1(\boldsymbol{K}) = J\boldsymbol{F}^{-\mathsf{T}}, \quad \widetilde{\mathbf{C}}_1(p) = \mu\mathbf{I} - p\bar{\mathbf{I}}, \\ &\boldsymbol{Q}_2(\boldsymbol{K}) = \boldsymbol{F}^{-\mathsf{T}}, \quad \widetilde{\mathbf{C}}_2(\boldsymbol{K}, p) = \mu\mathbf{I} - \frac{p}{J}\bar{\mathbf{I}} - p\big[\boldsymbol{F}^{-\mathsf{T}}\big]\big[\boldsymbol{F}^{-\mathsf{T}}\big]^{\mathsf{T}}. \end{aligned} \tag{3.50}$$

We use (3.50) for calculating the tangent stiffness matrix (3.43).

3.7 Solvability and Stability

Theorem 16. *The tangent stiffness matrix $\mathbb{K}_{t_h}$ is invertible (non-singular) if and only if the following four conditions hold:*

(i) $\ker(\mathbf{K}_h^{\mathbf{d1}}) = \{\mathbf{0}_{N^1\times 1}\}$,

(ii) $\ker(\mathbf{K}_h^{\mathbf{cd}}) \cap \ker(\mathbf{K}_h^{\mathbf{1d}}) = \{\mathbf{0}_{N^d\times 1}\}$,

(iii) $\ker(\mathbf{H}_h^{\mathbf{c}\ell}) = \{\mathbf{0}_{N^\ell\times 1}\}$,

(iv) $\ker(\mathbf{H}_h^{\mathbf{cc}}) \cap \big\{\mathbf{X} \in \ker(\mathbf{H}_h^{\ell\mathbf{c}}) : \mathbf{Y}^{\mathsf{T}}\mathbf{K}_h^{\mathbf{dc}}\mathbf{X} = 0, \forall \mathbf{Y} \in \ker(\mathbf{K}_h^{\mathbf{1d}})\big\} = \{\mathbf{0}_{N^c\times 1}\}$.

Proof. Rearrange the rows and the columns of $\mathbb{K}_{t_h}$ to obtain

$$\mathbb{K}_{t_h} = \begin{bmatrix} \mathbb{A}_h & \mathbb{B}_h^{\mathsf{T}} \\ \mathbb{B}_h & \mathbf{0} \end{bmatrix}, \quad \mathbb{A}_h = \begin{bmatrix} \mathbf{H}_h^{\mathbf{cc}} & \mathbf{0} \\ \mathbf{0} & \mathbf{0} \end{bmatrix}, \quad \mathbb{B} = \begin{bmatrix} \mathbf{H}_h^{\ell\mathbf{c}} & \mathbf{0} \\ \mathbf{K}_h^{\mathbf{dc}} & \mathbf{K}_h^{\mathbf{d1}} \end{bmatrix}, \quad \mathbb{B}_h^{\mathsf{T}} = \begin{bmatrix} \mathbf{H}_h^{\mathbf{c}\ell} & \mathbf{K}_h^{\mathbf{cd}} \\ \mathbf{0} & \mathbf{K}_h^{\mathbf{1d}} \end{bmatrix}.$$

Then, apply [64, Theorem 3.2.1] and use an argument similar to that of [64, §3.2.5]. □

Corollary 17. *The tangent stiffness matrix $\mathbb{K}_{t_h}$ is invertible, only if $0 \leqslant N^d - N^1 \leqslant N^c$ and $N^\ell \leqslant N^c$.*

Proof. Theorem 16, (i), (ii), and (iii) imply that $N^1 \leqslant N^d$, $N^d \leqslant N^c + N^1$, and $N^\ell \leqslant N^c$, respectively. □

Remark 18. Given a matrix $\mathbf{A}_{m\times n}$, there exist two unitary matrices $\mathbf{U}_{m\times m}$ and $\mathbf{V}_{n\times n}$ and a rectangular diagonal matrix $\mathbf{S}_{m\times n}$ with non-negative entries on the main diagonal such that $\mathbf{A} = \mathbf{U}\mathbf{S}\mathbf{V}^*$, where the superscript $*$ denotes the conjugate transpose. The diagonal entries of $\mathbf{S}$, $\mathsf{S}_{i,j}$ with $i = j$, are known as the singular values of $\mathbf{A}$. It is straightforward to show that $\ker(\mathbf{A}) = \{\mathbf{0}\}$, if and only if the smallest singular value of $\mathbf{A}$ is non-zero. This can be used to numerically check the conditions of Theorem 16. In particular, one can compute the smallest singular values of sparse matrices $\mathbf{K}_h^{\mathbf{d1}}$ and $\begin{bmatrix} \mathbf{K}_h^{\mathbf{dc}} & \mathbf{K}_h^{\mathbf{d1}} \end{bmatrix}^{\mathsf{T}}$ to check (i) and (ii), respectively.

Remark 19. Conditions of Theorem 16 can be rewritten as inf-sup conditions. For example, $\ker(\mathbf{K}_h^{\mathbf{d1}}) = \{\mathbf{0}_{N^1\times 1}\}$, where $\mathbf{K}_h^{\mathbf{d1}} : \mathbb{R}^{N^1} \to \mathbb{R}^{N^d}$, is equivalent to the following statement:

$$\exists \beta_h > 0, \quad \text{such that} \quad \inf_{\mathbf{X}\in\mathbb{R}^{N^1}} \sup_{\mathbf{Y}\in\mathbb{R}^{N^d}} \frac{\mathbf{Y}^{\mathsf{T}}\mathbf{K}_h^{\mathbf{d1}}\mathbf{X}}{\|\mathbf{X}\|_{\mathbb{R}^{N^1}} \|\mathbf{Y}\|_{\mathbb{R}^{N^d}}} \geqslant \beta_h.$$

Also see [26, Lemmas A.39 and A.40] and note that $\mathbb{R}^{N^{d}\star}$ can be identified with $\mathbb{R}^{N^d}$. One can also show that β_h is the smallest singular value of $\mathbf{K}_h^{\mathbf{d1}}$, see [26, Remark 2.23] and [64, §3.4.3].

Recall that $\mathbf{H}_h^{\mathbf{c}\ell}(\mathbf{q}_h^{\mathbf{c}})$ and $\mathbf{H}_h^{\mathbf{cc}}(\mathbf{q}_h^{\mathbf{c}}, \mathbf{q}_h^{\ell})$ are nonlinear operators. They depend on the state

of deformation of the body and vary at each iteration of Newton's method. Hence, it is difficult to draw a general conclusion for invertibility of $\mathbb{K}_{t_h}$ based on the conditions (iii) and (iv) of Theorem 16 without considering the physics of the problem. On the other hand, $\mathbf{K}_h^{\mathbf{cd}}$ and $\mathbf{K}_h^{\mathbf{1d}}$ are linear operators and remain unchanged throughout the deformation. Therefore, in the following discussions, we focus on conditions (i) and (ii) of Theorem 16.

Considering different meshes with few elements and counting the total degrees of freedom (N^1, N^c, N^d, N^ℓ), one can check that all the possible mixed formulations of the first and the second order satisfy $N^\ell \leqslant N^c$. However, many of them violate $0 \leqslant N^d - N^1 \leqslant N^c$, and hence, result in a singular tangent stiffness matrix $\mathbb{K}_{t_h}$. Those are $\mathsf{H2c}\bar{m}\mathsf{d}\bar{1}\mathsf{L}n$, $\mathsf{H2c}m\mathsf{d}\bar{1}\mathsf{L}n$, $\mathsf{H2c}\bar{m}\mathsf{d1L}n$, $\mathsf{H2c}m\mathsf{d1L}n$, $\mathsf{H1c}\bar{1}\mathsf{d1L}n$, $\mathsf{H}m\mathsf{c}\bar{1}\mathsf{d}\bar{2}\mathsf{L}n$, $\mathsf{H}m\mathsf{c}\bar{1}\mathsf{d2L}n$, $\mathsf{H}m\mathsf{c1d}\bar{2}\mathsf{L}n$, $\mathsf{H}m\mathsf{c1d2L}n$, and $\mathsf{H}m\mathsf{c}\bar{2}\mathsf{d2L}n$ for $m = 1, 2$ and $n = 0, 1, 2$. In addition, considering several arbitrary meshes and computing the smallest singular value of $\begin{bmatrix} \mathbf{K}_h^{\mathbf{dc}} & \mathbf{K}_h^{\mathbf{d1}} \end{bmatrix}^{\mathsf{T}}$, we conclude that $\ker(\mathbf{K}_h^{\mathbf{cd}}) \cap \ker(\mathbf{K}_h^{\mathbf{1d}}) = \{\mathbf{0}_{N^d \times 1}\}$ does not hold, in general, for $\mathsf{H}m\mathsf{c}\bar{n}\mathsf{d}\bar{n}\mathsf{L}r$ and $\mathsf{H}m\mathsf{c}n\mathsf{d}n\mathsf{L}r$ with $m, n = 1, 2$ and $r = 0, 1, 2$. The cases mentioned above are 75 out of 96 possible first and second order mixed methods. These cases have solvability issues for any mesh regardless of its size h.

In [42] based on the observations in several numerical examples it was reported that only 7 out of the 32 possible choices of the first and second-order CSFEMs for compressible solids result in solvable algebraic systems. Those observations agree with the above arguments because all the remaining 25 mixed methods violate one or both of the necessary conditions $\ker(\mathbf{K}_h^{\mathbf{d1}}) = \{\mathbf{0}_{N^1 \times 1}\}$ and $\ker(\mathbf{K}_h^{\mathbf{cd}}) \cap \ker(\mathbf{K}_h^{\mathbf{1d}}) = \{\mathbf{0}_{N^d \times 1}\}$. In fact, those 25 cases can be obtained directly from the 75 cases we mentioned above by removing the pressure field and the incompressibility constraint from the mixed formulations.

In view of Theorem 16, (i) and (ii), we have narrowed down the 96 possible choices of mixed FEMs to the following 21 solvable ones: $\mathsf{H1c1d}\bar{1}\mathsf{L}m$, $\mathsf{H1c}\bar{2}\mathsf{d}\bar{1}\mathsf{L}m$, $\mathsf{H1c}\bar{2}\mathsf{d1L}m$, $\mathsf{H1c2d}\bar{1}\mathsf{L}m$, $\mathsf{H1c2d1L}m$, $\mathsf{H1c2d}\bar{2}\mathsf{L}m$, and $\mathsf{H2c2d}\bar{2}\mathsf{L}m$ for $m = 0, 1, 2$. Satisfaction of the conditions of Theorem 16 for a given mesh is not enough; the *stability* of the

method requires that all the four conditions hold as the mesh gets refined and h goes to zero. Our numerical examples suggest that $\mathsf{H1c1d\bar{1}L0}$ and $\mathsf{H2c2d\bar{2}L1}$ have an overall good performance among the first-order and second-order elements, respectively. These elements are illustrated in Figure 3.4.

CHAPTER 4

COMPATIBLE-STRAIN MIXED FINITE ELEMENT METHODS FOR 3D NONLINEAR ELASTICITY

4.1 Polynomial Tensor Fields

Suppose $\mathcal{P}_r(\mathbb{R}^3)$ is the space of $\mathbb{R}$-valued polynomials in three variables $\{\mathrm{X}^1, \mathrm{X}^2, \mathrm{X}^3\}$ of degree at most $r \geqslant 0$ and suppose $\mathcal{H}_r(\mathbb{R}^3) \subset \mathcal{P}_r(\mathbb{R}^3)$ is the space of homogeneous polynomials of degree r, that is, all terms of members of $\mathcal{H}_r(\mathbb{R}^3)$ are of degree r. For $r < 0$, these spaces are assumed to be empty. By $\mathcal{P}_r(T\mathbb{R}^3)$ and $\mathcal{P}_r(\otimes^2 T\mathbb{R}^3)$ we denote the spaces of polynomial vector and $\binom{2}{0}$-tensor fields in $\mathbb{R}^3$ with Cartesian components in $\mathcal{P}_r(\mathbb{R}^3)$. The spaces $\mathcal{H}_r(T\mathbb{R}^3)$ and $\mathcal{H}_r(\otimes^2 T\mathbb{R}^3)$ are defined similarly. One can show that

$$\dim \mathcal{P}_r(\otimes^2 T\mathbb{R}^3) = 3 \dim \mathcal{P}_r(T\mathbb{R}^3) = \frac{3}{2}(r+1)(r+2)(r+3),$$
$$\dim \mathcal{H}_r(\otimes^2 T\mathbb{R}^3) = 3 \dim \mathcal{H}_r(T\mathbb{R}^3) = \frac{9}{2}(r+1)(r+2).$$

Using $\mathcal{P}_r$ fields, one can write the following polynomial complex:

$$0 \longrightarrow \mathcal{P}_r(T\mathbb{R}^3) \xrightarrow{\mathbf{grad}} \mathcal{P}_{r-1}(\otimes^2 T\mathbb{R}^3) \xrightarrow{\mathbf{curl}^{\mathrm{T}}} \mathcal{P}_{r-2}(\otimes^2 T\mathbb{R}^3) \xrightarrow{\mathbf{div}} \mathcal{P}_{r-3}(T\mathbb{R}^3) \longrightarrow 0. \tag{4.1}$$

Suppose $Y^I(\mathrm{X}^1, \mathrm{X}^2, \mathrm{X}^3)$ and $T^{IJ}(\mathrm{X}^1, \mathrm{X}^2, \mathrm{X}^3)$, $I, J = 1, 2, 3$, are the Cartesian components of a vector field $\boldsymbol{Y}$ and a $\binom{2}{0}$-tensor field $\boldsymbol{T}$. Now, we define the following operators

$$\mathrm{K}_1 : \mathcal{P}_r(T\mathbb{R}^3) \to \mathcal{P}_{r+1}(\mathbb{R}^3), \qquad \mathrm{K}_1(\boldsymbol{Y}) = \mathrm{X}^I Y^I,$$
$$\mathrm{K}_2 : \mathcal{P}_r(T\mathbb{R}^3) \to \mathcal{P}_{r+1}(T\mathbb{R}^3), \quad (\mathrm{K}_2(\boldsymbol{Y}))^I = \varepsilon_{IJL} \mathrm{X}^L Y^J,$$
$$\mathrm{K}_3 : \mathcal{P}_r(\mathbb{R}^3) \to \mathcal{P}_{r+1}(T\mathbb{R}^3), \qquad (\mathrm{K}_3(f))^I = \mathrm{X}^I f,$$

and

$$\mathbf{K}_1 : \mathcal{P}_r(\otimes^2 T\mathbb{R}^3) \to \mathcal{P}_{r+1}(T\mathbb{R}^3), \qquad (\mathbf{K}_1(\boldsymbol{T}))^I = \mathrm{X}^J T^{IJ},$$

$$\mathbf{K}_2 : \mathcal{P}_r(\otimes^2 T\mathbb{R}^3) \to \mathcal{P}_{r+1}(\otimes^2 T\mathbb{R}^3), \quad (\mathbf{K}_2(\boldsymbol{T}))^{IJ} = \varepsilon_{JLK}\mathrm{X}^K T^{IL},$$

$$\mathbf{K}_3 : \mathcal{P}_r(T\mathbb{R}^3) \to \mathcal{P}_{r+1}(\otimes^2 T\mathbb{R}^3), \qquad (\mathbf{K}_3(\boldsymbol{Y}))^{IJ} = \mathrm{X}^J Y^I.$$

It is easy to show that $\mathrm{K}_i \circ \mathrm{K}_{i+1} = 0$, and $\mathbf{K}_i \circ \mathbf{K}_{i+1} = 0$. In particular, one can write the following polynomial complex:

$$0 \longrightarrow \mathcal{P}_r(T\mathbb{R}^3) \xrightarrow{\mathbf{K}_3} \mathcal{P}_{r+1}(\otimes^2 T\mathbb{R}^3) \xrightarrow{\mathbf{K}_2} \mathcal{P}_{r+2}(\otimes^2 T\mathbb{R}^3) \xrightarrow{\mathbf{K}_1} \mathcal{P}_{r+3}(T\mathbb{R}^3) \longrightarrow 0,$$

Let grad and curl be the standard operators of vector analysis. The following theorem introduces some decompositions for $\mathcal{H}_r(T\mathbb{R}^3)$ and $\mathcal{H}_r(\otimes^2 T\mathbb{R}^3)$. We omit the proof of this theorem as it is similar to the proof of the theorem 20.

Theorem 20. *The following decompositions hold:*

$$\mathcal{H}_r(T\mathbb{R}^3) = \mathrm{K}_2\big(\mathcal{H}_{r-1}(T\mathbb{R}^3)\big) \oplus \mathrm{grad}\big(\mathcal{H}_{r+1}(\mathbb{R}^3)\big)\,, \tag{4.2a}$$

$$\mathcal{H}_r(T\mathbb{R}^3) = \mathrm{K}_3\big(\mathcal{H}_{r-1}(\mathbb{R}^3)\big) \oplus \mathrm{curl}\big(\mathcal{H}_{r+1}(T\mathbb{R}^3)\big)\,, \tag{4.2b}$$

$$\mathcal{H}_r(\otimes^2 T\mathbb{R}^3) = \mathbf{K}_2\big(\mathcal{H}_{r-1}(\otimes^2 T\mathbb{R}^3)\big) \oplus \mathbf{grad}\big(\mathcal{H}_{r+1}(T\mathbb{R}^3)\big)\,, \tag{4.3a}$$

$$\mathcal{H}_r(\otimes^2 T\mathbb{R}^3) = \mathbf{K}_3\big(\mathcal{H}_{r-1}(T\mathbb{R}^3)\big) \oplus \mathbf{curl}^{\mathsf{T}}\big(\mathcal{H}_{r+1}(\otimes^2 T\mathbb{R}^3)\big)\,, \tag{4.3b}$$

where

$$\dim \mathbf{K}_2\big(\mathcal{H}_r(\otimes^2 T\mathbb{R}^3)\big) = 3\dim \mathrm{K}_2\big(\mathcal{H}_r(T\mathbb{R}^3)\big) = 3(r+1)(r+3),$$

$$\dim \mathbf{K}_3\big(\mathcal{H}_r(T\mathbb{R}^3)\big) = 3\dim \mathrm{K}_3\big(\mathcal{H}_r(\mathbb{R}^3)\big) = \frac{3}{2}(r+1)(r+2),$$

$$\dim \mathbf{curl}^{\mathsf{T}}\big(\mathcal{H}_r(\otimes^2 T\mathbb{R}^3)\big) = 3\dim \mathrm{curl}\big(\mathcal{H}_r(T\mathbb{R}^3)\big) = 3r(r+2),$$

$$\dim \mathbf{grad}\big(\mathcal{H}_r(T\mathbb{R}^3)\big) = 3\dim \mathrm{grad}\big(\mathcal{H}_r(\mathbb{R}^3)\big) = \frac{3}{2}(r+1)(r+2).$$

The fact that $\mathcal{P}_r(T\mathbb{R}^3) = \mathcal{P}_{r-1}(T\mathbb{R}^3) \oplus \mathcal{H}_r(T\mathbb{R}^3)$ together with the decompositions introduced in the above theorem allows one to define the following subspaces of $\mathcal{P}_r(T\mathbb{R}^3)$:

$$\mathcal{P}_r^-(T\mathbb{R}^3) := \mathcal{P}_{r-1}(T\mathbb{R}^3) \oplus \mathrm{K}_2\big(\mathcal{H}_{r-1}(T\mathbb{R}^3)\big),$$
$$\mathcal{P}_r^{\ominus}(T\mathbb{R}^3) := \mathcal{P}_{r-1}(T\mathbb{R}^3) \oplus \mathrm{K}_3\big(\mathcal{H}_{r-1}(\mathbb{R}^3)\big).$$

Similarly, one can also define the following subspaces of $\mathcal{P}_r(\otimes^2 T\mathbb{R}^3)$:

$$\mathcal{P}_r^-(\otimes^2 T\mathbb{R}^3) := \mathcal{P}_{r-1}(\otimes^2 T\mathbb{R}^3) \oplus \mathbf{K}_2\big(\mathcal{H}_{r-1}(\otimes^2 T\mathbb{R}^3)\big),$$

$$\mathcal{P}_r^{\ominus}(\otimes^2 T\mathbb{R}^3) := \mathcal{P}_{r-1}(\otimes^2 T\mathbb{R}^3) \oplus \mathbf{K}_3\big(\mathcal{H}_{r-1}(T\mathbb{R}^3)\big),$$

where

$$\dim \mathcal{P}_r^-(\otimes^2 T\mathbb{R}^3) = 3\dim \mathcal{P}_r^-(T\mathbb{R}^3) = \frac{3}{2}r(r+2)(r+3),$$
$$\dim \mathcal{P}_r^{\ominus}(\otimes^2 T\mathbb{R}^3) = 3\dim \mathcal{P}_r^{\ominus}(T\mathbb{R}^3) = \frac{3}{2}r(r+1)(r+3),$$

Example 21. Let $(X, Y, Z) = (\mathrm{X}^1, \mathrm{X}^2, \mathrm{X}^3)$. For $r = 1$, $\dim \mathcal{P}_1(\otimes^2 T\mathbb{R}^3) = 36$ and $\mathcal{P}_1(\otimes^2 T\mathbb{R}^3)$ can be written as

$$\mathcal{P}_1(\otimes^2 T\mathbb{R}^3) = \big\{\mathbf{A}_0 + X\cdot\mathbf{A}_1 + Y\cdot\mathbf{A}_2 + Z\cdot\mathbf{A}_3,\ \forall \mathbf{A}_i \in \mathbb{R}^{3\times 3}\big\},$$

where $\mathbb{R}^{2\times 2}$ is the space of 3×3 matrices. In addition, $\dim \mathcal{P}_1^-(\otimes^2 T\mathbb{R}^3) = 18$ and

$\dim \mathcal{P}_1^{\ominus}(\otimes^2 T\mathbb{R}^3) = 12$, where

$$\mathcal{P}_1^{-}(\otimes^2 T\mathbb{R}^3) =$$
$$\left\{ \mathbf{A}_0 + \begin{bmatrix} a_1Z - a_2Y & a_2X - a_3Z & a_3Y - a_1X \\ b_1Z - b_2Y & b_2X - b_3Z & b_3Y - b_1X \\ c_1Z - c_2Y & c_2X - c_3Z & c_3Y - c_1X \end{bmatrix},\ \forall a_i, b_i, c_i \in \mathbb{R},\ \forall \mathbf{A}_k \in \mathbb{R}^{3\times 3} \right\},$$

$$\mathcal{P}_1^{\ominus}(\otimes^2 T\mathbb{R}^3) =$$
$$\left\{ \mathbf{A}_0 + \begin{bmatrix} aX & aY & aZ \\ bX & bY & bZ \\ cX & cY & cZ \end{bmatrix},\ \forall a, b, c \in \mathbb{R},\ \forall \mathbf{A}_k \in \mathbb{R}^{3\times 3} \right\}.$$

For $r = 2$, we have $\dim \mathcal{P}_2(\otimes^2 T\mathbb{R}^3) = 90$, $\dim \mathcal{P}_2^{-}(\otimes^2 T\mathbb{R}^3) = 60$, and $\dim \mathcal{P}_2^{\ominus}(\otimes^2 T\mathbb{R}^3) = 45$, where

$$\mathcal{P}_2(\otimes^2 T\mathbb{R}^3) = \big\{ \mathbf{A}_0 + X \cdot \mathbf{A}_1 + Y \cdot \mathbf{A}_2 + Z \cdot \mathbf{A}_3 +$$
$$X^2 \cdot \mathbf{A}_4 + XY \cdot \mathbf{A}_5 + XZ \cdot \mathbf{A}_6 + Y^2 \cdot \mathbf{A}_7 + YZ \cdot \mathbf{A}_8 + Z^2 \cdot \mathbf{A}_9,\ \forall \mathbf{A}_i \in \mathbb{R}^{3\times 3} \big\},$$

$$\mathcal{P}_2^{-}(\otimes^2 T\mathbb{R}^2) = \Bigg\{ \mathbf{A}_0 + X \cdot \mathbf{A}_1 + Y \cdot \mathbf{A}_2 + Z \cdot \mathbf{A}_3 +$$
$$\begin{bmatrix} a_1Z^2 - a_2Y^2 & a_3X^2 - a_6Z^2 & a_8Y^2 - a_4X^2 \\ b_1Z^2 - b_2Y^2 & b_3X^2 - b_6Z^2 & b_8Y^2 - b_4X^2 \\ c_1Z^2 - c_2Y^2 & c_3X^2 - c_6Z^2 & c_8Y^2 - c_4X^2 \end{bmatrix} +$$
$$\begin{bmatrix} -a_3XY + a_4XZ + a_5YZ & a_2XY + a_7XZ - a_8YZ & -(a_5 + a_7)XY - a_1XZ + a_6YZ \\ -b_3XY + b_4XZ + b_5YZ & b_2XY + b_7XZ - b_8YZ & -(b_5 + b_7)XY - b_1XZ + b_6YZ \\ -c_3XY + c_4XZ + c_5YZ & c_2XY + c_7XZ - c_8YZ & -(c_5 + c_7)XY - c_1XZ + c_6YZ \end{bmatrix},$$
$$\forall a_i, b_i, c_i \in \mathbb{R},\ \forall \mathbf{A}_k \in \mathbb{R}^{3\times 3} \Bigg\},$$

$$\mathcal{P}_2^{\ominus}(\otimes^2 T\mathbb{R}^2) = \Bigg\{ \mathbf{A}_0 + X\cdot\mathbf{A}_1 + Y\cdot\mathbf{A}_2 + Z\cdot\mathbf{A}_3 +$$

$$\begin{bmatrix} a_1X^2+a_2XY+a_3XZ & a_2Y^2+a_1XY+a_3YZ & a_3Z^2+a_1XZ+a_2YZ \\ b_1X^2+b_2XY+b_3XZ & b_2Y^2+b_1XY+b_3YZ & b_3Z^2+b_1XZ+b_2YZ \\ c_1X^2+c_2XY+c_3XZ & c_2Y^2+c_1XY+c_3YZ & c_3Z^2+c_1XZ+c_2YZ \end{bmatrix},$$

$$\forall a_i, b_i, c_i \in \mathbb{R},\ \forall \mathbf{A}_k \in \mathbb{R}^{3\times 3} \Bigg\}.$$

The spaces $\mathcal{P}_r^-(\otimes^2 T\mathbb{R}^3)$ and $\mathcal{P}_r^{\ominus}(\otimes^2 T\mathbb{R}^3)$ give one the following polynomial complexes:

$$0 \longrightarrow \mathcal{P}_r(T\mathbb{R}^3) \xrightarrow{\mathbf{grad}} \mathcal{P}_{r-1}(\otimes^2 T\mathbb{R}^3) \xrightarrow{\mathbf{curl}^{\mathsf{T}}} \mathcal{P}_{r-1}^{\ominus}(\otimes^2 T\mathbb{R}^3) \xrightarrow{\mathbf{div}} \mathcal{P}_{r-2}(T\mathbb{R}^3) \longrightarrow 0, \tag{4.4a}$$

$$0 \longrightarrow \mathcal{P}_r(T\mathbb{R}^3) \xrightarrow{\mathbf{grad}} \mathcal{P}_r^-(\otimes^2 T\mathbb{R}^3) \xrightarrow{\mathbf{curl}^{\mathsf{T}}} \mathcal{P}_{r-1}(\otimes^2 T\mathbb{R}^3) \xrightarrow{\mathbf{div}} \mathcal{P}_{r-2}(T\mathbb{R}^3) \longrightarrow 0, \tag{4.4b}$$

$$0 \longrightarrow \mathcal{P}_r(T\mathbb{R}^3) \xrightarrow{\mathbf{grad}} \mathcal{P}_r^-(\otimes^2 T\mathbb{R}^3) \xrightarrow{\mathbf{curl}^{\mathsf{T}}} \mathcal{P}_r^{\ominus}(\otimes^2 T\mathbb{R}^3) \xrightarrow{\mathbf{div}} \mathcal{P}_{r-1}(T\mathbb{R}^3) \longrightarrow 0. \tag{4.4c}$$

Note that (4.1) is a subcomplex of (4.4a), (4.4a) is a subcomplex of (4.4b), and (4.4b) is a subcomplex of (4.4c).

4.2 Finite Elements

Let $\widehat{\mathcal{T}}$ be a reference tetrahedral element with coordinates $\boldsymbol{\xi} = (\xi^1, \xi^2, \xi^3)$ shown in Figure 4.1. We denote the edges of $\widehat{\mathcal{T}}$ by $\widehat{\mathcal{E}}_i, i = 1, 2, \ldots, 6$ and their corresponding lengths by $\hat{\ell}_i, i = 1, 2, \ldots, 6$, and the faces of $\widehat{\mathcal{T}}$ by $\widehat{\mathcal{F}}_i, i = 1, 2, 3, 4$ and their corresponding areas by $\hat{A}_i, i = 1, 2, 3, 4$. For an edge joining two vertices i and j, one defines a unique orientation as $i \to j$, where $i < j$. We also define a unit tangent vector $\hat{\mathbf{t}}_i$ on each edge such that it agrees with the edge orientation. Moreover, on each face containing three edges $\widehat{\mathcal{E}}_i$, $\widehat{\mathcal{E}}_j$, and $\widehat{\mathcal{E}}_k$, we define a unit normal vector $\hat{\mathbf{n}}_l = \hat{\mathbf{t}}_i \times \hat{\mathbf{t}}_j$, where $i < j < k$.

Following [54, 26], we define a finite element as a triplet $(\mathcal{T}, \mathcal{P}(\mathcal{T}), \Sigma)$, where $\mathcal{T}$ is a

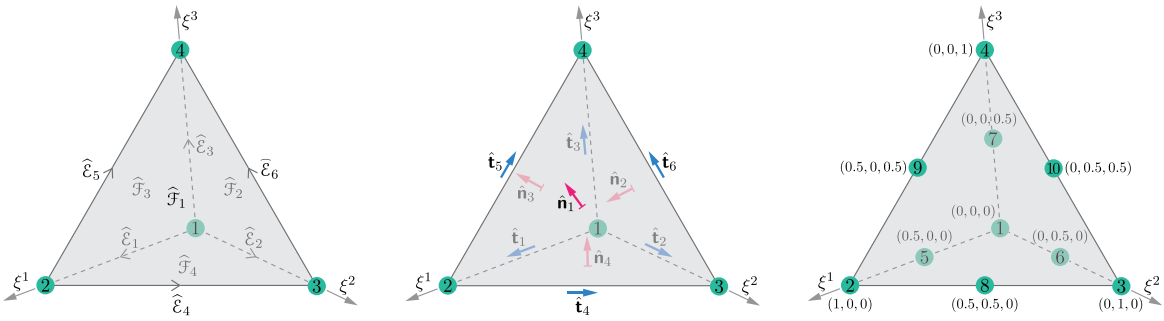

Figure 4.1: The four-node reference element and edge numbers and orientations (left), the reference directions for the unit tangent and normal vectors (middle), and the ten-node reference element (right).

tetrahedron in $\mathbb{R}^3$, $\mathcal{P}(\mathcal{T})$ is a space of polynomials on $\mathcal{T}$, and Σ is a set of $\mathbb{R}$-valued linear functionals acting on the members of $\mathcal{P}(\mathcal{T})$. The members of Σ are called the local degrees of freedom (DOF) and the local shape functions form a basis for $\mathcal{P}(\mathcal{T})$ (see [43, §3.1]). We consider the following *reference* finite elements for the four field variables:

$$
\begin{aligned}
&\left(\widehat{\mathcal{T}}, \mathcal{P}_r(T\widehat{\mathcal{T}}), \Sigma^{\widehat{\mathcal{T}},1}\right) && \text{for displacement } \boldsymbol{U},\\
&\left(\widehat{\mathcal{T}}, \mathcal{P}_r^-(\otimes^2 T\widehat{\mathcal{T}}), \Sigma^{\widehat{\mathcal{T}},\mathbf{c}-}\right), \left(\widehat{\mathcal{T}}, \mathcal{P}_r(\otimes^2 T\widehat{\mathcal{T}}), \Sigma^{\widehat{\mathcal{T}},\mathbf{c}}\right) && \text{for displacement gradient } \boldsymbol{K},\\
&\left(\widehat{\mathcal{T}}, \mathcal{P}_r^{\ominus}(\otimes^2 T\widehat{\mathcal{T}}), \Sigma^{\widehat{\mathcal{T}},\mathbf{d}-}\right), \left(\widehat{\mathcal{T}}, \mathcal{P}_r(\otimes^2 T\widehat{\mathcal{T}}), \Sigma^{\widehat{\mathcal{T}},\mathbf{d}}\right), && \text{for stress } \boldsymbol{P},\\
&\left(\widehat{\mathcal{T}}, \mathcal{P}_r(\widehat{\mathcal{T}}), \Sigma^{\widehat{\mathcal{T}},\ell}\right) && \text{for the pressure-like field } p.
\end{aligned}
\tag{4.5}
$$

Note that $\mathcal{P}_r(\widehat{\mathcal{T}}) = \mathcal{P}_r(\mathbb{R}^3)\big|_{\widehat{\mathcal{T}}}$ and $\mathcal{P}_r(T\widehat{\mathcal{T}})$, $\mathcal{P}_r(\otimes^2 T\widehat{\mathcal{T}})$, $\mathcal{P}_r^-(\otimes^2 T\widehat{\mathcal{T}})$, and $\mathcal{P}_r^{\ominus}(\otimes^2 T\widehat{\mathcal{T}})$ are defined similarly. The finite element for $\boldsymbol{U}$ is based on the standard Lagrange finite elements. For a vector field $\boldsymbol{V} : \widehat{\mathcal{T}} \to \mathbb{R}^3$, the set of local degrees of freedom is $\Sigma^{\widehat{\mathcal{T}},1} = \{V^1(\boldsymbol{\xi}_1), V^2(\boldsymbol{\xi}_1), V^3(\boldsymbol{\xi}_1), \ldots, V^1(\boldsymbol{\xi}_m), V^2(\boldsymbol{\xi}_m), V^3(\boldsymbol{\xi}_m)\}$, where $\boldsymbol{\xi}_i$ contains the coordinates of the i-th node of the m-node $\widehat{\mathcal{T}}$, where $m = 4$ ($m = 10$) for $r = 1$ ($r = 2$).

For $r = 1, 2$, a basis of the polynomial space $\mathcal{P}_r(T\widehat{\mathfrak{T}})$ includes

$$\boldsymbol{h}^{\widehat{\mathfrak{T}}}_{3i-2} = \begin{bmatrix} l^r_i \\ 0 \\ 0 \end{bmatrix}, \quad \boldsymbol{h}^{\widehat{\mathfrak{T}}}_{3i-1} = \begin{bmatrix} 0 \\ l^r_i \\ 0 \end{bmatrix}, \quad \boldsymbol{h}^{\widehat{\mathfrak{T}}}_{3i} = \begin{bmatrix} 0 \\ 0 \\ l^r_i \end{bmatrix}, \quad i = 1, 2, ..., m. \tag{4.6}$$

The Lagrange polynomials l^r_i for the four-node reference tetrahedron $\widehat{\mathfrak{T}}$ are

$$l^1_1 = 1 - \xi^1 - \xi^2 - \xi^3, \quad l^1_2 = \xi^1, \quad l^1_3 = \xi^2, \quad l^1_4 = \xi^3. \tag{4.7}$$

For the ten-node $\widehat{\mathfrak{T}}$, the Lagrange polynomials are $l^2_k = l^1_i(2l^1_i - 1)$ for the nodes at the vertices $i = 1, 2, 3, 4$ and $l^2_k = 4l^1_i l^1_j$ for the middle node of each edge joining vertices i and j as shown in Figure 4.1. We will use $\mathcal{P}_r(T\widehat{\mathfrak{T}}), r = 1, 2$ spanned by $\boldsymbol{h}^{\widehat{\mathfrak{T}}}_i$ to construct the approximation space of $\boldsymbol{U}$. To interpolate $\boldsymbol{K} \in H^{\mathbf{c}}$, we define two finite elements given in $(4.5)_2$ respectively based on the Nédélec 1^{st}-kind *edge* elements in $\mathbb{R}^3$ (NE1) [55] and the Nédélec 2^{nd}-kind *edge* elements in $\mathbb{R}^3$ (NE2) [56]. Let $\overrightarrow{\boldsymbol{T}}_I := \begin{bmatrix} T^{I1} & T^{I2} & T^{I3} \end{bmatrix}^{\mathsf{T}}$ be a vector containing the elements of the I-th row of a $\binom{2}{0}$-tensor $\boldsymbol{T}$. The set of the local degrees of freedom $\Sigma^{\widehat{\mathfrak{T}},\mathbf{c}-}$ ($\Sigma^{\widehat{\mathfrak{T}},\mathbf{c}}$) in $(4.5)_2$ is defined as $\left\{\phi^{\widehat{\mathfrak{T}},\hat{\mathcal{E}}_k}_{I,J}, \phi^{\widehat{\mathfrak{T}},\hat{\mathfrak{F}}_l}_{I,J}, \phi^{\widehat{\mathfrak{T}},\widehat{\mathfrak{T}}}_{I,J}\right\}$, where

$$\begin{aligned}
\phi^{\widehat{\mathfrak{T}},\hat{\mathcal{E}}_k}_{I,J}(\boldsymbol{T}) &= \int_{\hat{\mathcal{E}}_k} f_J \langle \overrightarrow{\boldsymbol{T}}_I, \hat{\mathbf{t}}_k \rangle \, d\hat{s}, \quad \forall f_J \text{ that form a basis for } \mathcal{P}_{r-1}(\mathbb{R}^3)\big|_{\hat{\mathcal{E}}_k} \left(\mathcal{P}_r(\mathbb{R}^3)\big|_{\hat{\mathcal{E}}_k}\right), \\
\phi^{\widehat{\mathfrak{T}},\hat{\mathfrak{F}}_l}_{I,J}(\boldsymbol{T}) &= \int_{\hat{\mathfrak{F}}_l} \langle \overrightarrow{\boldsymbol{T}}_I \times \boldsymbol{Y}_J, \hat{\mathbf{n}}_l \rangle d\hat{A} \;\; \forall \boldsymbol{Y}_J \text{ that form a basis for } \mathcal{P}_{r-2}(T\mathbb{R}^3)\big|_{\hat{\mathfrak{F}}_l} \left(\mathcal{P}^-_{r-1}(T\mathbb{R}^3)\big|_{\hat{\mathfrak{F}}_l}\right), \\
\phi^{\widehat{\mathfrak{T}},\widehat{\mathfrak{T}}}_{I,J}(\boldsymbol{T}) &= \int_{\widehat{\mathfrak{T}}} \langle \overrightarrow{\boldsymbol{T}}_I, \boldsymbol{Z}_J \rangle \, d\hat{V} \qquad \forall \boldsymbol{Z}_J \text{ that form a basis for } \mathcal{P}_{r-3}(T\mathbb{R}^3)\big|_{\widehat{\mathfrak{T}}} \left(\mathcal{P}^{\ominus}_{r-2}(T\mathbb{R}^3)\big|_{\widehat{\mathfrak{T}}}\right).
\end{aligned} \tag{4.8}$$

We next discuss the corresponding local shape functions of the two finite elements given in $(4.5)_2$. Let $\boldsymbol{v}^{\widehat{\mathfrak{T}},\hat{\mathcal{E}}_k}_J$, $\boldsymbol{v}^{\widehat{\mathfrak{T}},\hat{\mathfrak{F}}_l}_J$, and $\boldsymbol{v}^{\widehat{\mathfrak{T}},\widehat{\mathfrak{T}}}_J$ denote the shape functions of Nédélec edge elements that are associated to the $k-$th edge of $\widehat{\mathfrak{T}}$, the $l-$th face of $\widehat{\mathfrak{T}}$, and the entire $\widehat{\mathfrak{T}}$, respectively. We consider these vector-valued polynomials in $\mathbb{R}^3$ as row vectors and define the following

tensorial shape functions:

$$\boldsymbol{r}_{1,J}^{\hat{\mathfrak{T}},\hat{\mathcal{E}}_k} = \begin{bmatrix} \boldsymbol{v}_J^{\hat{\mathfrak{T}},\hat{\mathcal{E}}_k} \\ \mathbf{0} \\ \mathbf{0} \end{bmatrix}_{3\times 3}, \quad \boldsymbol{r}_{2,J}^{\hat{\mathfrak{T}},\hat{\mathcal{E}}_k} = \begin{bmatrix} \mathbf{0} \\ \boldsymbol{v}_J^{\hat{\mathfrak{T}},\hat{\mathcal{E}}_k} \\ \mathbf{0} \end{bmatrix}_{3\times 3}, \quad \boldsymbol{r}_{3,J}^{\hat{\mathfrak{T}},\hat{\mathcal{E}}_k} = \begin{bmatrix} \mathbf{0} \\ \mathbf{0} \\ \boldsymbol{v}_J^{\hat{\mathfrak{T}},\hat{\mathcal{E}}_k} \end{bmatrix}_{3\times 3}. \tag{4.9}$$

Similarly, we define $\boldsymbol{r}_{I,J}^{\hat{\mathfrak{T}},\hat{\mathcal{F}}_l}$ and $\boldsymbol{r}_{I,J}^{\hat{\mathfrak{T}},\hat{\mathfrak{T}}}$ for $I = 1,2,3$ using $\boldsymbol{v}_J^{\hat{\mathfrak{T}},\hat{\mathcal{F}}_l}$ and $\boldsymbol{v}_J^{\hat{\mathfrak{T}},\hat{\mathfrak{T}}}$, respectively. The polynomial spaces $\mathcal{P}_r^-(\otimes^2 T\hat{\mathfrak{T}})$ and $\mathcal{P}_r(\otimes^2 T\hat{\mathfrak{T}})$ in $(4.5)_2$ are spanned by a basis $\left\{\boldsymbol{r}_{I,J}^{\hat{\mathfrak{T}},\hat{\mathcal{E}}_k}, \boldsymbol{r}_{I,J}^{\hat{\mathfrak{T}},\hat{\mathcal{F}}_l}, \boldsymbol{r}_{I,J}^{\hat{\mathfrak{T}},\hat{\mathfrak{T}}}\right\}$ that are respectively based on the shape functions of NE1 and NE2. Moreover, the following relations hold:

$$\begin{aligned}
\phi_{M,N}^{\hat{\mathfrak{T}},\hat{\mathcal{E}}_p}\left(\boldsymbol{r}_{I,J}^{\hat{\mathfrak{T}},\hat{\mathcal{E}}_k}\right) &= \begin{cases} 1, \text{ if } p=k \text{ and } I=M \text{ and } J=N, \\ 0, \text{ otherwise}, \end{cases} \quad \phi_{M,N}^{\hat{\mathfrak{T}},\hat{\mathcal{E}}_p}\left(\boldsymbol{r}_{I,J}^{\hat{\mathfrak{T}},\hat{\mathcal{F}}_l}\right) = \phi_{M,N}^{\hat{\mathfrak{T}},\hat{\mathcal{E}}_p}\left(\boldsymbol{r}_{I,J}^{\hat{\mathfrak{T}},\hat{\mathfrak{T}}}\right) = 0, \\
\phi_{M,N}^{\hat{\mathfrak{T}},\hat{\mathcal{F}}_q}\left(\boldsymbol{r}_{I,J}^{\hat{\mathfrak{T}},\hat{\mathcal{F}}_l}\right) &= \begin{cases} 1, \text{ if } q=l \text{ and } I=M \text{ and } J=N, \\ 0, \text{ otherwise}, \end{cases} \quad \phi_{M,N}^{\hat{\mathfrak{T}},\hat{\mathcal{F}}_q}\left(\boldsymbol{r}_{I,J}^{\hat{\mathfrak{T}},\hat{\mathcal{E}}_k}\right) = \phi_{M,N}^{\hat{\mathfrak{T}},\hat{\mathcal{F}}_q}\left(\boldsymbol{r}_{I,J}^{\hat{\mathfrak{T}},\hat{\mathfrak{T}}}\right) = 0, \\
\phi_{M,N}^{\hat{\mathfrak{T}},\hat{\mathfrak{T}}}\left(\boldsymbol{r}_{I,J}^{\hat{\mathfrak{T}},\hat{\mathfrak{T}}}\right) &= \begin{cases} 1, \text{ if } I=M \text{ and } J=N, \\ 0, \text{ otherwise}, \end{cases} \quad \phi_{M,N}^{\hat{\mathfrak{T}},\hat{\mathfrak{T}}}\left(\boldsymbol{r}_{I,J}^{\hat{\mathfrak{T}},\hat{\mathcal{E}}_k}\right) = \phi_{M,N}^{\hat{\mathfrak{T}},\hat{\mathfrak{T}}}\left(\boldsymbol{r}_{I,J}^{\hat{\mathfrak{T}},\hat{\mathcal{F}}_l}\right) = 0.
\end{aligned} \tag{4.10}$$

Later in this section, we will provide the explicit expressions of some of the above shape functions that are used in our numerical examples. To interpolate $\boldsymbol{P} \in H^{\mathbf{d}}$, we define the two finite elements given in $(4.5)_3$ respectively based on the Nédélec 1^{st}-kind *face* elements in $\mathbb{R}^3$ (NF1) [55] and the Nédélec 2^{nd}-kind *face* elements in $\mathbb{R}^3$ (NF2) [56]. We define the set of the local degrees of freedom $\Sigma^{\hat{\mathfrak{T}},\mathbf{d}-}$ ($\Sigma^{\hat{\mathfrak{T}},\mathbf{d}}$) by $\left\{\psi_{I,J}^{\hat{\mathfrak{T}},\hat{\mathcal{F}}_l}, \psi_{I,J}^{\hat{\mathfrak{T}},\hat{\mathfrak{T}}}\right\}$, where

$$\begin{aligned}
\psi_{I,J}^{\hat{\mathfrak{T}},\hat{\mathcal{F}}_l}(\boldsymbol{T}) &= \int_{\hat{\mathcal{F}}_l} f_J \langle \overrightarrow{\boldsymbol{T}}_I, \hat{\mathbf{n}}_l \rangle \, d\hat{A}, \quad \forall f_J \text{ that form a basis for } \mathcal{P}_{r-1}(\mathbb{R}^3)\big|_{\hat{\mathcal{F}}_l}\left(\mathcal{P}_r(\mathbb{R}^3)\big|_{\hat{\mathcal{F}}_l}\right), \\
\psi_{I,J}^{\hat{\mathfrak{T}},\hat{\mathfrak{T}}}(\boldsymbol{T}) &= \int_{\hat{\mathfrak{T}}} \langle \overrightarrow{\boldsymbol{T}}_I, \boldsymbol{Z}_J \rangle \, d\hat{V}, \qquad \forall \boldsymbol{Z}_J \text{ that form a basis for } \mathcal{P}_{r-2}(T\mathbb{R}^3)\big|_{\hat{\mathfrak{T}}}\left(\mathcal{P}_{r-1}^-(T\mathbb{R}^3)\big|_{\hat{\mathfrak{T}}}\right).
\end{aligned} \tag{4.11}$$

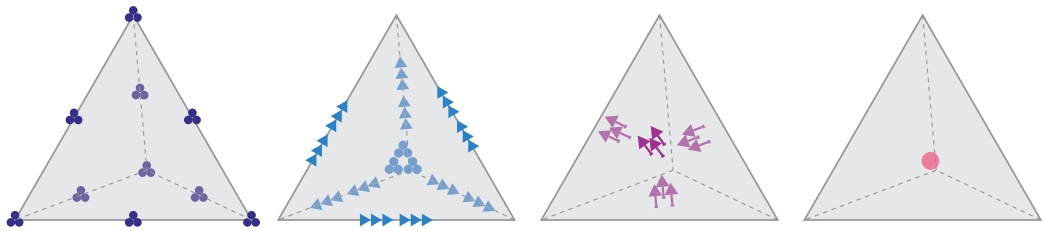

Figure 4.2: The schematic diagrams for the finite elements (4.13). The elements form left to right are for $\boldsymbol{U}$, $\boldsymbol{K}$, $\boldsymbol{P}$, and p. The total number of DOF is 88.

We denote the set of the local shape functions of $(4.5)_3$ by $\left\{\boldsymbol{s}_{I,J}^{\hat{\mathfrak{T}},\hat{\mathfrak{F}}_l}, \boldsymbol{s}_{I,J}^{\hat{\mathfrak{T}},\hat{\mathfrak{T}}}\right\}$. Both $\boldsymbol{s}_{I,J}^{\hat{\mathfrak{T}},\hat{\mathfrak{F}}_l}$ and $\boldsymbol{s}_{I,J}^{\hat{\mathfrak{T}},\hat{\mathfrak{T}}}$ are defined similar to (4.9) but using the vector-valued shape functions of Nédélec face elements, which we denote by $\boldsymbol{u}_J^{\hat{\mathfrak{T}},\hat{\mathfrak{F}}_l}$ and $\boldsymbol{u}_J^{\hat{\mathfrak{T}},\hat{\mathfrak{T}}}$. Also, we have

$$
\begin{aligned}
&\psi_{M,N}^{\hat{\mathfrak{T}},\hat{\mathfrak{F}}_q}\left(\boldsymbol{s}_{I,J}^{\hat{\mathfrak{T}},\hat{\mathfrak{F}}_l}\right) = \begin{cases} 1, & \text{if } q = l \text{ and } I = M \text{ and } J = N, \\ 0, & \text{otherwise,} \end{cases} \qquad \psi_{M,N}^{\hat{\mathfrak{T}},\hat{\mathfrak{F}}_q}\left(\boldsymbol{s}_{I,J}^{\hat{\mathfrak{T}},\hat{\mathfrak{T}}}\right) = 0, \\
&\psi_{M,N}^{\hat{\mathfrak{T}},\hat{\mathfrak{T}}}\left(\boldsymbol{s}_{I,J}^{\hat{\mathfrak{T}},\hat{\mathfrak{T}}}\right) = \begin{cases} 1, & \text{if } I = M \text{ and } J = N, \\ 0, & \text{otherwise,} \end{cases} \qquad \psi_{M,N}^{\hat{\mathfrak{T}},\hat{\mathfrak{T}}}\left(\boldsymbol{s}_{I,J}^{\hat{\mathfrak{T}},\hat{\mathfrak{F}}_l}\right) = 0.
\end{aligned}
\tag{4.12}
$$

For the reference finite element of pressure $(4.5)_4$, we have $\Sigma^{\hat{\mathfrak{T}},\ell} = \{\omega_i^{\hat{\mathfrak{T}}}\}$, where $\omega_i^{\hat{\mathfrak{T}}}(f) = \frac{1}{A}\int_{\hat{\mathfrak{T}}} p_i f \, d\hat{v}$ for all the polynomials p_i that form a basis for $\mathcal{P}_r(\mathbb{R}^3)\big|_{\hat{\mathfrak{T}}}$. Also, the set of local shape functions $\left\{t_i^{\hat{\mathfrak{T}}}\right\}$, which spans $\mathcal{P}_r(\hat{\mathfrak{T}})$, is $\{1\}$ for $r = 0$, $\{1, \xi^1, \xi^2, \xi^3\}$ for $r = 1$, and $\{1, \xi^1, \xi^2, (\xi^1)^2, (\xi^2)^2, (\xi^3)^2, \xi^1\xi^2, \xi^1\xi^3, \xi^2\xi^3\}$ for $r = 2$. Choosing p_i properly, one can show that $\omega_i^{\hat{\mathfrak{T}}}(t_j^{\hat{\mathfrak{T}}}) = \delta_{ij}$.

To extend 2D CSFEMs [43] to 3D, we first followed the same approach we had proposed in [43] and considered $r = 1, 2$ for the finite elements of $\boldsymbol{U}$, $\boldsymbol{K}$, and $\boldsymbol{P}$ and $r = 0, 1, 2$ for the finite elements of p in (4.5). This provides 96 combinations of elements for discretizing the boundary-value problem (2.13). Using the matrix formulation of the linearization of (2.13) for $\alpha = 0$ using the approach discussed in [43, §3.5], we concluded that all 96 choices lead to strictly singular or unstable methods in 3D. We will discuss

this further in the following sections. To overcome this limitation, we modify a suitable combination of elements among the aforementioned unstable 96 choices and propose the following convergent finite elements for $\boldsymbol{U}$, $\boldsymbol{K}$,$\boldsymbol{P}$, and p:

$$\left(\widehat{\mathfrak{T}}, \mathcal{P}_2(T\widehat{\mathfrak{T}}), \Sigma^{\widehat{\mathfrak{T}},1}\right), \left(\widehat{\mathfrak{T}}, \overline{\mathcal{P}}_3(\otimes^2 T\widehat{\mathfrak{T}}), \overline{\Sigma}^{\widehat{\mathfrak{T}},\mathbf{c}}\right), \left(\widehat{\mathfrak{T}}, \mathcal{P}_1^{\ominus}(\otimes^2 T\widehat{\mathfrak{T}}), \Sigma^{\widehat{\mathfrak{T}},\mathbf{d}-}\right), \left(\widehat{\mathfrak{T}}, \mathcal{P}_0(\widehat{\mathfrak{T}}), \Sigma^{\widehat{\mathfrak{T}},\ell}\right), \tag{4.13}$$

where $\overline{\mathcal{P}}_3(\otimes^2 T\widehat{\mathfrak{T}}) := \mathcal{P}_1(\otimes^2 T\widehat{\mathfrak{T}}) \oplus \text{span}\left\{\boldsymbol{r}_{I,J}^{\widehat{\mathfrak{T}},\widehat{\mathfrak{T}}}\right\}_{I,J=1,2,3}$ for $\boldsymbol{r}_{I,J}^{\widehat{\mathfrak{T}},\widehat{\mathfrak{T}}} \in \mathcal{P}_3^-(\otimes^2 T\widehat{\mathfrak{T}})$, and $\overline{\Sigma}^{\widehat{\mathfrak{T}},\mathbf{c}}$ is the union of $\Sigma^{\widehat{\mathfrak{T}},\mathbf{c}}$ for $r = 1$ and $\left\{\phi_{I,J}^{\widehat{\mathfrak{T}},\widehat{\mathfrak{T}}}\right\}_{I,J=1,2,3} \subset \Sigma^{\widehat{\mathfrak{T}},\mathbf{c}-}$ for $r = 3$. The schematic diagram of (4.13) is illustrated in Figure 4.2. Moreover, the shape functions for the finite element of $\boldsymbol{U}$ in (4.13) are given by (4.6) for $r = 2$ and $m = 10$, and the shape function for the finite element of p in (4.13) is simply $t^{\widehat{\mathfrak{T}}} = 1$. We use the results of Arnold *et al.* [59] to provide the explicit expression of the shape functions for the finite elements of $\boldsymbol{K}$ and $\boldsymbol{P}$. The finite element of $\boldsymbol{K}$ in (4.13) has 6 shape functions associated to each edge $\widehat{\mathcal{E}}_k$ of $\widehat{\mathfrak{T}}$ and 9 shape functions associated to the entire $\widehat{\mathfrak{T}}$. Let us ignore the superscript of $l_i^1, i = 1, 2, 3, 4$ in (4.7) and consider $\nabla l_i = \begin{bmatrix} \partial l_i/\partial\xi^1 & \partial l_i/\partial\xi^2 & \partial l_i/\partial\xi^3 \end{bmatrix}$ as a row vector. Then, for an edge $\widehat{\mathcal{E}}_k$ joining two vertices i and j as shown in Figure 4.1, the 6 shape functions $\boldsymbol{r}_{I,2}^{\widehat{\mathfrak{T}},\widehat{\mathcal{E}}_k}, \boldsymbol{r}_{I,3}^{\widehat{\mathfrak{T}},\widehat{\mathcal{E}}_k}, I = 1, 2, 3$ are obtained using (4.9) and the following vector-valued shape functions for NE2 of order 1 [59]:

$$\boldsymbol{v}_1^{\widehat{\mathfrak{T}},\widehat{\mathcal{E}}_k} = l_i \nabla l_j, \quad \boldsymbol{v}_2^{\widehat{\mathfrak{T}},\widehat{\mathcal{E}}_k} = l_j \nabla l_i.$$

The 9 remaining shape functions $\boldsymbol{r}_{I,1}^{\widehat{\mathfrak{T}},\widehat{\mathfrak{T}}}, \boldsymbol{r}_{I,2}^{\widehat{\mathfrak{T}},\widehat{\mathfrak{T}}}, \boldsymbol{r}_{I,3}^{\widehat{\mathfrak{T}},\widehat{\mathfrak{T}}}, I = 1, 2, 3$ are obtained similar to (4.9) and using the following vector-valued shape functions for NE1 of order 3 [59]:

$$\boldsymbol{v}_1^{\widehat{\mathfrak{T}},\widehat{\mathfrak{T}}} = l_3 l_4 \boldsymbol{w}_{12}, \quad \boldsymbol{v}_2^{\widehat{\mathfrak{T}},\widehat{\mathfrak{T}}} = l_2 l_4 \boldsymbol{w}_{13}, \quad \boldsymbol{v}_3^{\widehat{\mathfrak{T}},\widehat{\mathfrak{T}}} = l_2 l_3 \boldsymbol{w}_{14},$$

where $\boldsymbol{w}_{ij} = l_i \nabla l_j - l_j \nabla l_i$. The finite element of $\boldsymbol{P}$ in (4.13) has 3 shape functions $\boldsymbol{s}_I^{\widehat{\mathfrak{T}},\widehat{\mathfrak{F}}_l}, I = 1, 2, 3$ associated to each face $\widehat{\mathfrak{F}}_l$ of $\widehat{\mathfrak{T}}$ that contains the three vertices i, j, and k

according to Figure 4.1. These shape functions are obtained similar to (4.9) and using the following vector-valued shape function for NF1 of order 1[59]:

$$\boldsymbol{u}^{\hat{\mathcal{T}},\hat{\mathcal{F}}_l} = l_i \nabla l_j \times \nabla l_k - l_j \nabla l_i \times \nabla l_k + l_k \nabla l_i \times \nabla l_j.$$

Next we explain how to calculate the shape functions in an arbitrary element in a mesh using the shape functions of the reference finite elements. Let $\mathcal{B}_h$ be a triangulation of the reference configuration $\mathcal{B}$ consisting of arbitrary tetrahedra $\mathcal{T}$ such that the intersection of any two distinct tetrahedra is either empty or a common face/edge/vertex of each. The discretization parameter h is defined as $h := \max \operatorname{diam} \mathcal{T},\ \forall \mathcal{T} \in \mathcal{B}_h$. We define a local ordering for vertices of each $\mathcal{T} \in \mathcal{B}_h$ by assigning the numbers $1, 2, 3, 4$ to them. We then denote the Cartesian coordinates of the i-th vertex of $\mathcal{T}$ by a column vector $\mathbf{X}_i^{\mathcal{T}} = \begin{bmatrix} \mathsf{X}_i^{1,\mathcal{T}} & \mathsf{X}_i^{2,\mathcal{T}} & \mathsf{X}_i^{3,\mathcal{T}} \end{bmatrix}^{\mathsf{T}}$ and define the following affine transformation:

$$\mathbf{T}_{\mathcal{T}} : \hat{\mathcal{T}} \longrightarrow \mathcal{T}, \quad \mathbf{T}_{\mathcal{T}}(\boldsymbol{\xi}) := \mathbf{J}_{\mathcal{T}} \boldsymbol{\xi} + \mathbf{X}_1^{\mathcal{T}}, \tag{4.14}$$

where $\mathbf{J}_{\mathcal{T}} = \begin{bmatrix} \mathbf{X}_2^{\mathcal{T}} - \mathbf{X}_1^{\mathcal{T}} & \mathbf{X}_3^{\mathcal{T}} - \mathbf{X}_1^{\mathcal{T}} & \mathbf{X}_4^{\mathcal{T}} - \mathbf{X}_1^{\mathcal{T}} \end{bmatrix}_{3\times 3}$. Note that $\mathbf{T}_{\mathcal{T}}$ is bijective and $\mathbf{J}_{\mathcal{T}}$ is invertible. Consider an element $\mathcal{T} \in \mathcal{B}_h$, we denote its edges by $\mathcal{E}_i^{\mathcal{T}} = \mathbf{T}_{\mathcal{T}}(\hat{\mathcal{E}}_i)$, $i = 1, 2, \ldots, 6$, and its faces by $\mathcal{F}_i^{\mathcal{T}} = \mathbf{T}_{\mathcal{T}}(\hat{\mathcal{F}}_i)$, $i = 1, 2, 3, 4$. We assume that $\mathcal{E}_i^{\mathcal{T}}$ inherits the orientation of its reference counterpart $\hat{\mathcal{E}}_i$. Moreover, the tangent vector $\mathbf{t}_i$ defined on $\mathcal{E}_i^{\mathcal{T}}$ inherits the orientation of $\mathcal{E}_i^{\mathcal{T}}$, and the normal vector on $\mathcal{F}_l^{\mathcal{T}}$ containing three edges $\mathcal{E}_i^{\mathcal{T}}$, $\mathcal{E}_j^{\mathcal{T}}$, and $\mathcal{E}_k^{\mathcal{T}}$ such that $i < j < k$ is defined as $\mathbf{n}_l = \mathbf{t}_i \times \mathbf{t}_j$. One can show that $\mathbf{t}_i = \mathbf{J}_{\mathcal{T}} \hat{\mathbf{t}}_i$ and $\mathbf{n}_i = \det \mathbf{J}_{\mathcal{T}} \mathbf{J}_{\mathcal{T}}^{-\mathsf{T}} \hat{\mathbf{n}}_i$. For efficient assembly of the finite elements of $\boldsymbol{K} \in H^{\mathbf{c}}$ and $\boldsymbol{P} \in H^{\mathbf{d}}$, we use the numbering scheme discussed in [62]. Using this scheme, one first assumes that every vertex in a mesh $\mathcal{B}_h$ has a distinct global number and then the local ordering of four vertices of every tetrahedron in that mesh $\mathcal{T} \in \mathcal{B}_h$ agree with the *ascending* order of the global numbers of its four vertices. Therefore, considering the edge orientations of the reference element shown in Figure 4.1, the orientation of every edge in the mesh is from a

vertex with a smaller global number to a vertex with a larger global number. The advantage of this scheme is that the orientation of a common edge between some elements in a mesh is uniquely defined and is identical to that of the edge in any of those elements. It follows that some elements in a mesh sharing a common edge have an identical tangent vector on that edge, and any two elements with a common face have an identical normal vector on that face. For an illustration of this, see [62, Figue 5.2]. Note that using this scheme, the normal vectors of all the exterior faces of the mesh are *not* pointed outward, and $o_{\mathcal{T}} = \operatorname{sign}(\det \mathbf{J}_{\mathcal{T}})$ can be either 1 or -1.

Consider the following mappings:

$$
\begin{aligned}
&\mathbf{T}^{1}_{\mathcal{T}} : C^0(T\widehat{\mathcal{T}}) \longrightarrow C^0(T\mathcal{T}), \quad \mathbf{T}^{1}_{\mathcal{T}}(\widehat{\boldsymbol{V}}) := \widehat{\boldsymbol{V}} \circ \mathbf{T}^{-1}_{\mathcal{T}},\\
&\mathbf{T}^{\mathbf{c}}_{\mathcal{T}} : H^{\mathbf{c}}(T\widehat{\mathcal{T}}) \longrightarrow H^{\mathbf{c}}(T\mathcal{T}), \quad \mathbf{T}^{\mathbf{c}}_{\mathcal{T}}(\widehat{\boldsymbol{V}}) := \mathbf{J}^{-\mathsf{T}}_{\mathcal{T}}\widehat{\boldsymbol{V}} \circ \mathbf{T}^{-1}_{\mathcal{T}},\\
&\mathbf{T}^{\mathbf{d}}_{\mathcal{T}} : H^{\mathbf{d}}(T\widehat{\mathcal{T}}) \longrightarrow H^{\mathbf{d}}(T\mathcal{T}), \quad \mathbf{T}^{\mathbf{d}}_{\mathcal{T}}(\widehat{\boldsymbol{V}}) := \frac{1}{\det \mathbf{J}_{\mathcal{T}}}\mathbf{J}_{\mathcal{T}}\widehat{\boldsymbol{V}} \circ \mathbf{T}^{-1}_{\mathcal{T}},\\
&\mathbf{T}^{\ell}_{\mathcal{T}} : L^2(\widehat{\mathcal{T}}) \longrightarrow L^2(\mathcal{T}), \quad \mathbf{T}^{\ell}_{\mathcal{T}}(\hat{f}) := \hat{f} \circ \mathbf{T}^{-1}_{\mathcal{T}},
\end{aligned}
\tag{4.15}
$$

where $\mathbf{T}^{\mathbf{c}}_{\mathcal{T}}$ and $\mathbf{T}^{\mathbf{d}}_{\mathcal{T}}$ are known as the Piola transforms. For a $\binom{2}{0}$-tensor $\boldsymbol{T}$, we calculates the Piola transforms separately for each row:

$$
\mathbf{T}^{\mathbf{c}}_{\mathcal{T}}(\boldsymbol{T}) := \begin{bmatrix} \mathbf{T}^{\mathbf{c}}_{\mathcal{T}}(\overrightarrow{\boldsymbol{T}_1})^{\mathsf{T}} \\ \mathbf{T}^{\mathbf{c}}_{\mathcal{T}}(\overrightarrow{\boldsymbol{T}_2})^{\mathsf{T}} \\ \mathbf{T}^{\mathbf{c}}_{\mathcal{T}}(\overrightarrow{\boldsymbol{T}_3})^{\mathsf{T}} \end{bmatrix},
$$

and $\mathbf{T}^{\mathbf{d}}_{\mathcal{T}}(\boldsymbol{T})$ is calculated similarly. Using [43, Proposition 8], (4.15), and the local shape functions in the reference element $\widehat{\mathcal{T}}$, we can obtain the local shape functions in any element $\mathcal{T} \in \mathcal{B}_h$ enabling us to locally interpolate the four field variables $(\boldsymbol{U}, \boldsymbol{K}, \boldsymbol{P}, p)$ over that element. In particular, the local shape functions for $\boldsymbol{U}$ are obtained by $\boldsymbol{h}^{\mathcal{T}}_k = \mathbf{T}^{1}_{\mathcal{T}}\left(\boldsymbol{h}^{\hat{\mathcal{T}}}_k\right)$; the local shape functions for $\boldsymbol{K}$ are $\boldsymbol{r}^{\mathcal{T},\mathcal{E}_k}_{I,J} = \mathbf{T}^{\mathbf{c}}_{\mathcal{T}}\left(\boldsymbol{r}^{\hat{\mathcal{T}},\hat{\mathcal{E}}_k}_{I,J}\right)$, $\boldsymbol{r}^{\mathcal{T},\mathcal{F}_l}_{I,J} = \mathbf{T}^{\mathbf{c}}_{\mathcal{T}}\left(\boldsymbol{r}^{\hat{\mathcal{T}},\hat{\mathcal{F}}_l}_{I,J}\right)$, and $\boldsymbol{r}^{\mathcal{T},\mathcal{T}}_{I,J} = \mathbf{T}^{\mathbf{c}}_{\mathcal{T}}\left(\boldsymbol{r}^{\hat{\mathcal{T}},\hat{\mathcal{T}}}_{I,J}\right)$; the local shape functions for $\boldsymbol{P}$ are $\boldsymbol{s}^{\mathcal{T},\mathcal{F}_l}_{I,J} = \mathbf{T}^{\mathbf{d}}_{\mathcal{T}}\left(\boldsymbol{s}^{\hat{\mathcal{T}},\hat{\mathcal{F}}_l}_{I,J}\right)$ and $\boldsymbol{s}^{\mathcal{T},\mathcal{T}}_{I,J} = \mathbf{T}^{\mathbf{d}}_{\mathcal{T}}\left(\boldsymbol{s}^{\hat{\mathcal{T}},\hat{\mathcal{T}}}_{I,J}\right)$;

and $t_i^{\mathcal{T}} = \mathbf{T}_{\mathcal{T}}^{\ell}\left(t_i^{\hat{\mathcal{T}}}\right)$ gives the local shape functions for p. Using [43, Proposition 8] and (4.15), one can also obtain the local degrees of freedom for the finite elements of any element $\mathcal{T} \in \mathcal{B}_h$. For example, considering (4.11), $\psi_{I,J}^{\mathcal{T},\mathcal{F}_l}(\boldsymbol{T}) = \left(\psi_{I,J}^{\hat{\mathcal{T}},\hat{\mathcal{F}}_l} \circ \mathbf{T}_{\mathcal{T}}^{\mathbf{d}^{-1}}\right)(\boldsymbol{T})$ and $\psi_{I,J}^{\mathcal{T},\mathcal{T}}(\boldsymbol{T}) = \left(\psi_{I,J}^{\hat{\mathcal{T}},\hat{\mathcal{T}}} \circ \mathbf{T}_{\mathcal{T}}^{\mathbf{d}^{-1}}\right)(\boldsymbol{T})$ are the degrees of freedom for the finite element of $\mathcal{T}$ that we use for $\boldsymbol{P}$. The other degrees of freedom can be written similarly using their reference counterparts. In this work, the traction boundary conditions are imposed weakly through (2.14); one does not need to impose them directly by calculating the related degrees of freedom on the boundary of the mesh. Thus, in practice, all degrees of freedom, even those on the boundary of the mesh, are obtained by solving the final discrete system; calculating their explicit expressions are not required.

4.3 Finite Element Spaces

Next, we introduce some conforming finite element spaces to discretize (2.13) and (2.19). Let $\mathcal{F}_h^i$ be the set of all *interior* faces of a 3D mesh $\mathcal{B}_h$. Given a face $\mathcal{F} \in \mathcal{F}_h^i$, there are two elements $\mathcal{T}, \mathcal{T}' \in \mathcal{B}_h$ such that $\mathcal{F} = \mathcal{T} \cap \mathcal{T}'$. Suppose $\boldsymbol{V}$ is a vector-valued function and $\boldsymbol{T}$ is a tensor-valued function both defined on $\mathcal{B}_h$ with limits on both sides of $\forall \mathcal{F} \in \mathcal{F}_h^i$. We define the following notions of jump across a face $\mathcal{F} \in \mathcal{F}_h^i$:

$$[\![\boldsymbol{V}]\!]_{\mathcal{F}} := \boldsymbol{V}_{\mathcal{T}'} - \boldsymbol{V}_{\mathcal{T}}, \quad [\![\mathsf{t}\boldsymbol{T}]\!]_{\mathcal{F}} := (\boldsymbol{T}_{\mathcal{T}'} - \boldsymbol{T}_{\mathcal{T}})\,\mathbf{t}, \quad [\![\mathsf{n}\boldsymbol{T}]\!]_{\mathcal{F}} := (\boldsymbol{T}_{\mathcal{T}'} - \boldsymbol{T}_{\mathcal{T}})\,\mathbf{n}, \tag{4.16}$$

where $\boldsymbol{V}_{\mathcal{T}} := \boldsymbol{V}|_{\mathcal{T}}$ and $\boldsymbol{T}_{\mathcal{T}} := \boldsymbol{T}|_{\mathcal{T}}$ and $\boldsymbol{V}_{\mathcal{T}'}$ and $\boldsymbol{T}_{\mathcal{T}'}$ are defined similarly. $\mathbf{t}$ ($\mathbf{n}$) is a unit vector tangent (normal) to $\mathcal{F}$. We write $[\![\mathsf{t}\boldsymbol{T}]\!]_{\mathcal{F}} = \mathbf{0}$ ($[\![\mathsf{n}\boldsymbol{T}]\!]_{\mathcal{F}} = \mathbf{0}$), if the jump is zero for any unit vector $\mathbf{t}$ ($\mathbf{n}$) on $\mathcal{F}$. Note that all the above jumps are vector-valued functions in 3D.

Consider the following finite element spaces:

$$
\begin{aligned}
V_{h,r}^{1} &:= \left\{ \boldsymbol{V}_h \in L^2(T\mathcal{B}_h) : \forall \mathcal{T} \in \mathcal{B}_h,\ \boldsymbol{V}_h|_{\mathcal{T}} \in \mathcal{P}_r(T\mathcal{T}),\ \forall \mathcal{F} \in \mathcal{F}_h^i,\ [\![\boldsymbol{V}_h]\!]_{\mathcal{F}} = \boldsymbol{0} \right\}, \\
V_{h,r}^{\mathbf{c}-} &:= \left\{ \boldsymbol{T}_h \in L^2(\otimes^2 T\mathcal{B}_h) : \forall \mathcal{T} \in \mathcal{B}_h,\ \boldsymbol{T}_h|_{\mathcal{T}} \in \mathcal{P}_r^-(\otimes^2 T\mathcal{T}),\ \forall \mathcal{F} \in \mathcal{F}_h^i,\ [\![\mathsf{t}\boldsymbol{T}_h]\!]_{\mathcal{F}} = \boldsymbol{0} \right\}, \\
V_{h,r}^{\mathbf{c}} &:= \left\{ \boldsymbol{T}_h \in L^2(\otimes^2 T\mathcal{B}_h) : \forall \mathcal{T} \in \mathcal{B}_h,\ \boldsymbol{T}_h|_{\mathcal{T}} \in \mathcal{P}_r(\otimes^2 T\mathcal{T}),\ \forall \mathcal{F} \in \mathcal{F}_h^i,\ [\![\mathsf{t}\boldsymbol{T}_h]\!]_{\mathcal{F}} = \boldsymbol{0} \right\}, \\
V_{h,r}^{\mathbf{d}-} &:= \left\{ \boldsymbol{T}_h \in L^2(\otimes^2 T\mathcal{B}_h) : \forall \mathcal{T} \in \mathcal{B}_h,\ \boldsymbol{T}_h|_{\mathcal{T}} \in \mathcal{P}_r^{\ominus}(\otimes^2 T\mathcal{T}),\ \forall \mathcal{F} \in \mathcal{F}_h^i,\ [\![\mathsf{n}\boldsymbol{T}_h]\!]_{\mathcal{F}} = \boldsymbol{0} \right\}, \\
V_{h,r}^{\mathbf{d}} &:= \left\{ \boldsymbol{T}_h \in L^2(\otimes^2 T\mathcal{B}_h) : \forall \mathcal{T} \in \mathcal{B}_h,\ \boldsymbol{T}_h|_{\mathcal{T}} \in \mathcal{P}_r(\otimes^2 T\mathcal{T}),\ \forall \mathcal{F} \in \mathcal{F}_h^i,\ [\![\mathsf{n}\boldsymbol{T}_h]\!]_{\mathcal{F}} = \boldsymbol{0} \right\}, \\
V_{h,r}^{\ell} &:= \left\{ f_h \in L^2(\mathcal{B}_h) : \forall \mathcal{T} \in \mathcal{B}_h,\ f_h|_{\mathcal{T}} \in \mathcal{P}_r(\mathcal{T}) \right\}.
\end{aligned}
$$

Note that the above sapces are conforming, i.e., $V_{h,r}^{1} \subset H^1(T\mathcal{B}_h)$, $V_{h,r}^{\mathbf{c}-} \subset V_{h,r}^{\mathbf{c}} \subset H^{\mathbf{c}}(\mathcal{B}_h)$, $V_{h,r}^{\mathbf{d}-} \subset V_{h,r}^{\mathbf{d}} \subset H^{\mathbf{d}}(\mathcal{B}_h)$, and $V_{h,r}^{\ell} \subset L^2(\mathcal{B}_h)$. Recalling the definition of $\overline{\mathcal{P}}_3(\otimes^2 T\mathcal{T})$ in (4.13), we define

$$
\overline{V}_{h,3}^{\mathbf{c}} := V_{h,1}^{\mathbf{c}} \oplus \left\{ \boldsymbol{T}_h \in L^2(\otimes^2 T\mathcal{B}_h) : \forall \mathcal{T} \in \mathcal{B}_h,\ \boldsymbol{T}_h|_{\mathcal{T}} \in \text{span} \left\{ \boldsymbol{r}_{I,J}^{\mathcal{T},\mathcal{T}} \right\}_{I,J=1,2,3} \subset \mathcal{P}_3^-(\otimes^2 T\mathcal{T}) \right\}. \tag{4.17}
$$

Note that $\left(\boldsymbol{r}_{I,J}^{\mathcal{T},\mathcal{T}}\mathbf{t}\right)\big|_{\mathcal{F}} = \boldsymbol{0}$ for $I, J = 1, 2, 3$ and for every $\mathcal{F}$ in the mesh and $\overline{V}_{h,3}^{\mathbf{c}} \subset H^{\mathbf{c}}(\mathcal{B}_h)$.

4.4 Compatible-Strain Mixed Finite Element Methods

Here, we write the following mixed finite element method for the boundary-value problem of *incompressible* nonlinear elastostatics (2.13) based on the reference elements (4.13) and the corresponding approximation spaces ($V_{h,2}^{1}$, $\overline{V}_{h,3}^{\mathbf{c}}$, $V_{h,1}^{\mathbf{d}-}$, $V_{h,0}^{\ell}$) defined in the previous section:

Given a body force $\boldsymbol{B}$ of L^2-class, a boundary displacement $\overline{\boldsymbol{U}}$ on Γ_d of $H^{1/2}$-class, a boundary traction $\overline{\boldsymbol{T}}$ on Γ_t of L^2-class, and a stability constant $\alpha \geqslant 0$, find $(\boldsymbol{U}_h, \boldsymbol{K}_h, \boldsymbol{P}_h, p_h) \in V^1_{h,2}(\Gamma_d, \overline{\boldsymbol{U}}) \times \overline{V}^{\mathbf{c}}_{h,3} \times V^{\mathbf{d}-}_{h,1} \times V^{\ell}_{h,0}$ such that

$$
\begin{aligned}
&\langle\!\langle \boldsymbol{P}_h, \mathbf{grad}\, \boldsymbol{\Upsilon}_h \rangle\!\rangle + \alpha s_{h_1}(\boldsymbol{U}_h, \boldsymbol{K}_h, \boldsymbol{\Upsilon}_h) = f_h(\boldsymbol{\Upsilon}_h), && \forall \boldsymbol{\Upsilon}_h \in V^1_{h,2}(\Gamma_d),\\
&\langle\!\langle \widetilde{\boldsymbol{P}}(\boldsymbol{K}_h), \boldsymbol{\kappa}_h \rangle\!\rangle - \langle\!\langle \boldsymbol{P}_h, \boldsymbol{\kappa}_h \rangle\!\rangle + \langle\!\langle p_h \boldsymbol{Q}(\boldsymbol{K}_h), \boldsymbol{\kappa}_h \rangle\!\rangle + \alpha s_{h_2}(\boldsymbol{U}_h, \boldsymbol{K}_h, \boldsymbol{\kappa}_h) = 0, && \forall \boldsymbol{\kappa}_h \in \overline{V}^{\mathbf{c}}_{h,3},\\
&\langle\!\langle \mathbf{grad}\, \boldsymbol{U}_h, \boldsymbol{\pi}_h \rangle\!\rangle - \langle\!\langle \boldsymbol{K}_h, \boldsymbol{\pi}_h \rangle\!\rangle = 0, && \forall \boldsymbol{\pi}_h \in V^{\mathbf{d}-}_{h,1},\\
&\langle\!\langle C(J_h), q_h \rangle\!\rangle = 0, && \forall q_h \in V^{\ell}_{h,0},
\end{aligned}
\tag{4.18}
$$

where

$$
f_h(\boldsymbol{\Upsilon}_h) = \langle\!\langle \rho_0 \boldsymbol{B}, \boldsymbol{\Upsilon}_h \rangle\!\rangle + \int_{\Gamma_t} \langle \overline{\boldsymbol{T}}, \boldsymbol{\Upsilon}_h \rangle \, dA
$$

and

$$
\begin{aligned}
s_{h_1}(\boldsymbol{U}_h, \boldsymbol{K}_h, \boldsymbol{\Upsilon}_h) &= \langle\!\langle \mathbf{grad}\, \boldsymbol{U}_h, \mathbf{grad}\, \boldsymbol{\Upsilon}_h \rangle\!\rangle - \langle\!\langle \boldsymbol{K}_h, \mathbf{grad}\, \boldsymbol{\Upsilon}_h \rangle\!\rangle,\\
s_{h_2}(\boldsymbol{U}_h, \boldsymbol{K}_h, \boldsymbol{\kappa}_h) &= \langle\!\langle \boldsymbol{K}_h, \boldsymbol{\kappa}_h \rangle\!\rangle - \langle\!\langle \mathbf{grad}\, \boldsymbol{U}_h, \boldsymbol{\kappa}_h \rangle\!\rangle.
\end{aligned}
$$

Similarly, one can define the following mixed finite element method for the boundary-value problem of *compressible* nonlinear elastostatics (2.19):

Given $(\boldsymbol{B}, \overline{\boldsymbol{U}}, \boldsymbol{T})$ and $\alpha \geqslant 0$, find $(\boldsymbol{U}_h, \boldsymbol{K}_h, \boldsymbol{P}_h) \in V^1_{h,2}(\Gamma_d, \overline{\boldsymbol{U}}) \times \overline{V}^{\mathbf{c}}_{h,3} \times V^{\mathbf{d}-}_{h,1}$ such that

$$
\begin{aligned}
\langle\!\langle \boldsymbol{P}_h, \mathbf{grad}\, \boldsymbol{\Upsilon}_h \rangle\!\rangle + \alpha s_{h_1}(\boldsymbol{U}_h, \boldsymbol{K}_h, \boldsymbol{\Upsilon}_h) &= f_h(\boldsymbol{\Upsilon}_h), && \forall \boldsymbol{\Upsilon}_h \in V^1_{h,2}(\Gamma_d),\\
\langle\!\langle \widehat{\boldsymbol{P}}(\boldsymbol{K}_h), \boldsymbol{\kappa}_h \rangle\!\rangle - \langle\!\langle \boldsymbol{P}_h, \boldsymbol{\kappa}_h \rangle\!\rangle + \alpha s_{h_2}(\boldsymbol{U}_h, \boldsymbol{K}_h, \boldsymbol{\kappa}_h) &= 0, && \forall \boldsymbol{\kappa}_h \in \overline{V}^{\mathbf{c}}_{h,3},\\
\langle\!\langle \mathbf{grad}\, \boldsymbol{U}_h, \boldsymbol{\pi}_h \rangle\!\rangle - \langle\!\langle \boldsymbol{K}_h, \boldsymbol{\pi}_h \rangle\!\rangle &= 0, && \forall \boldsymbol{\pi}_h \in V^{\mathbf{d}-}_{h,1}.
\end{aligned}
\tag{4.19}
$$

Remark 22 (Compatibility of Strain and Continuity of Traction)**.**

(i) Recalling (4.16) and considering a displacement gradient field $\boldsymbol{K}_h$ on a 3D mesh $\mathcal{B}_h$, the Hadamard jump condition is defined as the zero jump $[\![\mathrm{t}\boldsymbol{K}_h]\!]_{\mathcal{F}} = \mathbf{0}$ for any

tangent vector on $\mathcal{F}$ and the three edges enclosing $\mathcal{F}$. A necessary condition for the existence of $\boldsymbol{U}_h \in H^1(T\mathcal{B}_h)$ such that $\boldsymbol{K}_h = \mathbf{grad}\,\boldsymbol{U}_h$ is that the Hadamard jump condition holds $\forall \mathcal{F} \in \mathcal{F}_h^i$ [63]. By construction, the mixed finite element methods (4.18) and (4.19) satisfy this necessary condition as $\boldsymbol{K}_h \in \overline{V}_{h,3}^{\mathbf{c}} \subset H^{\mathbf{c}}(\mathcal{B}_h)$.

(ii) Let $\boldsymbol{P}_h$ be a stress field on a 3D mesh $\mathcal{B}_h$. The localization of the balance of linear momentum requires that $[\![\mathsf{n}\boldsymbol{P}_h]\!]_{\mathcal{F}} = \mathbf{0}$, $\forall \mathcal{F} \in \mathcal{F}_h^i$, that is, the traction vector associated with $\boldsymbol{P}_h$ is continuous across all the internal faces of $\mathcal{B}_h$. By construction, (4.18) and (4.19) satisfy this requirement as $\boldsymbol{P}_h \in V_{h,1}^{\mathbf{d}-} \subset H^{\mathbf{d}}(\mathcal{B}_h)$.

4.5 Matrix Formulation

The procedure of obtaining the matrix formulation of (4.18) or (4.19) is similar to that of 2D CSFEMs, which we discussed in detail in [43, §3.4]. Hence, in this section, we only write the final formulations needed for the implementation and studying the stability of the 3D CSFEMs. One can write (4.18) in the following matrix form

$$\mathbb{K}_h \mathbb{Q}_h + \mathbb{N}_h(\mathbb{Q}_h) = \mathbb{F}_h, \tag{4.20}$$

where

$$\mathbb{K}_h = \begin{bmatrix} \alpha \mathbf{M}_h^{\mathbf{11}} & \alpha \mathbf{M}_h^{\mathbf{1c}} & \mathbf{K}_h^{\mathbf{1d}} & \mathbf{0} \\ \alpha \mathbf{M}_h^{\mathbf{1c}} & \alpha \mathbf{M}_h^{\mathbf{cc}} & \mathbf{K}_h^{\mathbf{cd}} & \mathbf{0} \\ \mathbf{K}_h^{\mathbf{d1}} & \mathbf{K}_h^{\mathbf{dc}} & \mathbf{0} & \mathbf{0} \\ \mathbf{0} & \mathbf{0} & \mathbf{0} & \mathbf{0} \end{bmatrix} \quad \mathbb{Q}_h = \begin{bmatrix} \mathbf{q}_h^{\mathbf{1}} \\ \mathbf{q}_h^{\mathbf{c}} \\ \mathbf{q}_h^{\mathbf{d}} \\ \mathbf{q}_h^{\ell} \end{bmatrix},$$

$$\mathbb{N}_h(\mathbb{Q}_h) = \begin{bmatrix} \mathbf{0} \\ \mathbf{N}_h^{\mathbf{c}}(\mathbf{q}_h^{\mathbf{c}}, \mathbf{q}_h^{\ell}) \\ \mathbf{0} \\ \mathbf{N}_h^{\ell}(\mathbf{q}_h^{\mathbf{c}}) \end{bmatrix}, \quad \mathbb{F}_h = \begin{bmatrix} \mathbf{F}_h^{\mathbf{1}} + \mathbf{F}_{\Gamma_t}^{\mathbf{1}} \\ \mathbf{0} \\ \mathbf{0} \\ \mathbf{0} \end{bmatrix}.$$

The column vectors $\mathbf{q}_h^{\mathbf{l}}$, $\mathbf{q}_h^{\mathbf{c}}$, $\mathbf{q}_h^{\mathbf{d}}$, $\mathbf{q}_h^{\ell}$ contain all the unknown global degrees of freedom for $\boldsymbol{U}$, $\boldsymbol{K}$, $\boldsymbol{P}$, and p, respectively. Let n be the total number of nodes in $\mathcal{B}_h$ except those lying on the displacement boundary Γ_d, and let $n_{\mathcal{E}}$, $n_{\mathcal{F}}$, and $n_{\mathcal{T}}$ be the total number of edges, faces, and elements in $\mathcal{B}_h$, respectively. The number of degrees of freedom in $\mathbf{q}_h^{\mathbf{l}}$, $\mathbf{q}_h^{\mathbf{c}}$, $\mathbf{q}_h^{\mathbf{d}}$, and $\mathbf{q}_h^{\ell}$ is $3n$, $6n_{\mathcal{E}} + 9n_{\mathcal{T}}$, $3n_{\mathcal{F}}$, and $n_{\mathcal{T}}$, respectively, see Figure 4.2. The total number of degrees of freedom is $N = 3n + 6n_{\mathcal{E}} + 3n_{\mathcal{F}} + 10n_{\mathcal{T}}$. The size of $\mathbb{K}_h$ is $N \times N$, and the size of $\mathbb{Q}_h$, $\mathbb{N}_h$, and $\mathbb{F}_h$ is $N \times 1$. Let us define $\boldsymbol{V}_{\mathcal{T}} := \boldsymbol{V}_h|_{\mathcal{T}}$ and $\boldsymbol{T}_{\mathcal{T}} := \boldsymbol{T}_h|_{\mathcal{T}}$ for any discrete vector field $\boldsymbol{V}_h$ and any discrete tensor field $\boldsymbol{T}_h$. The global *sparse* matrices $\mathbf{M}_h^{\mathbf{ll}}$, $\mathbf{M}_h^{\mathbf{lc}}$, $\mathbf{M}_h^{\mathbf{cc}}$, $\mathbf{K}_h^{\mathbf{ld}}$, and $\mathbf{K}_h^{\mathbf{cd}}$ in $\mathbb{K}_h$ are respectively the result of assembling a set of $n_{\mathcal{T}}$ local matrices that are obtained from calculating $\langle\!\langle \mathbf{grad}\, \boldsymbol{U}_{\mathcal{T}}, \mathbf{grad}\, \boldsymbol{\Upsilon}_{\mathcal{T}} \rangle\!\rangle$, $-\langle\!\langle \boldsymbol{K}_{\mathcal{T}}, \mathbf{grad}\, \boldsymbol{\Upsilon}_{\mathcal{T}} \rangle\!\rangle$, $\langle\!\langle \boldsymbol{K}_{\mathcal{T}}, \boldsymbol{\kappa}_{\mathcal{T}} \rangle\!\rangle$, $\langle\!\langle \boldsymbol{P}_{\mathcal{T}}, \mathbf{grad}\, \boldsymbol{\Upsilon}_{\mathcal{T}} \rangle\!\rangle$, and $-\langle\!\langle \boldsymbol{P}_{\mathcal{T}}, \boldsymbol{\kappa}_{\mathcal{T}} \rangle\!\rangle$ $\forall \mathcal{T} \in \mathcal{B}_h$. Moreover, $\mathbb{K}_h$ is a symmetric matrix and $\mathbf{M}_h^{\mathbf{cl}} = (\mathbf{M}_h^{\mathbf{lc}})^{\mathsf{T}}$, $\mathbf{K}_h^{\mathbf{dl}} = (\mathbf{K}_h^{\mathbf{ld}})^{\mathsf{T}}$, and $\mathbf{K}_h^{\mathbf{dc}} = (\mathbf{K}_h^{\mathbf{cd}})^{\mathsf{T}}$. For given $\mathbf{q}_h^{\mathbf{c}}$ and $\mathbf{q}_h^{\ell}$, one obtains the global vectors $\mathbf{N}_h^{\mathbf{c}}(\mathbf{q}_h^{\mathbf{c}}, \mathbf{q}_h^{\ell})$ and $\mathbf{N}_h^{\ell}(\mathbf{q}_h^{\mathbf{c}})$ in $\mathbb{N}_h$ by assembling a set of $n_{\mathcal{T}}$ local vectors that are obtained form calculating the nonlinear term $\langle\!\langle \widetilde{\boldsymbol{P}}(\boldsymbol{K}_{\mathcal{T}}) + p_{\mathcal{T}} \boldsymbol{Q}(\boldsymbol{K}_{\mathcal{T}}), \boldsymbol{\kappa}_{\mathcal{T}} \rangle\!\rangle$ and $\langle\!\langle C(J_{\mathcal{T}}), q_{\mathcal{T}} \rangle\!\rangle$ $\forall \mathcal{T} \in \mathcal{B}_h$, respectively. Similarly, for a given body force $\boldsymbol{B}$, one obtains $\mathbf{F}_h^{\mathbf{l}}$ in $\mathbb{F}_h$ by calculating $\langle\!\langle \rho_0 \boldsymbol{B}, \boldsymbol{\Upsilon}_{\mathcal{T}} \rangle\!\rangle$ $\forall \mathcal{T} \in \mathcal{B}_h$. Finally, for a given traction $\overline{\boldsymbol{T}}$ on Γ_t, one obtains $\mathbf{F}_{\Gamma_t}^{\mathbf{l}}$ in $\mathbb{F}_h$ through assembling all the local vectors obtained from $\int_{\mathcal{F}_t^{\mathcal{T}}} \langle \overline{\boldsymbol{T}}, \boldsymbol{\Upsilon}|_{\mathcal{F}_t^{\mathcal{T}}} \rangle \, dA$ for every face $\mathcal{F}_t^{\mathcal{T}}$ lying on Γ_t. See [43, (3.21)-(3.33)] for details of calculating the local matrices and vectors in each element. To obtain the matrix form of (4.19) for compressible solids, we modify (4.20) by setting $p_h = 0$ ($\mathbf{q}_h^{\ell} = \mathbf{0}$) and removing the fourth row and the fourth column of $\mathbb{K}_h$ and the forth entries of $\mathbb{Q}_h$, $\mathbb{N}_h$, and $\mathbb{F}_h$. We also use $\widehat{\boldsymbol{P}}(\boldsymbol{K})$ instead of $\widetilde{\boldsymbol{P}}(\boldsymbol{K})$ in our calculations.

Using Newton's method, one can approximate the solution of the nonlinear equation (4.20) iteratively by $\mathbb{Q}_h^{(i+1)} = \mathbb{Q}_h^{(i)} - \mathbb{K}_{t_h}^{-1}\left(\mathbb{Q}_h^{(i)}\right) \mathbb{R}_h\left(\mathbb{Q}_h^{(i)}\right)$, where $\mathbb{R}_h(\mathbb{Q}_h) = \mathbb{K}_h \mathbb{Q}_h + \mathbb{N}_h(\mathbb{Q}_h) - \mathbb{F}_h$ is the residual vector and $\mathbb{K}_{t_h}$ is the tangent stiffness matrix (Jacobian matrix)

given by

$$\mathbb{K}_{t_h}(\mathbf{q}_h^{\mathbf{c}}, \mathbf{q}_h^{\ell}) = \begin{bmatrix} \alpha \mathbf{M}_h^{11} & \alpha \mathbf{M}_h^{1\mathbf{c}} & \mathbf{K}_h^{1\mathbf{d}} & \mathbf{0} \\ \alpha \mathbf{M}_h^{1\mathbf{c}} & \alpha \mathbf{M}_h^{\mathbf{cc}} + \mathbf{H}_h^{\mathbf{cc}}(\mathbf{q}_h^{\mathbf{c}}, \mathbf{q}_h^{\ell}) & \mathbf{K}_h^{\mathbf{cd}} & \mathbf{H}_h^{\mathbf{c}\ell}(\mathbf{q}_h^{\mathbf{c}}) \\ \mathbf{K}_h^{\mathbf{d}1} & \mathbf{K}_h^{\mathbf{dc}} & \mathbf{0} & \mathbf{0} \\ \mathbf{0} & \mathbf{H}_h^{\ell\mathbf{c}}(\mathbf{q}_h^{\mathbf{c}}) & \mathbf{0} & \mathbf{0} \end{bmatrix}. \tag{4.21}$$

The matrix $\mathbf{H}_h^{\mathbf{cc}}(\mathbf{q}_h^{\mathbf{c}}, \mathbf{q}_h^{\ell})$ $\left(\mathbf{H}_h^{\mathbf{c}\ell}(\mathbf{q}_h^{\mathbf{c}})\right)$ contains the derivative of components of $\mathbf{N}_h^{\mathbf{c}}(\mathbf{q}_h^{\mathbf{c}}, \mathbf{q}_h^{\ell})$ in $\mathbb{N}_h$ with respect to components of $\mathbf{q}_h^{\mathbf{c}}$ ($\mathbf{q}_h^{\ell}$). Also, $\mathbf{H}_h^{\ell\mathbf{c}}(\mathbf{q}_h^{\mathbf{c}})$ contains the derivative of components of $\mathbf{N}_h^{\ell}(\mathbf{q}_h^{\mathbf{c}})$ in $\mathbb{N}_h$ with respect to components of $\mathbf{q}_h^{\mathbf{c}}$. Linearizing $\langle\!\langle \widetilde{\boldsymbol{P}}(\boldsymbol{K}) + p\boldsymbol{Q}(\boldsymbol{K}), \boldsymbol{\kappa} \rangle\!\rangle$ in $(2.13)_2$ at a given displacement gradient $\boldsymbol{K}^0 \in H^{\mathbf{c}}(\mathcal{B})$ and a given pressure $p^0 \in L^2(\mathcal{B})$ gives $\langle\!\langle \widetilde{\boldsymbol{A}}(\boldsymbol{K}^0, p^0) : \boldsymbol{K}, \boldsymbol{\kappa} \rangle\!\rangle + \langle\!\langle p\boldsymbol{Q}(\boldsymbol{K}^0), \boldsymbol{\kappa} \rangle\!\rangle$, where $\widetilde{\boldsymbol{A}}$ is the elasticity tensor and $(\widetilde{\boldsymbol{A}} : \boldsymbol{K})^{IJ} = \widetilde{A}^{IJMN} K^{MN}$. Also, linearizing $\langle\!\langle C(J(\boldsymbol{K})), q \rangle\!\rangle$ in $(2.13)_4$ at $\boldsymbol{K}^0$ results in $\langle\!\langle \boldsymbol{Q}(\boldsymbol{K}^0) : \boldsymbol{K}, q \rangle\!\rangle = \langle\!\langle \boldsymbol{K}, q\boldsymbol{Q}(\boldsymbol{K}^0) \rangle\!\rangle$, where $\boldsymbol{Q} : \boldsymbol{K} = Q^{IJ} K^{IJ}$. After discretization, for given $\boldsymbol{K}_h^0$ and p_h^0 (or $\mathbf{q}_h^{\mathbf{c}}$ and $\mathbf{q}_h^{\ell}$), one can calculate the local matrices for $\langle\!\langle \widetilde{\boldsymbol{A}}_{\mathcal{T}}(\boldsymbol{K}_{\mathcal{T}}^0, p_{\mathcal{T}}^0) : \boldsymbol{K}_{\mathcal{T}}, \boldsymbol{\kappa}_{\mathcal{T}} \rangle\!\rangle$, $\langle\!\langle p_{\mathcal{T}} \boldsymbol{Q}(\boldsymbol{K}_{\mathcal{T}}^0), \boldsymbol{\kappa}_{\mathcal{T}} \rangle\!\rangle$, and $\langle\!\langle \boldsymbol{K}_{\mathcal{T}}, q_{\mathcal{T}} \boldsymbol{Q}(\boldsymbol{K}_{\mathcal{T}}^0) \rangle\!\rangle$ $\forall \mathcal{T} \in \mathcal{B}_h$ to assemble $\mathbf{H}_h^{\mathbf{cc}}$, $\mathbf{H}_h^{\mathbf{c}\ell}$, and $\mathbf{H}_h^{\ell\mathbf{c}}$, respectively. For more details, see [43, (3.36)], and note that $\mathbf{H}_h^{\mathbf{c}\ell} = (\mathbf{H}_h^{\ell\mathbf{c}})^{\mathsf{T}}$. For compressible solids, (4.21) simplifies to

$$\mathbb{K}_{t_h}(\mathbf{q}_h^{\mathbf{c}}) = \begin{bmatrix} \alpha \mathbf{M}_h^{11} & \alpha \mathbf{M}_h^{1\mathbf{c}} & \mathbf{K}_h^{1\mathbf{d}} \\ \alpha \mathbf{M}_h^{1\mathbf{c}} & \alpha \mathbf{M}_h^{\mathbf{cc}} + \widehat{\mathbf{H}}_h^{\mathbf{cc}}(\mathbf{q}_h^{\mathbf{c}}) & \mathbf{K}_h^{\mathbf{cd}} \\ \mathbf{K}_h^{\mathbf{d}1} & \mathbf{K}_h^{\mathbf{dc}} & \mathbf{0} \end{bmatrix}, \tag{4.22}$$

where $\widehat{\mathbf{H}}_h^{\mathbf{cc}}(\mathbf{q}_h^{\mathbf{c}})$ is obtained by linearizing $\langle\!\langle \widehat{\boldsymbol{P}}(\boldsymbol{K}_h), \boldsymbol{\kappa}_h \rangle\!\rangle$ in $(4.19)_2$.

4.6 Constitutive Equations

We use neo-Hookean materials for our numerical examples. However, note that our formulation can use any elastic constitutive equation. For compressible solids, we use

the energy function

$$\widehat{W}(I_1, I_3) = \frac{\mu}{2}(I_1 - 3) - \frac{\mu}{2}\ln I_3 + \frac{\kappa}{8}(\ln I_3)^2, \tag{4.23}$$

where μ and κ are respectively the shear and bulk moduli at the ground state. Recalling that $\boldsymbol{F} = \boldsymbol{I} + \boldsymbol{K}$, the constitutive relation reads

$$\hat{\boldsymbol{P}}(\boldsymbol{K}) = \mu\left(\boldsymbol{F} - \boldsymbol{F}^{-\mathsf{T}}\right) + \kappa \ln J \boldsymbol{F}^{-\mathsf{T}}.$$

To calculate $\mathbb{K}_{t_h}$ defined in (4.22), one needs to obtain the elasticity tensor $\hat{\boldsymbol{A}}(\boldsymbol{K})$ by taking the derivative of components of $\hat{\boldsymbol{P}}(\boldsymbol{K})$ with respect to components of $\boldsymbol{K}$. In the implementation (see [43, (3.36)]), it is more convenient to represent the elasticity tensor as a matrix $\hat{\mathbf{A}}$, whose size is 9×9 in 3D. Let $\lceil \boldsymbol{T} \rceil$ be a vector representation of a tensor $\boldsymbol{T}$ and $[\boldsymbol{V}]_\times$ be a skew-symmetric matrix representing a vector $\boldsymbol{V}$ that are defined as

$$\lceil \boldsymbol{T} \rceil := \begin{bmatrix} T^{11} & T^{12} & T^{13} & T^{21} & T^{22} & T^{23} & T^{31} & T^{32} & T^{33} \end{bmatrix}^{\mathsf{T}},$$

$$[\boldsymbol{V}]_\times := \begin{bmatrix} 0 & -V^3 & V^2 \\ V^3 & 0 & -V^1 \\ -V^2 & V^1 & 0 \end{bmatrix}.$$

Considering (4.23), one obtains

$$\hat{\mathbf{A}}(\boldsymbol{K}) = \mu \mathbf{I} + (\mu - \kappa \ln J + \kappa)\lceil \boldsymbol{F}^{-\mathsf{T}} \rceil \lceil \boldsymbol{F}^{-\mathsf{T}} \rceil^{\mathsf{T}} - \frac{(\mu - \kappa \ln J)}{J} \mathbf{S}(\boldsymbol{F}),$$

where $\mathbf{I}$ is the 9×9 identity matrix and

$$\mathbf{S}(\boldsymbol{F}) := \begin{bmatrix} \mathbf{0} & -\left[\overrightarrow{\boldsymbol{F}}_3\right]_\times & \left[\overrightarrow{\boldsymbol{F}}_2\right]_\times \\ \left[\overrightarrow{\boldsymbol{F}}_3\right]_\times & \mathbf{0} & -\left[\overrightarrow{\boldsymbol{F}}_1\right]_\times \\ -\left[\overrightarrow{\boldsymbol{F}}_2\right]_\times & \left[\overrightarrow{\boldsymbol{F}}_1\right]_\times & \mathbf{0} \end{bmatrix}_{9\times 9}.$$

For incompressible solids with $I_3 = 1$, we use the neo-Hookean energy function

$$\widetilde{W}(I_1) = \frac{\mu}{2}(I_1 - 3). \tag{4.24}$$

Then, the constitutive part of stress is $\widetilde{P}(\boldsymbol{K}) = \mu(\boldsymbol{I} + \boldsymbol{K})$. To impose the incompressibility constraint $J = 1$, we use the constraint functions $C_1(J) = J - 1$ or $C_2(J) = \ln J$; we choose the function that results in a better numerical performance of our method in a given example. To obtain $\mathbb{N}_h$ in (4.20) and $\mathbb{K}_{t_h}$ in (4.21), one needs the following matrices:

$$\begin{aligned} &\boldsymbol{Q}_1(\boldsymbol{K}) = J\boldsymbol{F}^{-\mathsf{T}}, \quad && \widetilde{\mathbf{A}}_1(\boldsymbol{K}, p) = \mu\mathbf{I} + p\,\mathbf{S}(\boldsymbol{F}), \\ &\boldsymbol{Q}_2(\boldsymbol{K}) = \boldsymbol{F}^{-\mathsf{T}}, && \widetilde{\mathbf{A}}_2(\boldsymbol{K}, p) = \mu\mathbf{I} - p\left[\boldsymbol{F}^{-\mathsf{T}}\right]\left[\boldsymbol{F}^{-\mathsf{T}}\right]^{\mathsf{T}} + \frac{p}{J}\mathbf{S}(\boldsymbol{F}). \end{aligned}$$

4.7 Solvability and Stability

Theorem 23. *For $\alpha > 0$, the tangent stiffness matrix $\mathbb{K}_{t_h}$ of incompressible solids (4.21) is non-singular if and only if the following conditions hold.*

(i) $\ker(\mathbf{H}_h^{\mathbf{c}\ell}) = \{\mathbf{0}_{N^\ell \times 1}\}$,

(ii) $\ker(\mathbf{K}_h^{\mathbf{1d}}) \cap \ker(\mathbf{B}_0^{\ell\mathbf{c}}\mathbf{K}_h^{\mathbf{cd}}) = \{\mathbf{0}_{N^d \times 1}\}, \quad \big(\ker(\mathbf{K}_h^{\mathbf{cd}}) \subseteq \ker(\mathbf{B}_0^{\ell\mathbf{c}}\mathbf{K}_h^{\mathbf{cd}})\big)$,

(iii) $\ker\left(\mathbf{H}_h^{\mathbf{cc}} + \alpha\mathbf{M}_h^{\mathbf{cc}} - \alpha\mathbf{M}_h^{\mathbf{c1}}\left(\mathbf{M}_h^{11}\right)^{-1}\mathbf{M}_h^{\mathbf{1c}}\right) \cap \ker\left(\mathbf{K}_h^{\mathbf{dc}} - \mathbf{K}_h^{\mathbf{d1}}\left(\mathbf{M}_h^{11}\right)^{-1}\mathbf{M}_h^{\mathbf{1c}}\right) \cap \ker\left(\mathbf{H}_h^{\mathbf{c}\ell}\right) = \{\mathbf{0}_{N^c \times 1}\}$,

where $\mathbf{B}_0^{\ell\mathbf{c}}$ is a matrix whose rows form a basis for $\ker(\mathbf{H}_h^{\ell\mathbf{c}})$. For $\alpha = 0$, $\mathbb{K}_{t_h}$ is non-singular if and only if (i) and (ii) and the following conditions hold.

$(iii)'$ $\ker(\mathbf{K}_h^{\mathbf{d1}}) = \{\mathbf{0}_{N^1\times 1}\}$,

$(iv)'$ $\ker(\mathbf{H}_h^{\mathbf{cc}}) \cap \ker\left(\mathbf{B}_0^{\mathbf{1d}}\mathbf{K}_h^{\mathbf{dc}}\right) \cap \ker\left(\mathbf{H}_h^{\mathbf{c}\ell}\right) = \{\mathbf{0}_{N^c\times 1}\}$,

where $\mathbf{B}_0^{\mathbf{1d}}$ *is a matrix whose rows form a basis for* $\ker(\mathbf{K}_h^{\mathbf{d1}})$.

Proof. Rearrange the rows and the columns of $\mathbb{K}_{t_h}$ to obtain

$$\mathbb{K}_{t_h} = \begin{bmatrix} \mathbb{A}_h & \mathbb{B}_h^{\mathsf{T}} \\ \mathbb{B}_h & \mathbf{0} \end{bmatrix}, \quad \mathbb{A}_h = \begin{bmatrix} \mathbf{H}_h^{\mathbf{cc}} & \mathbf{0} \\ \mathbf{0} & \mathbf{0} \end{bmatrix} + \alpha \begin{bmatrix} \mathbf{M}_h^{\mathbf{cc}} & \mathbf{M}_h^{\mathbf{c1}} \\ \mathbf{M}_h^{\mathbf{1c}} & \mathbf{M}_h^{\mathbf{11}} \end{bmatrix},$$
$$\mathbb{B}_h = \begin{bmatrix} \mathbf{K}_h^{\mathbf{dc}} & \mathbf{K}_h^{\mathbf{d1}} \\ \mathbf{H}_h^{\ell\mathbf{c}} & \mathbf{0} \end{bmatrix}, \quad \mathbb{B}_h^{\mathsf{T}} = \begin{bmatrix} \mathbf{K}_h^{\mathbf{cd}} & \mathbf{H}_h^{\mathbf{c}\ell} \\ \mathbf{K}_h^{\mathbf{1d}} & \mathbf{0} \end{bmatrix}.$$

Then, according to [64, Theorem 3.2.1], the matrix $\mathbb{K}_{t_h}$ is non-singular if and only if the following holds:

(1) The restriction of $\mathbb{A}_h$ to $\ker(\mathbb{B}_h)$ is surjective (or equivalently injective),

(2) $\mathbb{B}_h$ is surjective (or equivalently $\mathbb{B}_h^{\mathsf{T}}$ is injective or $\ker(\mathbb{B}_h^{\mathsf{T}}) = \{\mathbf{0}\}$).

Consider the following sets:

$$S_1 := \left\{ \begin{bmatrix} \mathbf{0}_{N^c\times 1} \\ \mathbf{Y}_{N^1\times 1} \end{bmatrix} : \mathbf{0} \neq \mathbf{Y} \in \ker(\mathbf{K}_h^{\mathbf{d1}}) \right\},$$
$$S_2 := \left\{ \begin{bmatrix} \mathbf{X}_{N^c\times 1} \\ \mathbf{Y}_{N^1\times 1} \end{bmatrix} : \mathbf{0} \neq \mathbf{X} \in \ker(\mathbf{H}_h^{\ell\mathbf{c}}) \text{ and } \mathbf{K}_h^{\mathbf{dc}}\mathbf{X} + \mathbf{K}_h^{\mathbf{d1}}\mathbf{Y} = \mathbf{0} \text{ for some } \mathbf{Y} \in \mathbb{R}^{N^1} \right\},$$
$$S_1' := \left\{ \begin{bmatrix} \mathbf{0}_{N^d\times 1} \\ \mathbf{Y}_{N^\ell\times 1} \end{bmatrix} : \mathbf{0} \neq \mathbf{Y} \in \ker(\mathbf{H}_h^{\mathbf{c}\ell}) \right\},$$
$$S_2' := \left\{ \begin{bmatrix} \mathbf{X}_{N^d\times 1} \\ \mathbf{Y}_{N^\ell\times 1} \end{bmatrix} : \mathbf{0} \neq \mathbf{X} \in \ker(\mathbf{K}_h^{\mathbf{1d}}) \text{ and } \mathbf{K}_h^{\mathbf{cd}}\mathbf{X} + \mathbf{H}_h^{\mathbf{c}\ell}\mathbf{Y} = \mathbf{0} \text{ for some } \mathbf{Y} \in \mathbb{R}^{N^\ell} \right\}.$$

Then, one can show that

$$\ker\left(\mathbb{B}_h\right) = \left\{\mathbf{0}_{(N^c+N^1)\times 1}\right\} \sqcup S_1 \sqcup S_2 \quad \text{and} \quad \ker\left(\mathbb{B}_h^{\mathsf{T}}\right) = \left\{\mathbf{0}_{(N^d+N^\ell)\times 1}\right\} \sqcup S_1' \sqcup S_2'.$$

Therefore, the requirement (2) $(\ker(\mathbb{B}_h^{\mathsf{T}}) = \{\mathbf{0}\})$ is equivalent to $S_1' = S_2' = \varnothing$. It is straightforward to show that $S_1' = \varnothing$ is equivalent to (i). We write $S_2' = \varnothing$ as $\ker(\mathbf{K}_h^{\mathbf{1d}}) \cap s_2' = \{\mathbf{0}\}$, where $s_2' = \left\{\mathbf{X} : \mathbf{K}_h^{\mathbf{cd}}\mathbf{X} = -\mathbf{H}_h^{\mathbf{c}\ell}\mathbf{Y} \text{ for some } \mathbf{Y} \in \mathbb{R}^{N^\ell}\right\}$. Using $\mathrm{Im}(\mathbf{H}_h^{\mathbf{c}\ell}) = \ker(\mathbf{H}_h^{\ell\mathbf{c}})^\perp$, where the superscript $\perp$ indicates the orthogonal complement, one can readily show that $s_2' = \left\{\mathbf{X} : \mathbf{b}_0^{\mathsf{T}}\mathbf{K}_h^{\mathbf{cd}}\mathbf{X} = 0, \forall \mathbf{b}_0 \in \ker(\mathbf{H}_h^{\ell\mathbf{c}})\right\}$. Let $\mathbf{B}_0^{\ell\mathbf{c}}$ be a matrix such that whose rows form a basis for $\ker(\mathbf{H}_h^{\ell\mathbf{c}})$, then $s_2' = \ker(\mathbf{B}_0^{\ell\mathbf{c}}\mathbf{K}_h^{\mathbf{cd}})$. Therefore, $S_2' = \varnothing$ is equivalent to (ii). Next, we assume that $\alpha > 0$ and show that (1) is equivalent to (iii). For $\alpha > 0$, one can write

$$\ker(\mathbb{A}_h) = \left\{ \begin{bmatrix} \mathbf{X}_{N^c\times 1} \\ \mathbf{Y}_{N^1\times 1} \end{bmatrix} : \ \mathbf{X} \in \ker\left(\mathbf{H}_h^{\mathbf{cc}} + \alpha\mathbf{M}_h^{\mathbf{cc}} - \alpha\mathbf{M}_h^{\mathbf{c}1}\left(\mathbf{M}_h^{11}\right)^{-1}\mathbf{M}_h^{1\mathbf{c}}\right) \text{ and } \right.$$
$$\left. \mathbf{Y} = -\left(\mathbf{M}_h^{11}\right)^{-1}\mathbf{M}_h^{1\mathbf{c}}\mathbf{X} \right\},$$

where use was made of the fact that $\mathbf{M}_h^{11}$ is a Gram matrix and positive-definite by construction (and so injective). Note that (1) is equivalent to $\ker(\mathbb{A}_h) \cap \ker(\mathbb{B}_h) = (\ker(\mathbb{A}_h) \cap \{\mathbf{0}\}) \sqcup (\ker(\mathbb{A}_h) \cap S_1) \sqcup (\ker(\mathbb{A}_h) \cap S_2) = \{\mathbf{0}\}$, which is equivalent to $\ker(\mathbb{A}_h) \cap S_1 = \ker(\mathbb{A}_h) \cap S_2 = \varnothing$. We know that $\mathbb{A}_h\mathbf{Q} \neq \mathbf{0}$, $\forall \mathbf{Q} \in S_1$, due to injectivity of $\mathbf{M}_h^{11}$, so $\ker(\mathbb{A}_h) \cap S_1 = \varnothing$ is trivial. The remaining condition $\ker(\mathbb{A}_h) \cap S_2 = \varnothing$ simplifies to (iii). For $\alpha = 0$, one can write

$$\ker(\mathbb{A}_h) = \left\{ \begin{bmatrix} \mathbf{X}_{N^c\times 1} \\ \mathbf{Y}_{N^1\times 1} \end{bmatrix} : \mathbf{X} \in \ker\left(\mathbf{H}_h^{\mathbf{cc}}\right) \text{ and } \mathbf{Y} \in \mathbb{R}^{N^1} \right\}.$$

Now, $\ker(\mathbb{A}_h) \cap S_1 = \varnothing$ simplifies to $(iii)'$, and $\ker(\mathbb{A}_h) \cap S_2 = \varnothing$ simplifies to $(iv)'$. $\square$

Corollary 24. *For $\alpha > 0$, the tangent stiffness matrix $\mathbb{K}_{t_h}$ of compressible solids (4.22) is non-singular if and only if the following conditions hold:*

(i) $\ker(\mathbf{K}_h^{\mathbf{1d}}) \cap \ker(\mathbf{K}_h^{\mathbf{cd}}) = \{\mathbf{0}_{N^d \times 1}\}$,

(ii) $\ker\left(\mathbf{H}_h^{\mathbf{cc}} + \alpha\mathbf{M}_h^{\mathbf{cc}} - \alpha\mathbf{M}_h^{\mathbf{c1}}\left(\mathbf{M}_h^{\mathbf{11}}\right)^{-1}\mathbf{M}_h^{\mathbf{1c}}\right) \cap \ker\left(\mathbf{K}_h^{\mathbf{dc}} - \mathbf{K}_h^{\mathbf{d1}}\left(\mathbf{M}_h^{\mathbf{11}}\right)^{-1}\mathbf{M}_h^{\mathbf{1c}}\right) = \{\mathbf{0}_{N^c \times 1}\}$.

For $\alpha = 0$, $\mathbb{K}_{t_h}$ is non-singular if and only if (i) and the following conditions hold:

$(ii)'$ $\ker(\mathbf{K}_h^{\mathbf{d1}}) = \{\mathbf{0}_{N^1 \times 1}\}$,

$(iii)'$ $\ker(\mathbf{H}_h^{\mathbf{cc}}) \cap \ker\left((\mathbf{B}_0^{\mathbf{d1}})^{\mathsf{T}}\mathbf{K}_h^{\mathbf{dc}}\right) = \{\mathbf{0}_{N^c \times 1}\}$.

Corollary 25. *If the tangent stiffness matrix $\mathbb{K}_{t_h}$ is non-singular, then*

(1) $N^d \leqslant N^c + N^1$ *for $\alpha \geqslant 0$ and for both compressible and incompressible solids,*

(2) $N^\ell \leqslant N^c$ *only for incompressible solids,*

(3) $N^1 \leqslant N^d$ *only for $\alpha = 0$.*

Proof. Given that $\ker(\mathbf{K}_h^{\mathbf{cd}}) \subseteq \ker(\mathbf{B}_0^{\ell\mathbf{c}}\mathbf{K}_h^{\mathbf{cd}})$, both Theorem 23 (ii) and Corollary 24 (i), imply (1). Theorem 23 (i) implies (2). Both Theorem 23 $(iii)'$ and Corollary 24 $(ii)'$, imply (3). □

In view of Theorem 23, one can see how adding (2.15) to the weak formulation (2.13) may improve the stability and the performance of the resulting finite element methods. Without the stabilization terms ($\alpha = 0$), the violation of $\ker(\mathbf{K}_h^{\mathbf{d1}}) = \{\mathbf{0}_{N^1 \times 1}\}$ or more strongly $N^d \leqslant N^1$ leads to a singular tangent stiffness matrix $\mathbb{K}_{t_h}$. This restricts the choices of finite elements for the displacement and stress in both 2D and 3D. In particular, considering $(\boldsymbol{U}_h, \boldsymbol{P}_h)$ in $V_{h,m}^1 \times V_{h,n}^{\mathbf{d}-}$ or $V_{h,m}^1 \times V_{h,n}^{\mathbf{d}}$ such that $m < n$ results in a singular $\mathbb{K}_{t_h}$ in both 2D and 3D independent of the size of the mesh. Adding the stabilization terms (2.15) ($\alpha > 0$) overcomes this limitation and enables one to improve the convergence

of the displacement field by discretizing it using second-order shape functions without the need for modifying the finite elements of other fields. For instance, for $\alpha = 0$, the finite elements (4.13) result in a singular system, but they converge to correct solutions for large values of α. To avoid the singularity of (4.13) for $\alpha = 0$, we have no choice but to approximate the displacement field using first-order polynomials and to compromise the rate of convergence of the method. Also, note that approximating the displacement $\boldsymbol{U}$ in a second-order polynomial space leads to a more accurate discretization of $\boldsymbol{K} = \mathbf{grad}\,\boldsymbol{U}$ as the intersection of image of $\mathbf{grad}$ and the approximation space of $\boldsymbol{K}$ becomes larger at the discrete level.

We next discuss how modifying the finite element of the displacement gradient $\boldsymbol{K}$ in (4.13) and its resulting finite element space (4.17) lead to solvability of the mixed finite element methods (4.18) and (4.19). Let $(\boldsymbol{U}_h, \boldsymbol{K}_h, \boldsymbol{P}_h) \in V^1_{h,m} \times V^{\mathbf{c}-}_{h,n}(V^{\mathbf{c}}_{h,n}) \times V^{\mathbf{d}-}_{h,k}(V^{\mathbf{d}}_{h,k})$ for $m, n, k = 1, 2$, which results in 32 different combinations (note that pressure is not relevant here). In 3D, all 32 combinations except $V^1_{h,m} \times V^{\mathbf{c}}_{h,2} \times V^{\mathbf{d}-}_{h,1}, m = 1, 2$ result in a singular $\mathbb{K}_{t_h}$. These combinations either give $N^d > N^c + N^1$ for any mesh or their smallest singular value of $\begin{bmatrix} \mathsf{K}^{\mathbf{dc}}_h & \mathsf{K}^{\mathbf{d}1}_h \end{bmatrix}^{\mathsf{T}}$ goes to zero as one refines the mesh (see [43, Remark 16]). Any of these two cases is a violation of Theorem 23 (ii) (or Corollary 24 (i)). The two remaining choices $V^1_{h,m} \times V^{\mathbf{c}}_{h,2} \times V^{\mathbf{d}-}_{h,1}, m = 1, 2$ are not practical as they have poor performances relative to their expensive computational cost. $V^{\mathbf{c}}_{h,2}$ of displacement gradient has 90 degrees of freedom per element, which significantly increases the computational cost, but paired with the lowest-order space of stress $V^{\mathbf{d}-}_{h,1}$, it cannot improve the overall convergence of the method. To resolve this issue, we proposed $\overline{V}^{\mathbf{c}}_{h,3}$ in (4.17) and considered $(\boldsymbol{U}_h, \boldsymbol{K}_h, \boldsymbol{P}_h) \in V^1_{h,2} \times \overline{V}^{\mathbf{c}}_{h,3} \times V^{\mathbf{d}-}_{h,1}$. Note that, in each element, $\overline{V}^{\mathbf{c}}_{h,3}$ has only 9 degrees of freedom more than the first-order space $V^{\mathbf{c}}_{h,1}$ with 36 degrees of freedom (see Figure 4.2). Hence, it does not increase the computational cost of the method significantly. Moreover, we observe that the smallest singular value of $\begin{bmatrix} \mathsf{K}^{\mathbf{dc}}_h & \mathsf{K}^{\mathbf{d}1}_h \end{bmatrix}^{\mathsf{T}}$ for $V^1_{h,2} \times \overline{V}^{\mathbf{c}}_{h,3} \times V^{\mathbf{d}-}_{h,1}$ remains positive as we refine different arbitrary meshes.

We have discussed so far that, for $\alpha > 0$, (4.18) and (4.19) do not result in a singular $\mathbb{K}_{t_h}$ even if $\ker(\mathbf{K}_h^{\mathbf{d1}}) \neq \{\mathbf{0}_{N^1\times 1}\}$, and they result in $N^d \leqslant N^c + N^1$ and $\ker(\mathbf{K}_h^{\mathbf{1d}}) \cap \ker(\mathbf{K}_h^{\mathbf{cd}}) = \{\mathbf{0}_{N^d\times 1}\}$, which are required for satisfying Theorem 23 (ii) or Corollary 24 (i). These have been made possible through studying the linear operators $\mathbf{K}_h^{\mathbf{cd}}$ and $\mathbf{K}_h^{\mathbf{1d}}$ in $\mathbb{K}_{t_h}$, which are independent of the physics of the problem. The *stability* of (4.18) requires that all the conditions of Theorem 23 hold as one refines the mesh. However, given the nonlinear nature of the problems of interest here, this is difficult to check. In particular, the nonlinear operators $\mathbf{H}_h^{\mathbf{cc}}(\mathbf{q}_h^{\mathbf{c}}, \mathbf{q}_h^{\ell})$ and $\mathbf{H}_h^{\mathbf{c}\ell}(\mathbf{q}_h^{\mathbf{c}})$ in $\mathbb{K}_{t_h}$ depend on the material properties of the body and its state of deformation. Therefore, one cannot draw a general conclusion for stability or convergence of the mixed methods only by studying the formulations and without considering the physics of the problem. Based on the various numerical examples presented in the next chapter, we observe that (4.18) and (4.19) have an overall good performance in capturing the large deformations of incompressible and compressible solids in 3D.

CHAPTER 5

NUMERICAL EXAMPLES

In this chapter, we consider several examples to assess the performance of CSFEMs in capturing the deformed configurations of compressible and incompressible solids in dimensions two and three. We use the Frobenius norm $\|\boldsymbol{T}\| := (\sum_{I,J} T^{IJ}T^{IJ})^{\frac{1}{2}}$ for $\boldsymbol{K}_h$ and $\boldsymbol{P}_h$ in the deformed configurations. We use the L^2-norm for $\boldsymbol{U}_h$, $\boldsymbol{K}_h$, $\boldsymbol{P}_h$, and p_h over the entire mesh in convergence analyses. We use $\alpha = 1e6$ in all 3D examples (the solutions actually converge for smaller values of α in each example; assuming larger values does not change the solutions).

5.1 Examples for 2D Compressible Solids

5.1.1 Example 1: Shearing Plate

As the first example, following [22], we consider a clamped square plate subject to shear loads. The side length of the plate is $1\ \mathrm{mm}$ and we assume the following displacement field (see Figure 5.1):

$$\boldsymbol{U}_e = \begin{bmatrix} \frac{1}{2}Y^3 + \frac{1}{2}\sin\left(\frac{\pi Y}{2}\right) \\ \\ 0 \end{bmatrix}.$$

We assume a neo-Hookean material with energy function $W_1(\boldsymbol{F})$ given in (3.46a), with $\mu = \kappa = 1\ \mathrm{N/mm^2}$. Using $\boldsymbol{U}_e$, it is straightforward to calculate the deformation gradient $\boldsymbol{F}_e$, the first Piola-Kirchhoff stress tensor $\boldsymbol{P}_e$, the body force, and the boundary traction. Then, ($\boldsymbol{U}_e$, $\boldsymbol{F}_e$, $\boldsymbol{P}_e$) can be considered as the exact solution of the square plate clamped on the bottom and subject to shear loads on the other sides as shown in Figure 5.1.

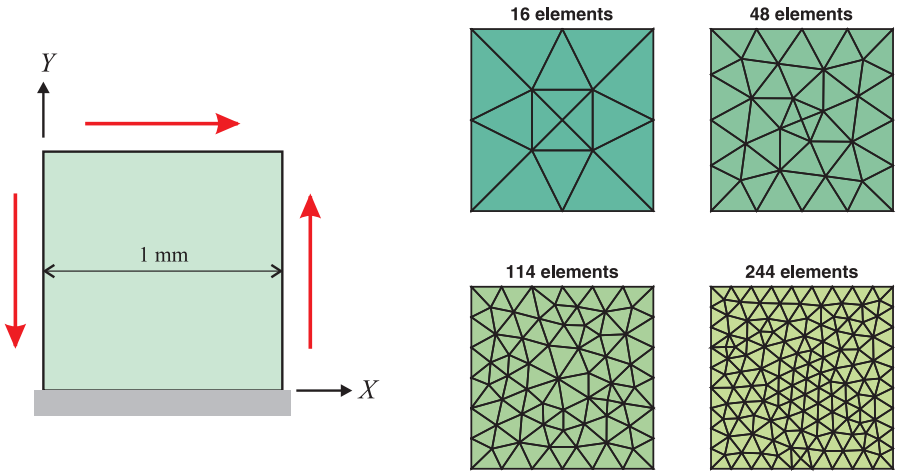

Figure 5.1: The shearing plate example: Geometry and boundary conditions (left), four unstructured meshes (right).

As we mentioned in §3.4, there are 32 possible first-order and second-order CSFEMs. Our numerical experiments suggest that the 7 combinations have a better performance among all the first-order and second-order CSFEMs. All these 7 combinations pass the patch test in the sense discussed in [65, §4.6]. For the meshes shown in Figure 5.1, the L^2-norm of errors associated to each of these CSFEMs are given in Table 5.1. We observe that although H1c$\bar{2}$d$\bar{1}$, H1c$\bar{2}$d1, H1c2d$\bar{1}$, and H1c2d$\bar{2}$ have more degrees of freedom than H1c1d$\bar{1}$, they do not result in more accurate approximations.

For studying convergence orders of the above CSFEMs, in Figure 5.2, we have plotted the L^2-norms of errors versus the maximum diameter h for some uniform meshes. The convergence order of displacement is close to 2 for all methods. This is the optimal convergence order for all these CSFEMs except for H2c2d$\bar{2}$. The convergence order of $\boldsymbol{P}$ is close to 1 for all methods. The order of convergence of $\boldsymbol{K}$ is close to 1 for all methods except H2c2d$\bar{2}$, for which the convergence order is 2. By considering some other meshes, we see that errors and convergence orders of $\boldsymbol{U}$ and $\boldsymbol{K}$ are not very sensitive to the underlying meshes. However, except for H1c2d1, H1c2d$\bar{2}$, and H2c2d$\bar{2}$, errors and convergence rates of $\boldsymbol{P}$ are more mesh-dependent. Based on the above discussions, one may use H1c1d$\bar{1}$, H1c2d1, and H2c2d$\bar{2}$, in practice.

Figure 5.3 shows the deformed configuration, $\|\boldsymbol{K}\|$, and $\|\boldsymbol{P}\|$ corresponding to the exact solution, H1c1d$\bar{1}$, and H2c2d$\bar{2}$. Solutions for CSFEMs are calculated for the mesh with 114 elements shown in Figure 5.1. Note that due to the interelement continuities of H^{c} and H^{d}-conformal finite element spaces, $\|\boldsymbol{K}\|$ and $\|\boldsymbol{P}\|$ obtained using CSFEMs are not continuous, in general.

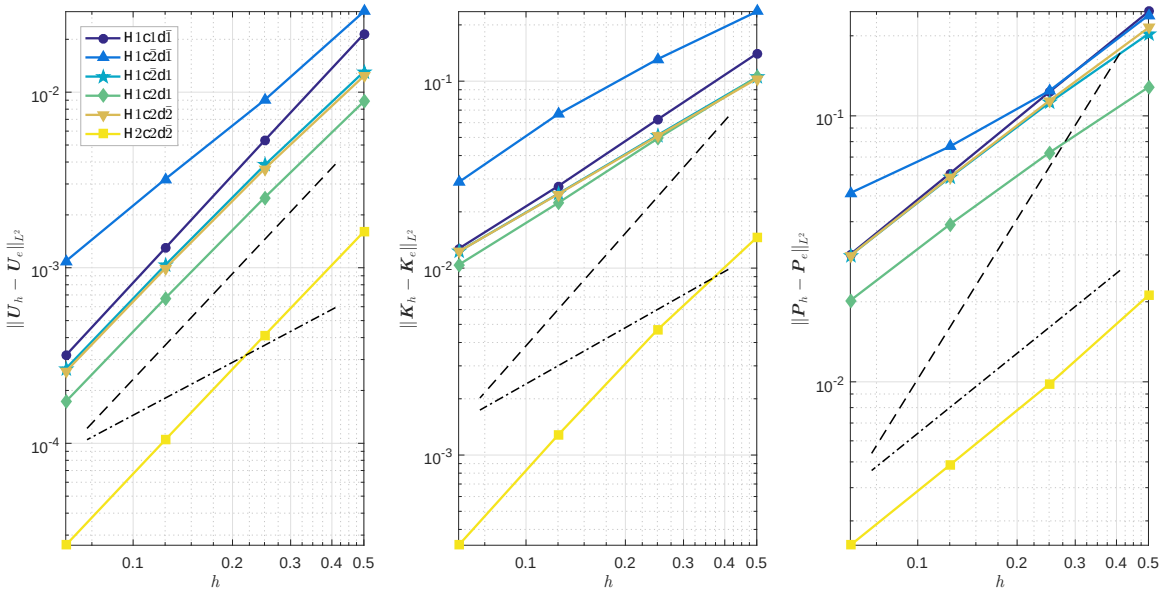

Figure 5.2: L^2-norms of errors in approximating displacement, displacement gradient, and stress versus the maximum diameter h for the shearing plate example. In each diagram, different curves correspond to different CSFEMs. The points on each curve correspond to uniform meshes consisting of 16 ($h = 0.5$), 64 ($h = 0.25$), 256 ($h = 0.125$), and 1024 ($h = 0.0625$) cells. In each diagram, the dash-dot line and the dashed line have the slopes 1 and 2, respectively.

Table 5.1: Convergence and error of different CSFEMs for the shearing plate example. DOF is the total number of degrees of freedom for each mesh, ($\boldsymbol{U}_e$, $\boldsymbol{F}_e$, $\boldsymbol{P}_e$) is the exact solution, and ($\boldsymbol{U}_h$, $\boldsymbol{F}_h$, $\boldsymbol{P}_h$) is the approximate solution for each CSFEM.

CSFEM	#Elements	#DOF	$\|\boldsymbol{U}_h - \boldsymbol{U}_e\|_{L^2}$	$\|\boldsymbol{K}_h - \boldsymbol{K}_e\|_{L^2}$	$\|\boldsymbol{P}_h - \boldsymbol{P}_e\|_{L^2}$
H1c1d$\bar{1}$	16	194	1.43e-02	1.00e-01	3.09e-01
	48	546	2.34e-03	3.41e-02	1.08e-01
	114	1238	8.92e-04	1.90e-02	5.49e-02
	244	2586	3.42e-04	8.94e-03	3.70e-02
H1c$\bar{2}$d$\bar{1}$	16	258	2.46e-02	2.01e-01	3.01e-01
	48	738	4.93e-03	7.82e-02	1.13e-01
	114	1694	2.00e-03	4.61e-02	5.90e-02
	244	3562	7.31e-04	2.52e-02	3.88e-02
H1c$\bar{2}$d1	16	314	8.56e-03	8.53e-02	2.91e-01
	48	898	1.75e-03	1.97e-02	8.58e-02
	114	2060	6.95e-04	9.66e-03	2.94e-02
	244	4330	3.13e-04	6.16e-03	1.97e-02
H1c2d$\bar{1}$	16	346	9.53e-02	5.77e-01	1.89e-01
	48	994	2.39e-02	3.69e-01	9.03e-02
	114	2288	1.10e-02	2.66e-01	5.88e-02
	244	4818	5.57e-03	2.01e-01	3.87e-02
H1c2d1	16	402	5.65e-03	1.00e-01	6.34e-02
	48	1154	1.44e-03	2.65e-02	2.09e-02
	114	2654	6.49e-04	1.74e-02	1.54e-02
	244	5586	2.93e-04	1.01e-02	8.72e-03
H1c2d$\bar{2}$	16	466	9.35e-03	8.88e-02	2.02e-01
	48	1346	3.14e-03	4.59e-02	1.18e-01
	114	3110	1.32e-03	2.99e-02	8.17e-02
	244	6562	6.37e-04	1.97e-02	5.38e-02
H2c2d$\bar{2}$	16	522	1.50e-03	1.51e-02	2.66e-02
	48	1506	4.14e-04	4.65e-03	1.04e-02
	114	3476	1.80e-04	2.13e-03	6.47e-03
	244	7330	8.07e-05	9.67e-04	4.17e-03

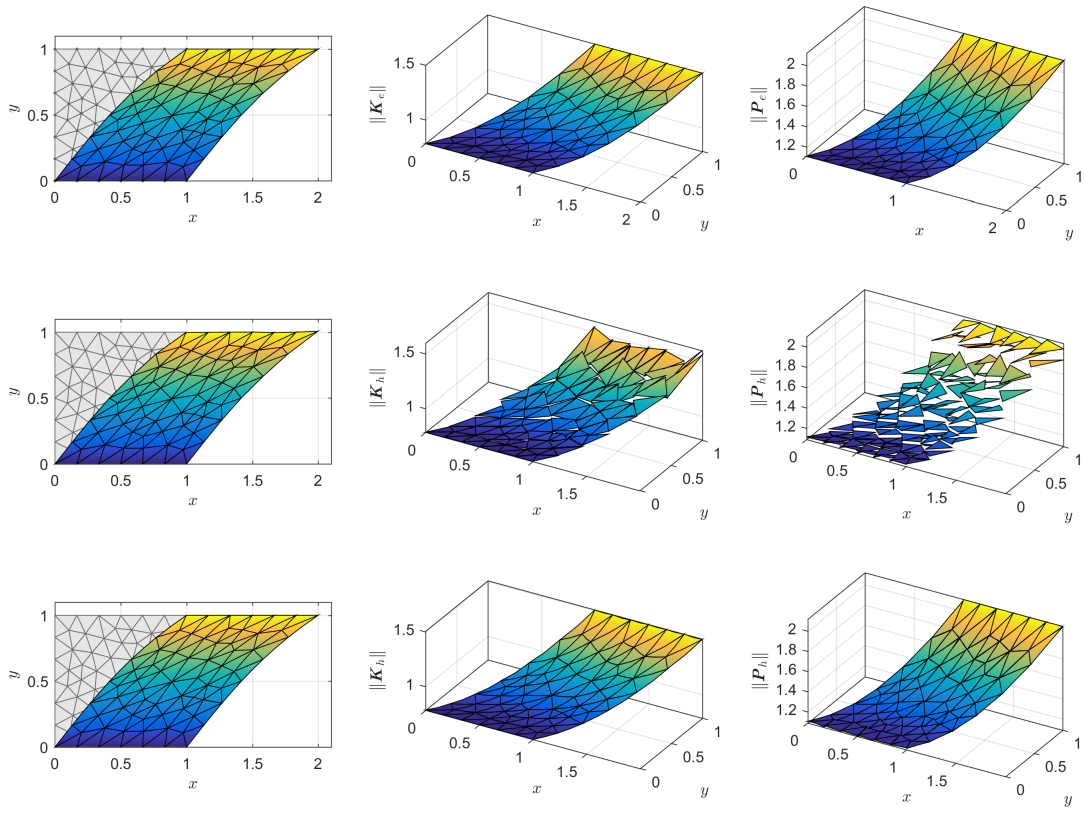

Figure 5.3: The comparison between the deformed configuration, the norm of displacement gradient $\|\boldsymbol{K}\|$, and the norm of stress $\|\boldsymbol{P}\|$ associated to the exact solution of the shearing plate example and those obtained by CSFEMs. Colors indicate values of $\|\boldsymbol{U}\|$, $\|\boldsymbol{K}\|$, and $\|\boldsymbol{P}\|$ in the first, the second, and the third columns, respectively. Lighter colors indicate larger values. The first, the second, and the third rows correspond to the exact solution, H1c1d$\bar{1}$, and H2c2d$\bar{2}$, respectively. The underlying mesh of CSFEMs has 114 cells.

5.1.2 Example 2: Cook's Membrane

For studying the performance of CSFEMs in bending and in the near-incompressible regime, we consider the standard Cook's membrane problem shown in Figure 5.4. We use the energy function $W_2(\boldsymbol{F})$, with $\mu = 80.194\ \mathrm{N/mm^2}$, and $\kappa = 400889.8\ \mathrm{N/mm^2}$.

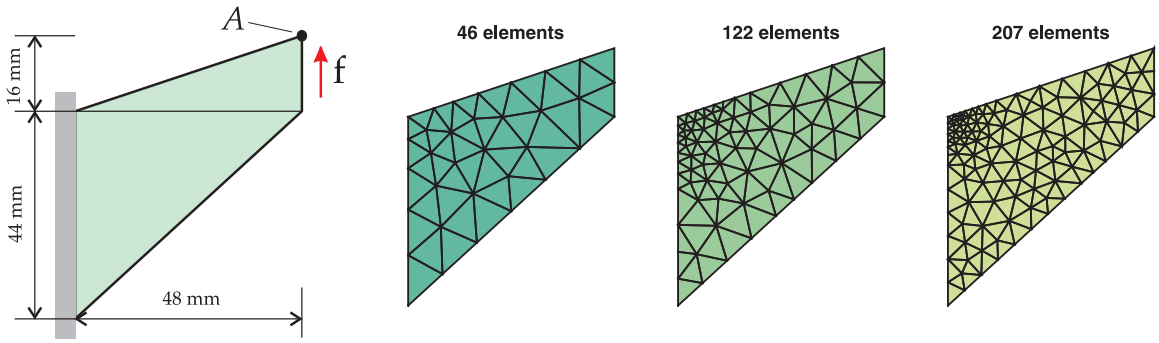

Figure 5.4: Cook's membrane: Geometry, boundary conditions, and three unstructured meshes.

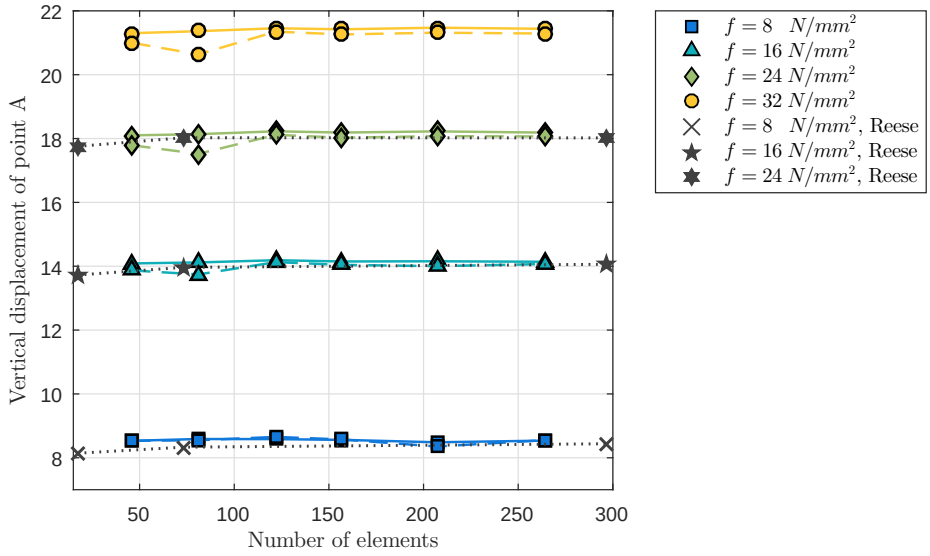

Figure 5.5: Cook's membrane: Vertical displacement of point A in Figure 5.4 for different values of the shearing force f versus the number of elements in the mesh. The dashed and the solid lines are the results obtained by H1c1d$\bar{1}$ and H2c2d$\bar{2}$, respectively. The underlying meshes have 46, 81, 122, 157, 207, and 264 elements. The dotted lines indicate the results of Reese [66].

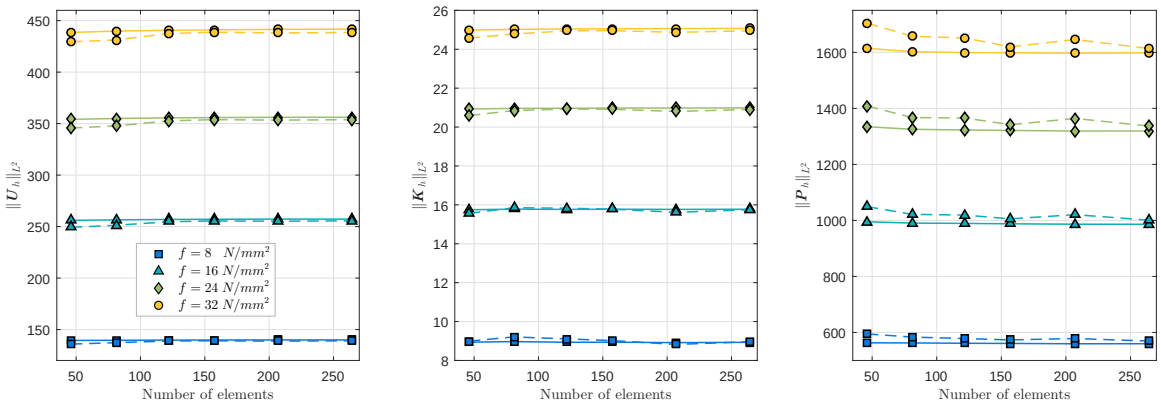

Figure 5.6: Cook's membrane: L^2-norms of displacement, displacement gradient, and stress (for different values of the shearing force f) versus the number of elements in the mesh. The dashed and the solid lines are obtained by H1c1d$\bar{1}$ and H2c2d$\bar{2}$, respectively. The underlying meshes have 46, 81, 122, 157, 207, and 264 elements.

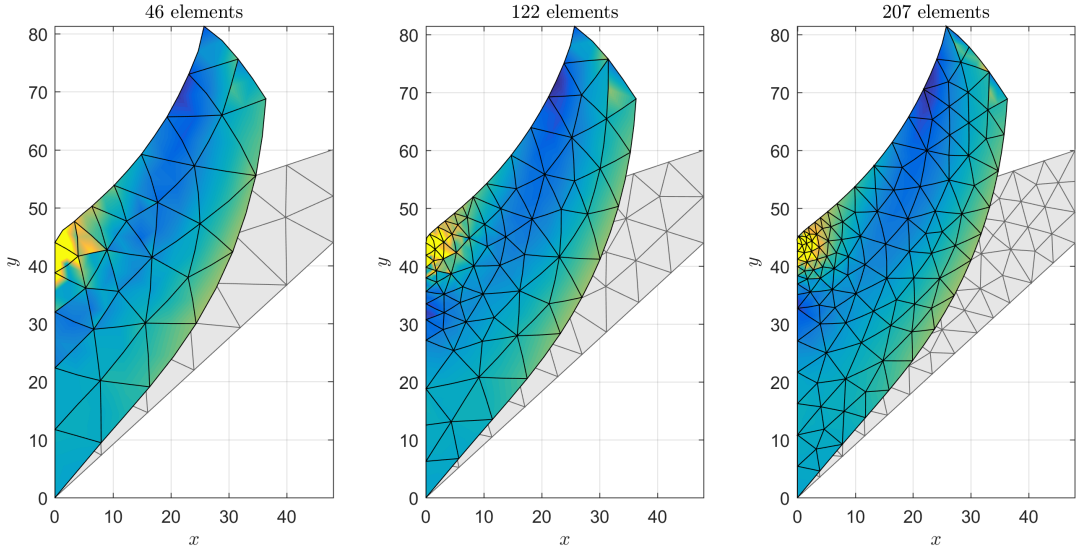

Figure 5.7: Deformed configurations of Cook's membrane using H2c2d$\bar{2}$ and the meshes of Figure 5.4, with the shear force $f = 32\ \mathrm{N/mm^2}$. Colors indicate values of the norm of stress $\|\boldsymbol{P}\|$, where lighter colors correspond to larger values of $\|\boldsymbol{P}\|$.

To investigate the pointwise convergence of the approximate solutions, in Figure 5.5, we have plotted vertical displacement of point A for different meshes and for different values of the shearing force f. We use H1c1d$\bar{1}$ and H2c2d$\bar{2}$ and compare our results with

those of Reese [66]. We observe that both of these CSFEMs give good approximations for relatively coarse meshes.

Figure 5.6 shows the global convergence of H1c1d$\bar{1}$ and H2c2d$\bar{2}$. We plot L^2-norms of displacement, displacement gradient, and stress for different meshes. One observes that these CSFEMs have comparable accuracy for $\boldsymbol{U}$ and $\boldsymbol{K}$. However, as the shearing force increases, H1c1d$\bar{1}$ becomes less accurate in approximating $\boldsymbol{P}$. Figure 5.7 shows the deformed configuration of Cook's membrane for the meshes of Figure 5.4 by using H2c2d$\bar{2}$ and $f = 32\ \mathrm{N/mm^2}$. Colors in this figure indicate the values of $\|\boldsymbol{P}\| := (\sum_{I,J} P^{IJ} P^{IJ})^{1/2}$, with lighter colors corresponding to larger values of $\|\boldsymbol{P}\|$.

5.1.3 Example 3: Inhomogeneous Compression

Next, we consider a plate under compression shown in Figure 5.8. The horizontal (vertical) displacement of the top (bottom) of the plate is constrained to be zero, and the material properties are the same as those of the previous example. Many enhanced strain methods suffer from the hourglass instability in this problem, e.g. see Reese [66] and references therein. Due to the symmetry of this problem, as shown in Figure 5.8, we only consider the right half of the plate.

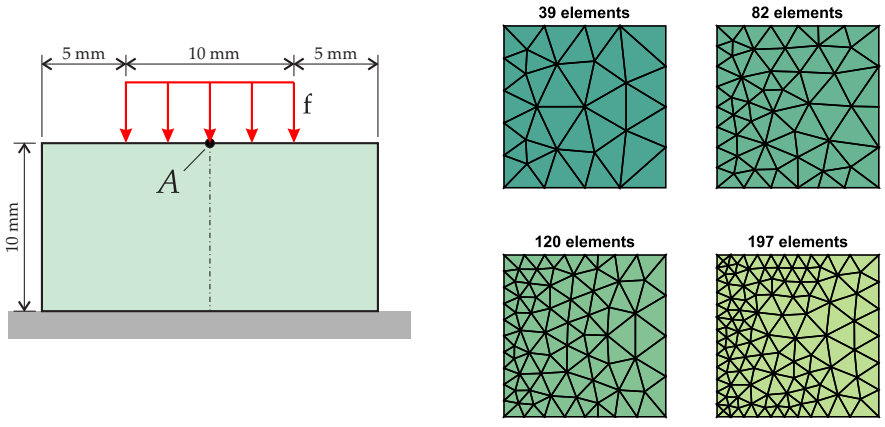

Figure 5.8: The inhomogeneous compression example: Geometry, boundary conditions, and four unstructured meshes. Note that using the symmetry of this example, only half of the plate is modeled.

Figure 5.9 depicts the vertical displacement of point A in Figure 5.8 for different values of the force f. Displacements are obtained by using H2c2d$\bar{2}$. Our results agree with those of Reese [66], which are obtained by using hourglass stabilization techniques. We observe that all the first-order and second-order CSFEMs except H2c2d$\bar{2}$ become unstable if the displacement of point A is more than 30% of the height of the plate. However, H2c2d$\bar{2}$ remains stable without using any additional stabilization technique. Figure 5.10 shows L^2-norms of $\boldsymbol{U}$, $\boldsymbol{K}$, and $\boldsymbol{P}$. One observes that H2c2d$\bar{2}$ has a good global convergence behavior in this example. Finally, in Figure 5.11, we have plotted the deformed configuration and $\|\boldsymbol{P}\|$ for the force $f = 600\ \mathrm{N/mm^2}$, which results in displacement of point A being 65% of plate height.

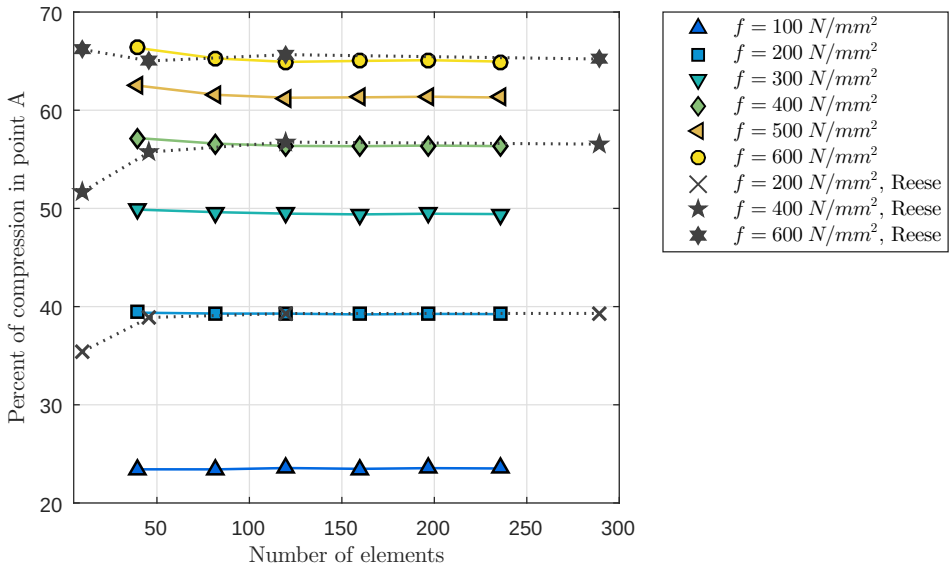

Figure 5.9: The inhomogeneous compression example: Vertical displacement of point A of Figure 5.8 for different values of the force f versus the number of elements in the mesh. The results are obtained by using H2c2d$\bar{2}$. The underlying meshes have 39, 82, 120, 160, 197, and 236 elements. The dotted lines indicate the results of Reese [66].

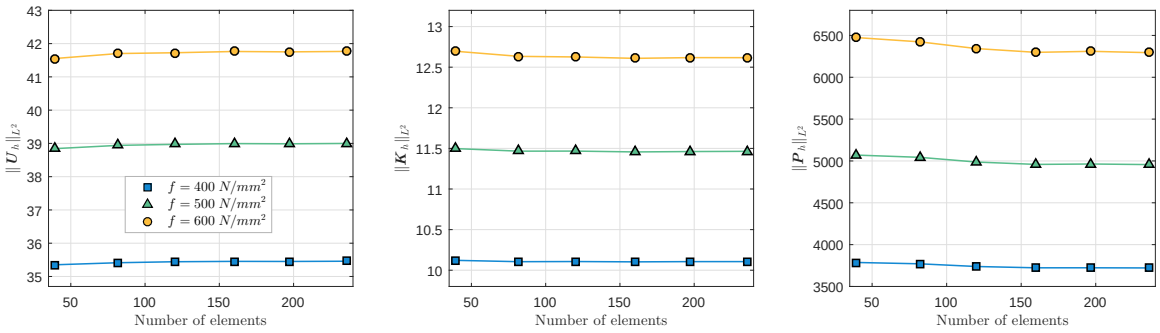

Figure 5.10: The inhomogeneous compression example: L^2-norms of displacement, displacement gradient, and stress (for different values of the compressing force f) versus the number of elements in the mesh. The results are obtained by using H2c2d$\bar{2}$. The underlying meshes have 39, 82, 120, 160, 197, and 236 elements.

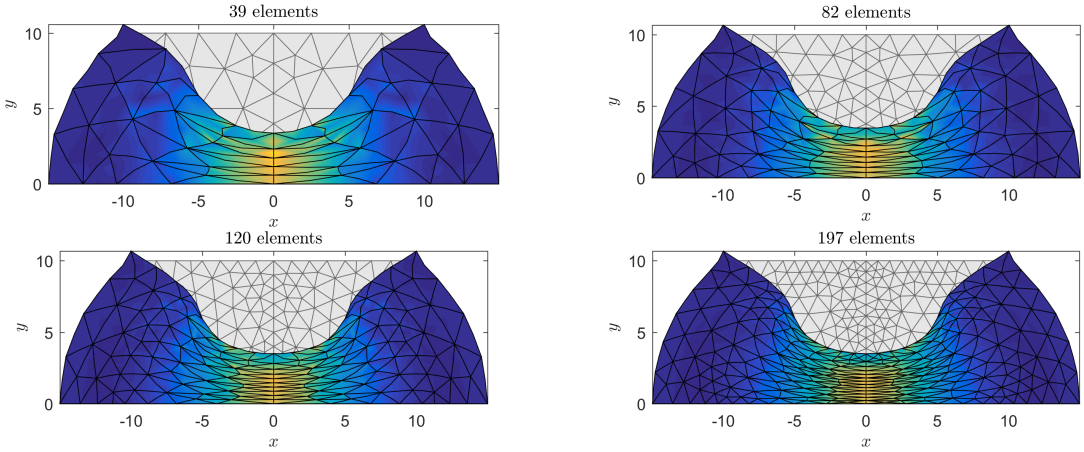

Figure 5.11: Deformed configurations of the inhomogeneous compression example using H2c2d$\bar{2}$ and the meshes of Figure 5.8. The plate is under the force $f = 600\ \mathrm{N/mm^2}$, which results in displacement at the middle point A being 65% of the plate height. Colors indicate values of the norm of stress $\|\boldsymbol{P}\|$ with lighter colors corresponding to higher values of $\|\boldsymbol{P}\|$.

5.1.4 Example 4: Rubber Sealing

Next, we consider the compression of a rubber sealing studied in [67]. The geometry of the sealing is shown in Figure 5.12. The Ogden material with energy function $W_3(\boldsymbol{F})$ given in

(3.46c) is assumed with the following parameters

$$\kappa = 1000\ \mathrm{N/mm^2},\ m = 3,$$
$$\mu_1 = 0.63\ \mathrm{N/mm^2},\ \mu_2 = 0.0012\ \mathrm{N/mm^2},\ \mu_3 = -0.01\ \mathrm{N/mm^2},$$
$$\alpha_1 = 1.3,\ \alpha_2 = 5,\ \alpha_3 = -2.$$

We impose a vertical displacement v on the top of the sealing. Due to the symmetry of the problem, we only consider half of the sealing. Four unstructred meshes of the sealing are shown in Figure 5.12.

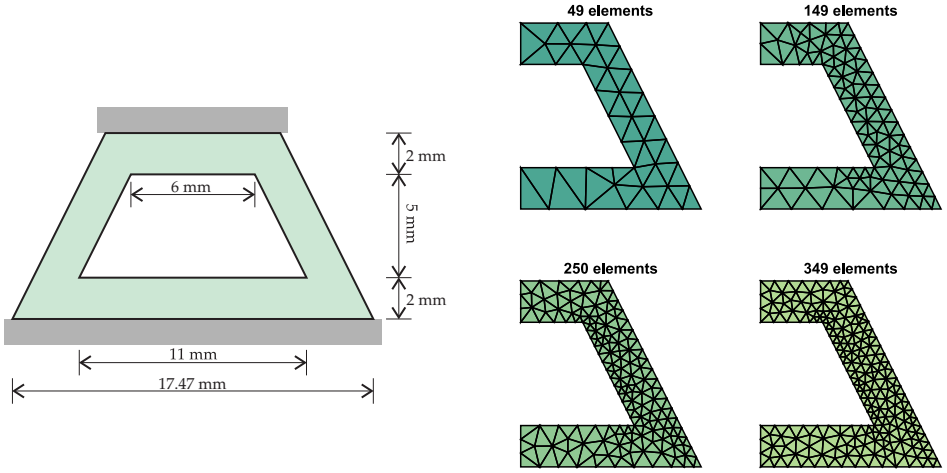

Figure 5.12: The rubber sealing example: Geometry, boundary conditions, and four unstructured meshes. Using symmetry of this problem, only half of the sealing is modeled.

In Figure 5.13, we have plotted L^2-norms of $\boldsymbol{U}_h$, $\boldsymbol{K}_h$, and $\boldsymbol{P}_h$ for different meshes under various vertical displacements v. The dashed and the solid curves are calculated by using $\mathsf{H1c1d}\bar{1}$ and $\mathsf{H2c2d}\bar{2}$, respectively. We observe that $\mathsf{H2c2d}\bar{2}$ converges rapidly. However, $\mathsf{H1c1d}\bar{1}$ has a poor performance in approximating $\boldsymbol{K}$ and $\boldsymbol{P}$. Figure 5.14 shows the deformed configurations of the sealing with $v = -2.2$ mm using the meshes of Figure 5.12. The results are obtained using $\mathsf{H2c2d}\bar{2}$ and colors indicate values of $\|\boldsymbol{P}\|$, where lighter colors correspond to higher values.

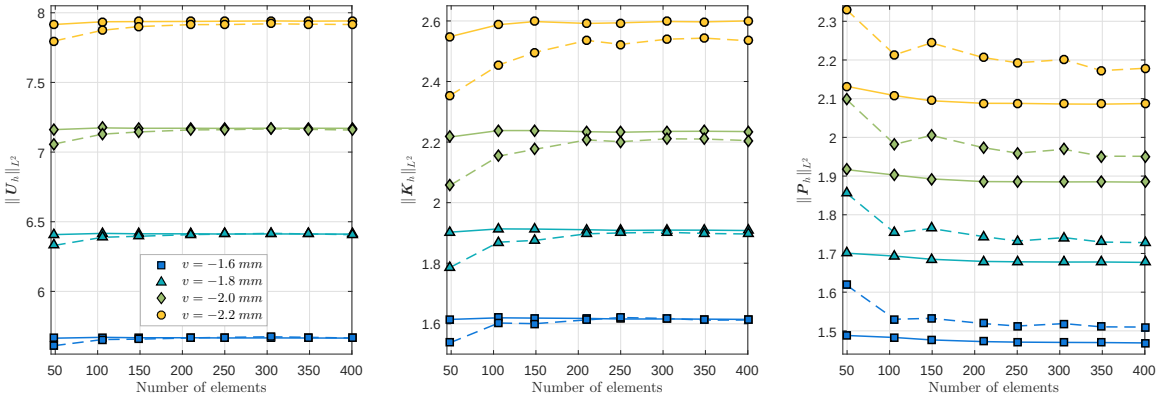

Figure 5.13: The rubber sealing example: L^2-norms of displacement, displacement gradient, and stress versus the number of elements in the mesh. Different curves indicate results associated to different values of the vertical displacement v at the sealing upper boundary. The dashed and the solid curves are obtained using H1c1d$\bar{1}$ and H2c2d$\bar{2}$, respectively. The underlying meshes have 49, 106, 149, 210, 250, 305, 349, and 400 elements.

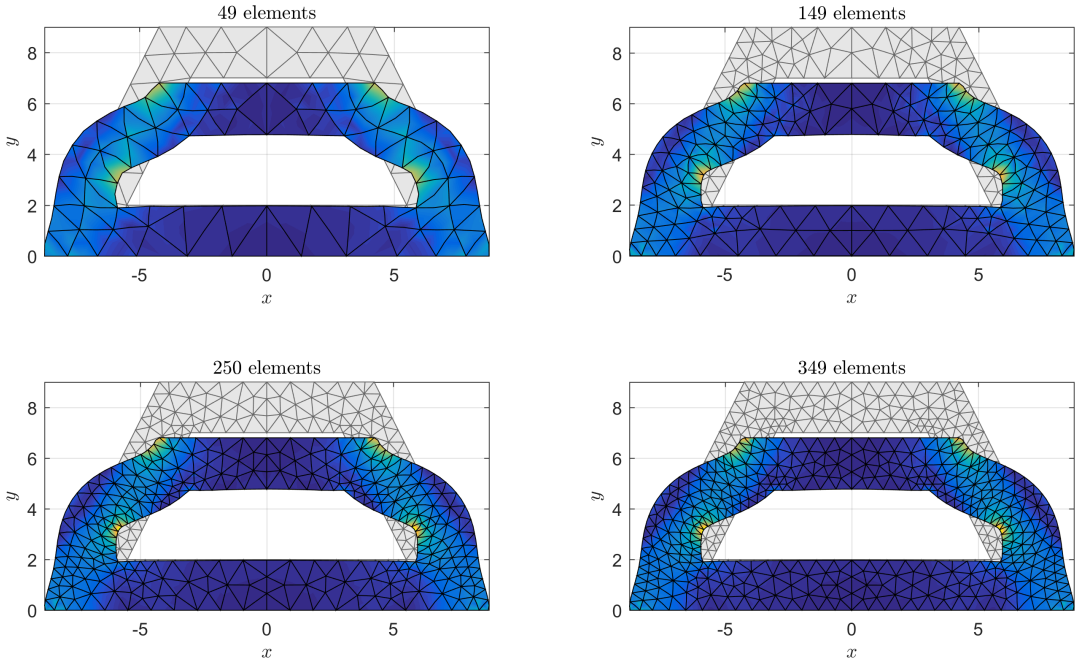

Figure 5.14: Deformed configurations of the rubber sealing example using H2c2d$\bar{2}$ and the meshes of Figure 5.12. The imposed vertical displacement at the upper boundary of the sealing is $v = -2.2$ mm (almost 25% shortening). Colors indicate values of the norm of stress $\|\boldsymbol{P}\|$, where lighter colors correspond to higher values of $\|\boldsymbol{P}\|$.

5.1.5 Example 5: A Plate with Randomly Distributed Holes

For studying the performance of CSFEMs on domains with complex geometries, we consider a square plate containing some randomly distributed holes with arbitrary shapes as shown in Figure 5.15. The material properties are the same as those of the Cook's membrane example. We fix the bottom of the plate and impose the displacement field $\boldsymbol{U} = (0, v)$ at the top of the plate. Figure 5.15 shows three unstructured meshes for the plate.

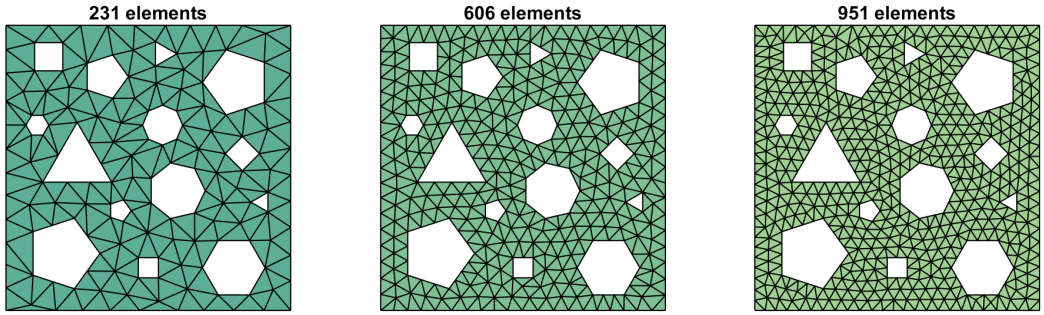

Figure 5.15: Three unstructured meshes for a plate with randomly distributed holes.

In Figure 5.16, we have plotted the L^2-norms of $\boldsymbol{U}$, $\boldsymbol{K}$, and $\boldsymbol{P}$ for various meshes under different values of the vertical displacement v at the top of the plate. The results are calculated using $\mathsf{H2c2d}\bar{2}$. One observes that even relatively coarse meshes lead to good approximations for stress. Figure 5.17 depicts the deformed configurations and the norm $\|\boldsymbol{P}\|$ associated to the meshes of Figure 5.15. The vertical displacement $v = 0.5$ mm is imposed at the top of the plate.

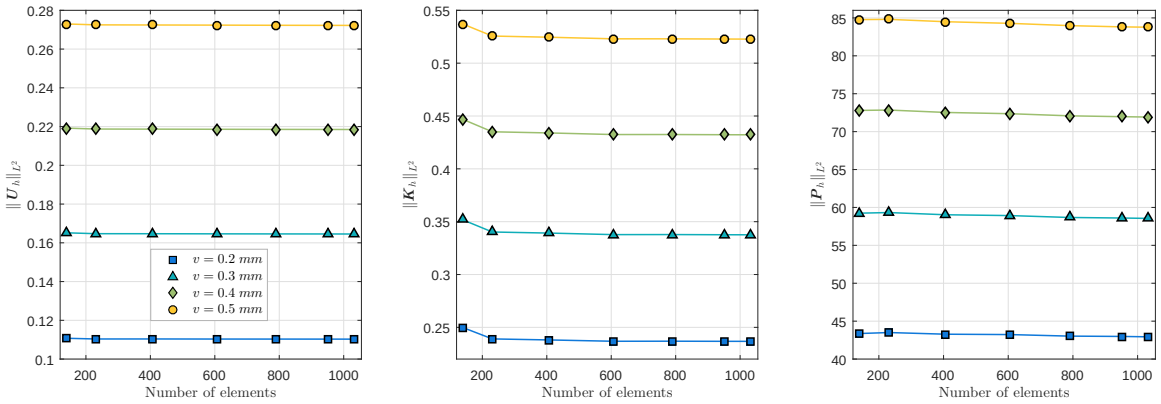

Figure 5.16: A plate with randomly distributed holes: L^2-norms of displacement, displacement gradient, and stress versus the number of elements in the mesh. Different curves indicate the results for different values of the vertical displacement v at the upper boundary of the plate. The results are obtained by using H2c2d$\bar{2}$. The underlying meshes have 139, 231, 407, 606, 789, 951, and 1033 elements.

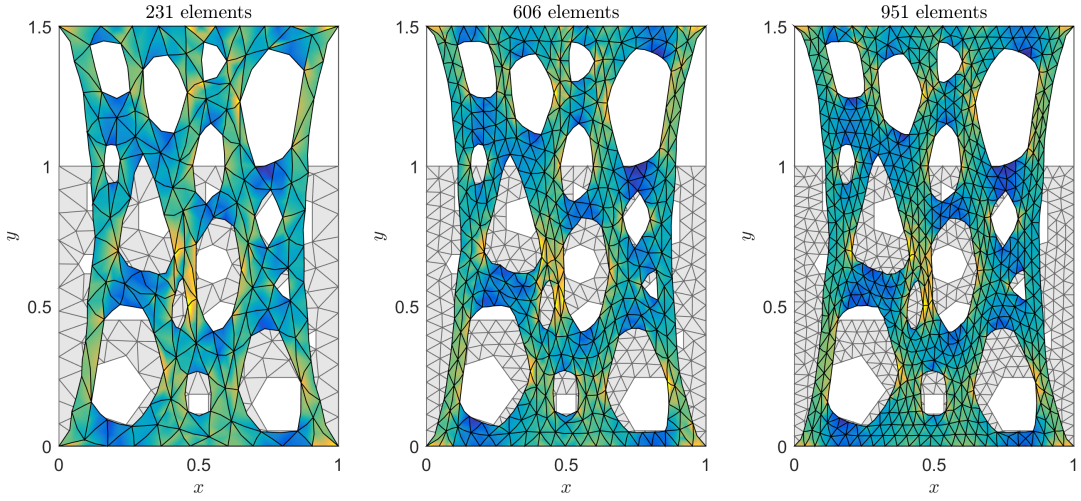

Figure 5.17: Deformed configurations of a plate with randomly distributed holes using H2c2d$\bar{2}$ and the meshes of Figure 5.15. The imposed vertical displacement at the upper boundary of the plate is $v = 0.5$ mm (50% stretch). Colors indicate values of the norm of stress $\|\boldsymbol{P}\|$, where lighter colors correspond to higher values of $\|\boldsymbol{P}\|$.

5.1.6 Example 6: Tension of a Heterogeneous Plate

As was mentioned in §3.4, the underlying $H^{\mathbf{c}}$ and $H^{\mathbf{d}}$-conformal finite element spaces of CSFEMs automatically satisfy the Hadamard jump condition and the zero traction

jumps at the internal edges, respectively. This fact can be used to model certain types of heterogeneous materials. More specifically, if inhomogeneities do not slide at the interfaces, i.e. at internal interfaces displacement is continuous and traction vectors are single-valued, then one can consider a single mesh for the entire heterogeneous structure and only associate different material properties to different elements depending on their locations.

To demonstrate the idea, we consider a simple heterogeneous square plate shown in Figure 5.18. The plate size is $1\ \mathrm{mm} \times 1\ \mathrm{mm}$ and there is a circular inhomogeneity of radius $0.25\ \mathrm{mm}$ at the center of the plate. The bottom of the plate is fixed and a $1\ \mathrm{mm}$ vertical displacement (100% stretch) is imposed on the top. Figure 5.18 shows four unstructured meshes for the plate. Instead of considering two separate meshes for the plate and the inhomogeneity and imposing suitable boundary conditions on their interfaces, we use a single mesh for the $1\ \mathrm{mm} \times 1\ \mathrm{mm}$ square and associate different material properties to elements depending on their position.

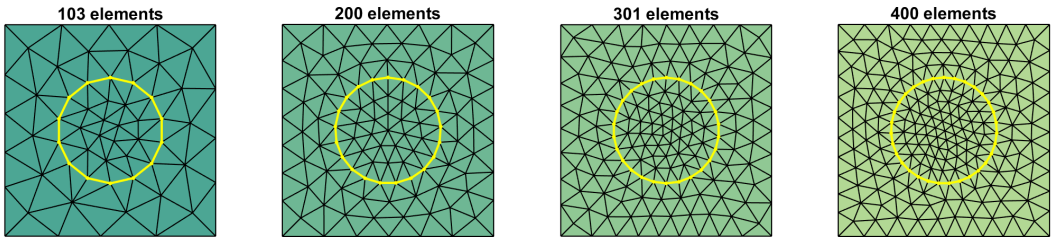

Figure 5.18: Four unstructured meshes for the heterogeneous plate example. The (yellow) circle indicates the interface between the plate and the circular inhomogeneity.

The energy function $W_2(\boldsymbol{F})$ with $(\kappa, \mu) = (120.291, 80.194)\ \mathrm{N/mm^2}$ is assumed for the plate. For the inhomogeneity, we use $W_2(\boldsymbol{F})$ with $(\kappa, \mu) = (\bar{\kappa}, \bar{\mu})$. The following four cases are studied: (i) A homogeneous plate: $(\bar{\kappa}, \bar{\mu}) = (120.291, 80.194)\ \mathrm{N/mm^2}$, (ii) a plate with a hole: $(\bar{\kappa}, \bar{\mu}) = (10^{-9}, 10^{-9})\ \mathrm{N/mm^2}$, (iii) $(\bar{\kappa}, \bar{\mu}) = (481.164, 320.776)\ \mathrm{N/mm^2}$, (iv) a rigid inhomogeneity: $(\bar{\kappa}, \bar{\mu}) = (10^9, 10^9)\ \mathrm{N/mm^2}$. Figure 5.19 shows the convergence of

solutions for these cases. The dashed and solid curves are obtained by using H1c1d$\bar{1}$ and H2c2d$\bar{2}$, respectively. One observes that except for the rigid inhomogeneity case, H1c1d$\bar{1}$ has a good performance.

Figure 5.20 depicts the deformed configuration of the case (iii) for the meshes of Figure 5.18. The results are calculated by using H2c2d$\bar{2}$ and colors indicate the values of the stress norm $\|\boldsymbol{P}\|$, where lighter colors correspond to higher values of $\|\boldsymbol{P}\|$. Finally, we have plotted the deformed configurations of the above four cases in Figure 5.21. The results are calculated by using H2c2d$\bar{2}$ and the underlying mesh has 200 elements. Colors indicate $\|\boldsymbol{P}\|$ and are normalized between all the deformed configurations so that the same colors in different configurations indicate the same values of $\|\boldsymbol{P}\|$. As one expects, $\|\boldsymbol{P}\|$ increases as the inhomogeneity becomes stiffer. For comparison purposes, we also considered tension of the same plate with a circular hole instead of the inhomogeneity and observed that the results coincide with those of case (ii) with a very soft inhomogeneity.

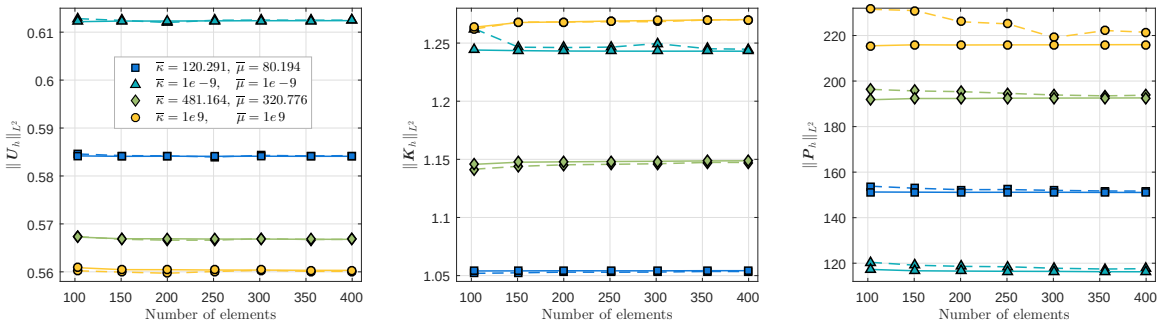

Figure 5.19: Tension of a heterogeneous plate: L^2-norms of displacement, displacement gradient, and stress for 100% tension versus the number of elements in the mesh. The plate material parameters are $\kappa = 120.291\ \mathrm{N/mm^2}$ and $\mu = 80.194\ \mathrm{N/mm^2}$ and those of the inhomogeneity $(\bar{\kappa}, \bar{\mu})$ are given in the legend. The dashed and the solid curves are obtained by using H1c1d$\bar{1}$ and H2c2d$\bar{2}$, respectively. The underlying meshes have 103, 151, 200, 251, 301, 356, and 400 elements.

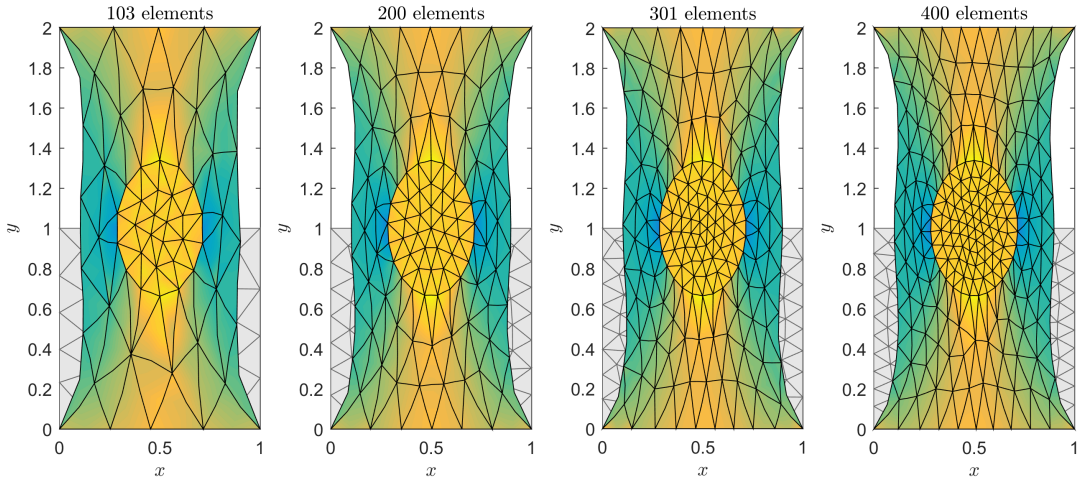

Figure 5.20: Deformed configurations of the heterogeneous plate under 100% stretch using H2c2d$\bar{2}$ and the meshes of Figure 5.18. The plate material parameters are $(\kappa, \mu) = (120.291, 80.194)\ \mathrm{N/mm^2}$ and those of the inhomogeneity are $(\bar{\kappa}, \bar{\mu}) = (481.164, 320.776)\ \mathrm{N/mm^2}$. Colors indicate values of the norm of stress $\|\boldsymbol{P}\|$, where lighter colors correspond to higher values of $\|\boldsymbol{P}\|$.

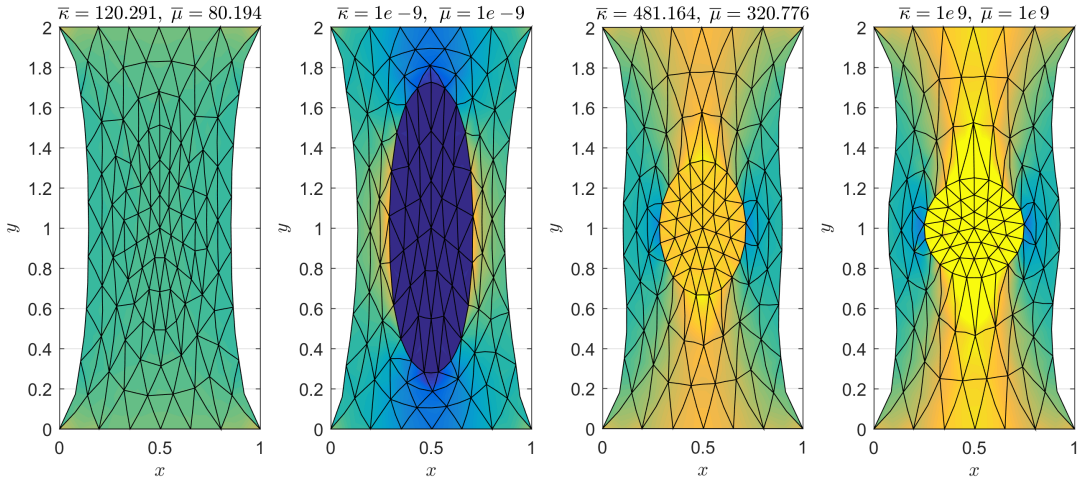

Figure 5.21: Deformed configurations of the heterogeneous plate under 100% stretch with different material properties for its inhomogeneity. Results are calculated using H2c2d$\bar{2}$ and the mesh has 200 elements. The plate material parameters are $(\kappa, \mu) = (120.291, 80.194)\ \mathrm{N/mm^2}$ and those of the inhomogeneity are written above the corresponding figure. Colors indicate values of the norm of stress $\|\boldsymbol{P}\|$, where lighter colors correspond to larger values of $\|\boldsymbol{P}\|$. Colors are normalized between figures such that the same colors in different figures indicate the same values.

5.2 Examples for 2D Incompressible Solids

5.2.1 Example 1: Inflation of a Cylindrical Shell.

We consider the inflation of an incompressible thick cylindrical shell shown in Figure 5.22. The inner boundary of the shell is traction free and the outer boundary is subjected to $\boldsymbol{U}_{\text{out}} = (\lambda - 1)\mathbf{X}$. We assume that there is no body force, i.e., $\boldsymbol{B} = \mathbf{0}$. Owing to the incompressibility constraint $J = 1$, one can obtain the exact solution of the problem as follows:

$$\boldsymbol{U}_e(\mathbf{X}) = \left(\frac{r(R)}{R} - 1\right)\mathbf{X},$$
$$p_e(\mathbf{X}) = -\mu\frac{R^2}{r(R)^2} + \frac{\mu(\lambda^2-1)R_{\text{out}}^2}{2}\left(\frac{1}{r(R_{\text{in}})^2} - \frac{1}{r(R)^2}\right) + \mu\ln\left(\frac{r(R_{\text{in}})}{R_{\text{in}}r(R)}R\right),$$

where $r(R) = \sqrt{R^2 + (\lambda^2-1)R_{\text{out}}^2}$ and $R = \|\mathbf{X}\|$. Having $\boldsymbol{U}_e$ and p_e, one can obtain $\boldsymbol{K}_e = \mathbf{grad}\,\boldsymbol{U}_e$ and $\boldsymbol{P}_e = \widetilde{\boldsymbol{P}}(\boldsymbol{K}_e) + p_e\boldsymbol{Q}(\boldsymbol{K}_e)$. The exact solution enables one to study and verify the accuracy and convergence of CSFEMs. Note that this is an example of a universal deformation [68]. For our numerical analysis, we assume that $R_{\text{in}} = 0.5\,\text{mm}$, $R_{\text{out}} = 1\,\text{mm}$, and $\lambda = 3$. We also assume $\mu = 1\ \text{N}/\text{mm}^2$ in (3.49) and use the constraint function $C(J) = J - 1$. Using symmetry of the problem, we model only a quarter of the shell in the numerical analysis (see the generated unstructured meshes in Figure 5.22). Using the symmetry and the numerical solutions of a quarter of the domain, one will be able to recover the solution for the entire domain.

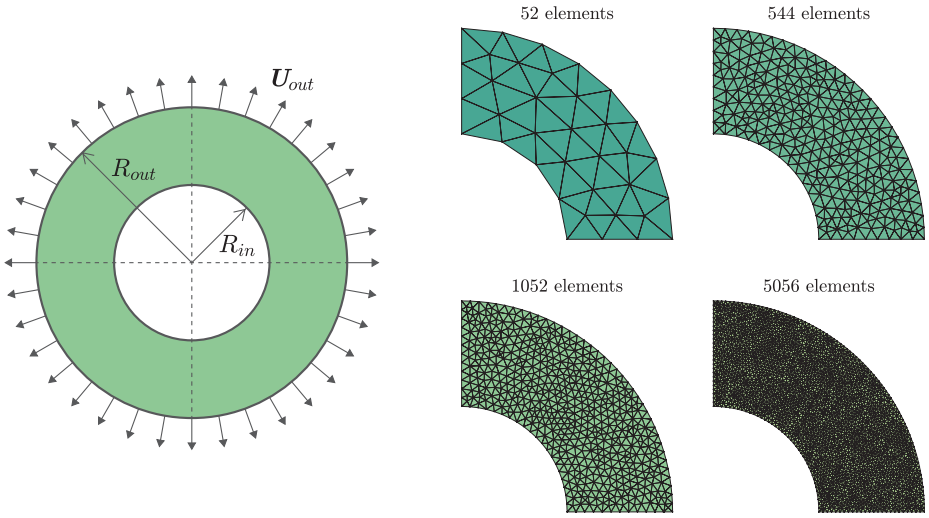

Figure 5.22: Inflation of a cylindrical shell: Geometry, boundary conditions, and four unstructured meshes.

As was discussed in §3.7, among the 96 possible choices of the first and second-order CSFEMs, only 21 may result in a non-singular tangent stiffness matrix $\mathbb{K}_{t_h}$ and the remaining 75 CSFEMs have solvability issues. We studied and compared the performance of the 21 solvable CSFEMs using the exact solution of this problem. Our numerical experiments indicate that the following 8 CSFEMs have good performance: H1c1d$\bar{1}$L0, H1c$\bar{2}$d$\bar{1}$L0, H1c$\bar{2}$d$\bar{1}$L1, H1c$\bar{2}$d1L0, H1c2d1L0, H2c2d$\bar{2}$L0, H2c2d$\bar{2}$L1, H2c2d$\bar{2}$L2. We do not consider the reaming 13 CSFEMs further due to their poor performance.

For the four meshes shown in Figure 5.22, the relative L^2-norm of errors associated with each of the above 8 CSFEMs are given in Table 5.2. Considering the relative errors of the four primary field variables $\boldsymbol{U}$, $\boldsymbol{K}$, $\boldsymbol{P}$, and p, H2c2d$\bar{2}$L1 (#7) is the most accurate method among all CSFEMs. Based on the number of degrees of freedom in the fourth column, H1c1d$\bar{1}$L0 (#1) has the least computational cost among all CSFEMs. Although for an identical mesh, H1c$\bar{2}$d$\bar{1}$L0, H1c$\bar{2}$d$\bar{1}$L1, H1c$\bar{2}$d1L0, and H2c2d$\bar{2}$L2 (#2 − #4 and #8) have (many) more degrees of freedom than H1c1d$\bar{1}$L0 (#1), none of them has a better relative error in approximating the four primary variables. For an identical mesh, H1c2d1L0 and H2c2d$\bar{2}$L0 (#5 and #6) are more accurate than H1c1d$\bar{1}$L0 (#1) in approximating the

four primary variables, but they are computationally much more expensive (more number of DOFs). In other words, it may be better to refine the mesh and use H1c1d$\bar{1}$L0 rather than using H1c2d1L0 or H2c2d$\bar{2}$L0 with a coarser mesh. Therefore, H2c2d$\bar{2}$L1 and H1c1d$\bar{1}$L0 ($\#1$ and $\#7$), which are shown in Figure 3.4, have an overall better performance among all CSFEMs. Between these two methods, if we compare H1c1d$\bar{1}$L0 with 56298 #DOF and H2c2d$\bar{2}$L1 with 34240 #DOF, we conclude that the latter method results in a more accurate solution for less computational cost.

To study the convergence order of CSFEMs, we plot the relative errors of the four primary variables versus the maximum diameter h of some unstructured meshes in Figure 5.23. Note that our observations in Table 5.2 also hold for Figure 5.23 with regard to accuracy. The convergence order of displacement $\boldsymbol{U}$ is close to 2 for all methods. The convergence order of displacement gradient $\boldsymbol{K}$ is close to 1 for all methods except H2c2d$\bar{2}$L1 and H2c2d$\bar{2}$L2, for which the convergence order is almost 2. For the stress $\boldsymbol{P}$, the convergence order is close to 1 for all methods except H2c2d$\bar{2}$L1, which has a convergence order of almost 2. We also observe that the convergence order of the pressure-like variable p and the stress $\boldsymbol{P}$ are the same for all methods. Based on the above discussions, we will use H1c1d$\bar{1}$L0 and H2c2d$\bar{2}$L1 in the following examples.

Table 5.2: Convergence and relative error of different CSFEMs for inflation of a cylindrical shell. DOF denotes the degrees of freedom for each mesh, ($\boldsymbol{U}_e$, $\boldsymbol{F}_e$, $\boldsymbol{P}_e$, p_e) is the exact solution, and ($\boldsymbol{U}_h$, $\boldsymbol{F}_h$, $\boldsymbol{P}_h$, p_h) is the approximate solution for each CSFEM.

#	CSFEM	#Elements	#DOF	$\frac{\|\boldsymbol{U}_h-\boldsymbol{U}_e\|_{L^2}}{\|\boldsymbol{U}_e\|_{L^2}}$	$\frac{\|\boldsymbol{K}_h-\boldsymbol{K}_e\|_{L^2}}{\|\boldsymbol{K}_e\|_{L^2}}$	$\frac{\|\boldsymbol{P}_h-\boldsymbol{P}_e\|_{L^2}}{\|\boldsymbol{P}_e\|_{L^2}}$	$\frac{\|p_h-p_e\|_{L^2}}{\|p_e\|_{L^2}}$
1	H1c1d$\bar{1}$L0	52	646	7.38e-03	1.19e-01	3.45e-01	4.98e-01
		544	6226	7.03e-04	3.04e-02	8.68e-02	1.67e-01
		1052	11902	3.63e-04	2.05e-02	7.43e-02	1.44e-01
		5056	56298	7.95e-05	9.54e-03	3.20e-02	5.98e-02
2	H1c$\bar{2}$d$\bar{1}$L0	52	854	6.97e-03	1.38e-01	1.76e-01	2.14e-01
		544	8402	6.28e-04	3.75e-02	4.11e-02	4.96e-02
		1052	16110	3.28e-04	2.61e-02	2.89e-02	3.56e-02
		5056	76522	7.20e-05	1.22e-02	1.40e-02	1.57e-02
3	H1c$\bar{2}$d$\bar{1}$L1	52	958	7.29e-03	1.46e-01	3.74e-01	7.29e-01
		544	9490	6.27e-04	4.02e-02	7.64e-02	1.34e-01
		1052	18214	3.21e-04	2.76e-02	5.21e-02	8.92e-02
		5056	86634	7.05e-05	1.28e-02	2.25e-02	3.62e-02
4	H1c$\bar{2}$d1L0	52	1028	7.18e-03	1.06e-01	3.73e-01	4.89e-01
		544	10094	6.86e-04	2.66e-02	1.00e-01	1.73e-01
		1052	19348	3.56e-04	1.83e-02	8.66e-02	1.44e-01
		5056	91860	7.84e-05	8.61e-03	3.75e-02	6.06e-02
5	H1c2d1L0	52	1306	7.32e-03	6.80e-02	6.56e-02	1.34e-01
		544	12874	6.57e-04	1.94e-02	1.85e-02	4.34e-02
		1052	24690	3.47e-04	1.36e-02	1.27e-02	3.06e-02
		5056	117310	7.56e-05	6.28e-03	5.64e-03	1.37e-02
6	H2c2d$\bar{2}$L0	52	1688	2.74e-03	4.45e-02	3.45e-02	1.09e-01
		544	16742	2.70e-04	1.37e-02	1.15e-02	3.84e-02
		1052	32136	1.46e-04	1.01e-02	8.29e-03	2.78e-02
		5056	152872	3.17e-05	4.64e-03	3.84e-03	1.29e-02
7	H2c2d$\bar{2}$L1	52	1792	1.16e-03	1.96e-02	5.41e-02	1.21e-01
		544	17830	8.51e-05	1.97e-03	8.70e-03	1.88e-02
		1052	34240	4.57e-05	1.07e-03	4.91e-03	1.06e-02
		5056	162984	1.02e-05	2.75e-04	1.42e-03	3.16e-03
8	H2c2d$\bar{2}$L2	52	1948	1.32e-03	3.21e-02	3.25e-01	1.07
		544	19462	9.42e-05	4.58e-03	1.07e-01	2.69e-01
		1052	37396	4.85e-05	2.53e-03	6.42e-02	1.51e-01
		5056	178152	1.04e-05	7.03e-04	2.35e-02	5.03e-02

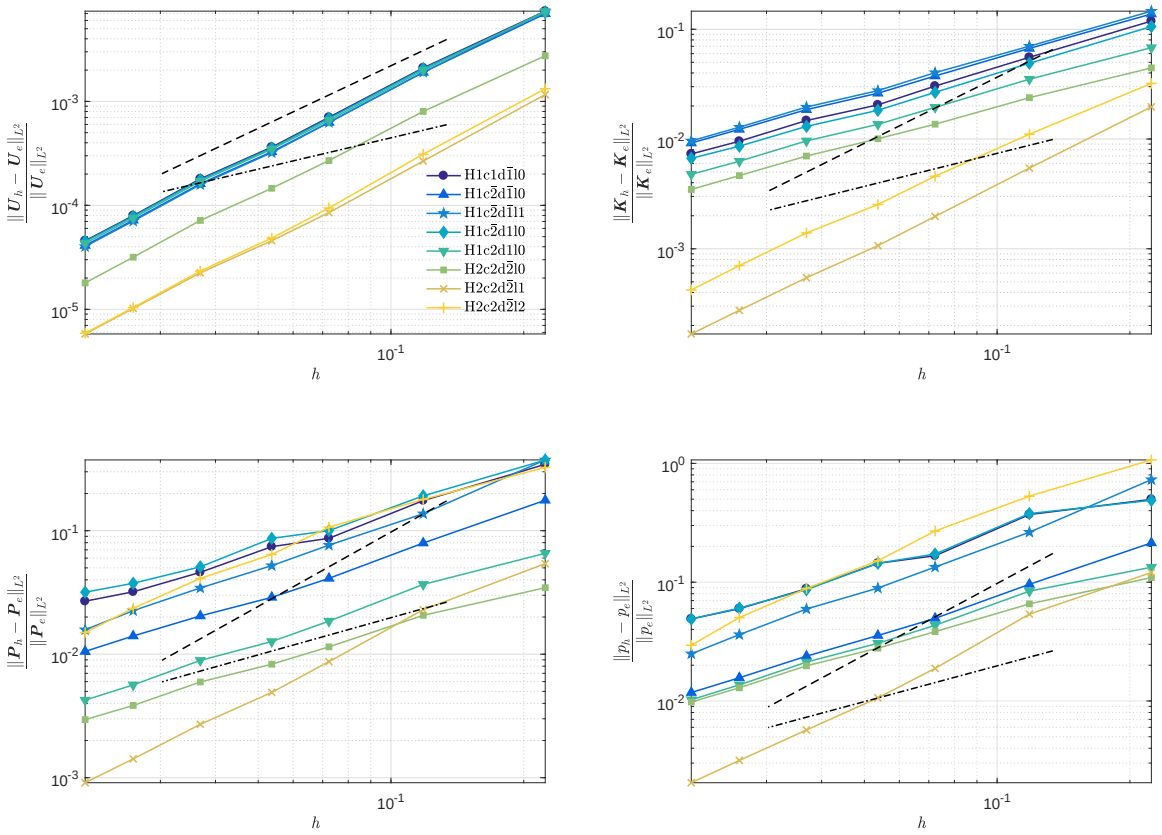

Figure 5.23: Relative L^2-norms of errors in approximating displacement, displacement gradient, stress, and pressure versus the maximum diameter h. In each diagram, different curves are associated with different CSFEMs. In each diagram, the dash-dot line and the dashed line have the slopes of 1 and 2, respectively.

5.2.2 Example 2: Cook's Membrane.

To assess the performance of CSFEMs in bending analysis, we consider the standard Cook's membrane problem shown in Figure 5.24. We assume $\mu = 1\ \mathrm{N/mm^2}$ and use the constraint function $C(J) = \ln J$. We investigate the pointwise convergence of H1c1d$\bar{1}$L0 and H2c2d$\bar{2}$L1 in Figure 5.25 by plotting the vertical displacement of point A indicated in Figure 5.24 for different meshes and for different values of the shearing force f. We also compare our results with those generated only for $f = 0.1\,\mathrm{N/mm^2}$ in the work of Chi *et al.* [36]. We observe that both CSFEMs provide good approximations for relatively coarse meshes and H2c2d$\bar{2}$L1 converges faster than H1c1d$\bar{1}$L0. Also, there is a good agreement

between CSFEMs and the method used in [36].

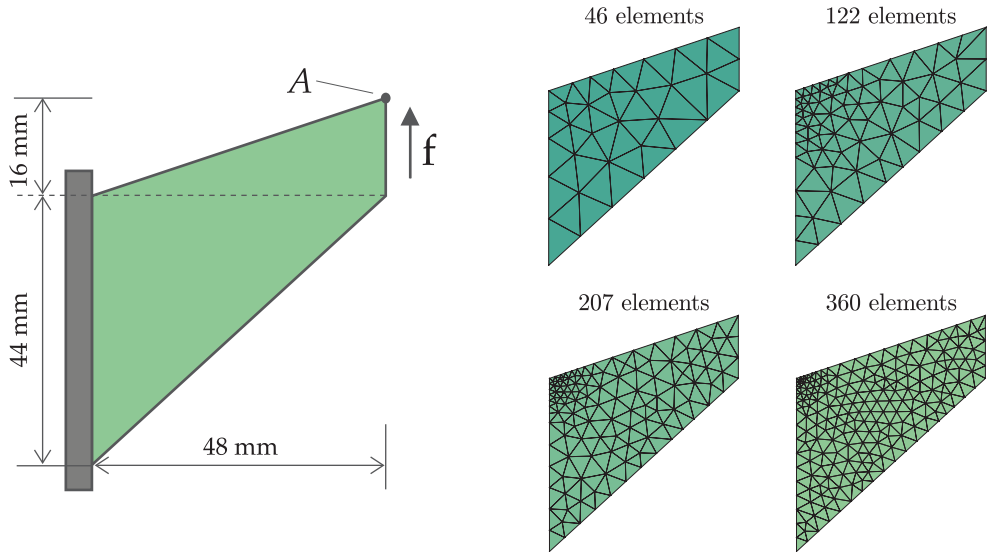

Figure 5.24: Cook's membrane: Geometry, boundary conditions, and four unstructured meshes.

Figures 5.26 and 5.27 depict the deformed configurations of Cook's membrane for the four meshes of Figure 5.24 and $f = 0.3\ \mathrm{N/mm^2}$ by using $\mathsf{H1c1d\bar{1}L0}$ and $\mathsf{H2c2d\bar{2}L1}$, receptively. In both figures, colors indicate the values of $\|\boldsymbol{P}_h\|$ in the first row and the values of the pressure p_h in the second row with lighter colors corresponding to larger values. The standard two-field mixed formulation of incompressible elasticity in terms of displacement and pressure is unstable if displacement is approximated by continuous piecewise linear polynomials and pressure with piecewise constant polynomials on triangular elements [26, 36]. Although $\mathsf{H1c1d\bar{1}L0}$ uses the same low-order polynomial spaces for displacement and pressure, as it can be observed from Figure 5.26, it is convergent and does not result in any numerical artifacts in the approximation of pressure. Note that in the mixed formulation of CSFEMs such as $\mathsf{H1c1d\bar{1}L0}$, displacement and pressure are not coupled directly with a bilinear term. In addition, comparing with the standard two-field mixed FEMs, $\mathsf{H1c1d\bar{1}L0}$ provides a more accurate approximation of strain and stress by approximating them directly in their domains of definition. In Figure 5.27, one observes the fast convergence of

H2c2d$\bar{2}$L1 in approximating stress and pressure and its accuracy even for a coarse mesh with 46 elements.

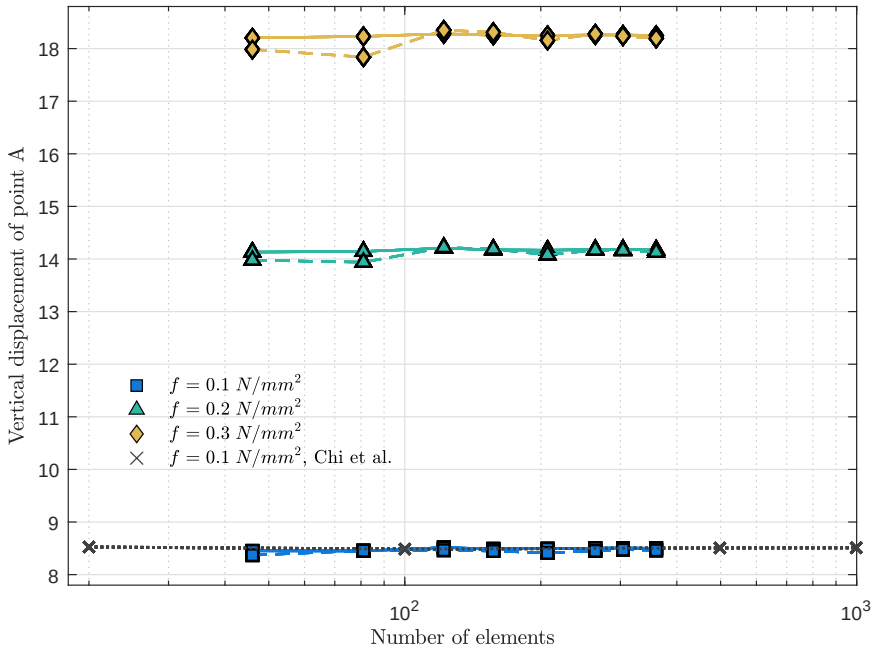

Figure 5.25: Cook's membrane: Vertical displacement of point A in Figure 5.24 for different values of the shearing force f versus the number of elements in the mesh. The dashed and the solid lines are generated using H1c1d$\bar{1}$L0 and H2c2d$\bar{2}$L1, respectively. The dotted line indicates the results of [36].

To study convergence, in Figure 5.28, we plot the L^2-norms of displacement, displacement gradient, stress, and pressure using H1c1d$\bar{1}$L0 (dashed lines) and H2c2d$\bar{2}$L1 (solid lines) and for different values of shearing force f. Considering the four primary variables and for all values of the shearing force f, one can see that H2c2d$\bar{2}$L1 converges rapidly. The convergence of H1c1d$\bar{1}$L0 is comparable to that of H2c2d$\bar{2}$L1 in approximating $\boldsymbol{U}$ and $\boldsymbol{K}$. However, the convergence of H1c1d$\bar{1}$L0 in approximating $\boldsymbol{P}$ and p becomes slower than that of H2c2d$\bar{2}$L1 as the value of the shearing force f increases.

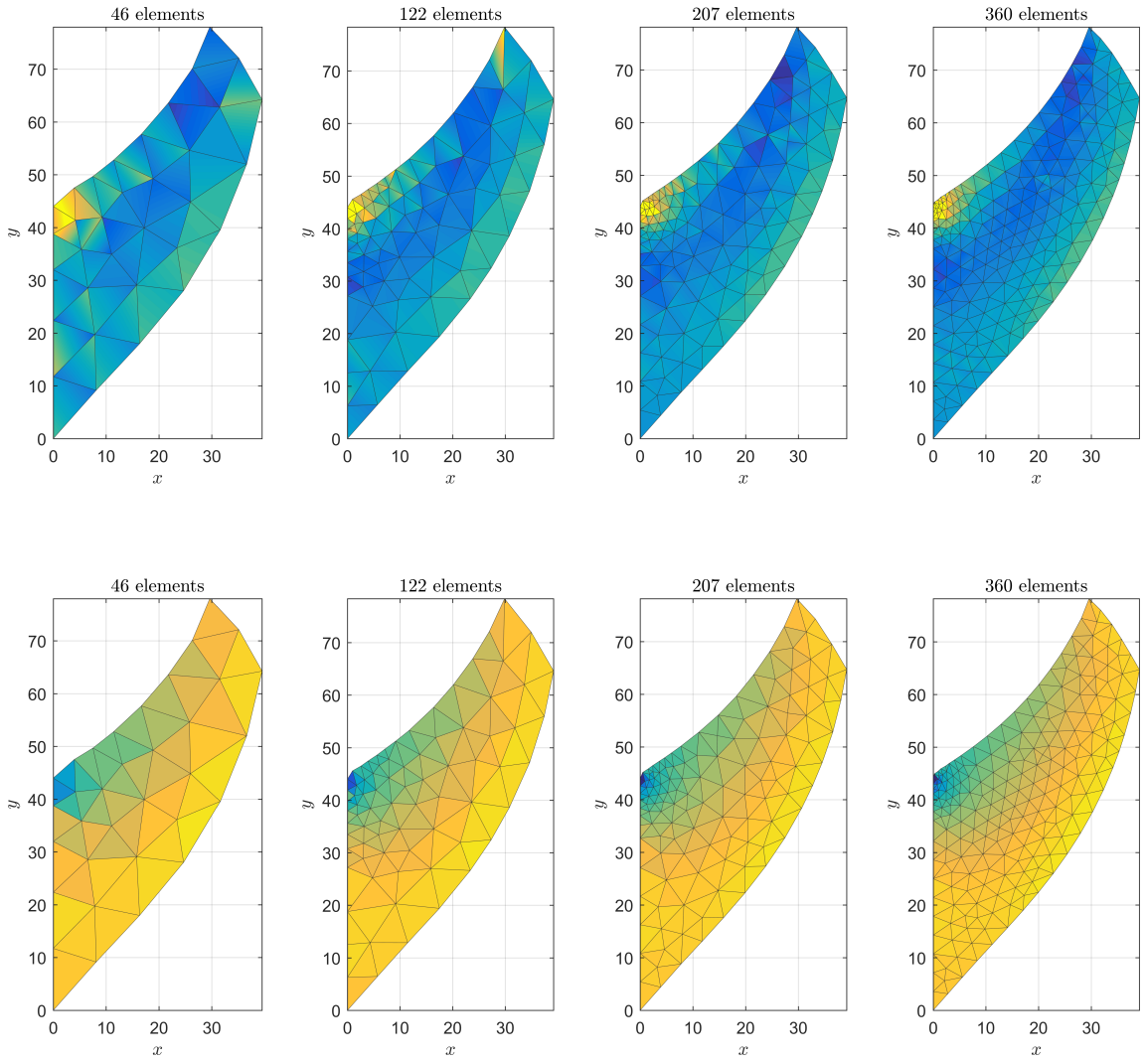

Figure 5.26: The deformed configurations of Cook's membrane for the shear force $f = 0.3\ \mathrm{N/mm^2}$ using H1c1d$\bar{1}$L0. Colors indicate values of $\|\boldsymbol{P}_h\|$ in the first row and pressure p_h in the second row, where lighter colors correspond to larger values.

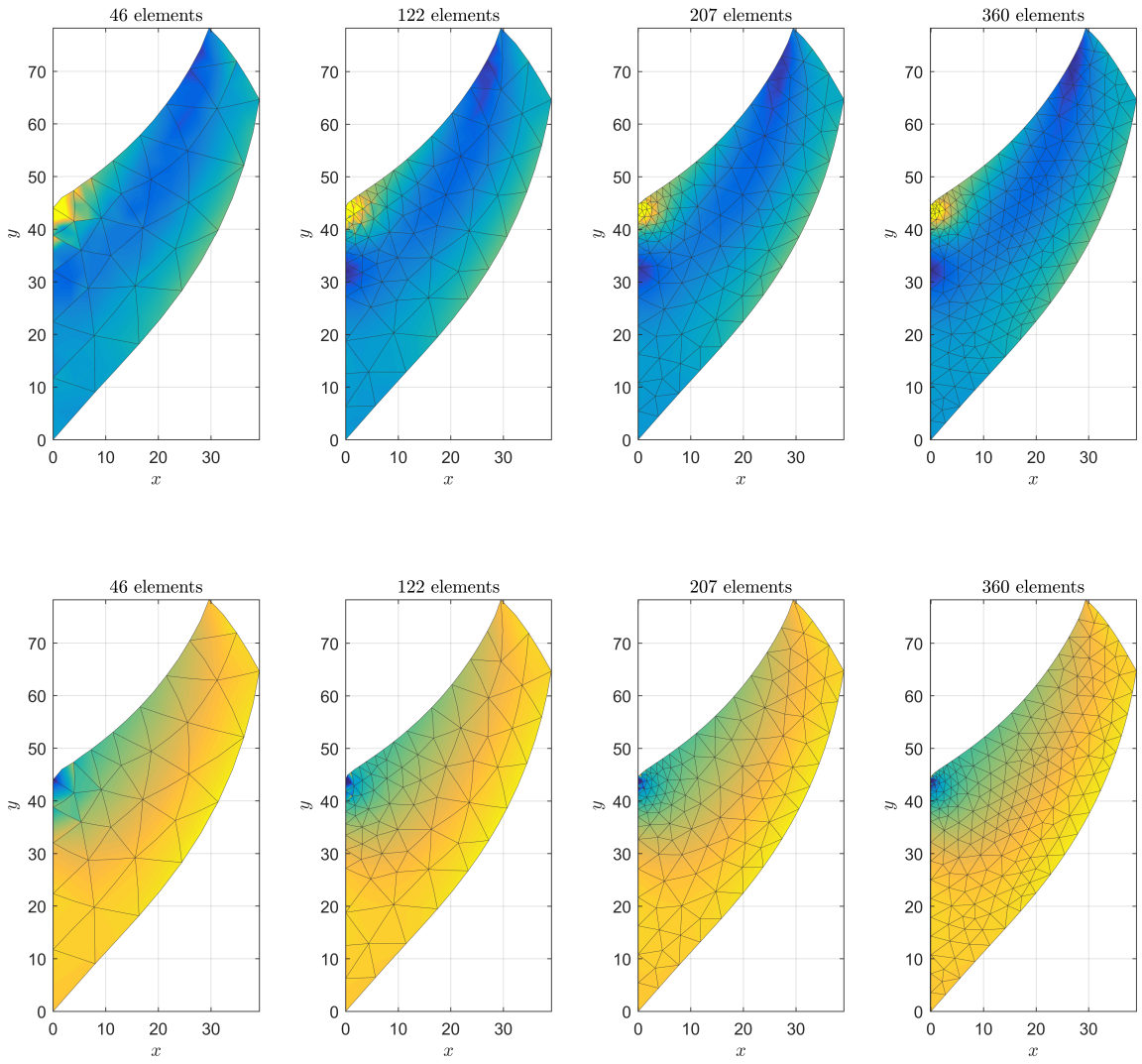

Figure 5.27: The deformed configurations of Cook's membrane for the shear force $f = 0.3\ \mathrm{N/mm^2}$ using H2c2d$\bar{2}$L1. Colors indicate values of $\|\boldsymbol{P}_h\|$ in the first row and pressure p_h in the second row, where lighter colors correspond to larger values.

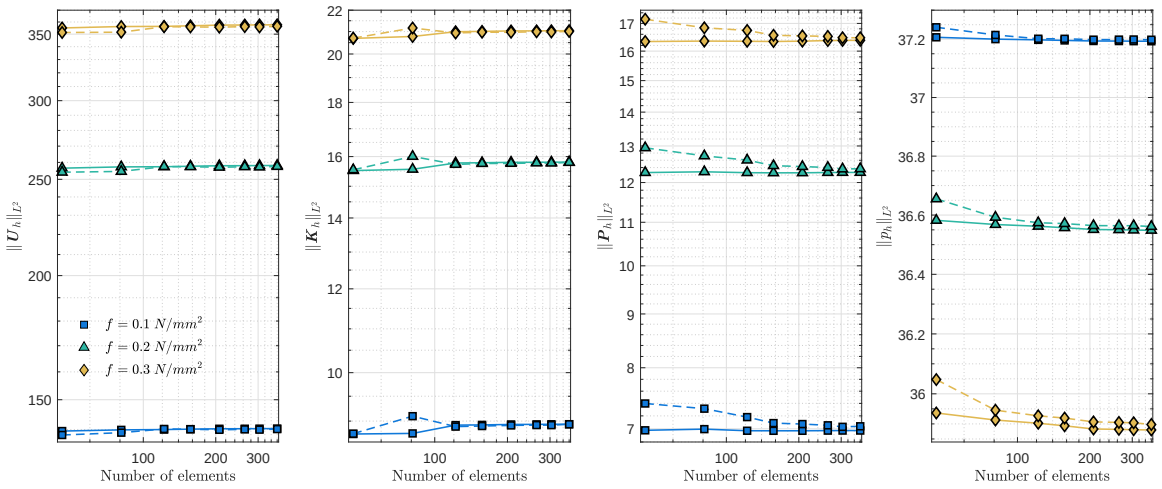

Figure 5.28: Cook's membrane: L^2-norms of displacement, displacement gradient, stress, and pressure versus the number of elements in the mesh for different values of the shearing force f. The dashed and the solid lines are obtained by using H1c1d$\bar{1}$L0 and H2c2d$\bar{2}$L1, respectively.

5.2.3 Example 3: Bending of an Arch.

Following [41], for further testing of H1c1d$\bar{1}$L0 and H2c2d$\bar{2}$L1 in bending problems, we consider bending of the arch shown in Figure 5.29. Note that f in Figure 5.29 is a uniformly distributed load in the radial direction. We assume $E = 250\,\mathrm{N/mm^2}$ and $\nu = 0.5$ ($\mu = E/2(1+\nu)$) and use $C(J) = \ln J$ as the constraint function. Because of the symmetry, we study half of the arch as shown in the generated meshes in Figure 5.29. Figure 5.30 shows the reference and the deformed states of the arch subjected to $f = 20\,\mathrm{N/mm^2}$ using H2c2d$\bar{2}$L1 and the mesh with 324 elements in Figure 5.29. The colors indicate the values of $\|\boldsymbol{K}_h\|$ with lighter colors corresponding to larger values. As one expects, the middle portion of the half of the arch at $x = 0.3$ ($x = -0.3$) is narrowed and stretched, and hence shows large values of $\|\boldsymbol{K}_h\|$.

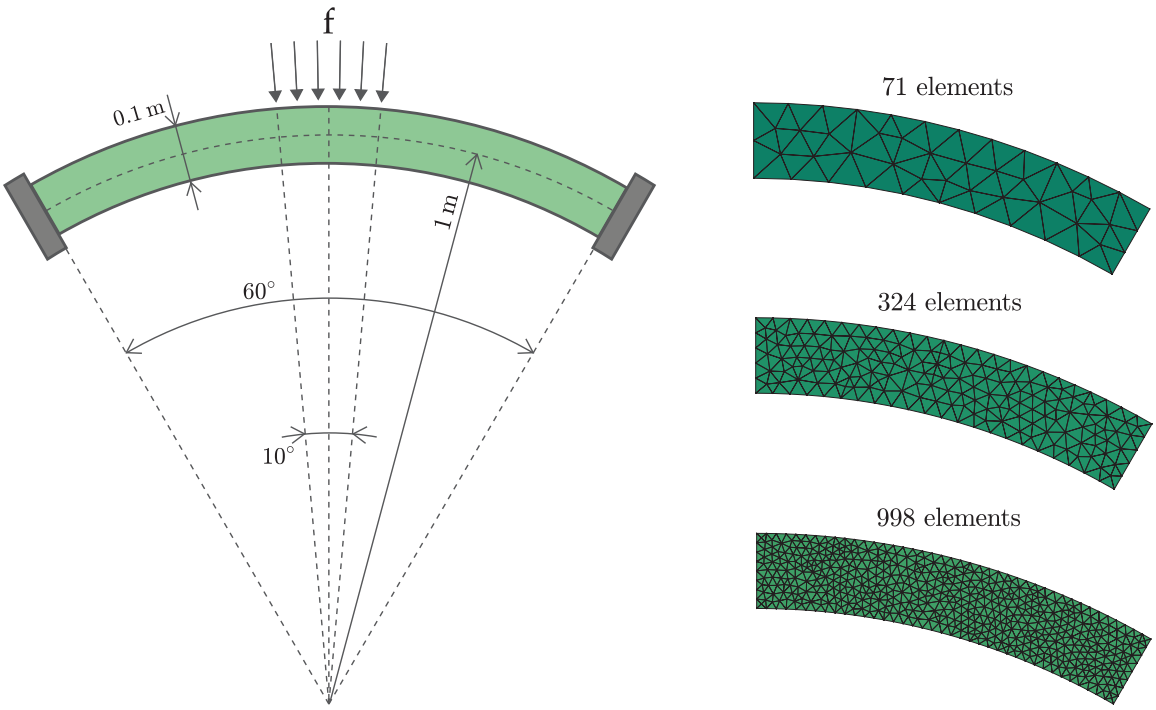

Figure 5.29: Bending of an arch: Geometry, boundary conditions, and three unstructured meshes.

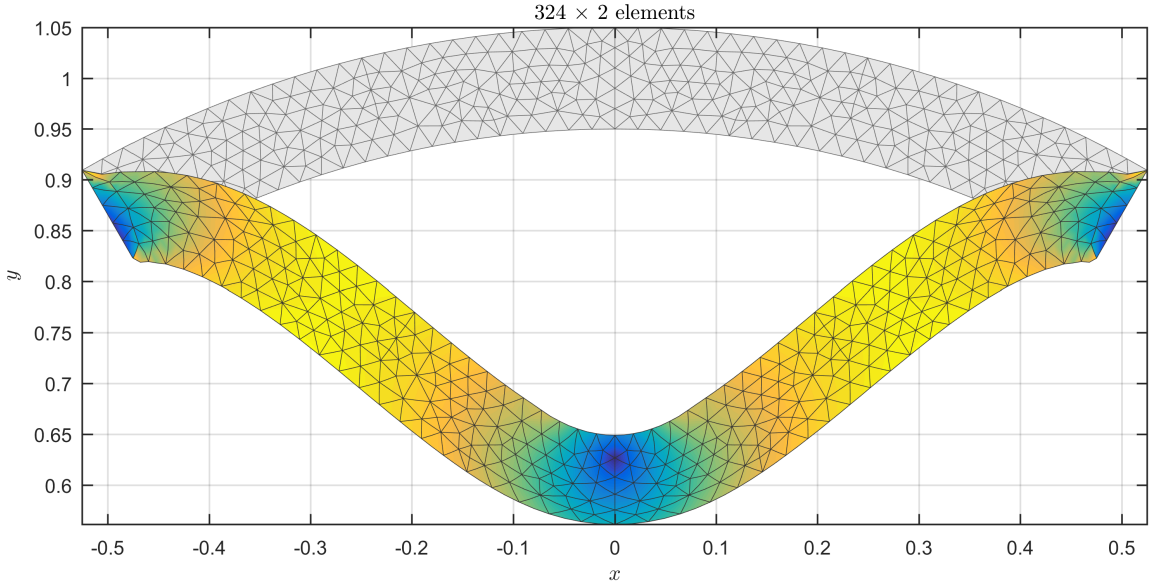

Figure 5.30: The reference and deformed configurations of the arch for the bending load $f = 20\ \mathrm{N/mm^2}$ using H2c2d$\bar{2}$L1. Colors indicate values of the norm of displacement gradient $\|\boldsymbol{K}_h\|$, where lighter colors correspond to larger values.

Figure 5.31 shows the convergence of H1c1d$\bar{1}$L0 (dashed lines) and H2c2d$\bar{2}$L1 (solid lines) for different values of the load f. We observe that both methods converge considering all the four primary fields and for all values of the transverse load f. However, H2c2d$\bar{2}$L1 has a faster convergence, and hence provides a more accurate approximation when using coarse meshes. Figure 5.32 shows the deformed configurations of half of the arch for $f = 20\,\mathrm{N/mm^2}$ using the meshes of Figure 5.29. The results are generated using H2c2d$\bar{2}$L1 and colors indicate the values of $\|\boldsymbol{P}_h\|$ in the first row and p_h in the second row, where lighter colors correspond to higher values. Comparing the mesh with 71 elements with the mesh with 998 elements, one can see the accuracy of H2c2d$\bar{2}$L1 in approximating stress and pressure even when using a coarse mesh.

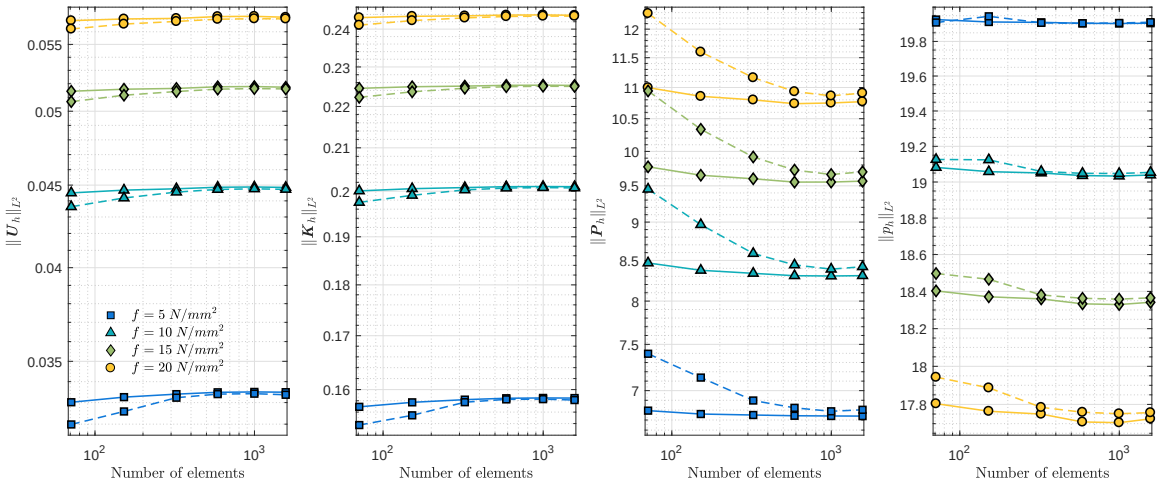

Figure 5.31: Bending of an arch: L^2-norms of displacement, displacement gradient, stress, and pressure versus the number of elements in the mesh for different values of the bending force f. The dashed and the solid lines are obtained using H1c1d$\bar{1}$L0 and H2c2d$\bar{2}$L1, respectively.

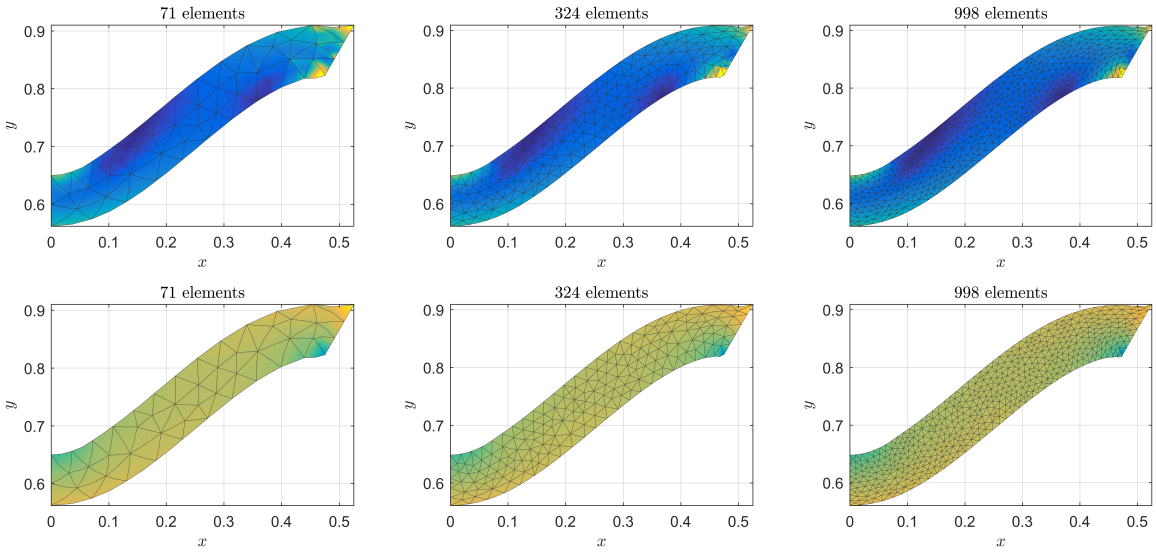

Figure 5.32: The deformed configurations of the arch for the bending load $f = 20\,\mathrm{N/mm^2}$ using H2c2d$\bar{2}$L1. Colors indicate values of the norm of stress $\|\boldsymbol{P}_h\|$ in the first row and the pressure p_h in the second row, where lighter colors correspond to larger values.

5.2.4 Example 4: Stretching a Block with a Hole at its Center.

We consider a square block with a hole at its center as shown in Figure 5.33. The block is subjected to uniform displacement boundaries of $(u, 0)$ at its right and $(-u, 0)$ at its left edge. The top and bottom edges are traction free. The goal of this example is to test the performance of CSFEMs at very large stretches. We assume $\mu = 1\,\mathrm{N/mm^2}$ and use $C(J) = J - 1$. Due to symmetry, we consider only a quarter of the block as shown in the generated meshes in Figure 5.33. Figure 5.34 illustrates the reference and the deformed configurations of the block using H2c2d$\bar{2}$L1 and the mesh with 184 elements in Figure 5.33. The boundary displacement $u = 1.5\,\mathrm{mm}$ results in a large stretch of 4. The colors indicate the values of $\|\boldsymbol{K}_h\|$ with lighter colors associated with larger values. The maximum of $\|\boldsymbol{K}_h\|$ is 6.5 at the boundary of the hole and $x = 0$. Figure 5.35 illustrates the convergence of H1c1d$\bar{1}$L0 (dashed lines) and H2c2d$\bar{2}$L1 (solid lines) for different values of the imposed boundary displacement u. We observe that H2c2d$\bar{2}$L1 converges rapidly considering all the primary variables and for all values of u. Also, considering displacement, displacement

gradient, and stress, H1c1d$\bar{1}$L0 has a good convergence, but it has a poor performance in approximating pressure for $stretch = 4$ ($u = 1.5\,\mathrm{mm}$). Figure 5.36 shows the deformed configurations of a quarter of the block for $u = 1.5\,\mathrm{mm}$ using the meshes of Figure 5.33. The results are obtained using H2c2d$\bar{2}$L1 and colors indicate the values of $\|\boldsymbol{P}_h\|$ in the first column and p_h in the second column, where lighter colors correspond to higher values. As one can observe, even for $stretch = 4$ and using a coarse mesh with 48 elements, H2c2d$\bar{2}$L1 provides an accurate distribution of stress and pressure.

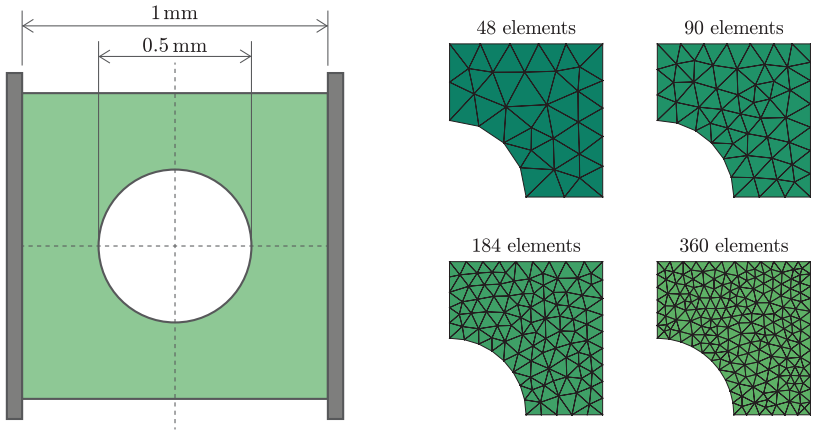

Figure 5.33: Stretching a block with a hole at its center: Geometry, boundary conditions, and four unstructured meshes.

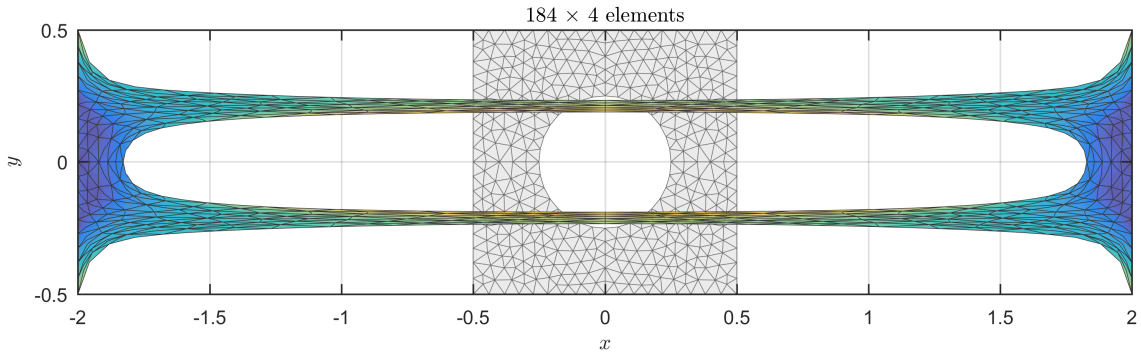

Figure 5.34: The reference and deformed configurations of a block with a hole for $u = 1.5\,\mathrm{mm}$ ($stretch = 4$) obtained by using H2c2d$\bar{2}$L1. Colors indicate values of the norm of displacement gradient $\|\boldsymbol{K}_h\|$, where lighter colors correspond to larger values such that $\max \|\boldsymbol{K}_h\| = 6.5$ is indicated by yellow.

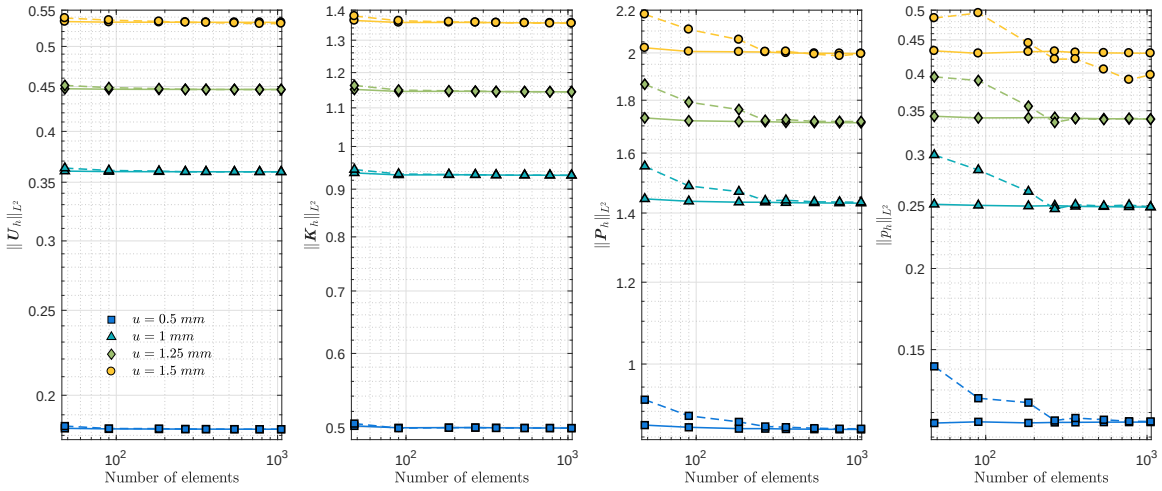

Figure 5.35: Stretching a block with a hole at its center: L^2-norms of displacement, displacement gradient, stress, and pressure versus the number of elements in the mesh. u in the legend is the horizontal displacement imposed at the right boundary. The left boundary is subjected to $-u$ simultaneously. The dashed and solid lines are generated by using H1c1d$\bar{1}$L0 and H2c2d$\bar{2}$L1, respectively.

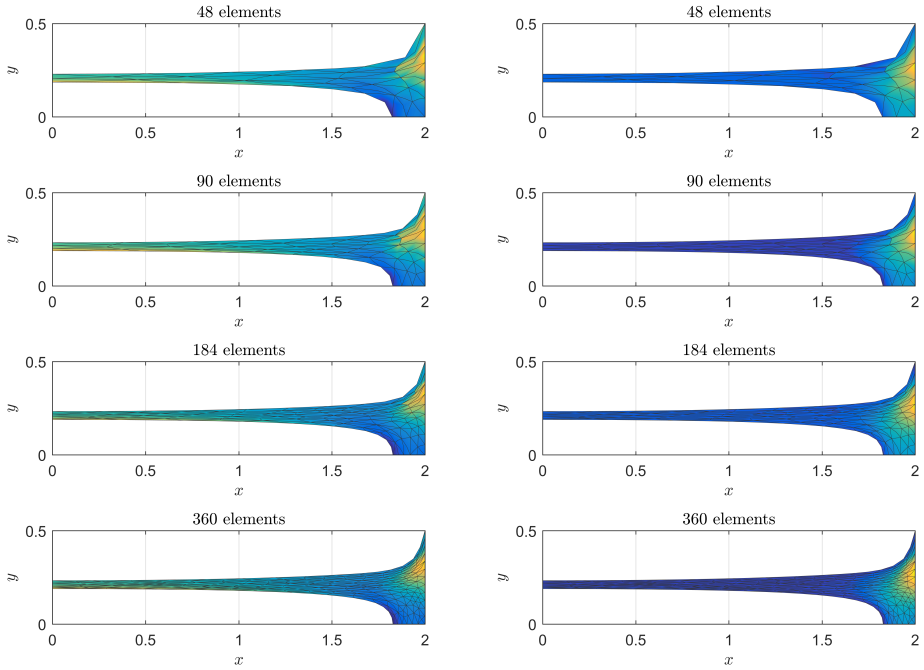

Figure 5.36: The deformed configurations of a quarter of a block with a hole for $u = 1.5\,\mathrm{mm}$ ($stretch = 4$) using H2c2d$\bar{2}$L1. Colors indicate values of the norm of stress $\|\boldsymbol{P}_h\|$ in the first column and the pressure p_h in the second column, where lighter colors correspond to larger values.

5.2.5 Example 5: Stretching a Block with Randomly Distributed Holes.

Next, we consider a block with randomly distributed holes as shown in Figure 5.37. The size of the block is $1\,\mathrm{mm} \times 1\,\mathrm{mm}$. The left edge of the block is fixed and the right edge is subjected to a uniform displacement boundary $(u, 0)$. The top and the bottom edges are traction free. Similar to the previous example, this example tests the performance of CSFEMs at very large stretches but for a more complex geometry. We again consider $\mu = 1\,\mathrm{N/mm^2}$ and $C(J) = J - 1$.

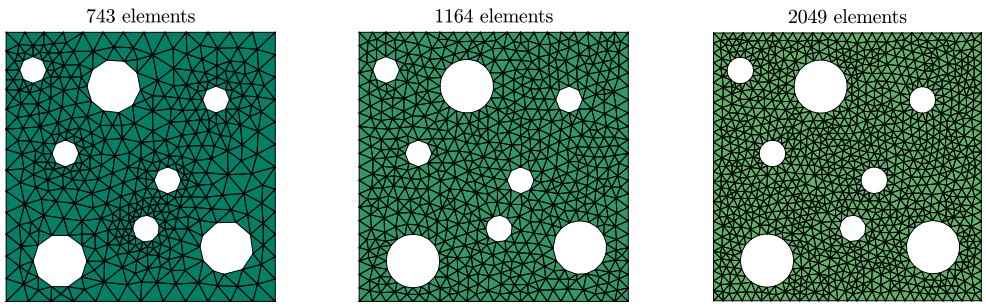

Figure 5.37: Three unstructured meshes for a square block with randomly distributed holes.

Figure 5.38 shows the reference and the deformed configurations of the block using H2c2d$\bar{2}$L1 and the mesh with 184 elements in Figure 5.37. The colors indicate the values of $\|\boldsymbol{K}_h\|$, where lighter colors correspond to larger values. The large values of $\|\boldsymbol{K}_h\|$ correspond to the boundaries of the middle portion of the holes with maximum $\|\boldsymbol{K}_h\|$ of approximately 5.5 at $(0.6, 0.5)$. Figure 5.39 illustrates the convergence of H1c1d$\bar{1}$L0 (dashed lines) and H2c2d$\bar{2}$L1 (solid lines) for different values of u. We observe that H2c2d$\bar{2}$L1 converges considering the four primary variables and for all values of u. We also see that H1c1d$\bar{1}$L0 has good convergence, in general, but it becomes inaccurate in approximating pressure with the increase of stretch to 3 ($u = 2\,\mathrm{mm}$). Note that we had similar observations in Figure 5.31. Using the meshes of Figure 5.37 and using H2c2d$\bar{2}$L1, in Figure 5.40 we illustrate the deformed configurations of the block for $u = 2\,\mathrm{mm}$. The

colors indicate the values of $\|\boldsymbol{P}_h\|$ in the first column and p_h in the second column with lighter colors corresponding to higher values. This mainly shows the stability of H2c2d$\bar{2}$L1 in approximating the stress and pressure without any numerical artifacts even for a complex geometry under a large stretch.

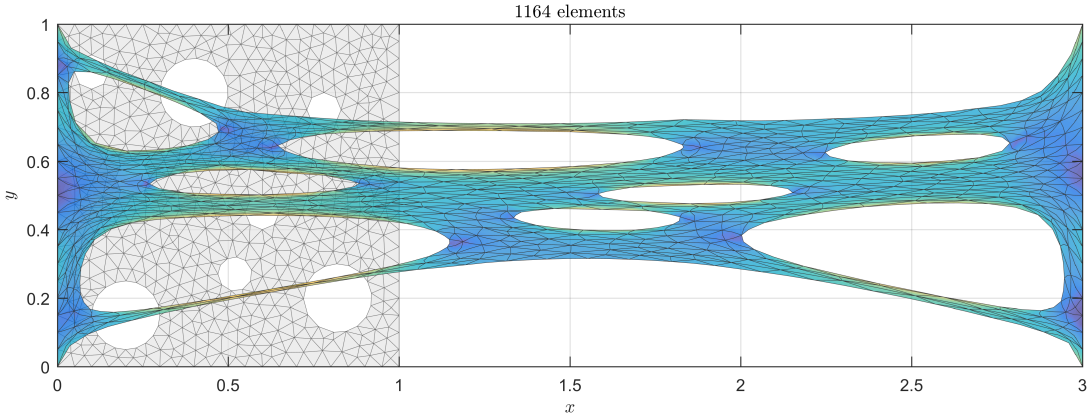

Figure 5.38: The reference and deformed configurations of the block with randomly distributed holes for $u = 2\,\mathrm{mm}$ ($stretch = 3$) obtained using H2c2d$\bar{2}$L1. Colors indicate values of the norm of displacement gradient $\|\boldsymbol{K}_h\|$, where lighter colors correspond to larger values such that $\max \|\boldsymbol{K}_h\| = 5.5$ is indicated by yellow.

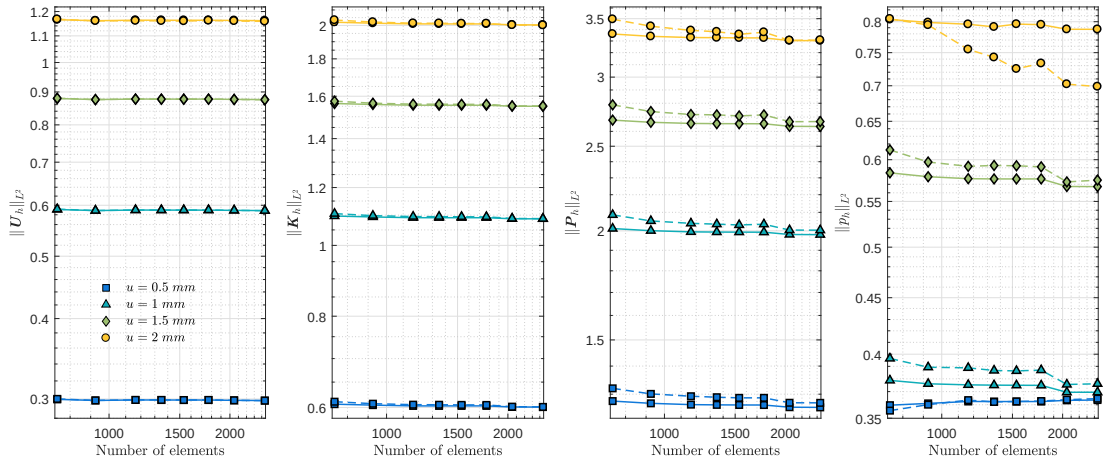

Figure 5.39: Stretching a block with randomly distributed holes: L^2-norms of displacement, displacement gradient, stress, and pressure versus the number of elements in the mesh. u in the legend stands for the horizontal displacement imposed at the right boundary. The dashed and solid lines are generated using H1c1d$\bar{1}$L0 and H2c2d$\bar{2}$L1, respectively.

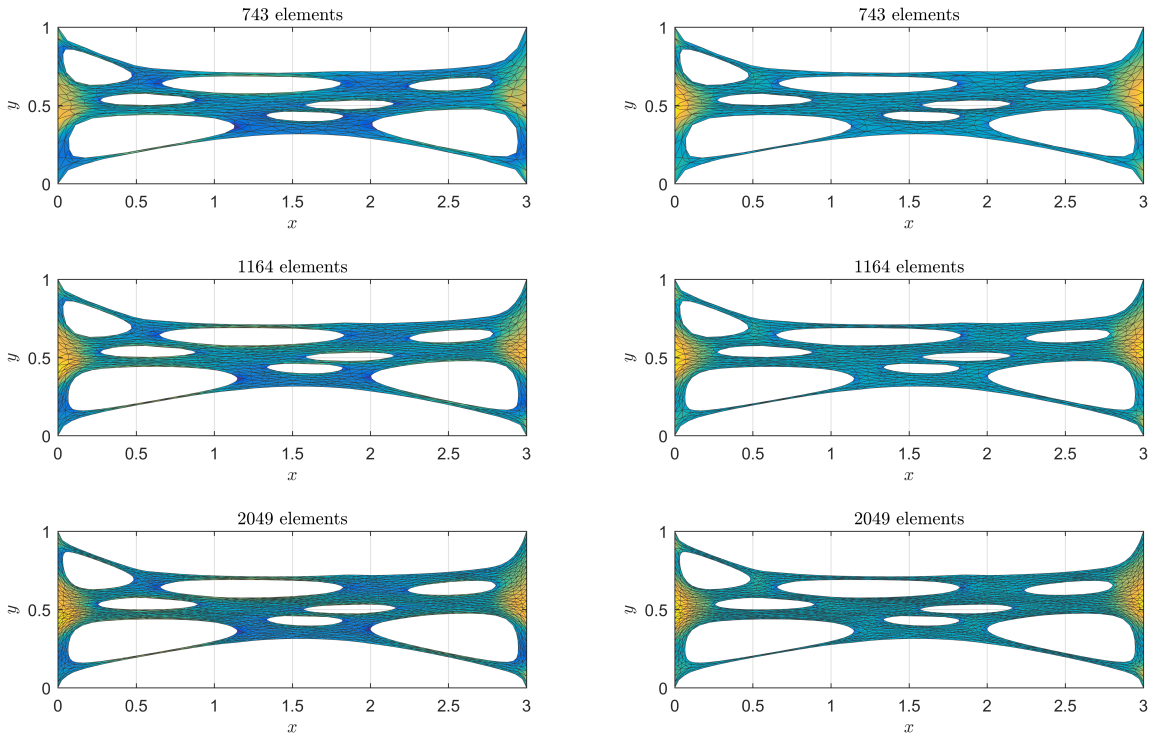

Figure 5.40: The deformed configurations of the block for $u = 2\,\mathrm{mm}$ ($stretch = 3$) using H2c2d$\bar{2}$L1. Colors indicate values of the norm of stress $\|\boldsymbol{P}_h\|$ in the first column and the pressure p_h in the second column, where lighter colors correspond to larger values.

5.2.6 Example 6: Rubber Reinforced with Rigid Particles.

As was discussed in Remark 14, the discrete fields $\boldsymbol{K}_h \in \breve{V}^{\mathbf{c}}_{h,r}$ and $\boldsymbol{P}_h \in \breve{V}^{\mathbf{d}}_{h,r}$ naturally satisfy, respectively, the Hadamard jump condition and the continuity of traction on all the internal edges of any mesh. This enables one to accurately model heterogeneous solids in which inhomogeneities do not slide at the interfaces, i.e., the displacement field is continuous at the interfaces. More specifically, we generate a mesh for the entire heterogeneous material such that the interfaces between all inhomogeneities lie completely on some internal edges of the mesh. Then we assign a different material model to the patch of elements within each inhomogeneity. Regardless of the refinement level of the generated mesh, CSFEMs naturally satisfy all the interface conditions of the heterogeneous solid at the discrete level.

As an application, we consider a square rubber block with edge length of $1\,\mathrm{mm}$ reinforced with 16 rigid circular particles with area fraction of 20% as it is shown in Figure 5.41. The left and the right edges of the block are subjected to uniform traction $(-f, 0)$ and $(0, f)$, respectively, and the top and the bottom edges are traction free. We consider $\mu_1 = 1\,\mathrm{N/mm^2}$ for the rubber matrix and $\mu_2 = 1e5\,\mathrm{N/mm^2}$ for the rigid particles, and we use $C(J) = J - 1$ for both of them.

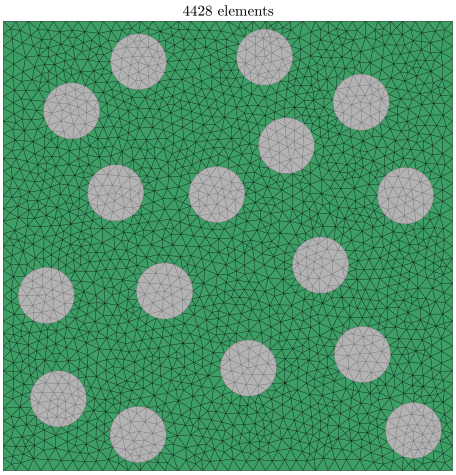

Figure 5.41: An unstructured mesh for a square rubber block with 16 particles with 20% area fraction.

Figure 5.42 shows the deformed configuration of the block for the tension load $f = 2.8\ \mathrm{N/mm^2}$ using H2c2d$\bar{2}$L1 and the mesh with 4428 elements given in Figure 5.41. We can see that the stretch due to the imposed boundary tractions is larger than 2. In the first plot, colors on the matrix indicate values of the norm of displacement gradient $\|\boldsymbol{K}_h\|$. As one expects, we obtain $\boldsymbol{K}_h = \mathbf{0}$ everywhere in the rigid particles. Furthermore, we observe that the large values of $\|\boldsymbol{K}_h\|$ occur in the portion of the matrix between two rigid particles of almost same vertical positions that were close to one another before deformation. In the second plot, colors on the matrix indicate values of the norm of stress $\|\boldsymbol{P}_h\|$. As can be seen, those points of the matrix at the left and right sides of every particle have the large values of stress. The third plot shows the values of pressure p_h in the matrix. Everywhere

in the particles, the computed values of p_h is almost $-\mu_2$. We observe that the positions of large values of pressure and stress in the matrix are almost the same; this is consistent with our observations of all the previous examples. Figure 5.43 shows that H2c2d$\bar{2}$L1 is convergent for different values of f.

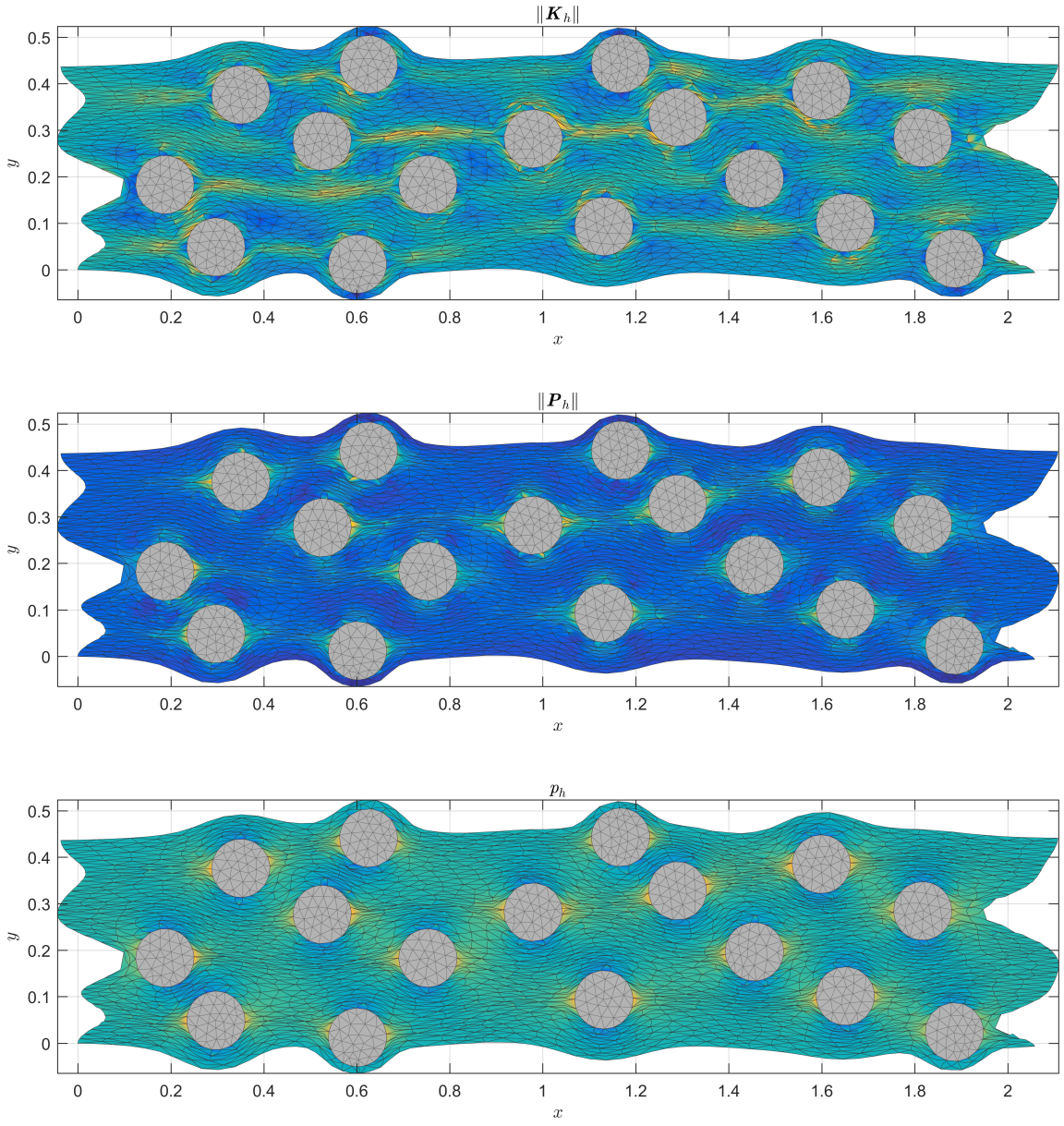

Figure 5.42: The deformed configuration of the block for $f = 2.8\,\mathrm{N/mm^2}$ using H2c2d$\bar{2}$L1 and the mesh with 4428 elements given in Figure 5.41. Colors on the matrix indicate values of the norm of displacement gradient in the first plot, the norm of stress in the second plot, and pressure in the third plot with lighter colors corresponding to larger values.

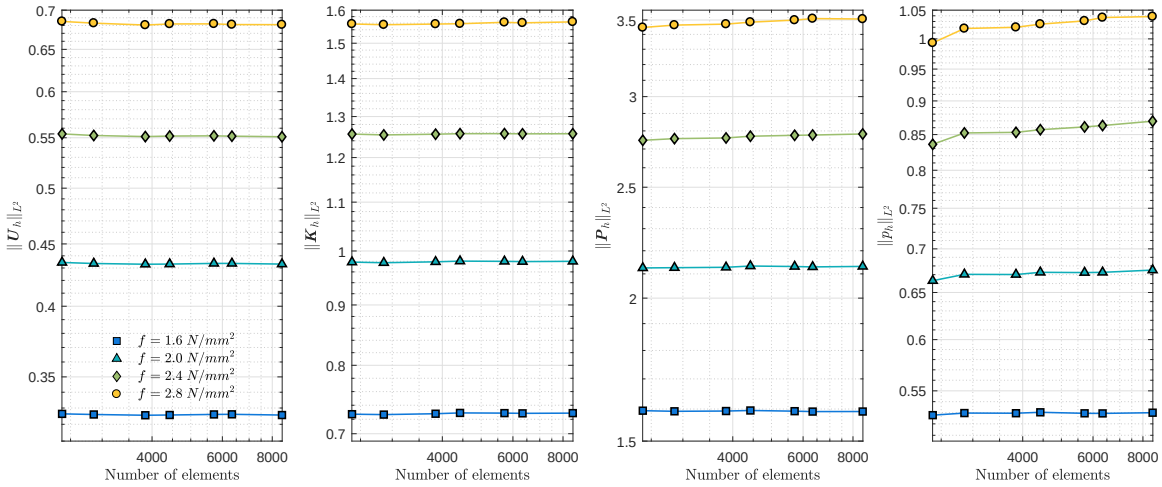

Figure 5.43: Rubber reinforced with rigid particles: L^2-norms of displacement over the entire domain and L^2-norms of displacement gradient, stress, and pressure over the matrix versus the number of elements in the mesh. The results are generated by using H2c2d$\bar{2}$L1.

5.3 Examples for 3D Compressible and Incompressible Solids

5.3.1 Example 1: Inflation of a Hollow Spherical Ball.

Let us consider an incompressible hollow spherical ball shown in Figure 5.44. We assume that the inner boundary of the ball is subjected to the displacement boundary condition $\boldsymbol{U}_{\text{in}} = (\lambda - 1)\mathbf{X}$, the outer boundary is traction free, and there are no body forces. This is an example of a universal deformation [68] and one can obtain the exact solution as follows:

$$\boldsymbol{U}_e(\mathbf{X}) = \left(\frac{r(R)}{R} - 1\right)\mathbf{X},$$
$$p_e(\mathbf{X}) = -\mu\frac{R_{\text{out}}^4}{r^4(R_{\text{out}})} + \frac{\mu}{2}\Big(g(R) - g(R_{\text{out}})\Big),$$

where $R = \|\mathbf{X}\|$, $r(R) = (R^3 + (\lambda^3 - 1)R_{\text{in}}^3)^{\frac{1}{3}}$, and $g(R) = \frac{R\left(3r^3(R) + (\lambda^3 - 1)R_{\text{in}}^3\right)}{r^4(R)}$. It follows that $\boldsymbol{K}_e = \mathbf{grad}\,\boldsymbol{U}_e$ and $\boldsymbol{P}_e = \widetilde{\boldsymbol{P}}(\boldsymbol{K}_e) + p_e\boldsymbol{Q}(\boldsymbol{K}_e)$. Having the exact solution, we assess the accuracy and convergence of CSFEM given in (4.18).

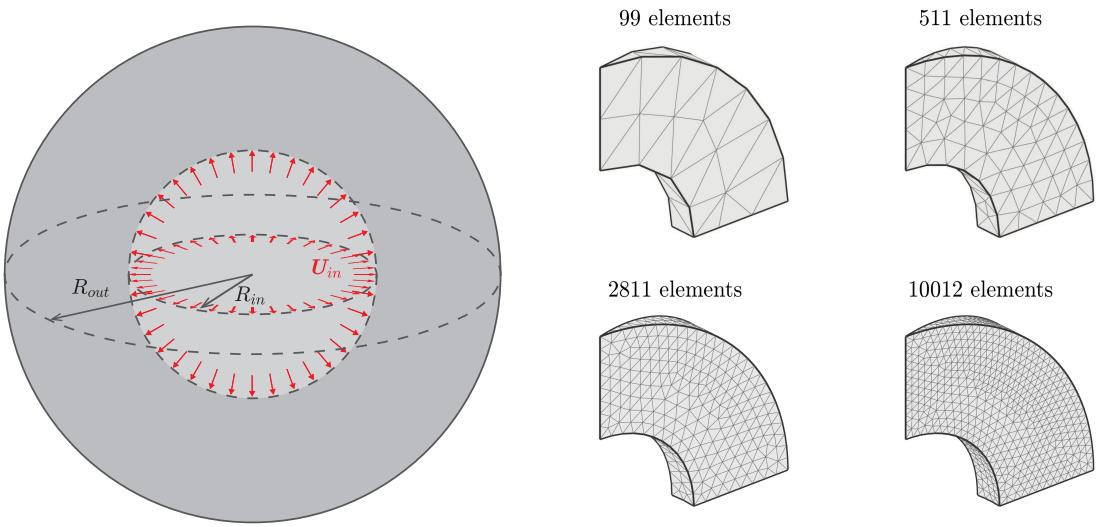

Figure 5.44: Inflation of a hollow spherical ball: Geometry and four unstructured meshes. The outer boundary of the shell is traction free.

For our computations, we consider the neo-Hookean energy function (4.24) with $\mu = 1\,\mathrm{N/mm^2}$, the constraint function $C(J) = J - 1$, $R_{\text{in}} = 0.5\,\mathrm{mm}$, $R_{\text{out}} = 1\,\mathrm{mm}$, and $\lambda = 3$. Using symmetry, we model only $1/24$ of a hemisphere as shown in Figure 5.44. To study the convergence order of (4.18), we plot the relative errors of the field variables versus the maximum diameter h of some unstructured meshes in a log-log graph in Figure 5.45. The convergence order of the displacement $\boldsymbol{U}_h$ is close to 2, and those of the displacement gradient $\boldsymbol{K}_h$, the stress $\boldsymbol{P}_h$, and the pressure-like variable p_h are almost 1. Figure 5.46 shows the reference and the deformed configurations of the four unstructured meshes given in Figure 5.44 obtained by CSFEM in (4.18) for $\lambda = 3$. Colors show the values of $\|\boldsymbol{K}_h\|$ in the first row and the values of p_h in the second row with lighter colors associated with the larger values.

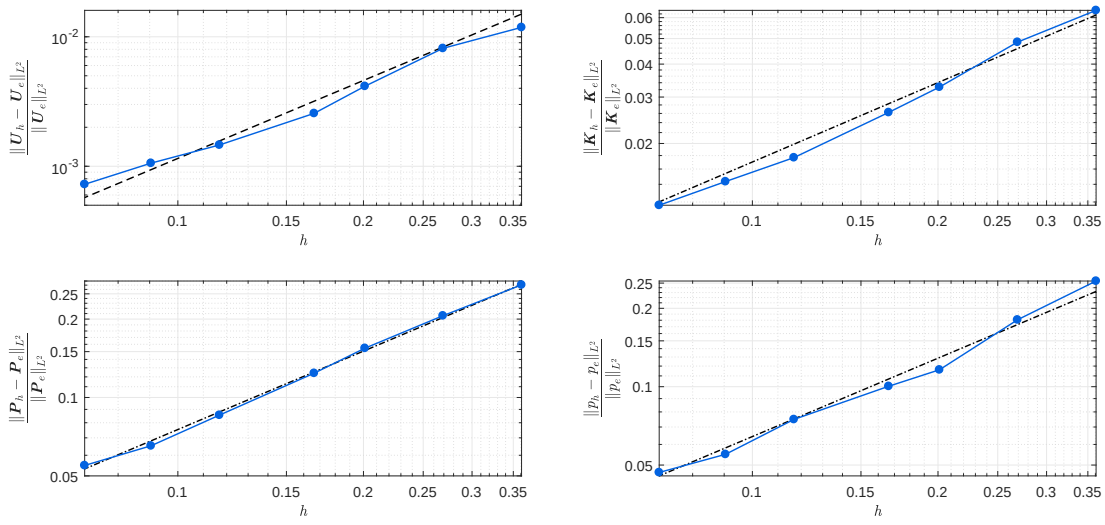

Figure 5.45: Relative L^2-norms of errors in approximating displacement, displacement gradient, stress, and pressure versus the maximum diameter h. The dash-dot line and the dashed line have the slopes of 1 and 2, respectively.

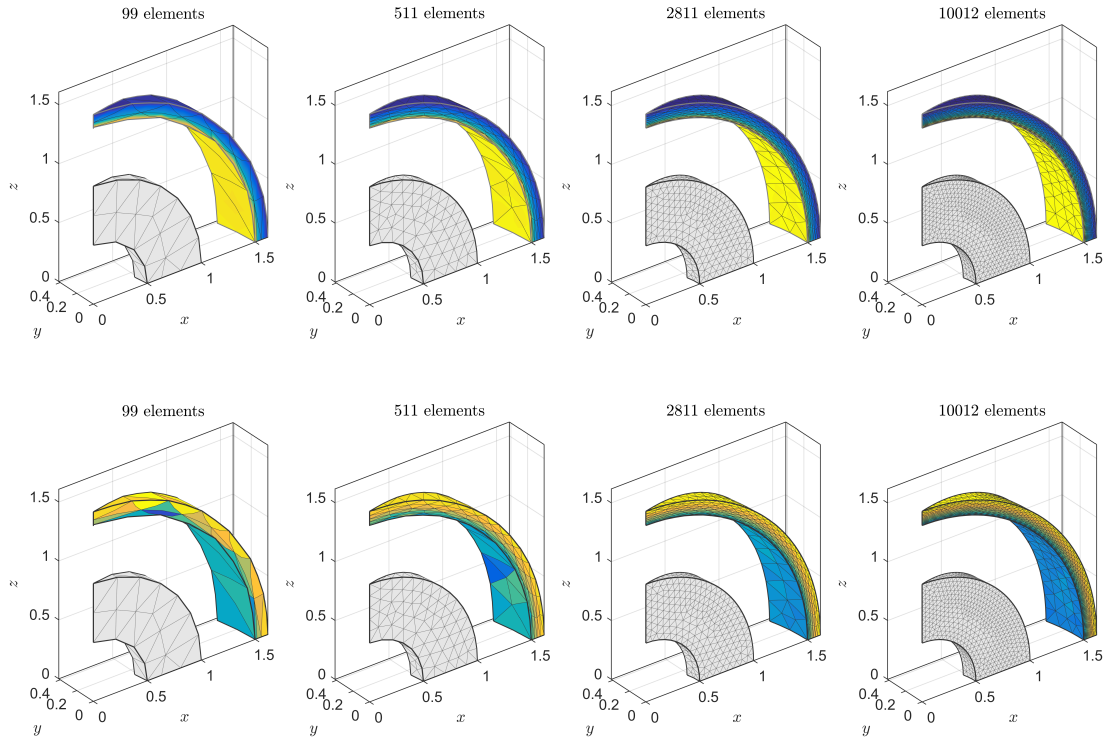

Figure 5.46: The reference and the deformed configurations of the sphere for $\lambda = 3$ using (4.18). Colors indicate values of $\|\boldsymbol{K}_h\|$ in the first row and pressure p_h in the second row, where lighter colors correspond to larger values.

5.3.2 Example 2: 3D Cook's Membrane.

In this example, the 3D Cook's membrane problem depicted in Figure 5.47 is analyzed in order to study the performance of CSFEMs in bending analysis. We consider two cases of tractions imposed on the right side of the membrane (on $16\,\mathrm{mm} \times 10\,\mathrm{mm}$ face): $\overline{\boldsymbol{T}}_1 = (0, f, 0)$ and $\overline{\boldsymbol{T}}_2 = (0, 2f, f)$. We use the energy function (4.24) with $\mu = 1\,\mathrm{N/mm^2}$ and $C(J) = \ln J$ to impose the incompressibility constraint. Figure 5.48 shows the convergence of the vertical displacement of point A indicated in Figure 5.47 for different values of traction $\overline{\boldsymbol{T}}_1 = (0, f, 0)$ using the mixed method (4.18). Since the membrane deforms in two dimensions, the results of the 3D analysis using (4.18) are compared to those obtained by a 2D analysis using H2c2d$\bar{2}$L1 in [43]. The comparison shows a good agreement between the two analyses. Considering $\overline{\boldsymbol{T}}_2 = (0, 2f, f)$, the membrane deforms in three dimensions, for which a similar convergence graph for point A is presented in Figure 5.49. The convergence of the independent field variables $(\boldsymbol{U}_h, \boldsymbol{K}_h, \boldsymbol{P}_h, p_h)$ obtained by the mixed method (4.18) is illustrated in Figure 5.50 for different values of $\overline{\boldsymbol{T}}_2 = (0, 2f, f)$. One observes that $\boldsymbol{U}_h$ and $\boldsymbol{K}_h$ have a faster convergence in comparison with $\boldsymbol{P}_h$ or p_h. The deformed configurations of the four mesh in Figure 5.53 using the mixed method (4.18) are given in Figure 5.51 and Figure 5.52 for $\overline{\boldsymbol{T}}_1 = (0, 0.3, 0)\ \mathrm{N/mm^2}$ and $\overline{\boldsymbol{T}}_2 = (0, 0.2, 0.1)\ \mathrm{N/mm^2}$, respectively. In both figures, colors indicate the values of $\|\boldsymbol{p}_h\|$ in the first row and the values of p_h in the second row with lighter colors corresponding to larger values. Figure 5.52 clearly shows the accuracy of CSFEM in approximating the stresses and the pressure in a large deformation of an incompressible solid even for relatively coarse meshes. It is well-known that the standard displacement-pressure mixed methods for incompressible materials approximate displacement accurately but suffer form numerical artifacts in approximating pressure (they are unable to provide an approximation of stress either). Although the mixed method (4.18) approximates the pressure p_h using piecewise constant shape functions it does not suffer from the numerical artifacts associated with these shape functions in the mixed formulations.

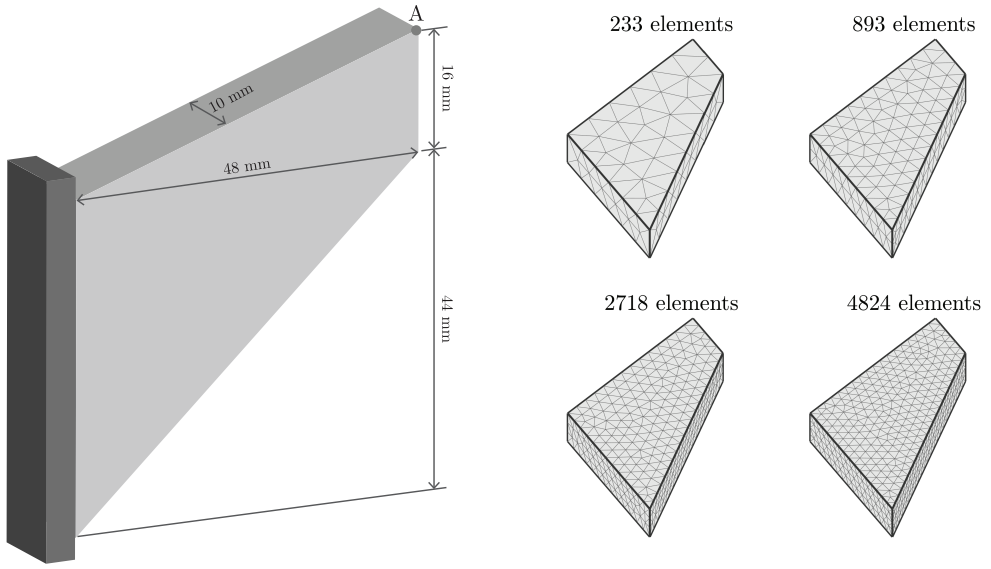

Figure 5.47: Cook's membrane: Geometry and four unstructured meshes.

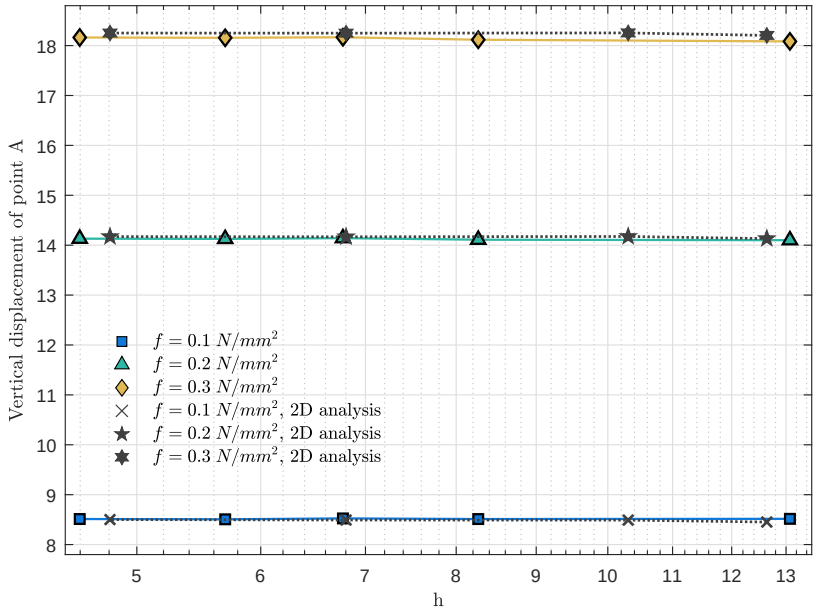

Figure 5.48: 3D Cook's membrane: Vertical displacement of point A in Figure 5.47 for different values of traction $\overline{\boldsymbol{T}}_1 = (0, f, 0)$ versus the maximum edge length h in the mesh using (4.18). The dotted line indicates the results of H2c2d$\bar{2}$L1 given in [43].

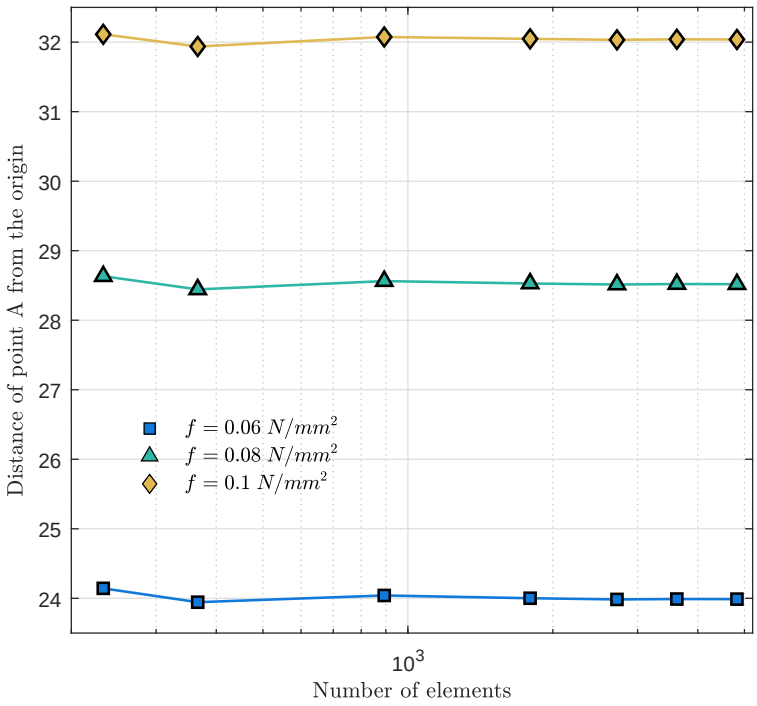

Figure 5.49: 3D Cook's membrane: Distance of point A from the origin in Figure 5.47 for different values of traction $\overline{\boldsymbol{T}}_2$ versus the number of elements in the mesh using (4.18).

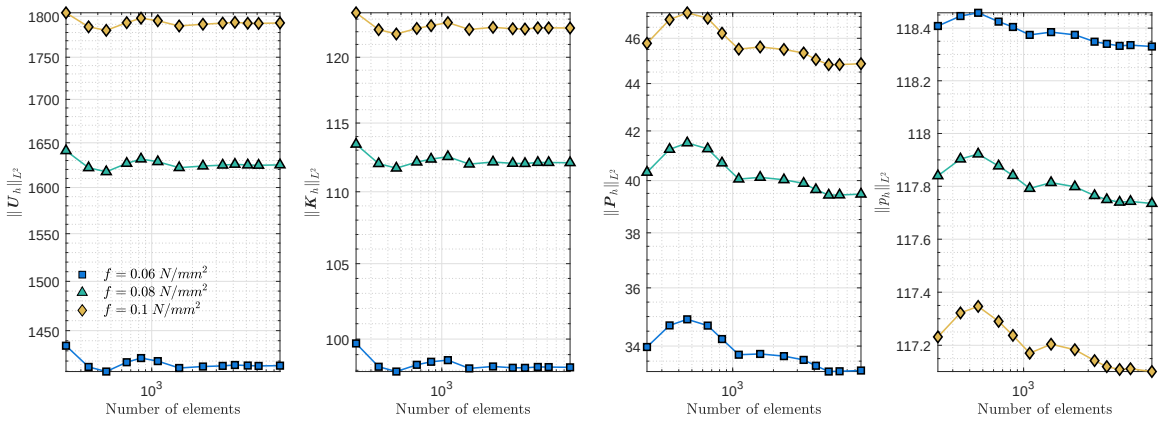

Figure 5.50: Cook's membrane: L^2-norms of displacement, displacement gradient, stress, and pressure versus the number of elements in the mesh for different values of traction $\overline{\boldsymbol{T}}_2$ using H2c1d$\bar{1}$L0.

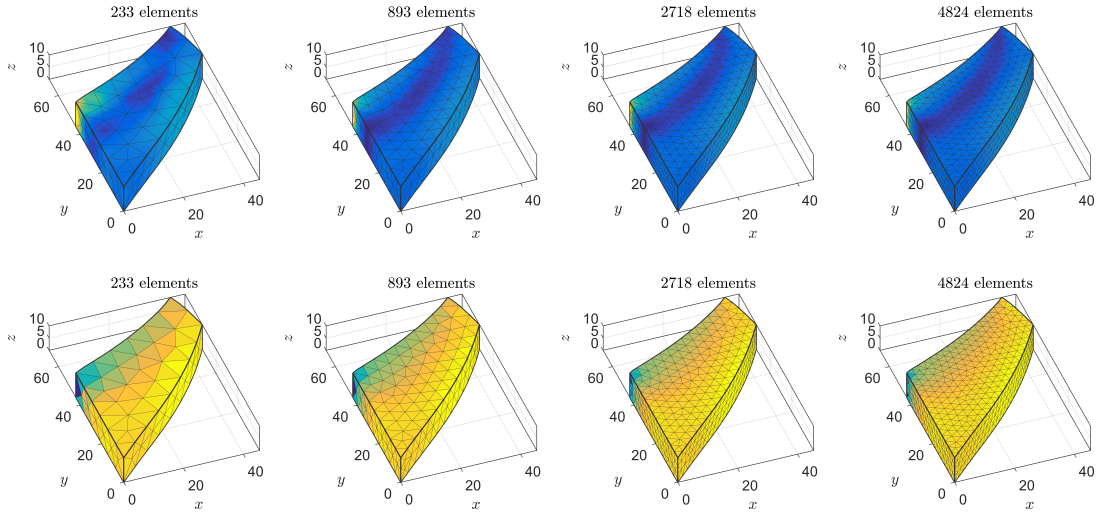

Figure 5.51: The deformed configurations of Cook's membrane for traction $\overline{\boldsymbol{T}}_2 = (0, 0.3, 0)$ using H2c1d$\bar{1}$L0. Colors indicate values of $\|\boldsymbol{P}_h\|$ in the first row and pressure p_h in the second row, where lighter colors correspond to larger values.

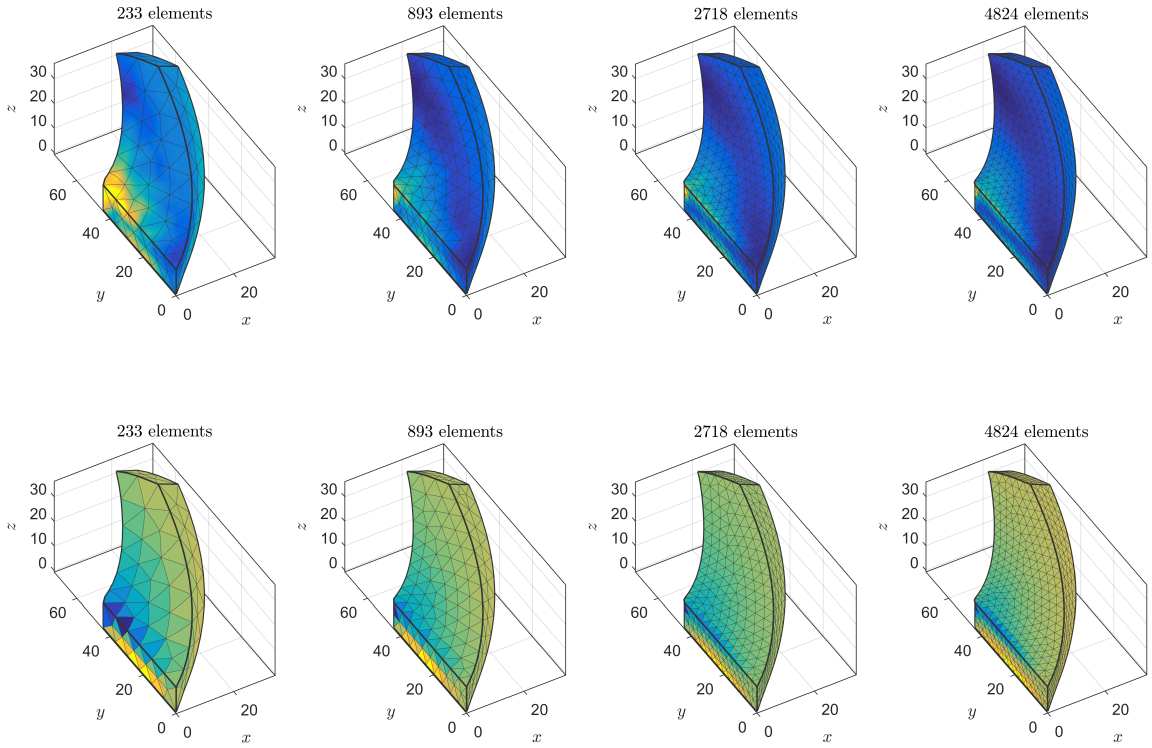

Figure 5.52: The deformed configurations of Cook's membrane for traction $\overline{\boldsymbol{T}}_2 = (0, 0.2, 0.1)$ using H2c1d$\bar{1}$L0. Colors indicate values of $\|\boldsymbol{P}_h\|$ in the first row and pressure p_h in the second row, where lighter colors correspond to larger values.

5.3.3 Example 3. Compression of a Near-Incompressible Block.

Let us consider a block under compression as shown in Figure 5.53. The length and the width of the block are $2\,\mathrm{mm}$ and its hight is $1\,\mathrm{mm}$. The square surface on the top of the block has an edge of $1\,\mathrm{mm}$ and is subjected to a traction $\overline{\boldsymbol{T}} = (0, 0, f)$. The vertical (horizontal) displacement at the bottom (top) of the block is zero. As shown in Figure 5.53, the meshes are generated for only a quarter of the block due to the symmetry of the problem.

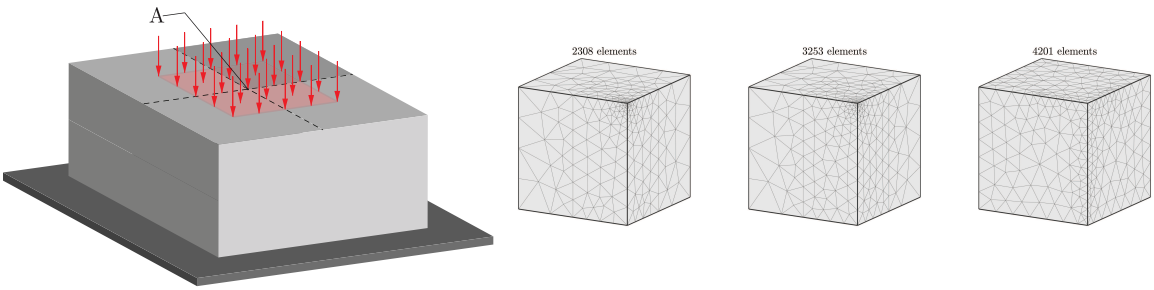

Figure 5.53: A block under compression.

A goal of this example is to test the performance of the mixed method (4.19) in the near-incompressible regime. The energy function (4.23) with $\lambda = 400889.806\,\mathrm{N/mm^2}$ and $\mu = 80.194\,\mathrm{N/mm^2}$ is considered for this example. Note tat many of the existing finite element methods are unable to solve this problem or suffer from numerical artifacts. Reese et.al developed a reduced-integration stabilized brick element and used it to solve this problem. Figure 5.54 illustrates the convergence of the vertical displacement of point A (see Figure 5.53) for different values of $\overline{\boldsymbol{T}} = (0, 0, f)$. The results obtained by (4.19) agree with those reported by Resee et. al. Figure 5.55 depicts the deformed configuration of the block for $\overline{\boldsymbol{T}} = (0, 0, 320)\ \mathrm{N/mm^2}$. Colors show the values of $\|\boldsymbol{K}_h\|$, where lighter colors are assigned to larger values.

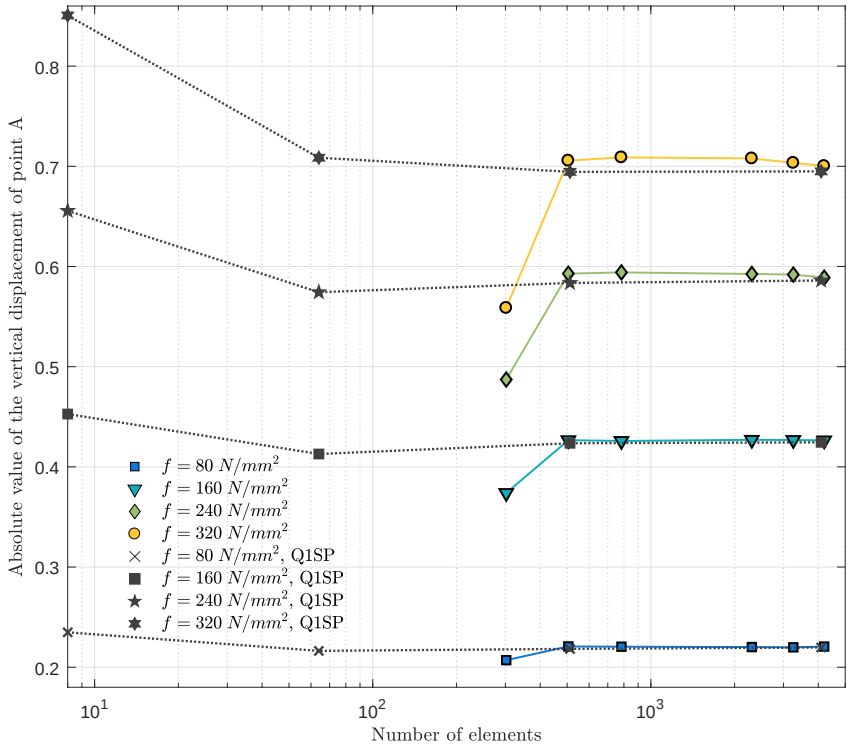

Figure 5.54: A block under compression: Absolute value of the vertical displacement of point A in Figure 5.53 for different values of traction $\overline{\boldsymbol{T}} = (0, 0, f)$ versus the number of elements. Q1SP indicates the results obtained by a reduced-integration stabilized brick element discussed in the work of Reese et al.

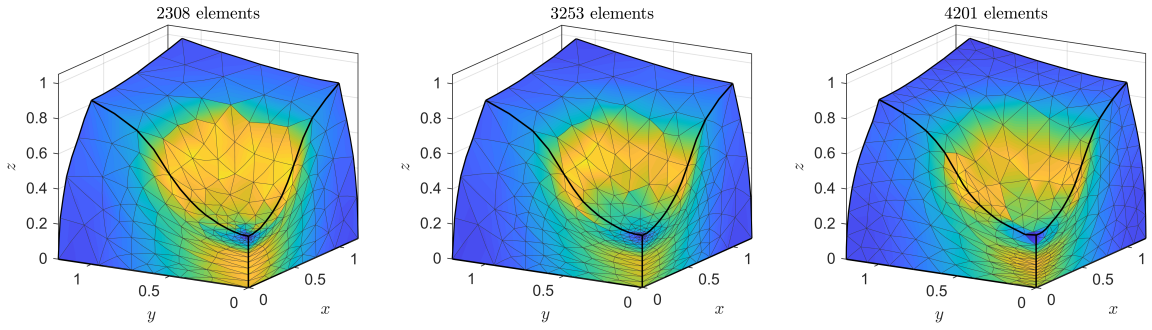

Figure 5.55: The deformed configurations of a block under compression. Colors indicate values of $\|\boldsymbol{K}_h\|$ with lighter colors correspond to larger values.

5.3.4 Example 4. Stretching a Heterogeneous Block.

As was mentioned in Remark 22, CSFEMs (4.18) and (4.19), by construction, satisfy the Hadamard jump condition and the continuity of traction on all the internal faces in a given mesh. This provides an efficient framework to study heterogeneous solids provided that the constituent materials do not slide at their interfaces, i.e., the displacement field is continuous at the material interfaces. One can generate a 3D mesh such that some of the internal faces of the mesh closely approximate the given material interfaces. Then, using CSFEMs, the necessary interface conditions are satisfied, and one only needs to implement the constitutive model of each constituent material.

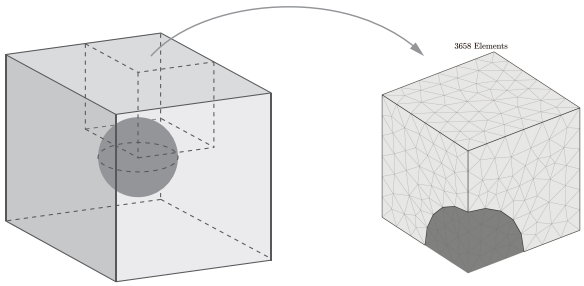

Figure 5.56: A heterogeneous block.

We consider an incompressible cubic block of edge $1\,\mathrm{mm}$ with a spherical inhomogeneity of diameter $0.5\,\mathrm{mm}$ at its center as shown in Figure 5.56. The bottom of the block at $Z = -0.5\,\mathrm{mm}$ and the top of the block at $Z = 0.5\,\mathrm{mm}$ are subjected to displacement boundaries $(0, 0, -0.5)\,\mathrm{mm}$ and $(0, 0, 0.5)\,\mathrm{mm}$, respectively (stretch = 2), and the other four sides are traction free. Using symmetry, we model only $1/8$ of the block as shown in Figure 5.56. The energy function (4.24) is considered for the block with $\mu = 1\,\mathrm{N/mm^2}$ for the matrix and $\mu = \bar{\mu}$ for the spherical inhomogeneity. $C(J) = J - 1$ is used for imposing the incompressibility constraint. We study four different cases: (i) a homogeneous block $\bar{\mu} = 1\,\mathrm{N/mm^2}$, (ii) a very soft inhomogeneity $\bar{\mu} = 1e-5\,\mathrm{N/mm^2}$, (iii) a reinforced block $\bar{\mu} = 4\,\mathrm{N/mm^2}$, and (iv) a rigid inhomogeneity $\bar{\mu} = 1e5\,\mathrm{N/mm^2}$. Figure

5.57 illustrates the convergence of the L^2-norm of the field variables $(\boldsymbol{U}_h, \boldsymbol{K}_h, \boldsymbol{P}_h, p_h)$ calculated on the matrix for all the four cases (the values of p_h become disproportionately large in the inhomogeneity for case (iv)). One can see that a significant change in the material properties of the inhomogeneity only slightly changes the convergence graph.

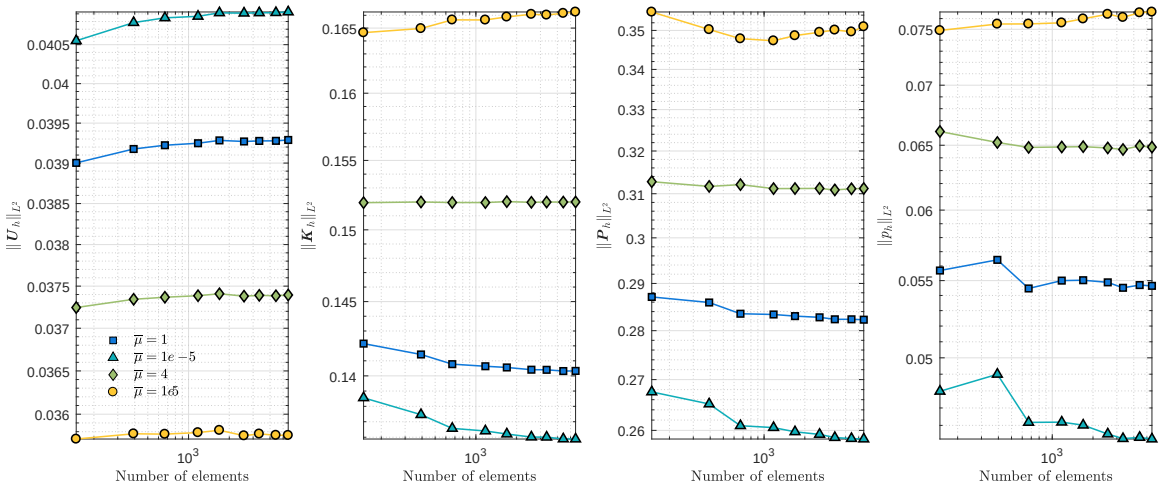

Figure 5.57: Stretching a heterogeneous block: L^2-norms of displacement, displacement gradient, and stress versus the number of elements in the mesh. The matrix material parameters is $\mu = 1\ \mathrm{N/mm^2}$.

Figure 5.58 shows the deformed configurations of $1/8$ of the block for all the four cases for a mesh consisting of 5450 elements. This corresponds to the last points on the convergence graphs given in Figure 5.57. Colors indicate the values of $\|\boldsymbol{K}_h\|$, $\|\boldsymbol{p}_h\|$, and p_h in the first, second, and third row, respectively, where the lighter colors are associated with larger values. As expected, the values of $\|\boldsymbol{K}_h\|$ ($\|\boldsymbol{P}_h\|$) in the inhomogeneity decrease (increase) as the inhomogeneity becomes stiffer. In contrast to case (i), one can see a discontinuous change of color from the matrix to the inhomogeneity in cases (ii)-(iv). As expected, the values of $\boldsymbol{K}_h$, $\boldsymbol{P}_h$, and p_h are continuous at the interface of the two regions in case (i) (homogeneous block) but they are discontinuous in cases (ii)-(iv) (heterogeneous blocks). Nevertheless, in all the four cases, the interface conditions are satisfied, i.e., $\boldsymbol{K}_h\boldsymbol{T}$ and $\boldsymbol{P}_h\boldsymbol{N}$ are continuous at the interface of the two regions, where $\boldsymbol{T}$ and $\boldsymbol{N}$ are

respectively a tangent vector field and a normal vector field on the interface. For case (ii), one observes that $\|\boldsymbol{p}_h\|$ is almost uniformly zero in the spherical inhomogeneity. Hence, the traction field on the interface of the two regions is zero as well, which must be the case as a very soft inhomogeneity behaves like a hole. We solved another example by considering a block with the same geometry and same boundary conditions but with an actual hole. It was observed that the L^2-norm of all the four field variables are equal to those calculated on the matrix for the case (ii).

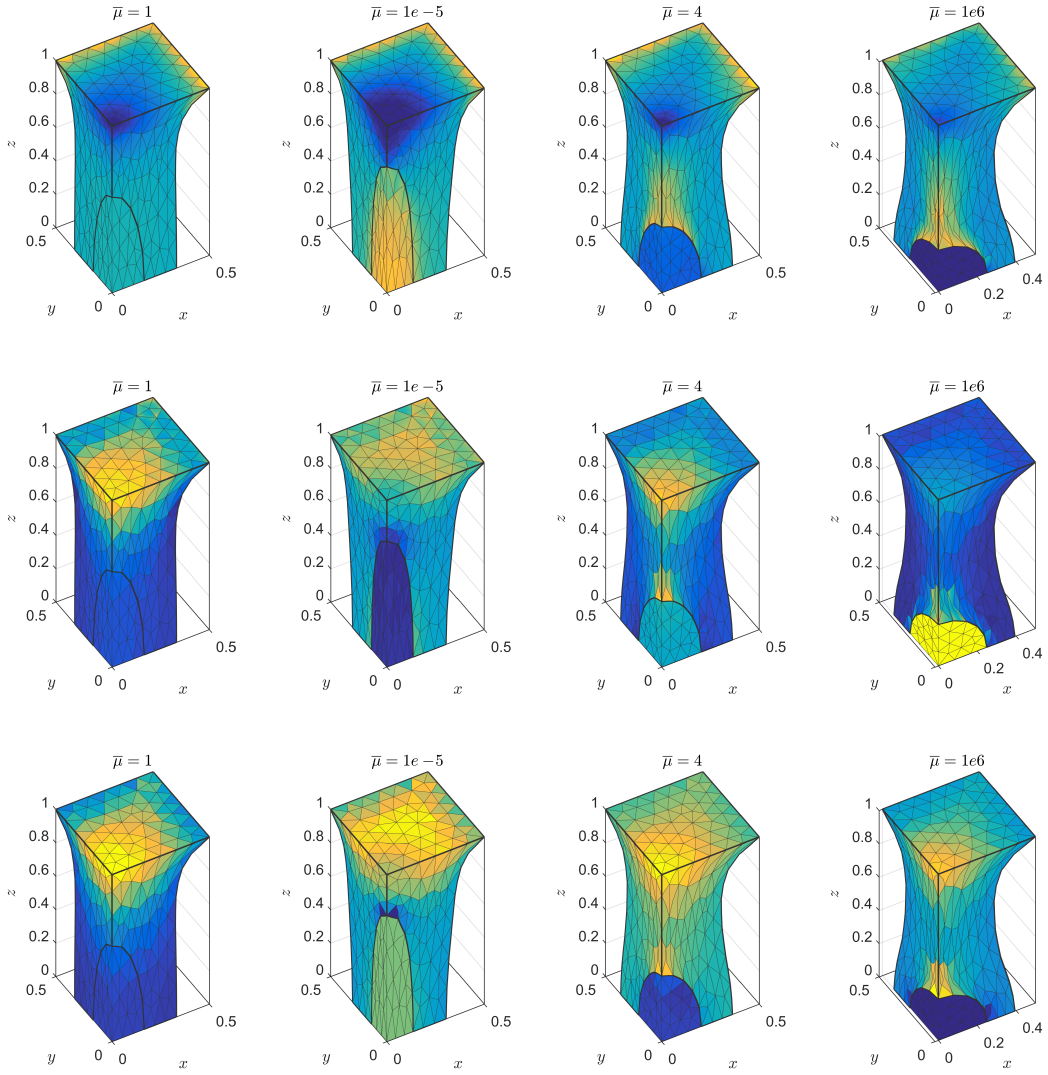

Figure 5.58: Stretch of $\lambda = 2$ of a cube with different spherical inhomogeneities. The shear modulus of the incompressible matrix is $\mu = 1$ $\mathrm{N/cm^2}$ and $\overline{\mu}$ stands for the shear modulus of the incompressible spherical inhomogeneities in each column.

5.3.5 Example 5: Stretching a Block with Randomly Distributed Holes.

Next, we assess the performance of CSFEM at very large strains for a complex geometry. Let us consider an incompressible cubic block of edge $1\,\mathrm{mm}$ with 6 spherical holes as shown in Figure 5.59. The coordinates of the center of the holes are $(0.25, 0.6, 0.6)$, $(0.7, 0.5, 0.3)$, $(0.6, 0.2, 0.7)$, $(0.2, 0.2, 0.2)$, $(0.3, 0.8, 0.2)$, $(0.8, 0.75, 0.7)$ and their diameters are respectively 0.4, 0.4, 0.3, 0.3, 0.3, 0.3. The left side of the block is fixed, the right side is subjected to a uniform displacement boundary $(u, 0, 0)$, and the other four sides are traction free. We use the energy function (4.24) with $\mu = 1\,\mathrm{N/mm^2}$ and $C(J) = J - 1$ to impose the incompressibility constraint. The reference and the deformed configurations of the block obtained by (4.18) for $u = 2\,\mathrm{mm}$ are shown in Figure 5.59. The mesh consists of 11756 elements and colors indicate the values of $\|\boldsymbol{K}_h\|$ with lighter colors corresponding to larger values. Note that this result corresponds to the last points on the convergence graphs given in Figure 5.60. One can see that all the holes are stretched severely along the x-axis. Hence, relative to the x-axis, the beginning and the end portions of the boundaries of each hole have lower values of $\|\boldsymbol{K}_h\|$ while the middle portion has larger values of $\|\boldsymbol{K}_h\|$. Figure 5.60 illustrates the convergence of (4.18) for different values of the displacement boundary condition $(u, 0, 0)$ imposed at the right side of the block. For all values of u, one observes that CSFEM given in (4.18) has good convergence considering all the four independent variables $(\boldsymbol{U}_h, \boldsymbol{K}_h, \boldsymbol{P}_h, p_h)$.

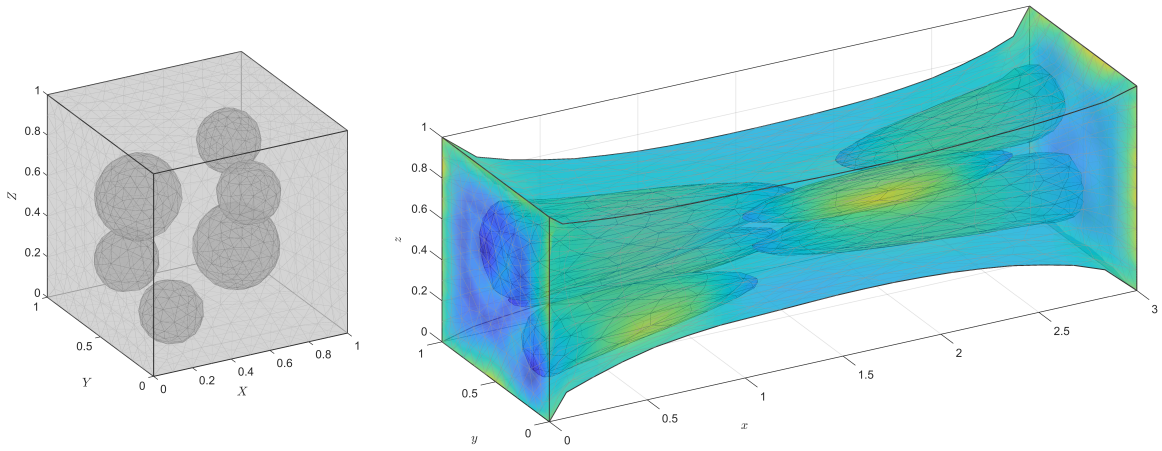

Figure 5.59: The reference (left) and deformed (right) configurations of a block with randomly distributed holes for $u = 2\,\mathrm{mm}$ ($stretch = 3$). The mesh consists of 11756 elements, and colors indicate values of the norm of displacement gradient $\|\boldsymbol{K}_h\|$, where lighter colors correspond to larger values.

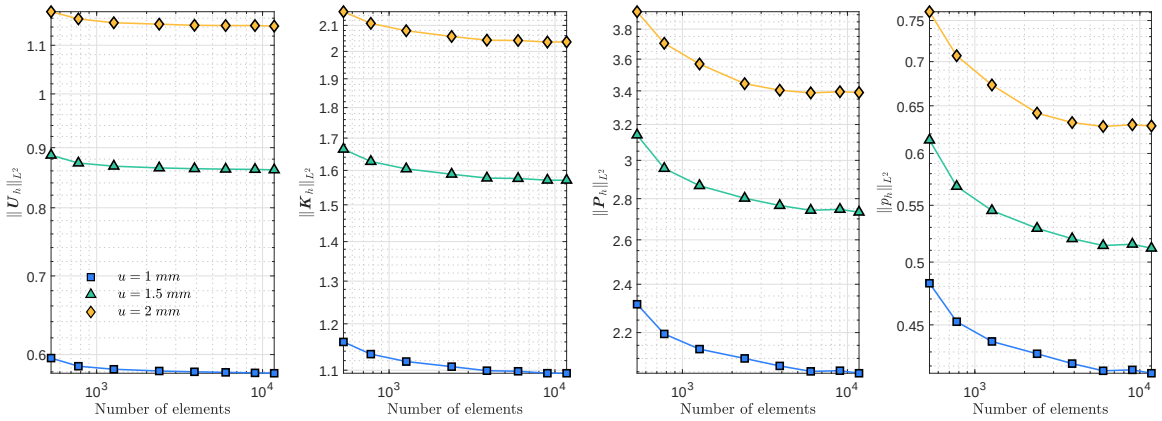

Figure 5.60: Stretching a block with randomly distributed holes: L^2-norms of displacement, displacement gradient, stress, and pressure versus the number of elements in the mesh.

CHAPTER 6

CONCLUDING REMARKS

We introduced a new class of mixed finite element methods–*compatible-strain mixed finite element methods* (CSFEMs)–for compressible and incompressible nonlinear elasticity in dimensions two and three. These finite element methods are based on a Hu-Washizu type functional with the displacement $\boldsymbol{U}$, the displacement gradient $\boldsymbol{K}$, the first Piola-Kirchhoff stress $\boldsymbol{P}$, and the pressure-like p as the independent unknowns. For solution spaces, we assumed $(\boldsymbol{U}, \boldsymbol{K}, \boldsymbol{P}, p) \in H^1(T\mathcal{B}) \times H^{\mathbf{c}}(\mathcal{B}) \times H^{\mathbf{d}}(\mathcal{B}) \times L^2(\mathcal{B})$, and to define the corresponding test spaces, we used the same Hilbert spaces. Next, we constructed some conforming finite element (piecewise polynomial) subspaces $V^1_{h,r} \subset H^1(T\mathcal{B}_h)$, $\breve{V}^{\mathbf{c}}_{h,r} \subset H^{\mathbf{c}}(\mathcal{B}_h)$, $\breve{V}^{\mathbf{d}}_{h,r} \subset H^{\mathbf{d}}(\mathcal{B}_h)$, and $V^{\ell}_{h,r} \subset L^2(\mathcal{B}_h)$. Then, CSFEMs were obtained by replacing the solution and test spaces of the four-field mixed formulation with the generated finite element subspaces. Due to interelement continuities of these subspaces, regardless of the refinement level of the mesh, CSFEMs approximate a continuous displacement and satisfy both the Hadamard jump conditions of displacement gradient and the continuity of traction on all the interfaces of elements in the mesh.

In comparison with the standard finite element methods for nonlinear elasticity, CSFEMs require more degrees of freedom. However, we observed that CSFEMs are stable and have good performances for problems for which many standard finite element methods fail or have a poor performance. In particular, CSFEMs do not suffer from numerical artifacts such as locking, checkerboarding of pressure, or hourglass-type instabilities. CSFEMs give accurate approximations of stress on domains with complex geometries. Such good performance is highly desirable in many applications. In capturing the nonlinear effects, we observed that CSFEMs remain stable up to very large strains. Moreover, as we demonstrated, CSFEMs provide an efficient framework for modeling solids undergoing

large deformations.

In future communications, we will extend CSFEMs to nonlinear elastic bodies with distributed finite eigenstrains. The anelastic part of any measure of strain that represents distortions, referential rearrangements, phase changes, etc., is called eigenstrain. Eigenstrains are created due to a host of anelastic phenomena in solids such as defects [69], thermal strains [70], biological growth [71], swelling [72], and the presence of inclusions and inhomogeneities [73, 74]. The extension of our finite element methods will provide an efficient framework to study these phenomena. The existing numerical schemes are based on a multiplicative decomposition of deformation gradient into elastic and anelastic parts: $\boldsymbol{F} = \boldsymbol{F}^e\boldsymbol{F}^a$. Our approach is conceptually different. We model the material manifold of such a body–the natural configuration of the body in which there is no stress–with a three-dimensional Riemannian manifold $(\mathcal{B}, \mathbf{G})$ and its deformation with a mapping $\varphi : \mathcal{B} \to \mathcal{S}$, where $(\mathcal{S}, \mathbf{g})$ denotes the ambient space [75]. To extend our methods, we modify our finite element approximations based on a discretization of the Riemannian manifold $(\mathcal{B}_h, \mathbf{G})$. In this approach, the material metric $\mathbf{G}$ explicitly depends on the distribution of eigenstrains.

REFERENCES

[1] P. Wriggers and S. Reese, "A note on enhanced strain methods for large deformations," *Computer Methods in Applied Mechanics and Engineering*, vol. 135, pp. 201–209, 1996.

[2] F. Auricchio, L. da Veiga Beirao, C. Lovadina, A. Reali, R. L. Taylor, and P. Wriggers, "Approximation of incompressible large deformation elastic problems: Some unresolved issues," *Computational Mechanics*, vol. 52, pp. 1153–1167, 2013.

[3] F. Auricchio, L. da Veiga Beirao, C. Lovadina, and A. Reali, "Stability of some finite element methods for finite elasticity problems," in *Mixed finite element technologies*, CISM Courses and Lectures, Springer-Verlag, Wien, 2009, pp. 179–206.

[4] T. Belytschko, Y. Krongauz, D. Organ, M. Fleming, and P. Krysl, "Meshless methods: An overview and recent developments," *Computer Methods in Applied Mechanics and Engineering*, vol. 139, 3–47, 1996.

[5] T. Belytschko, Y. Lu, and L. Gu, "Element-free Galerkin methods," *International Journal for Numerical Methods in Engineering*, vol. 37, pp. 229–256, 1994.

[6] G. Shi, "Manifold method of material analysis," *Transactions of the 9th Army Conference On Applied Mathematics and Computing, Report, No.92-1, U.S. Army Research Office*, 1991.

[7] G. MA, X. AN, and L. HE, "The numerical manifold method: A review," *International Journal of Computational Methods*, vol. 7, pp. 1–32, 2010.

[8] J. M. Melenk and I. Babuška, "The partition of unity finite element method: Basic theory and applications," *Computer Methods in Applied Mechanics and Engineering*, vol. 139, pp. 289–314, 1996.

[9] I. Babuška and J. M. Melenk, "The partition of unity method," *International Journal for Numerical Methods in Engineering*, vol. 40, pp. 727–758, 1997.

[10] T. Strouboulis, K. Copps, and I. Babuška, "The generalized finite element method," *Computer Methods in Applied Mechanics and Engineering*, vol. 190, pp. 4081–4193, 2001.

[11] I. Babuška and U. Banerjee, "Stable generalized finite element method (SGFEM)," *Computer Methods in Applied Mechanics and Engineering*, vol. 201–204, pp. 91–111, 2012.

[12] K. Srinivasan, K. Matouš, and P. Geubelle, "Generalized finite element method for modeling nearly incompressible bimaterial hyperelastic solids," *Computer Methods in Applied Mechanics and Engineering*, vol. 197, pp. 4882–4893, 2008.

[13] T. P. Fries and T. Belytschko, "The extended/generalized finite element method: An overview of the method and its applications," *International Journal for Numerical Methods in Engineering*, vol. 84, pp. 253–304, 2010.

[14] Y. Abdelaziz and A. Hamouine, "A survey of the extended finite element," *Computers & Structures*, vol. 86, pp. 1141–1151, 2008.

[15] A. R. Khoei, S. O. R. Biabanaki, and M. Anahid, "Extended finite element method for three-dimensional large plasticity deformations," *Computer Methods in Applied Mechanics and Engineering*, vol. 197, pp. 1100–1114, 2008.

[16] O. C. Zienkiewicz, R. L. Taylor, and J. M. Too, "Reduced integration technique in general analysis of plates and shells," *International Journal for Numerical Methods in Engineering*, vol. 3, pp. 275–290, 1971.

[17] T. J. R. Hughes, "Generalization of selective integration procedures to anisotropic and nonlinear media," *International Journal for Numerical Methods in Engineering*, vol. 15, pp. 1413–1418, 1980.

[18] T. Belytschko, J. S. J. Ong, W. K. Liu, and J. M. Kennedy, "Hourglass control in linear and nonlinear problems," *Computer Methods in Applied Mechanics and Engineering*, vol. 43, pp. 251–276, 1984.

[19] S. Reese and P. Wriggers, "A stabilization technique to avoid hourglassing in finite elasticity," *International Journal for Numerical Methods in Engineering*, vol. 48, 79–109, 2000.

[20] J. C. Simo and F. Armero, "Geometrically non-linear enhanced strain mixed methods and the method of incompatible modes," *International Journal for Numerical Methods in Engineering*, vol. 33, pp. 1413–1449, 1992.

[21] P. Wriggers, "Mixed finite element methods - theory and discretization," in *Mixed finite element technologies*, CISM Courses and Lectures, Springer-Verlag, Wien, 2009, pp. 131–177.

[22] N. C. Nguyen and J. Peraire, "Hybridizable discontinuous Galerkin methods for partial differential equations in continuum mechanics," *Journal of Computational Physics*, vol. 231, pp. 5955–5988, 2012.

[23] O. A. Ladyzhenskaya, *The mathematical theory of viscous incompressible flow*. Gordon and Breach Science Publishers, New York, 1969.

[24] I. Babuška, "The finite element method with Lagrangian multipliers," *Numerische Mathematik*, vol. 20, pp. 179–192, 1973.

[25] F. Brezzi, "On the existence, uniqueness and approximation of saddle-point problems arising from Lagrange multipliers," *RAIRO Analyse Numérique*, pp. 129–151, 1974.

[26] A. Ern and J. Guermond, *Theory and Practice of Finite Elements*. Springer-Verlag, New York, 2004.

[27] D. N. Arnold and R. Winther, "Mixed finite elements for elasticity," *Numerische Mathematik*, vol. 92, pp. 401–419, 2002.

[28] E. Kröner, "Allgemeine kontinuumstheorie der versetzungen und eigenspannungen," *Archive for Rational Mechanics and Analysis*, vol. 4, pp. 273–334, 1959.

[29] D. N. Arnold, R. S. Falk, and R. Winther, "Finite element exterior calculus, homological techniques, and applications," *Acta Numerica*, vol. 15, pp. 1–155, 2006.

[30] D. N. Arnold, R. S. Falk, and R. Winther, "Finite element exterior calculus: From Hodge theory to numerical stability," *Bulletin of the American Mathematical Society*, vol. 47, pp. 281–354, 2010.

[31] D. N. Arnold, F. Brezzi, and M. Fortin, "A stable finite element for the Stokes equations," *CALCOLO*, vol. 21, no. 4, pp. 337–344, 1984.

[32] C. Taylor and P. Hood, "A numerical solution of the Navier-Stokes equations using the finite element technique," *Computers & Fluids*, vol. 1, no. 1, pp. 73 –100, 1973.

[33] R. E. Nickell, R. I. Tanner, and B. Caswell, "The solution of viscous incompressible jet and free-surface flows using finite-element methods," *Journal of Fluid Mechanics*, vol. 65, no. 1, pp. 189–206, 1974.

[34] M. Bercovier and O. Pironneau, "Error estimates for finite element method solution of the Stokes problem in the primitive variables," *Numerische Mathematik*, vol. 33, no. 2, pp. 211–224, 1979.

[35] M. Crouzeix and P.-A. Raviart, "Conforming and nonconforming finite element methods for solving the stationary Stokes equations i," *Revue française d'automatique informatique recherche opérationnelle. Mathématique*, vol. 7, no. R3, pp. 33–75, 1973.

[36] H. Chi, C. Talischi, O. Lopez-Pamies, and G. H. Paulino, "Polygonal finite elements for finite elasticity," *International Journal for Numerical Methods in Engineering*, vol. 101, no. 4, pp. 305–328, 2015.

[37] T. Hughes, L. P. Franca, and M. Balestra, "A new finite element formulation for computational fluid dynamics: V. circumventing the babuška-brezzi condition: A stable petrov-galerkin formulation of the stokes problem accommodating equal-order interpolations," *Computer Methods in Applied Mechanics and Engineering*, vol. 59, no. 1, pp. 85–99, 1986.

[38] L. P. Franca, T. J. R. Hughes, A. F. D. Loula, and I. Miranda, "A new family of stable elements for nearly incompressible elasticity based on a mixed petrov-galerkin finite element formulation," *Numerische Mathematik*, vol. 53, no. 1, pp. 123–141, 1988.

[39] J. C. Simo, R. L. Taylor, and K. S. Pister, "Variational and projection methods for the volume constraint in finite deformation elasto-plasticity," *Computer Methods in Applied Mechanics and Engineering*, vol. 51, no. 1-3, pp. 177–208, 1985.

[40] J. A. Weiss, B. N. Maker, and S. Govindjee, "Finite element implementation of incompressible, transversely isotropic hyperelasticity," *Computer Methods in Applied Mechanics and Engineering*, vol. 135, no. 1-2, pp. 107–128, 1996.

[41] B. P. Lamichhane, "A mixed finite element method for non-linear and nearly incompressible elasticity based on biorthogonal systems," *International Journal for Numerical Methods in Engineering*, vol. 79, no. 7, pp. 870–886, 2009.

[42] A. Angoshtari, M. Faghih Shojaei, and A. Yavari, "Compatible-Strain Mixed Finite Element Methods for 2D compressible nonlinear elasticity," *Computer Methods in Applied Mechanics and Engineering*, vol. 313, pp. 596–631, 2017.

[43] M. Faghih Shojaei and A. Yavari, "Compatible-strain mixed finite element methods for incompressible nonlinear elasticity," *Journal of Computational Physics*, vol. 361, pp. 247 –279, 2018.

[44] M. Faghih Shojaei and A. Yavari, "Compatible-strain mixed finite element methods for 3D compressible and incompressible nonlinear elasticity," *In preparation*.

[45] A. Angoshtari and A. Yavari, "Differential complexes in continuum mechanics," *Archive for Rational Mechanics and Analysis*, vol. 216, pp. 193–220, 2015.

[46] A. Angoshtari and A. Yavari, "Hilbert complexes of nonlinear elasticity," *Zeitschrift für Angewandte Mathematik und Physik (ZAMP)*, vol. 67, no. 6, p. 143, 2016.

[47] D. N. Arnold, R. S. Falk, and R. Winther, "Mixed finite element methods for linear elasticity with weakly imposed symmetry," *Mathematics of Computation*, vol. 76, no. 260, pp. 1699–1723, 2007.

[48] P. Hauret and F. Hecht, "A discrete differential sequence for elasticity based upon continuous displacements," *SIAM Journal on Scientific Computing*, vol. 35, no. 1, B291–B314, 2013.

[49] A. Pechstein and J. Schöeberl, "Tangential-displacement and normal–normal-stress continuous mixed finite elements for elasticity," *Mathematical Models and Methods in Applied Sciences*, vol. 21, no. 08, pp. 1761–1782, 2011.

[50] O. Klaas, A. Maniatty, and M. S. Shephard, "A stabilized mixed finite element method for finite elasticity.: Formulation for linear displacement and pressure interpolation," *Computer Methods in Applied Mechanics and Engineering*, vol. 180, no. 1-2, pp. 65–79, 1999.

[51] A. Yavari, "On geometric discretization of elasticity," *Journal of Mathematical Physics*, vol. 49:022901, 2008.

[52] A. Yavari, "Compatibility equations of nonlinear elasticity for non-simply-connected bodies," *Archive for Rational Mechanics and Analysis*, vol. 209, pp. 237–253, 2013.

[53] J. L. Loday, *Cyclic Homology*. Springer-Verlog, Berlin, 1992.

[54] P. G. Ciarlet, *The Finite Element Method for Elliptic Problems*. North-Holland Publishing Co., Amsterdam, 1978.

[55] J. C. Nédélec, "Mixed finite elements in $\mathbb{R}^3$," *Numer. Math.*, vol. 35, no. 3, pp. 315–341, 1980.

[56] J. C. Nédélec, "A new family of mixed finite elements in $\mathbb{R}^3$," *Numerische Mathematik*, vol. 50, pp. 57–81, 1986.

[57] P. A. Raviart and J. M. Thomas, "A mixed finite element method for 2nd order elliptic problems," in *Mathematical aspects of finite element methods (Proc. Conf., Consiglio Naz. delle Ricerche (C.N.R.), Rome, 1975)*, Vol. 606 of Lecture Notes in Mathematics, Springer, Berlin, 1977, pp. 292–315.

[58] F. Brezzi, J. Douglas, Jr., and L. D. Marini, "Two families of mixed finite elements for second order elliptic problems," *Numerische Mathematik*, vol. 47, pp. 217–235, 1985.

[59] D. N. Arnold, R. S. Falk, and R. Winther, "Geometric decompositions and local bases for spaces of finite element differential forms," *Computer Methods in Applied Mechanics and Engineering*, vol. 198, pp. 1660–1672, 2009.

[60] P. Solin, K. Segeth, and I. Dolezel, *Higher-Order Finite Element Methods*. Chapman & Hall/CRC, 2004.

[61] F. Fuentes, B. Keith, L. Demkowicz, and S. Nagaraj, "Orientation embedded high order shape functions for the exact sequence elements of all shapes," *Computers & Mathematics with Applications*, vol. 70, no. 4, pp. 353–458, 2015.

[62] M. Rognes, R. C. Kirby, and A. Logg, "Efficient assembly of H(div) and H(curl) conforming finite elements," *E-prints arXiv*, vol. 1205.3085, 2012.

[63] A. Angoshtari and A. Yavari, "The weak compatibility equations of nonlinear elasticity and the insufficiency of the Hadamard jump condition for non-simply connected bodies," *Continuum Mechanics and Thermodynamics*, vol. 28, no. 5, pp. 1347–1359, 2016.

[64] D. Boffi, F. Brezzi, and M. Fortin, *Mixed Finite Element Methods and Applications*. Springer, 2013, vol. 44.

[65] T. J. R. Hughes, *The Finite Element Method*. Prentice-Hall, Englewood Cliffs, NJ, 2000.

[66] S. Reese, "On the equivalence of mixed element formulations and the concept of reduced integration in large deformation problems," *The International Journal of Nonlinear Sciences and Numerical Simulation*, vol. 3, pp. 1–33, 2002.

[67] U. Brink and E. Stein, "A posteriori error estimation in large-strain elasticity using equilibrated local Neumann problems," *Computer Methods in Applied Mechanics and Engineering*, vol. 161, pp. 77–101, 1998.

[68] J. L. Ericksen, "Deformations possible in every isotropic, incompressible, perfectly elastic body," *Zeitschrift für Angewandte Mathematik und Physik (ZAMP)*, vol. 5, no. 6, pp. 466–489, 1954.

[69] S. Sadik and A. Yavari, "Small-on-large geometric anelasticity," *Proceedings of the Royal Society of London A*, vol. 472, no. 2195, 2016.

[70] A. Ozakin and A. Yavari, "A geometric theory of thermal stresses," *Journal of Mathematical Physics*, vol. 51, no. 3, p. 032 902, 2010.

[71] A. Yavari, "A geometric theory of growth mechanics," *Journal of Nonlinear Science*, vol. 20, pp. 781–830, 2010.

[72] T. J. Pence and H. Tsai, "Swelling-induced microchannel formation in nonlinear elasticity," *IMA Journal of Applied Mathematics*, vol. 70, no. 1, pp. 173–189, 2005.

[73] A. Golgoon, S. Sadik, and A. Yavari, "Circumferentially-symmetric finite eigenstrains in incompressible isotropic nonlinear elastic wedges," *International Journal of Non-Linear Mechanics*, vol. 84, pp. 116–129, 2016.

[74] A. Golgoon and A. Yavari, "On the stress field of a nonlinear elastic solid torus with a toroidal inclusion," *Journal of Elasticity*, vol. 128, no. 1, pp. 115–145, 2017.

[75] A. Yavari and A. Goriely, "Nonlinear elastic inclusions in isotropic solids," *Proceedings of the Royal Society A*, vol. 469, no. 2160, p. 20 130 415, 2013.